COMPUTATIONAL METHODS AND TELECOMMUNICATION IN ELECTRICAL ENGINEERING AND FINANCE

May 6-9, 2018, Sarajevo,
Bosnia and Herzegovina

book of proceedings

INTERNATIONAL
UNIVERSITY OF SARAJEVO

COMPUTATIONAL METHODS AND TELECOMMUNICATION IN ELECTRICAL ENGINEERING AND FINANCE

INTERNATIONAL UNIVERSITY OF SARAJEVO

General Chair:
Taha Imeci
International University of Sarajevo

Technical Program Chairs:
Izudin Dzafic
Tarik Namas
International University of Sarajevo

Finance Chair:
Ibrahim Inal
International University of Sarajevo

Short Course/Tutorial Chair:
Atef Elsherbeni
Colorado School of Mines

Local Arrangements Chair:
Senad Hodzic
International University of Sarajevo

Conference Secretariat:
Adnan Beganovic
International University of Sarajevo

Website Administrator:
Osman Gursoy
International University of Sarajevo

Table of Contents

Page No.

2.4 GHz Microstrip Patch Antenna for WiFi Applications

Alminko Kašibović, Aida Bubalo, Ilham Hošić

Department of Electrical Engineering
International University of Sarajevo
Sarajevo, Bosnia and Herzegovina

***Abstract* – In this project we proposed Microstrip Patch Antenna for Wireless Signal 2.4 GHz with its projection, design, simulations and final analysis. This antenna is implemented using "inset-feed" antenna design. FR-4 dielectric is used as a substrate for the proposed antenna. This antenna is useful for 2.4GHz frequency, which comes under ISM (Industrial, Scientific, and Medical) band of frequency. The designed antenna shows the return loss of -22 dB and 5.27 dBi gain at the design frequency of 2.4 GHz. Simulations will be made in Sonnet software.**

***Keywords* – Inset-feed, FR-4, microstrip patch**

I. INTRODUCTION

Microstrip patch antennas are popular due to their light weight, low profile and easy fabrication with monolithic microwave integrated circuits (MMICs). Due to their compact and planar structure Microstrip antennas are popular for their attractive applications like satellite and wireless communications [1]. Usage of wireless networks increased as consumers became aware of the advantages of this technology and as new and better applications were invented. In different countries Bluetooth has been developed to regulate the interaction of different devices in such wireless networks [2]. Despite some disadvantages of patch antennas, like low efficiency, narrow bandwidth, and less gain because of their small size and high return loss, these antennas are still very popular. By making some modifications like slot cut and different shapes many researchers have tried to overcome the demerits of these antennas [3]. The return loss of antenna is controlled by proper impedance matching of feed line and the patch. The inset feeding is one of the popular techniques for matching. Impedance of patch varies with feeding location. Various antenna performance parameters can be controlled by proper feeding technique and location [4].

II. GEOMETRY

The geometry of an antenna is mainly affected by operational frequency. Mathematical calculations are guiding the dimensions of contours [5].

Table I: Antenna Parameters

Contour	W	H	A	B	C	D.L.T.
Length	40.0	29.14	7.0	1.59	2.67	1.0

All dimensions are in millimeters. D.L.T. means Dielectric Layer Thickness. We will use an array of two patches of the following shape:

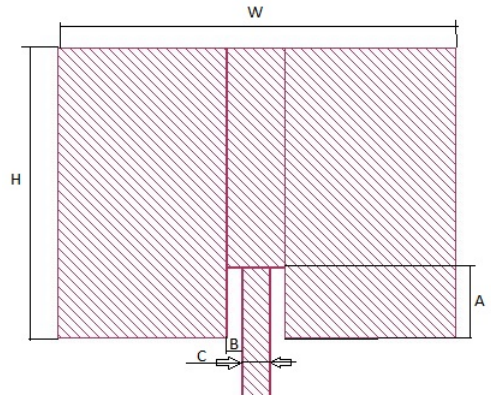

Fig. 1: Geometry

Fig. 2: S11 (Reflection)

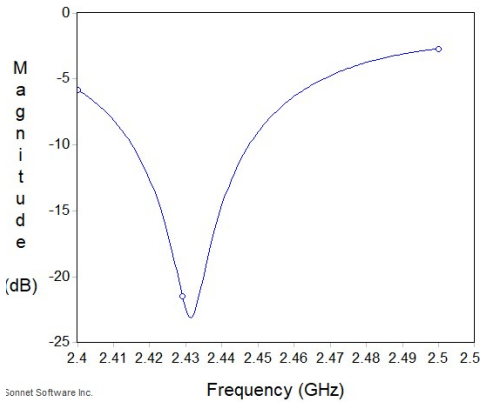

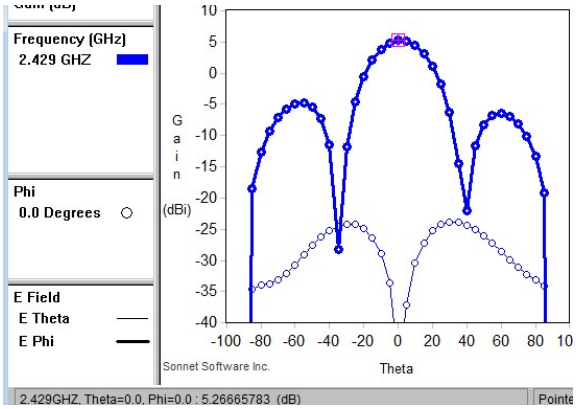

Fig. 3: Theta Polarization

III. Parametric Studies

The geometry should be flexible enough so that in the case of error during production, antenna would still work properly in default frequency range. Width and height of geometry determine operational frequency, so the only parameters that can change are A, B, C and thickness of the dielectric layer.

Parametric study is as follows:

Table II: Parametric Studies

Contour A		*Contour B*		*Contour C*	
Length	Gain [dB]	Length	Gain [dB]	Length	Gain [dB]
6.83	5.26	0.76	5.26	2.29	5.23
7.33	5.27	1.02	5.27	3.30	5.26
7.59	5.27	1.78	5.27	3.81	5.24

As it can be seen from the table, design is not affected by minor changes in geometry.

Table III: Dielectric Layer Thickness

D.L.T	0.99	0.98	1.01
Gain [dB]	5.27	5.28	5.26

As it can be seen from the Table II, small improvement can be accomplished by minor changes in contours.

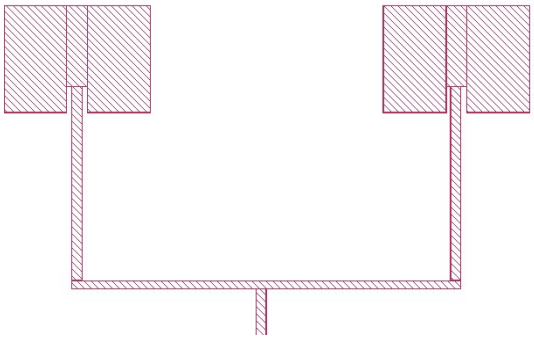

Fig. 4: Array Geometry

IV. Conclusion

In this project an antenna for WiFi applications is proposed with its scheme and simulation results. The objective of this project is to find a suitable design of an antenna that will give us the best response. After trying many different designs, and changing our approach we came to a solution that gives us the best results. Simulation outputs were most affected by feed indentation and dielectric thickness. We changed dielectric thickness from 0.4 to 1.6 mm as this range is the most common in antenna manufacturing industry. During the making of this project, we have learned a lot about electromagnetism and simulations.

V. References

[1]. Y. K. Choukiker, S. K. Behera, B. K. Pandey and R. Jyoti, "Optimization of plannar antenna for ISM band using PSO ,"2010 Second International conference on Computing, Communication and Networking Technologies, Karur, 2010, pp. 1-4..
[2]. Fan Yang et.al “Wide band E-shaped patch antennas for wireless communications,” IEEE Trans. Antennas Propag., Vol. 49, 1094 1100, 2001. F. Yang, Xue-Xia Zhang, Xiaoning Ye and Y. Rahmat-Samii, "Wide-band E-shaped patch antennas for wireless communications," in IEEE Transactions on Antennas and Propagation, vol. 49, no. 7, pp. 1094-1100, Jul 2001
[3]. P. kumar Deb, T. Moyra and P. Bhowmik, "Return loss and bandwidth enhancement of microstrip antenna using Defected Ground Structure (DGS)," 2015 2nd International Conference on Signal Processing and Integrated Networks (SPIN), Noida, 2015, pp. 25-29.
[4]. Y. Hu, D. R. Jackson, J. T. Williams, S. A. Long and V. R. Komanduri, "Characterization of the Input Impedance of the Inset-Fed Rectangular Microstrip Antenna," in IEEE Transactions on Antennas and Propagation, vol. 56, no. 10, pp. 3314-3318, Oct. 2008.
[5]. C.A. Balanis, Antenna Theory, 2nd edition. New York: John Wiley & Sons, Inc., 1997

Wind Flow Computation Over Hilly Terrain With Advanced RANS Turbulence Model

Kemal Turan
Faculty of Engineering and Natural Sciences
International University of Sarajevo
Hrasnička cesta 15, 71000 Sarajevo
kturan@ius.edu.ba

Muhamed Hadžiabdić
Faculty of Engineering and Natural Sciences
International University of Sarajevo
Hrasnička cesta 15, 71000 Sarajevo
mhadziabdic@ius.edu.ba

Abstract

The usage of wind energy is on a constant rise and today, together with solar energy, it represents the main contributor to renewable energy worldwide [1]. *In the early days of the wind exploration, the wind farms were mainly placed in offshore and flat terrains. However, as the wind energy gains in popularity, the wind farms have expanded from its traditional flat regions to hilly terrain and even into mountain regions and urban areas. This expansion brought a problem of accurate prediction of wind energy potential and equally important prediction of wind characteristics at micro-locations. Detailed information about wind at the micro-location appears to be of critical importance for a correct decision on micro-siting of wind turbines. The linear models, used by wind engineering community in the last decades, proved to be inaccurate when terrain significantly differs from the flat one* [2]. *Hence, the computational wind engineering (CWE) community turns their attention to Computational Fluid Dynamics (CFD) techniques as a solution for the problems of wind assessment on complex terrains. CFD for atmospheric flow relies on the conventional Reynolds-averaged Navier–Stokes (RANS) approach which includes turbulence models of various complexity. The complex terrain often implies complex flow dynamics that cannot be captured by the widely used two-equation k-ε model due to its fundamental deficiencies* [3]. *The present study explores the capability of an advanced four-equation ζ-f turbulence model proposed by* [4] *for predicting wind over Askervein Hill, well-documented benchmark case. The ζ-f model applies elliptic relaxation approach to the wall modeling, and it combines it with an advanced compound wall treatment to facilitate a smooth transition from wall function approach, needed when the computational mesh is coarse, to the integration of up to the wall, when mesh resolution is fine. Preliminary results show improvements comparing to the results obtained by k-ε model. The full paper will present model details as well as the presentation of various results obtained by two models.*

Keywords: *Wind energy, Askervein Hill, RANS modeling, complex terrain.*

INTRODUCTION

Assessment of wind resource and wind farm turbine siting design is important and demanding task for wind engineers. Accurate prediction of possible power production and wind flow dynamics has an essential role in the success of a wind farm project in a particular location. Experimental methods are expensive and time consuming to do assessments above. On the other side, numerical methods are relatively much cheaper and quicker. Linear and nonlinear numerical methods are commonly used techniques to compute wind speed, wind energy density, and the average annual energy production of a proposed wind farm.

Wind energy capacity is an increase over the world. Initially, the offshore and flat terrains were chosen as a wind farm location. However, wind farms have expanded to mild to rough, hilly terrains. This expansion brought another problem within, linear models, even nonlinear methods with standard turbulence model (linear eddy viscosity models, LEVMs) cannot capture the complex flow dynamics due to their fundamental deficiencies [3]. Hence, the wind engineering community turns their attention to Computational Fluid Dynamics (CFD) techniques as a solution for the problems of wind assessment on complex terrains. CFD is based on numerical solution of Navier-Stokes (N-S) equations that describe the fluid flow in all flow regimes. CFD for atmospheric flow modeling relies on the conventional Reynolds-averaged Navier–Stokes (RANS) approach which includes turbulence models of various complexity. The k-ϵ model mostly used two-equation model due to its robustness and computational efficiency. Nevertheless, the *k*-ϵ model fails to predict turbulence dynamics in complex terrains due to its fundamental deficiencies [3]. Therefore, there is a particular need for better turbulence model to accurately predict wind flow dynamic. In the last two decades, there are new generation of RANS models with better physical foundations. Durbin's eddy-viscosity type four equation $\overline{v^2}$ - *f* model and ζ-f [5] brought remarkable improvements in turbulence modeling. The ζ-f model is based on the computationally more robust version of Durbin's elliptic relaxation model. Both models are better in computing wall-bounded flow and might be a better alternative for ABL flow modeling compare to standard two-equation models.

We computed a steady wind flow over Askervein Hill with constant roughness with advanced eddy-viscosity based RANS *ζ-f* model and k-ϵ model. Even though, the hill geometry seems relatively smooth and simple in its geometry,

an accurate capturing of flow dynamics on the lee side is a challenging task for today's most advanced numerical methods. Comparisons are made with the available intensive measurement from Taylor and Tunessien [6] and other RANS results previously obtained by other researchers.

TERRAIN AND WIND CHARACTERISTICS

The Askervein hill is well-documented benchmark case frequently used for validation of CFD methods for wind computation on complex terrain. The hill is located on the west coast of island South Uist in the Outer Hebrides of Scotland. It is nearly elliptical with the minor and major axis of 1 km, and 2 km respectively oriented along NW-SE direction (see Fig. 1). The height of the Askervein hill is 116m from its surrounding ground (and 126m from the sea level); it is surrounded by flat plain at the upwind, and with relatively larger hills at the downwind direction. The hill has a moderate slope, the surface of the hill covered with grass and some flat rocks. Aerodynamic roughness is taken to be zo ≈ 0.03m by based on the field measurement [6].

The data used for the present work is the TU-03B data set which was collected for three hours period. The weather condition was neutrally stable, and the wind was blowing steadily from 210º perpendicular to the central axis of the hill. Therefore, the hills at the downwind of the hill do not affect the flow field significantly [7]. In Fig.1 reference site (RS), line A, and line AA are shown where the most of the measuring masts were located along. Wind is considered as undisturbed at RS, which is used for inlet validation. Askervein Hill can be considered as an idealized case meaning that the hill is considered isolated from the effect of other hills and atmospheric stability is considered neutral which often is not the case in the atmospheric flow. Even with this simplifications, Askervein Hill remains a challenging task for numerical computations/ simulations to match results with the full-scale measurements.

GEOMETRY AND COMPUTATIONAL SETUP

The digital terrain data is obtained from STL surface data with 20 m of resolution available from the publicly open source. The STL surface was converted to the real solid surface by surface generation and editing software (Rhinoceros 5.0). The terrain surface was rotated to align 210º incoming flow direction.

Although many studies were done on the Askervein hill, no consensus was reached about the dimension of the computational domain. Castro et al. [8] argued that domain size has no significant effects on results for the Askervein hill. In the present study domain size of 4200 m x 4200 m x 1000 m along x, y, and z-direction is adopted by centering on the hilltop respectively.

In the present work Fluent Gambit 2.4 was used to create the computational mesh from the previously established surface. The number of grid points is 180, 180 and 36 in the x, y, and z-direction respectively. Most of the grid cells are clustered around the hill (Δx= 24m, Δy= 24m, Δz_{min}=1m). The first cell layer is 1 m above the ground, and cell size expanded in the z-direction with an expansion factor of 1.2. Final mesh contains 1.2 million of hexahedral cells.

Incoming wind direction is 210 degrees concerning the Northside. The wind direction stayed constant during the measurements, and it determines the mesh orientation. The inlet is fixed on the western side of the computational domain, and the outlet is the eastern side. On the lateral side of the domain pressure boundary is imposed, and at the top side, the symmetry boundary condition is used. The wall is modeled as a rough wall with constant roughness height $z_0 = 0.03\,m$. Inflow velocity and turbulence profiles at the inlet plane were obtained from fully developed channel flow computation.

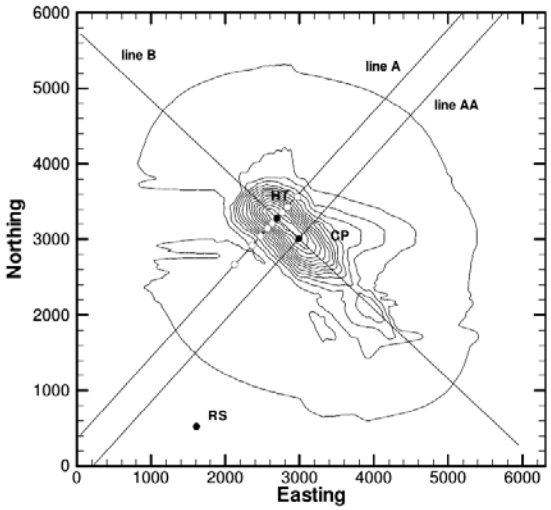

Figure 1 Askervein Hill topographic map with measurement lines.

On the lateral side of the domain pressure boundary is imposed and at the top side, the symmetry boundary condition is used. The wall is modeled as a rough wall with constant roughness height $z_0 = 0.03\,m$. Inflow velocity and turbulence profiles were obtained from fully developed channel flow computation.

T-FlowS in-house CFD code was used in all computations. The code is based on finite volume method with collocated arrangement and second-order accuracy in both time and space. The computational settings include the SIMPLE algorithm for pressure-velocity coupling and SMART scheme for the convective terms and the central differencing scheme for the diffusion terms in the momentum equation and the turbulence model equations. The flow field is initialized by the values set for the inlet boundary conditions. The convergence criteria of the scaled residuals for all variables and the continuity equation are set as 10^{-7}, time step was set to 0.01.

The inlet profile is obtained by channel computation by using data from the reference station (RS) measurements during the run TU-03B. The mean flow values at RS is U = 8.6 m/s at z = 10 m and friction velocity is u∗= 0.61m/s. The results from the ζ-f model are shown in Fig. 2 next to measurements. A good match between the measured and computed results confirms that correct inflow condition was

imposed to the main domain. Roughness value significantly affects the results in the inflow plane.

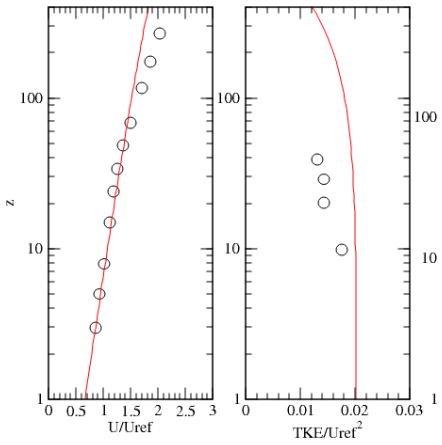

Figure 2 Computed vertical profiles of a channel flow with a rough-wall boundary, using ζ-f model. Normalized turbulent kinetic energy (TKE) (right), normalized streamwise velocity (left). Note: *Uref* is the streamwise velocity, at reference station 10*m* above the ground level.

RESULTS

The measurements were presented by Taylor and Teunissen [6] in a nondimensional way: the mean velocity values are given in the form of the fractional speed-up ratio (ΔS):

$$\Delta S(x, y, \Delta z) = \frac{U(x, y, \Delta z) - U_0(\Delta z)}{U_0(\Delta z)} \qquad (1)$$

where *Δz* is the height above the ground and U_0 (Δz) is the value of the undisturbed streamwise velocity at the inlet of the domain. The turbulent kinetic energy *k* is given in as:

$$k^*(x, y, \Delta z) = \frac{k(x, y, \Delta z)}{U_{10}^2} \qquad (2)$$

where U_{10} is the mean streamwise velocity at 10 m above the ground level at RS.

The incoming wind speed for the TU-03B data set is 8.9 m/s, the incoming angle is 210º, and it is assumed constant. Fig. 3 shows a comparison of the fractional speed-up ratio for steady inflow condition along the line A and the line AA (see the Figure 1) at 10 m above the ground level. The results along line AA is in good agreement with experimental results of Taylor and Teunissen and Castro et al. [6]. More considerable differences of ΔS (28 %) occurred in the downstream of the line A after 390 m of the HT (hilltop) seen in the Fig. 3 where the intermittent separation and recirculation of flow occurs due to hill slope. In this region (downstream of HT), both k-ϵ

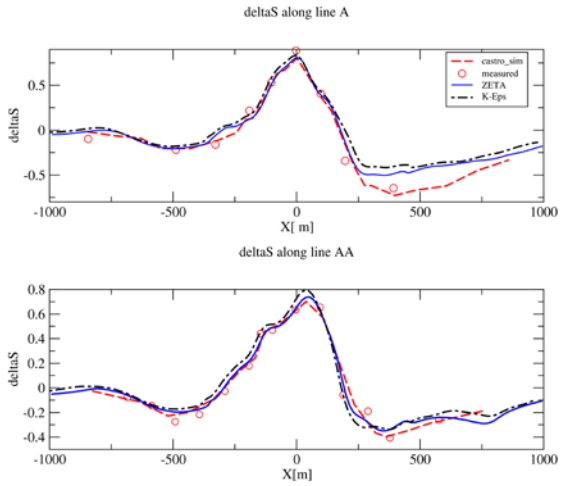

Figure 3 Results showing ΔS along the line A (upper), and line AA (lower). Note that x =0 in the upper figure corresponds the hilltop (HT), and in the lower center point (CT).

and ζ-f model overpredicted the minimum value of the ΔS. This region sensitive to grid horizontal grid resolution, first cell height from the wall, and the roughness value. Therefore, any change in those parameters above will lead a different result on the lee side of the hill.

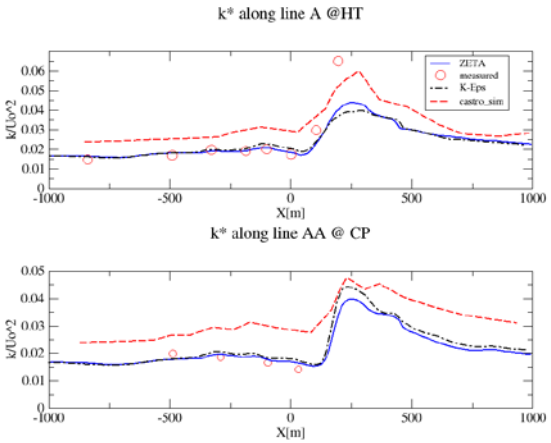

Figure 4 Results showing the normalized turbulent kinetic energy k* along the line A (upper), and line AA (lower). Note that x =0 in the upper figure correspond the hilltop (HT), and in the lower center point (CT).

The resulting values of k^*(normalized turbulent kinetic energy with reference velocity at 10 m agl. at RS) along line AA and line A are shown in Fig. 4. The present results, using the standard k - ε and ζ-f model are in good agreement with experimental values on the windward side of the hill on both line A and line AA. However, significant discrepancies found on the lee side of the hill, i.e., k^* is underestimated (46 %) along the line A. The ζ-f model predicts better maximum k^* along the line A compare to the k-ϵ model. The results obtained by Castro et al. [7] using standard k-ϵ turbulence model overestimated k^* even on the windward side of the hill where the flow is undisturbed, i.e., their results of k^* deviates around 12 % from the measurements. However, Castro et al.

captured the peak value on the lee-side of the hill where the flow is separated along the line A much better. Higher values of turbulent kinetic energy on the lee-side are likely due to large-scale intermittency or unsteady flow separation which is not modeled with RANS equations [7].

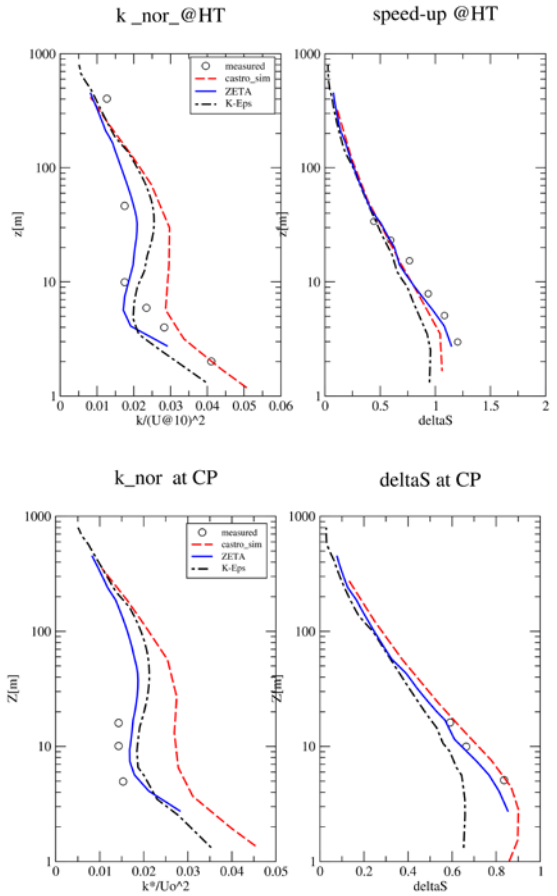

Figure 5 Vertical profiles of the fractional speed-up ratio (ΔS) (right), and normalized turbulent kinetic energy $k^*/U_0\text{^}2$ (left) at the HT (upper), and CP (below).

In the Fig. 5 a comparison of the vertical profiles of the fractional speed-up and normalized turbulent kinetic energy at the HT and CP with available measurements data are presented. The results are in good agreement with measurement in general, particularly ζ-f model outperformed k-ϵ model, and result published by Castro et al. The k^* increased as the distance to the ground decreased particularly more visible at HT. Experimental results are indicating increasing ΔS with lower heights, but computation gives nearly constant profile below 5m agl.

CONCLUSION

Steady three-dimensional wind flow over complex terrain has been computed with elliptic relaxation ζ-f, and standard k-ϵ model under neutral stability condition. Numerical results from the two different model was compared with available experimental data. The results are indicating that ζ-f model can predict mean velocity and turbulent kinetic energy closer to the measurements. Hence, elliptic relaxation ζ -f model is suitable for atmospheric boundary layer flow.

From the results, it is clear that ζ -f model might substitute the two-equation models, without compromising much from the computational cost and robustness. The model showed positive improvements in the computation of the ABL flow in complex terrain over standard two equation k-ϵ model. In more complex terrains ζ-f models benefit would be more profound.

References

[1] European Wind Energy Association, "EWEA 2013 Annual Report," Eur. Wind Energy Assoc., 2013.

[2] N. G. Mortensen, A. J. Bowen, and I. Antoniou, "IMPROVING WAsP PREDICTIONS IN (TOO) COMPLEX TERRAIN," Ewec, p. 9, 2006.

[3] K. Hanjalic, "Will RANS Survive LES? A View of Perspectives," J. Fluids Eng., vol. 127, no. 5, p. 831, 2005.

[4] K. Hanjalić, M. Popovac, and M. Hadžiabdić, "A robust near-wall elliptic-relaxation eddy-viscosity turbulence model for CFD," Int. J. Heat Fluid Flow, vol. 25, no. 6, pp. 1047–1051, 2004.

[5] K. Hanjalić, M. Popovac, and M. Hadžiabdić, "A robust near-wall elliptic-relaxation eddy-viscosity turbulence model for CFD," Int. J. Heat Fluid Flow, vol. 25, no. 6, pp. 1047–1051, 2004.

[6] P. a. Taylor and H. W. Teunissen, "Askervein Hill Project Report - 1983.pdf." 1983.

[7] F. A. Castro, J. M. L. M. Palma, and A. S. Lopes, "Simulation of the askervein flow. Part 1: Reynolds averaged navier-stokes equations (k-epsilon turbulence model)," Boundary-Layer Meteorol., vol. 107, no. 3, pp. 501–530, 2003.

[8] F. A. Castro, "Numerical Methods for the Simulation of Atmospheric Flows over Complex Terrain," 1997.

Weighted Additive Wavelet Transform for Ultrasonic Image Despeckling

Nur Huseyin Kaplan[1]
[1]*Department of Electrical and Electronics Engineering*
Erzurum Technical University
Erzurum, Turkey
huseyin.kaplan@erzurum.edu.tr

Isin Erer[2]
[2]*Department of Electronics and Communication Engineering*
Istanbul Technical University
Istanbul, Turkey
ierer@itu.edu.tr

***Abstract*—In this study, a weighted additive wavelet transform (WATWT) based despeckling algorithm for ultrasonic images is proposed. WATWT decomposes the input image into several detail layers and a residual image. The residual image can be considered as the despeckled result. The weighting function used is similar to the range kernel of bilateral filter. The weighting function is simply determined by enhancing quantitative indexes. Quantitative comparisons, as well as visual comparisons show that the performance of the proposed method is better than the former methods.**

***Index Terms*—Ultrasonic image, despeckling, wavelets, image processing**

I. Introduction

Although ultrasounic imaging is a safe and low-cost image modality, the applications of ultrasonic imaging like diagnosis is limited because of the poor quality of the images. The main reason for poor image quality is speckle noise [1].

Speckle is a multiplicative noise, which is generated by random phased scatterers within the ultrasound beam resolution cells [2]. Speckle noise degrades the image quality, and makes it difficult to discriminant details which is important for medical diagnosis [1], [2]

Speckle noise reduction (despeckling) is a very important process, in which the speckle present in the image is surpressed while the important details of the image is kept as much as possible [1]–[6].

The conventional methods, such as Enhanced Lee Filtering (ELH) [3], provide despeckled images, however they cannot provide good results when edge preserving should be considered, along with despeckling. In order to perform smoothing with edge preserving, bilateral filters (BF) are widely used [4]. BF based SAR despeckling is performed in [5], by determining the bilateral filter parameters according to the despeckling indexes, equivalent number of looks (ENL) [6] and edge save index (ESI) [7]. Recently, an improved bilateral filter (IBF) based SAR despeckling algorithm has been proposed [5]. The spatial parameter of the bilateral filter is eliminated and adjacent homogeneous pixels are utilized to compute the output of the filter for the current pixel. The range parameter is again determined so as to enhance ENL and ESI indexes [5]. In this study, a weighted additive wavelet transform (WAWT) [8] is used for SAR image despeckling. The WAWT is a combination of the well-known additive wavelet transform [9] and a weighting function similar to the Gaussian range kernel in bilateral filtering [8].

II. Ultrasonic Image Despeckling by Weighted Additive Wavelet Transform

Weighted AWT (WAWT) output of an image at the pixel location p can be given as

$$W[I]_p = \frac{1}{k}\sum_{q\in S} h(q)c_{\sigma_r}(p,q)I_q \tag{1}$$

Here, q is the location of neighbouring pixels, $h(q)$ is the spline filter [9] and σ_r is the Gaussian kernel. The normalization parameter is:

$$k = \sum_{q\in S} h(q)c_{\sigma_r}(p,q) \tag{2}$$

and the Gaussian kernel

$$c_{\sigma_r}(p,q) = \frac{1}{\sigma_r^2} exp(-\frac{[I]_p^2 + [I]_q^2}{\sigma_r^2} \tag{3}$$

The output of this filter is the smoothed image by WAWT. For further decomposition, at each level l the filter h is extended by filling $2(i-1)$ zeros between the initial entries and double the σ_r parameter at each level. The filter output at ith level can be given as:

$$W^i[I]_p = \frac{1}{k}\sum_{q\in S} h_{i-1}(q)c_{\sigma_r}^{i-1}(p,q)W^i[I]_q \tag{4}$$

The difference between two adjacent filtering outputs is called the detail layer of the image at that level.

$$DET^i[I] = W^{i-1}[I] - W^i[I] \tag{5}$$

For L levels of decomposition, the original image is decomposed as:

$$I = W^L[I] + \sum_{i=1}^{L} DET^i[I] \tag{6}$$

into its detail layers and the residual image. Due to the weighting parameter, the image details are kept in the residual

image while the speckle and redundant information are transferred into the detail layers. Thus residual image provides the despeckled result. The despeckling algorithm does not require any further postprocessing unlike bilateral filtering based ones [4], [5]. WAWT, also do not require determination of a window size as in bilateral filtering. The window size of the bicubic spline filter is directly chosen as the window size.

The parameter selection is made by optimizing the ENL and ESI metrics. Greater ENL values indicate the despeckling capability, while higher ESI values show the edge preservation ability in the horizontal (ESI-H) or vertical (ESI-V) directions. The optimum σ_r value is found experimentally as 0.06.

III. Experimental results

The despeckling results obtained by the proposed method are compared to Enhanced Lee Filtering (ELF) and Improved Bilateral Filtering (IBF) [5]. For bilateral filtering, the corresponding filter is applied 2 times after halving the value of the σ_r parameter as postprocessing.

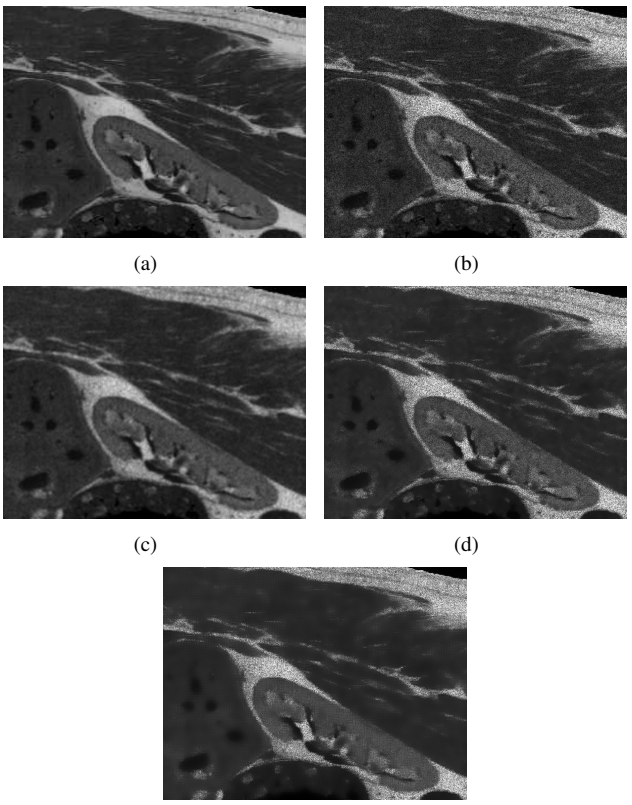

(a) (b) (c) (d) (e)

Fig. 1. (a) Original Kidney image (b)Synthetic noisy image, Despeckling Results for (c) Enhanced Lee Filtering [3] (d) Improved Bilateral Filtering [5] (e) Proposed method

Fig.1.a shows the original ultrasonic image used for despeckling, available at http://field-ii.dk/?examples.html. Fig.1.b is the synthetic noisy image and Fig.1.c-e, show despeckling results obtained for Enhanced Lee Filtering (ELF) [3], Improved Bilateral Filtering (IBF) [5], and the proposed method, respectively. It is seen that ELF yields blurred result, but still a great amount of speckle remains. Both IBF and proposed method provide clearer results however the amount of speckle is more in IBF result.

TABLE I
Quantitative Comparison of Fig.1

Figure	Methods	ENL Smooth Area	ESI Horizontal	ESI Vertical
Fig.2	Original	164.6122	1	1
	ELF [3]	379.2332	0.1566	0.1893
	IBF [5]	430.1681	0.5365	0.5439
	Proposed	**605.0674**	**0.6223**	**0.6305**

The smooth area in Fig.1 is selected for ESI metric. The performance metrics evaluated for Fig.1 are given in Table 1. Table 1 shows that the best scores are obtained by the proposed method. Thus, the proposed method despeckles the image better than the former methods while ensuring good edge preservation.

IV. Conclusions

The weighted additive wavelet transform is applied to ultrasonic image despeckling. The speckled image is decomposed into a residual and several detail subimages. The residual image represents the despeckled result. The weight parameter is determined by optimizing ENL and ESI indexes. The method may be considered as multiscale bilateral filtering where the Gaussian kernel is approximated by the a trous kernel which eliminates further postprocessing unlike former bilateral filter based methods. Both visual and quantitative comparisons show that the proposed method outperforms former methods, both in despeckling and in edge preserving qualities.

References

[1] C. Binjin, X. Yang, X. Jianguo, and X. Haihong, "Ultrasonic speckle suppression based on a novel multiscale thresholding technique." *2010 5th International Symposium On I/V Communications and Mobile Network*, Rabat, pp. 1-5, 2010.

[2] J. Jin, Y. Liu, Q. Wang, and S. Yi, "Ultrasonic speckle reduction based on soft thresholding in quaternion wavelet domain." *2012 IEEE International Instrumentation and Measurement Technology Conference Proceedings*, Graz, 2012.

[3] A. Lopes, R. Touzi, and W. Nezry, "Adaptive speckle filters and scene heterogeneity." *IEEE Transactions on Geoscience and Remote Sensing.* vol. 28, pp. 992–1000, 1990.

[4] W.G. Zhang, F. Liu, and L.C. Jiao, "SAR image despeckling via bilateral filtering." *Electronics Letters* vol. 45, no.15, pp. 781-783, 2009.

[5] W.G. Zhang, Q. Zhang, and C.S. Yang, "Improved bilateral filtering for SAR image despeckling." *Electronics Letters* vol. 47, no. 4, pp. 286-288, 2011.

[6] H. Xie, L.E. Pierce, and F.T. Ulaby, "SAR speckle reduction using wavelet denoising and Markov random field modeling." *IEEE Transactions on Geoscience Remote Sensing*. vol. 40, no. 10, pp. 2196-2212, 2002.

[7] L.L. Tang, P. Jiang, C.D.Dai, and J.J. Thomas, "Evaluation of smoothing filters suppressing speckle noise on SAR images." *Remote Sensing of Environment*, vol. 11, no. 3, pp. 206-211, 1996.

[8] R. Fattal, "Edge avoiding wavelets and their applications." *ACM. Trans. Graphics*, vol. 28, no. 3, pp. 1–10, 2009.

[9] J. Nunez, X. Otazu, O. Fors, A. Prades, V. Pala, and R. Arbiol, "Multiresolution-based image fusion with additive wavelet decomposition." *IEEE Transactions on Geoscience and Remote Sensing*, vol. 37, no.3, pp. 1204-1211, 1999.

Voltage-mode CMOS Ternary Inverter Circuit

Fatma Sarica, Avni Morgul
Department of Electrical- Electronics Engineering
Maltepe University
Istanbul, Turkey
e-mail: fatmasarica, avnimorgul @maltepe.edu.tr

***Abstract*—In this paper, voltage mode CMOS ternary inverter circuit is proposed. Inverter circuit is designed in a 0.18µm standard CMOS technology with a supply voltage of ±0.9V and simulated using HSpice.**

Keywords—multiple-valued logic; inverter; ternary; voltage-mode;

I. INTRODUCTION

The use of circuits with more than two logic levels namely Multi-valued logic (MVL) has been considered as a solution to the interconnection and routing problem of the large-scale integrated circuits. Such circuits have a potential for increasing the information content on a single wire, thus reducing chip area consumed by interconnection wiring and functional units in very large scale integration. MVL circuits can be realized as current-mode or voltage-mode. Current-mode circuits allow higher radices and faster circuits at the expense of higher power consumption and larger chip sizes, which becomes more problematic as the radix increases [1-2]. On the other hand, voltage mode circuits has the advantage of lower power consumption. But the circuit realizations are complex and the supply voltage ranges limit the radices.

Among all the bases, it has been shown that base-3 is the most efficient radix to implement the MVL circuits which are also known as *ternary circuits* [3].

It is well-known that inverter is one of the most important circuit elements in digital design which is also true for the MVL circuits. The inverter design is an important starting point for establishing a MVL circuit library. Various voltage-mode multi-valued inverter circuit studies can be found in the literature where most of them are far from optimum, according to VLSI design criteria. Some of the proposed ternary circuits are using resistor elements [4-5] which is not suitable for integrated circuit design. Some others use CMOS circuit elements that require a nonstandard production process such as depletion devices [6-7]. There are also studies that use multi-threshold devices [8-9] to adjust the voltage levels at the output. Another approach to set the voltage level is using several voltage supplies [10-11] which obviously is an unwanted situation in VLSI design.

In this paper we proposed a new voltage-mode ternary inverter circuit that uses standard n-well CMOS devices. The circuit uses ±0.9V dual voltage source as supply voltage. Transistor dimensions are in minimum ranges to reduce the total area consumption.

II. PROPOSED TERNARY INVERTER

A standard ternary inverter is a single input single output circuit where the input output relationship is given by

$$\bar{x} = 2 - x \tag{1}$$

where x is considered as an input and ‘2’ corresponds to the high level, ‘1’ corresponds to the middle level and ‘0’ corresponds to the low level. Voltage levels associated with the logic levels are given in Table 1.

TABLE I. TERNARY LOGIC LEVELS

Voltage Level	Logic Level
+V	2
0	1
-V	0

The ternary inverter circuit proposed is shown in Fig.1. The idea lies behind the circuit operation is basically based on binary inverter circuit principle. When a ternary input signal is applied to a standard binary inverter with dual power supplies, the inverter output can successfully produces logic level ‘0’ and ‘2’ but fails at logic level ‘1’.

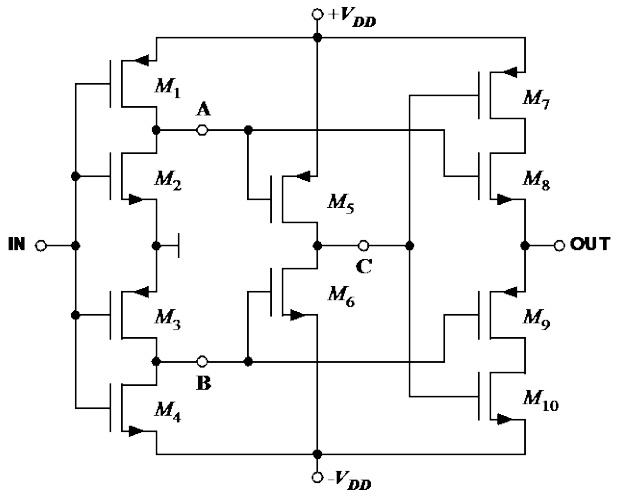

Fig. 1. Proposed ternary inverter circuit

As it can be observed from the voltage transfer characteristic given in Fig. 2, if a standard binary inverter is driven with

ternary input it does not remain stable around 0V (logic level '1') because of the steep transition around 0V.

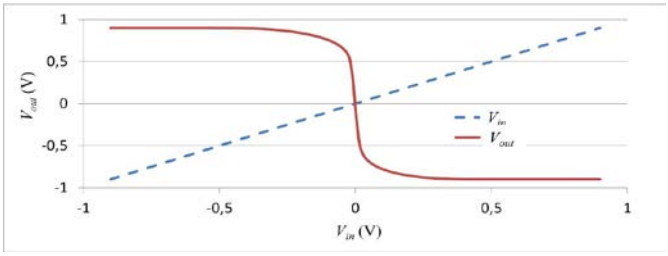

Fig. 2. Ternary input signal applied to dual suppy standard inverter

To overcome this problem, two inverters made of M_1-M_2 and M_3-M_4 transistor pairs, shown in Figure 3, are used. The input signal is applied simultaneously to these transistor pairs inverts the input signals into two discrete levels, which are positive and negative levels at the nodes **A** and **B**. Voltage transfer characteristics of these positive and negative inverters are shown in Fig. 4.

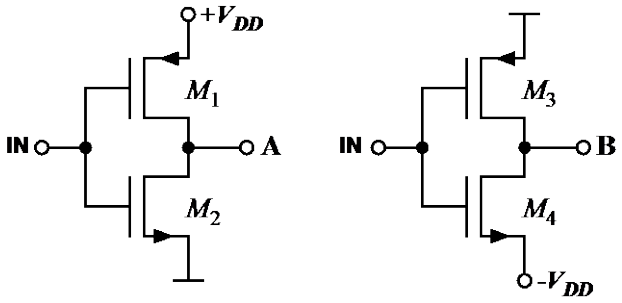

Fig. 3. Positive and negative inverters

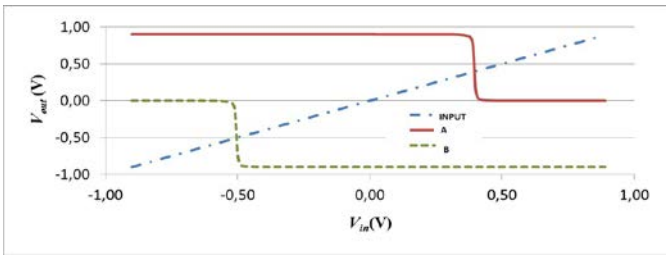

Fig. 4. Voltage transfer characteristics of the positive and negative inverters

These *A* and *B* signals are applied to M_5-M_6 transistor pairs to transform the input signal to discrete level ternary signal with a considerably high noise margin. This reshaped input signal is marked as '**C**' in Fig.1 and applied to the M_7-M_{10} transistors where M_8 and M_9 are controlled by the **A** and **B** signals respectively, that are produced by the positive and negative inverters. If the input logic becomes '0', **A**, **B**, and **C** signals become '2', '1' and '0' respectively and the output circuit finds a path to the V_{DD} through M_7 and M_8 and becomes logic '2'. If the input logic becomes '1', **A**, **B** and **C** signals become '2', '1' and '1' respectively and makes the output logic '1'. Finally, applying the '2' to the input results **A**, **B**, and **C** signals to be '1', '0', and '2' respectively and output finds a path to $-V_{DD}$ through M_9 and M_{10} transistors and become logic '0'.

III. Simulation Results

The proposed ternary inverter circuit is designed and simulated in a standard 0.18µm CMOS technology. The circuit operates under dual power supply voltages which are ±0.9V. The transistor dimensions are chosen to be *W/L*=0.36/0.18 (in µm) for all transistors. DC transfer characteristic of the proposed inverter circuit is shown in Fig. 5.

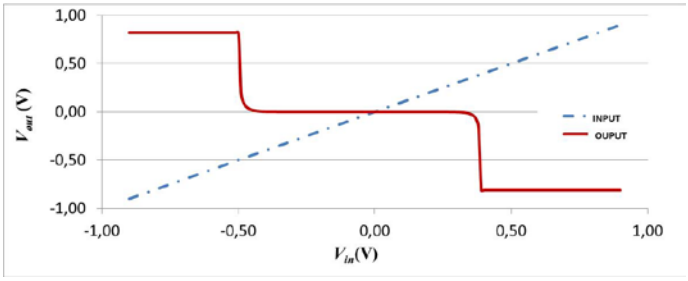

Fig. 5. Ternary inverter output

IV. Conclusion

A new voltage mode ternary CMOS inverter circuit has been proposed. The circuit uses only minimum size standard CMOS transistors and dual power supplies. Operation of the circuit has been verified using HSpice simulations with 0.18µm CMOS fabrication technology.

References

[1] Temel, T., A. Morgul, and N. Aydin, "Signed Higher-Radix Full-Adder Algorithm and Implementation with Current-Mode Multi-Valued Logic Circuits", *IEE Proceedings-Circuits, Devices and Systems*, vol.153, no.5, pp.489-496, 2006.

[2] T. Temel, ed., System and Circuit Design for Biologically-Inspired Intelligent Learning. *IGI Global*, 2010.

[3] Hayes, B., "Computing Science: Third Base", *American Scientist*, vol. 89, no.6, pp. 490-494, 2001.

[4] Wu, X.W. and Prosser, F.P., "CMOS Ternary Logic Circuits", *IEE Proceedings G-Circuits, Devices and Systems*, vol. *137*, no.1, pp.21-27, 1990.

[5] Dhande, A. P., Narkhede, S.S., and Dudam, S. S., "VLSI Implementation of Ternary Gates Using Tanner Tool", *Devices, Circuits and Systems (ICDCS), IEEE 2nd International Conference on*, pp. 1-5, 2014.

[6] Heung, A. and Mouftah, H.T., "Depletion/Enhancement CMOS for a Lower Power Family of Three-Valued Logic Circuits", *IEEE Journal of Solid-State Circuits*, vol.20, no.2, pp.609-616, 1985.

[7] Balla, P. C. and A. Antoniou, "Low Power Dissipation MOS Ternary Logic Family", *IEEE Journal of Solid-State Circuits*, vol. 19, no. 5, pp. 739-749, 1984.

[8] Dhande, A. P. and V. T. Ingole, "Design and Implementation of 2 bit Ternary ALU Slice", *Proc. Int. Conf. IEEE-Sci. Electron., Technol. Inf. Telecommun*, pp. 17-21, 2005.

[9] Doostaregan, A., M. H. Moaiyeri, K. Navi, and O. Hashemipour, "On the Design of New Low-Power CMOS Standard Ternary Logic Gates", I*Computer Architecture and Digital Systems (CADS), 15th CSI International Symposium on*, pp. 115-120, 2010.

[10] Toto, F., and R. Saletti, "CMOS Dynamic Ternary Circuit with Full Logic Swing and Zero-Static Power Consumption", *Electronics Letters*, vol.34, no. 11, pp.1083-1084, 1998.

[11] Sendi, M.S.E., M.Sharifkhani, and A.M. Sodagar, "CMOS-Compatible Structure for Voltage-Mode Multiple-Valued Logic Circuits", *Electronics, Circuits and Systems (ICECS), 18th IEEE International Conference on*, pp. 438-441, 2011.

T Shaped Circular Sector Patch Antenna

G. Kemal Oğuz, B. Furkan Genç, Göksel Çankaya, Kaan İrken, Ş. Taha İmeci
Department of Electrical and Electronics Engineering
Istanbul Commerce University
Istanbul, Turkey

***Abstract*— In this paper, a t shaped circular sector patch antenna is designed, simulated, fabricated. The operating frequency is 15.5 GHz with -17.5 dB input match and 6.67 dB gain. Moreover, the antenna has very simple structure thus gathering less fabrication errors when we compared to previously similar works.**

Keywords—Single band; T shaped Antenna; microstrip patch antenna..

I. INTRODUCTION

Microsrtip antennas are used for number of wireless applications such as WLAN, Wi-Fi, Bluetooth and many other applications. A simple microstrip patch antenna consists of a conducting patch and ground plane between them is a dielectric medium called the substrate having a particular value of dielectric constant.[1] Fr4 is used for this antenna. Circular patches were reported to lose less energy by radiation and thus provide larger quality factors than other configurations such as rectangular patches [2].We used notch cutting method in order to adjust the frequency bandwidth. By doing this we prevented the narrow bandwidth. Antenna was designed and simulated by using Sonnet Suites [3].

II. DESIGN AND SIMULATION RESULTS

When a microstrip patch antenna are being designed we have to consider some mathematical parameters such as width of the metallic path, patch length, effective length and EPSILON-r. Adjusting the sizes of bottom rectangular we increased the gain.Fr4' s thickness is 1.6 mm. = 4.4. We can find the width with the following formula. Where, c = speed of light E_r = Dielectric constant of substrate.[5]

$$W = \frac{c}{2f_0\sqrt{\frac{(E_r+1)}{2}}} \quad (1)$$

$$E_{reff} = \frac{E_r+1}{2} + \frac{E_r-1}{2}\left[1+12\frac{h}{W}\right]^{\frac{-1}{2}} \quad (2)$$

Calculation of length extension;

$$\Delta = 0.412 \times h \frac{\left(E_{reff}+0.3\right)\left(\frac{W}{h}+0.264\right)}{\left(E_{reff}-0.258\right)\left(\frac{W}{h}+0.8\right)} \quad (3)$$

Where h = height of the substrate also the lenth of the patch is can be calculated from

$$L = \frac{C_0}{2f_r\sqrt{E_{reff}}} - 2\Delta L \quad (4)$$

We changed our feeding point and we looked our simulation results. By doing this we found the appropriate point and when this point blocked the cross polarization we found the best place. We used coaxial feeding for current density and adjusted the S11. By using the above equations we designed our antenna , a circular microstrip patch antenna is designed at a resonant frequency of 15.5 GHz.

TABLE II. FREQUENCIES, S11 AND GAİN TABLE FOR DIFFERENT THICKNESS

Thickness	***Frequency***	***S11***	***Gain***
1.59 mm	15.7 GHz	-9.08 dB	6.67 dB
1.65 mm	15.7 GHz	-9.19 dB	6.35 dB
1.70 mm	15.7 GHz	-9.25 dB	6.30 dB
1.75 mm	15.7 GHz	-9.30 dB	6.25 dB

We have successfully built our antenna according to its design paramaters. Its shown in figure 2.

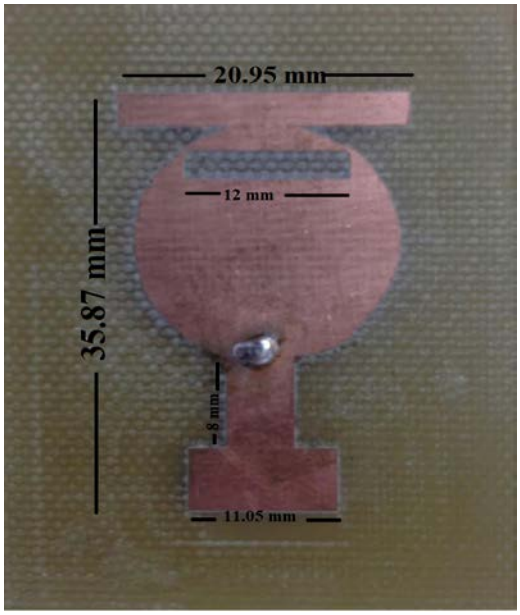

Fig. 1 Top view of the fabricated antenna

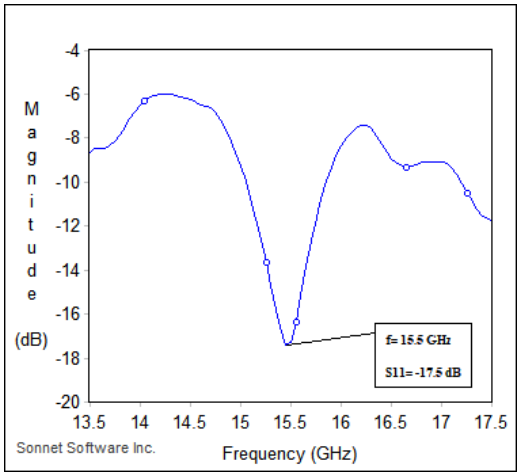

Fig 2. Simulated S11 graph of the designed antenna

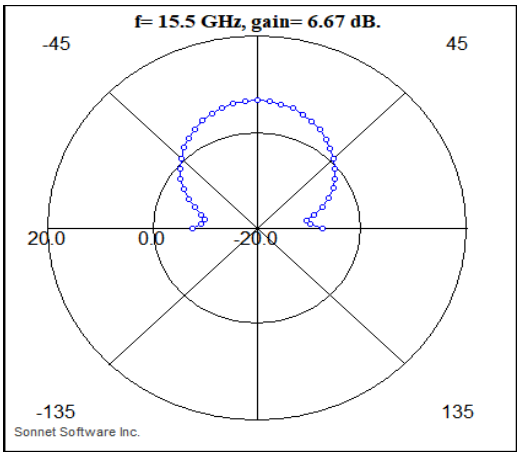

Fig 3.simulated gain graph of the designed antenna

III. CONCLUSION

In this work t-shaped circular sector patch antenna was designed and simulated. The operating frequency is 15.5 GHz with -17.5 dB input match and 6.67 dB gain.. Proposed antenna can be used in different applications such as in wireless communication, S band applications etc. Fabrication process of the antenna is continuing.

IV. ACKNOWLEGMENT

This research was supported by Istanbul Commerce University we rhank our colleagues from Istanbul Commerce University who provided insight and expertise that greatly assisted the research , although they may not agree with all of the interpretations /conclusions of this paper.

V. REFERENCES

[1] M. A. Afridi, “Microstrip Patch antenna – Designing at 2.4 Gjz Frequency,” Science Signpost Publishing, Biological and Chemical Research, Vol. 2015 , 128-132, 2015.

[2] G. K. Oğuz, Ş. T. İmeci, “A Compact Size Circular Sector Patch Antenna For Ku-band Applications”, Applied Computational Electromagnetics Society Symposium (ACES), Electronic ISBN: 978-0-9960078-3-2, March 2017.

[3] Sonnet Suites, version 14.52, www.sonnetsoftware.com.

[4] V. Thakur, S. Kashyap, “A Review Paper on Techniques and design for Microstrip Patch Antenna”, International Journal of Advanced Reasearch in Electrical, Electronics and Instrumantation Engineering, Vol. 4, Issue 2, February 2015.

[5] N. Kalambe, D. Thakur, S. Paul, “Review of Microstrip Patch antenna Using UWB for Wireless Communication Devices”, International Journal of Computer Science and Mobile Computing, Vol. 4, Issue. 1, pg- 128-133, January 2015.

Stock Index Forecasting using Wavelet Decomposed Neural Networks

Ajla Kulaglic
Faculty of Computer and Informatics Engineering,
Istanbul Technical University,
Istanbul, Turkey
kulaglic@itu.edu.tr

Burak Berk Üstündağ
Faculty of Computer and Informatics Engineering,
Istanbul Technical University,
Istanbul, Turkey
berk@berk.tc

***Abstract*— In this study, we discuss forecasting strategies based on the assumption that the time series characteristics include different time scales. Firstly, wavelet decomposition of the original time series is performed for the purpose to decompose the data into varying scales of temporal resolution. In the next phase, each subseries is used to forecast stock index rates using Neural Network model. The presented model showed a consistent performance in predicting the stock index rates.**

Keywords—*wavelet neural network, discrete wavelet transformation, neural networks, stock index forecasting, STOXX Europe 600 index, financial time series,*

I. INTRODUCTION

Financial market is a complex system involving huge amount of information to produce an output. Those information ranging from fundamental information to socio-political events and news to investor's behavior to produce an outcome [1]. These modeling approaches due to a complex market dynamics and large-scale structural shifts in economy failures to accurately represent and predict big movements in national and financial markets. Finance literature suggests two approaches for predicting the movements of stock prices: fundamental and technical analysis [1]. As the name saying, fundamental analysis includes fundamental indicators of a market, such as Return on Equity (ROE), Earning Per Share (EPS) and Price to Earnings (PE) ration are used, while in technical analysis the stock prices changes are predicted based on the behavior of previous stock price values. In the context of financial modeling and predicting the movements of stock prices machine learning techniques can assist. The capability of various machine learning techniques to capture and model non-stationary and non-linear data cause their wide applicability in time series forecasting [4,5,6,7,8 and 9]. These models due to their limitations suffer from the problem of overfitting and getting stuck in local optima. Overcoming these issues and accomplish accuracy of these models can be done by improving the algorithms, preprocessing the data or both [2]. The data preprocessing allows us to transform the data into a format that reveals certain characteristics. In recent times, signal processing techniques have been used for decomposition. The time series mostly using different variations of Wavelet Transformation (WT) are decomposed into time-frequency and time-domain. Good local representation of a signal in both time and frequency domain, simultaneously is one of the main advantages of WT. Fourier Transform (FT) decomposes the signal only in frequency domain where the information related to occurrence of frequency is not captured and it eliminates the time resolution [2]. Practical applications of WT in finance and economics can be found in [2,3,5,6,9 and 10]. In [2] they use modified version of Discrete WT (DWT); where they overcome the requirement for data to be dyadic and have the highly dependent output. Modified DWT (MDWT) is circular shift invariant and is not limited with the dyadic length constraint. Several different Neural Network (NN) models have been adopted to predict the financial time series, especially stock prices [4,5,6,7,8 and 9]. In [1] they use Recurrent Neural Network (RNN) for financial forecasting with their ability to represent certain computational structures in a parsimonious mode. In [3] they use Dynamic RNN where they provided five-days ahead forecasts. In [2] the temporal relationship series are constructed via internal states, while in [3] by incorporating autoregressive filters into a full RNN structure a temporal dimension is implemented. The paper presents an approach depicting the use of wavelet transformation for decomposition time series data and the use of wavelet coefficients as inputs to the self-organizing map for forecasting performance. The paper is organized as follows. Section 2 presents the briefly explanation of methods and materials used in this study. Section 3 discusses results and section 4 provides concluding remarks.

II. METHODS AND MATERIALS

A. Data Set

This study examined STOXX Europe 600 index derived from STOXX Europe Total Market Index (TMI) [11]. The STOXX Europe 600 represents companies across 17 countries of the European region. The data are collected day-by-day from 01.01.2000 to 31.12.2011 except weekends and holidays, including 2871 points. Special attention was paid to stock market crash of March 2003 and March 2009. The idea behind the selection of this period was to test the methodology under extreme scenarios within sudden changes in time series data. The input data set, with its decomposition is shown in Fig. 1.

B. Wavelet Decomposed Neural Network

Wavelet Decomposed Neural Network (DWNN) combine the theory of wavelet transformations and neural networks in one. Firstly, the original data are decomposed into discrete wavelets by DWT so unclear temporal structures are exposed for further evaluation of the data. Secondly, the decomposed data are used as an input element to a neural network to capture valuable information during the training processes. The main idea in WDNN is the wavelet decomposition of the time-series

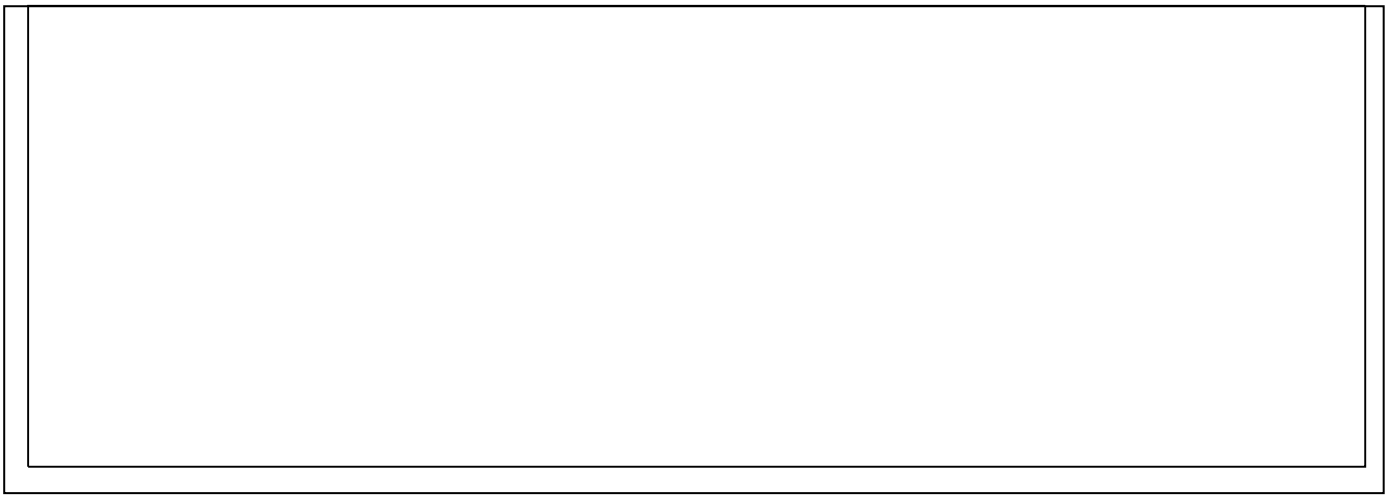

Fig.1. Scheme of proposed model

data and the application of the DWT as input of NN model. The used model is represented in Fig. 1.

III. Results

The changes in stock index market typically not last for a long time [1]. The methodology used in this study considered the decomposed short-term historical stock index market prices as well as the day of year as inputs. The overall procedure is governed by the following equation:

$$y(k) = f(y(k-1), y(k-2), y(k-3),..., y(k-n), D(k)) \quad (1)$$

where y(k) is the decomposed stock index price at time k, n is the number of historical days, and D(k) is the day of year. The performance of DWNNs are evaluated using the determination coefficient (R^2) and the root mean square error (RMSE). In this study, as well as in study [2] the level of decomposition is 3, with different arrangement of coefficients obtained at level 3. Firstly, we used 3 level decomposition from low- and high- frequencies together, 4 approximations and 4 detailed coefficients. Secondly, we used 3 level approximation coefficients as inputs to our NN. For this purpose, back propagation feed forward neural network has been utilized. The proposed network has three layers, with 1000 neurons in the hidden layer. Obtained results show the differences in determination coefficients as well as in root mean square error. Coefficient of determination (R^2) for first experiment where both frequencies obtained at level 3 are used is 0.996 with RMSE of 25. When we use only 3 level approximation DWT coefficients the R^2 is 0.901 with RMSE of 41.

IV. Conclusion

In this study the DWT decomposition is used for feature extraction of stock indices, where decomposed coefficients are used as inputs to the NN for estimation performances. The proposed model is useful for estimating the stock indices since it is a decomposition-based model. Using the DWT as the source of problem decomposition, it helps to deconstruct the time-series into various frequency components. Here the level of DWT decomposition is 3 using Haar mother wavelet function. The work can be extended to other levels to study the effect of different level of decompositions as well as the use of different wavelet functions. The DWT offers a better picture of the stock indices data as well as analyzing the changes in data at different scale. The second part of this study is estimation using NN model. The proposed model is data adaptive model and using the different decomposition of time-series data can help in increasing the accuracy of the estimation.

References

[1] M. G. Novak, D. Veluscek, “Prediction of stock price movement based on daily high prices”, Quantitative Finance, doi:10.1080/14697688.2015.1070960, 2015

[2] D. Jothimani, R. Shankar, S.S. Yadav, “Discrete Wavelet Transform-Based Prediction of Stock Index: A Study of National Stock Exchange Fifty Index”, Journal of Financial Management and Analysis, 28(2), 35-49, 2015.

[3] A. Aussem, J.Campbell, F.Murtagh, “Wavelet-Based Feature Extraction and Decomposition Strategies for Financial Forecasting”, Journal of Computational Intelligence in Finance, March/April, 1998.

[4] C. L. Giles, S. Lawrence, A. C. Tsoi, “Noisy Time Series Prediction using Reccurent Neural Network and Grammatical Inference”, Machine Learning, Volume 44, No. ½, July/August, pp.161-183, 2001.

[5] S. Lahmiri, “Wavelet low- and high-frequency components as features for predicting stock prices with backpropagation neural networks”, Journal of King Saud University – Computer and Information Sciences, pp. 218-227(26:2014)

[6] L. Ortega, K. Khashanah, “A neuro-wavelet model for the short-term forecasting of high-frequency time series of stock returns”, Journal of Forecasting, pp.134-146, (33:2014)

[7] B. Al-Hnaity, M.Abbod, “A novel hybrid ensemble model to predict FTSE100 index by combining neural network and EEMD”, 2015 European Control Conference (ECC), pp. 3021-3028, 2015

[8] H. Tao, “A wavelet neural network model for forecasting exchange rate integrated with genetic algorithm”, IJCSNS International Journal of Computer Science and Network Security, 6:60-63, 2006.

[9] J. F. Kaashoek, H.K. van Dijk, “Neural network pruning applied to real exchange rate anaylsis”, Journal of Forecasting, 21:559-577, 2002.

[10] C. Tang, “Financial Time Series Forecasting Using Improved Wavelet Neural Network”, Master Thesis, 2009.

[11] https://en.wikipedia.org/wiki/STOXX_Europe_600 last visit: 30.03.2018

Recent Advances in Cancer Treatment using Intertitial Microwave Antennas

Hulusi Acikgoz, Burak Uzman, Adem Yılmaz
Electrical and Electronics Engineering Department
KTO Karatay University
Konya, Turkey
e-mail: hulusi.acikgoz@karatay.edu.tr

***Abstract*— In this paper, recent advances in microwave treatment of cancerous biological tissues are presented. Several antenna types developed for this purpose are thoroughly reviewed and common issues encountered while performing ablation are discussed. A major problem, i.e. backward heating, arising during ablation is introduced and solutions proposed for its mitigation are given. We compare solutions presented in the literature with the one recently proposed i.e. the use of the most remarkable material, the 1-atom thick graphene material.**

Keywords—Microwave Cancer Treatment, Coaxial Antennas, Backward Heating, Graphene Material

I. INTRODUCTION

Over the past decade, there has been considerable effort deployed to the treatment of patients affected with cancer. Due to many advantages, such as fast heating process, larger ablated zone, treatment using microwaves has become an important alternative to the well-known common techniques such as radiofrequency, surgery and chemotherapy. Several antennas has been developed for this purpose whose aims are to improve the efficiency and the effectiveness of the treatment.

However, there have been concerns about using microwave coaxial antennas for the treatment of cancerous tissues. In fact, despite the wide consensus on the benefits of using microwaves for cancer treatment such as given above, damage caused to the healthy tissue by the surface currents propagating on the antenna conductor during the treatment seems to be one of the major factors for restraining its utilization.

Surface currents generated at the slot of the coaxial cable and propagating towards the feed-line increase the Specific Absorption Rate (SAR) along the antenna. This phenomenon is the major cause for the increase of the healthy tissue temperature that cause its desiccation. To address this issue, numerous techniques have been developed and studied. Some of them are based on the use of external cooling system either by water or gas flow along the antenna [1]. Other contributors have brought electromagnetic solutions where the geometry of the antenna is changed to block the propagation of the surface currents. A cylindrical choke of $\lambda/4$ of length and electrically connected to the outer conductor and/or a cap at the end of the antenna are added for this purpose [2, 3]. A floating sleeve was also proposed by [4] with the aim to mitigate this unwanted heating along with the control of the impedance of the antenna. However, the introduction of an external metallic element to the design of the antenna may substantially increase the radial size of the interstitial antenna and this may be damaging for the tissue being treated. Therefore, there is an urge to develop new methods to stop or at least reduce the propagation of these surface currents. Some of the proposed structures are presented in Fig. 1.

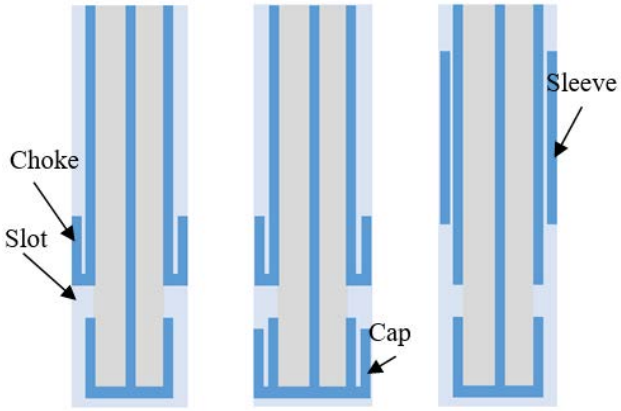

Fig.1: From left to right: choke, cap-choke and floating sleeve antennas

It has been shown that adding a second slot closed to the first one can achieve a higher localized heating region around the tip of the antenna [5]. Most recently, we have demonstrated the possibility of using the 1-atom thick graphene material for reducing surface currents [6]. Indeed, graphene has attracted attention for its extra-ordinary electrical, thermal and mechanical properties. In this work, we combine both the double slot structure and the graphene material layer wrapped on the outer conductor of the antenna. Hereafter, the result obtained when using graphene layer for reducing the backward heating problem is presented and compared with the most commonly used structures, the normal slot antenna, choke and sleeve antennas.

II. RESULTS

In Fig.2 the double slot coaxial antenna with the graphene layer wrapped on its outer conductor is shown. For the sake of simplicity, the dielectric catheter is not drawn. The antenna model inserted in a biological tissue is simulated

using a commercial high frequency electromagnetic software.

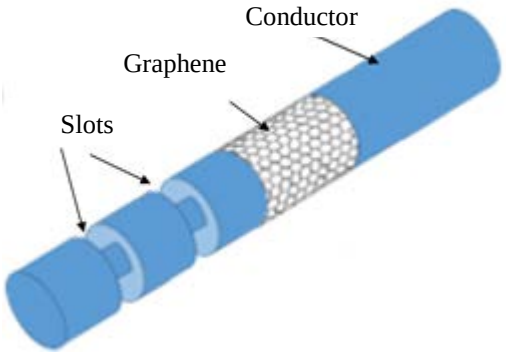

Fig.2: Double slot antenna with the graphene layer

The specific absorption rate calculated along the antenna, from its tip to the feed line, at 1.5mm from the catheter is plotted in Fig. 3.

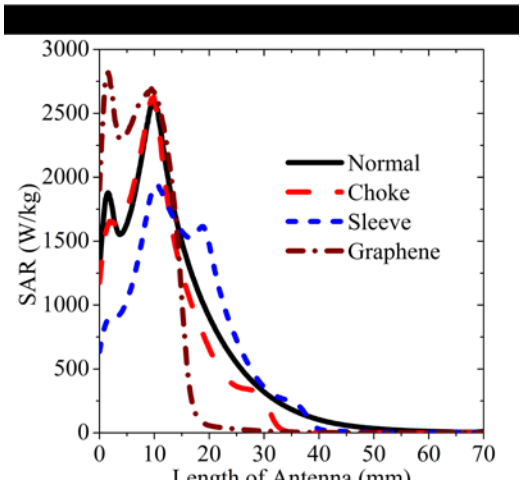

Fig.3. SAR deposited along the catheter for various type of antenna

It is obvious from Fig. 3 that the 1-atom thick graphene layer outperforms when compared to other structures. Higher SAR is deposited near the slots (from 0 to 15 mm) and then it is drastically reduced after. This is due to high surface impedance of graphene at microwave frequencies. The closest performance to the graphene coated antenna is obtained with the choke antenna. In this case, the reduction of the SAR occurs only about 15 mm after the position where the graphene layer is located.

III. Conclusion

In this work, we compared the performances of several techniques for reduction of the backward heating problem due to surface currents propagating on the outer conductor of a double slot coaxial antenna. It has been shown that using graphene material allows to mitigate this problem and the obtained SAR is better than those given by choke or sleeve antennas. More results, especially on the thermal analysis, will be presented at the conference.

References

[1] Kuang M. et al., "Liver cancer: increased microwave delivery to ablation zone with cooled-shaft antenna--experimental and clinical studies", *Radiology*, vol. 242, vo 3, pp. 914–924, 2007.

[2] Brace C.L.**,** **"**Microwave tissue ablation: biophysics, technology and applications", *Crit Rev Biomed Eng.*, vol. 38, no. 1, pp. 65–78, 2010.

[3] Lin J.C., Wang Y.J., "The cap-choke catheter antenna for microwave ablation treatment", *IEEE Transactions on Biomedical Engineering*, vol. 43, No. 6, pp. 657-660, 1996.

[4] Yang D. et al., "A floating sleeve antenna yields localized hepatic microwave ablation", *IEEE Trans. Biomed. Eng.*, vol. 53, pp. 533–537, 2006.

[5] Saito K, Yoshimura H, Ito K, Aoyagi Y, Horita H. Clinical trials of interstitial microwave hyperthermia by use of coaxial-slot antenna with two slots. IEEE Trans Microw Theory Tech. 2004;52:1987–1991. doi: 10.1109/TMTT.2004.832005.

[6] H. Acikgoz, R. Mittra, "Suppression of Surface Currents at Microwave Frequency Using Graphene -Application to Microwave Cancer Treatment", The Applied Computational Electromagnetic Society Journal (ACES Journal), Vol. 31, No. 6, June 2016.

Parallel Coupled Lines Microstrip Bandpass Filter in 1.86-2.0 GHz

Yigit Can Yılmaz, Omur Akbaba, Kaan Atasaven, Yagız Tolunay[1]
[1]Department of Electrical and Electronics Engineering
Antalya Bilim University
Antalya, Turkey

Oguzhan Salih Gungor[2]
[2]Department Of Electrical and Electronics Engineering
Selcuk University
Konya, Turkey

S.Taha Imeci[3]
[3]Department of Electrical Electronics Engineering
International University of Sarajevo
Bosnia, Sarajevo

***Abstract*—Design of a parallel-coupled-line microstrip band pass filter is presented in this paper. The purpose of this research show that analysis, techniques, parameters, values at dual simulation frequencies of 1.86 GHz - 2.00 GHz. Based on the theoretical analysis, has foregoing values a bandpass filter is presented. Overall, considering the applications of circuit, more rigorous designs in other frequency ranges can be also achieved. Parametric studies performed by changing the geometry and dielecrtric values in order to meet the design specifications and see the fabrication tolerances.**

***Keywords*—parallel; coupled; line; microstrip, filter.**

I. INTRODUCTION

While a radio frequency module working, it receives or transmits signal with distortion or with parasite. That makes signal complicated. Filters are used for eliminating these signals. Filters can be classified in 4 categories based on frequency characteristic: low-pass filters, high-pass filters, band-pass filters and band-stop filters [1]. Multiple filters can be used in one system. The bandpass filter is an electronic device or circuit that allows signals which are in a specified gap to pass and stops other signals. Band-pass filter is the combination of high-pass and low-pass filters. One of the most used type of band-pass filter is parallel coupled-lines microstrip filter. Microstrip filters can be easily fabricated. Microstrip filters are used in radars, measurement and test devices [2]. In this paper, design and simulation results of parallel coupled microstrip band-pass filter which passes 1.86-2.00 GHz are given. The purpose of the work is to create compact and easily fabricable filters.

II. MODELING AND ANALYSIS

This coupled parallel bandpass filter was designed for 1.86 – 2.00 GHz bandwidth. The midpoint of the frequency is 1.93 GHz and Bandwidth of signal is 140 MHz. This filter is a 5th order Chebyshev filter. FR4 was used as dielectric which has dielectric constant (Ɛr) = 4.4. The dielectric's with (W) is 30 mm, length (L) is 169 mm, thickness (t) is 1mm and Loss tangent (Tan δ) is 0. While designing this filter, same type filters were researched and some steps were followed from resources which are similar to this filter [3].

Design and Sonnet Software test results were shown in figure 1 and figure 2.

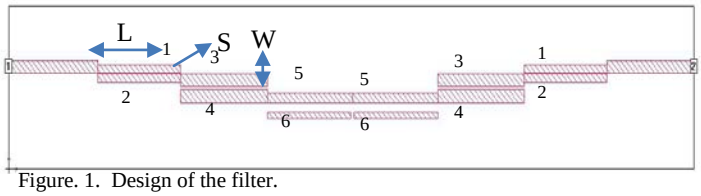

Figure. 1. Design of the filter.

TABLE I. DİMENSİONS OF STRİPS LİNES

N (pair)	*Width (mm)*	*Length (mm)*	*Space (mm)*
1	1.534	20.47	0.1705
2	2.386	21.47	0.5114
3	1.875	20.97	1.534
4	1.875	20.97	1.534
5	2.386	21.47	0.5114
6	1.534	20.47	0.1705

The values which are used for coupled parallel bandpass filter were shown in table 1. For calculations, these formulas can be used shown below.

For calculating odd and even impedances:

$$(Z_{0e})_{j,j} = \frac{1}{Y_0}\frac{1}{Y_0}\left[[1 + \left(\frac{J_{j,j+1}}{Y_0}\right) + \left(\frac{J_{j,j+1}}{Y_0}\right)^2\right] \quad (1)$$

$$(Z_{0e})_{j,j} = \frac{1}{Y_0}\left[[1 - \left(\frac{J_{j,j+1}}{Y_0}\right) + \left(\frac{J_{j,j+1}}{Y_0}\right)^2\right] \quad (2)$$

For bandwidth:

$$FBW = \frac{W_2 - W_1}{W_0} \quad (3)$$

For R and C values:

$$L_S = \left(\frac{1}{FBW W_0}\right) Z_0 g \quad (4)$$

$$C_s = \left(\frac{FBW}{W_0}\right) Z_0 g \quad (5)$$

$$L_p = \left(\frac{FBW}{W_0}\right) \frac{Z_0}{g} \quad (6)$$

$$C_p = \left(\frac{1}{FBW W_0}\right) \frac{g}{Z_0} \quad (7)$$

For center frequency:

$$\omega_0 = \sqrt{\omega_1 \omega_2} \quad (8)$$

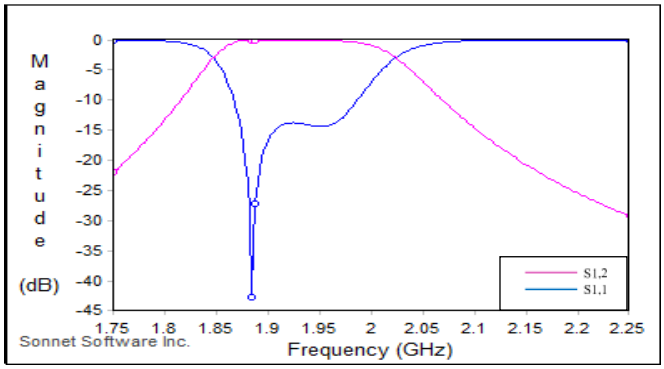

Figure. 2. Simulation results of the filter.

According to the response data, maximum S11 value is -43 dB at 1.88 GHz and S12 is approximately 0 dB between 1.86 - 2 GHz.

Width of microstrip lines were varied and results were shown in table 2 and table 3.

TABLE II. CORNER FREQUENCİES WHEN WİDTHS OF LİNES ARE DOUBLED

Varying Width (doubled)	**Corner frequency (dB-GHz)**		
S11	#1 (-4.96, 1.918)	#2 (-9.38, 1.978)	#3 (-5.97, 1.874)
S12	#1 (-0.0211, 1.912)	#2 (-2.07, 1.974)	#3 (-0.094, 1.82)

TABLE III. CORNER FREQUENCİES WHEN WİDTHS OF LİNES ARE HAVED

Varying Width (halved)	**Corner frequency (dB-GHz)**		
S11	#1 (-11.106, 1.978)	#2 (-6,626, 1.958)	#3 (-6.38, 2.08)
S12	#1 (-0.26, 1.972)	#2 (-0.333, 1.934)	#3 (-0.25, 1.976)

Equations which are shown below are used for making necessary modification and to prevent wavelength deflections [4].

$$\lambda = \frac{c}{f\sqrt{\varepsilon_{eff}}} \quad (9)$$

$$\varepsilon_{eff} = \frac{\varepsilon_r + 1}{2} \quad (10)$$

III. CONCLUSION

The fundamental function of filter that experimenters designed in this project is to limit the 1.86-2.00 GHz bandwidth of the output signal to the desired minimum necessary to convey data at the desired speed and in the desired form as experimenters designed in the project. In other term, the designed band pass filter is an electronic device to allow signals which are between two specific frequencies, meanwhile; it does not allow any other frequencies to pass. In addition, Conventional parallel-coupled microstrip line filter had some disadvantages. One of the important disadvantage is this kind of filters too large, particularly filter orders or other multi-fractional microwave devices aim to good selectivity [5]. In this academic paper parametric studies were conducted and the results were discussed. In this article, it was achieved that designing a microstrip bandpass filter in 1.86-2.00 GHz band. Simulation and design were made by using Sonnet Suites. [6].

REFERENCES

[1] S.Shirin, CH.R.Phani Kumar, "Implementation of Nth Order Bandpass filter" S.Shirin et al, / (IJCSIT) International Journal of Computer Science and Information Technologies, Vol. 3 (3) , 2012,4359 – 4361

[2] Pozar, D. M., Microwave engineering. Wiley, John & Sons, 2007

[3] Vipul Dabhi, Ved Vyas Dwivedi, "Analytical Study and Realization of Microstrip Parallel Coupled Bandpass Filter at 2 GHz", IEEE, 2016

[4] B. Eren, B. Akyüz, M. Dıkkafa, Ö. Alaca, T. İmecı and O. S. Güngör, "Microstrip dual-bandpass filter design," 2017 25th Signal Processing and Communications Applications Conference (SIU) , Antalya , 2017 , pp.1-4. doi:10.1109/SIU.2017.7960274URL:http://ieeexplore.ieee.org/stamp/stamp.jsp?tp=&arnumber=7960274&isnumber=7960135

[5] P.-H. Deng and L.-C. Dai, "Unequal Wilkinson power dividers with favorable selectivity and highisolation using coupled-line filter transformers," IEEE Trans. Microw. Theory Tech., vol. 60, no. 6, pp. 1810-1815, June 2012.

[6] In this academic paper, parametric studies were conducted and the results were discussed. In this article, it was achieved that designing a microstrip bandpass filter in 1.86-2.00 GHz band. Simulation and design were made by using Sonnet Suites.

Optimal Combination of Three Volatilities for Better Black-Scholes Option Pricing

Mahmet Can,
International University of Sarajevo
Faculty of Engineering
Hrasnicka Cesta Ilıdza, Sarajevo BiH 71210
mcan@ius.edu.ba

Sadi Fadda
International University of Sarajevo
Faculty of Business Administration
Hrasnicka Cesta Ilıdza, Sarajevo BiH 71210
sadifadda@gmail.com

***Abstract*— The most popular parametric formula (B-S) used in pricing the European-style options is given by Black-Scholes (1973). The prediction power of (B-S) strongly rely on the accuracy of the independent variables: spot price, strike price, time to maturity, risk free interest rate and market volatility. To improve the accuracy, many volatility models are proposed. Also Day and Lewis (1992) [1] introduced the idea of combining implied volatility and EGARCH. In this article an optimal combination of market implied volatility, GARCH(1,1), and GJR(1,1) is made, and the prediction power of B-S is doubled.**

***Keywords*— Black-Scholes, Implied volatility, GARCH (1,1), GJR(1,1), optimal combination, option pricing, S&P100, put options, call options.**

I. INTRODUCTION

The main measure of an investment risk, whether of a single financial instrument stock, bond, forward or a portfolio, is its volatility. While considering the simplicity of calculating an implied volatility based on a given market price of an instrument, it is the volatility of the approaching period through which the instrument is to be held that actually matters. In this paper, three different volatilities are combined to get a new one.

For many decades Black-Scholes [2] formula and its modifications are used to price European style put, and call options. The formula depends on five parameters, spot price, *S*, strike price, *K*, time to maturity, *T*, risk free interest rate *r*, and market volatility s. For calls "c" or puts "p" the formulae are

$$c = S\,N(d_1) - Ke^{-rT}\,N(d_2), \quad (1)$$

and

$$p = Ke^{-rT}\,N(-d_2) - SN(-d_1) \quad (2)$$

Where

$$d_1 = \frac{\ln(S/K)+(r+s^2/2)T}{s\sqrt{T}}, \quad (3)$$

and

$$d_2 = d_1 - s\sqrt{T}. \quad (4)$$

In (1) and (2), N(x) is the cumulative standard normal distribution function. Indeed the probability that option gets exercised is $N(d_2)$. It is multiplied by the strike price and then discounted to its present time value, giving the expected value of the cost of exercising an option.

N(d1) is the factor which measures how much the present value of the asset exceeds its current market price [3]. The product of N(d1) and option spot-price is the expected value of receiving the stock at option's maturity. Therefore the option price must be equal to the difference of these two expected values.

There are many objections to B-S option pricing formula. Fisher Black [4] states that the market prices of listed options tend to differ from the values calculated by the Black-Scholes formula methodically. Especially extremely-out-of-money options tend to be overpriced, while into-the-money ones tend to be underpriced. He also adds that options having time-to-maturity below three months do tend to be overpriced.

Since the introduction of Black-Scholes-Merton in [2], most of the research efforts have been to remove some of the restrictions or assumptions in the Black–Scholes model. Among those are the premises of the log-normality of returns or that of constant volatility.

Meanwhile several volatility models are proposed. Implied, historical, conditional probabilities are some of them [5]-[6]. Works [7-9] supported the claim that implied volatility outperforms historical volatility. In [10] it is demonstrated that the implied volatilities of at-the-money options give better results than any other combination of available implied volatilities.

In this article, using the implied volatility computed from B-S formula as the target, and a least square formulation, an optimal combination of the three volatilities, implied volatility, GARCH(1,1), and GJR(1,1), the prediction power of B-S is doubled.

2. MATERIALS AND METHODS

The data used in this article is S&P100 European Style Index also known as XEO, 75, 694 call options throughout one year from October3, 2013 to September 29, 2014, and 141,397 put options in the same period.

To find the optimum combination of the three volatility models, first a target volatility, that is when used with other parameters in B-S formula, will exactly yield the market price of the option, is computed. It is observed that the option price in B-S formula is an increasing function of the volatility. An iterative scheme is set. Iteration starts by the implied volatility supplied by the data set. If computed option price is less than the market price of the option, and then volatility is slightly increased till, computed option price is the same as the market price. If computed option price is more than the market price of the option, and then volatility is slightly decreased till, computed option price is the same as the market price. The volatility *V* of the balanced state is a kind of implied volatility of the B-S formula. Then a linear combination

$$V = aX + bY + cZ + d \qquad (5)$$

of X= implied volatility, Y= GARCH(1,1), and Z= GJR(1,1) is found, which is the best in the sense of least squares. The coefficients of optimal combination are found as in Table 1.

TABLE 1.
COEFFICIENTS OF OPTIMAL COMBINATION FOR OPTIONS

	a	b	c	d
Puts	0.8099	0.5858	-0.4629	0.0610
Calls	0.8769	0.4952	-0.3737	0.0439

Option price depends on the parameters strike price, *K*, time to maturity, *T*, risk free interest rate *r*, which are known from today. If we predict the tomorrow's spot price *S*, using the best estimate *s* for the market volatility, the optimum option prices for tomorrow can be calculated. Option prices in our dataset are predicted one day before, and when compared with the realized prices, it is seen that the success of B-S formula is doubled.

TABLE 2.
ABSOLUTE MEAN ERRORS IN PRICING

	Implied Volatility	Optimal Volatility
Puts	5.2490$	3.5773$
Calls	6.0252$	3.6573$

3. CONCLUSIONS

Since the introduction of Black-Scholes-Merton in 1973, most of the research efforts have been targeted to remove constant volatility condition. For this several volatility models are proposed. Implied, historical, conditional probabilities are among them. Some researchers also tried optimization processes to assign appropriate weights to volatilities involved. In this research work implied volatility, GARCH(1,1), and GJR(1,1) are combined thorough a least squares technique, and , the prediction power of B-S is doubled.

REFERENCES

[1] T.E. Day, C.M. Lewis Stock market volatility and the information content of stock index options Journal of Econometrics 52 (1992) 267-287. North-Holland

[2] F. Black, and M. Scholes, The Pricing of Options and Corporate Liabilities, The Journal of Political Economy, Vol. 81, No. 3 (May - Jun., 1973), pp. 637-654

[3] L.T. Nielsen, Understanding N(d1) and N(d2): Risk-Adjusted Probabilities in the Black-Scholes Model , INSEAD, Boulevard de Constance, 77305 Fontainebleau Cedex, France, 1992

[4] F. Black, Fact and Fantasy in the Use of Options, Financial Analysts Journal, July/August 1975, Volume 31 Issue 4 pp. 36-

[5] S. Fadda, Volatility Estimation Through Historical Prices of Indexes Southeast Europe Journal of Soft Computing Vol.5 No1 March 2016 (21-26)

[6] S. Fadda, M. Can, Forecasting Conditional Variance of S&P100 Returns Using Feedforward and Recurrent Neural Networks Southeast Europe Journal of Soft Computing Vol.6 No.1 March 2017 (58-69)

[7] Latané and Rendleman (1976), Standard Deviations Of Stock Price Ratios Implied In Option Prices, The Journal of Finance, Volume 31, Issue 2, May 1976 , Pages 369–381

[8] R.Schmalensee, R.R. TrippiCommon, Stock Volatility Expectations Implied By Option Premia, Journal of Finance, Volume 33, Issue 1, March 1978, Pages 129–147

[9] D,P, Chiras and S. Manaster (1978) The information content of option prices and a test of market efficiency, Journal of Financial Economics, Volume 6, Issues 2–3, June–September 1978, Pages 213-234.

[10] S. Beckers, Standard deviations implied in option prices as predictors of future stock price variability, Journal of Banking & Finance, Volume 5, Issue 3, September 1981, Pages 363-381

Microwave Imaging of Breast Cancer Tumor Using Vivaldi Antenna

İlhami Ünal
Materials Institute, MİLTAL
TÜBİTAK MAM
Gebze, Kocaeli, Turkey
ilhami.unal@tubitak.gov.tr

Bahattin Türetken
Depart.of Electrical-Electronics Eng.
Karabük University
Karabük, Turkey
bahattinturetken@karabuk.edu.tr

Abstract— **In this paper, contribution of ultra-wide band (UWB) Vivaldi antennas on tumor detection capability of a radar-based UWB microwave imaging system is investigated by using an realistic breast phantom through simulation and experimental studies. The designed Vivaldi antenna operates efficiently across the band from 4.5 GHz to 10.5 GHz, and it's immersed in a coupling medium in order to get a good impedance matching with the breast phantom via simulations. Images are successfully formed by using delay-and-sum (DAS) algorithm. The proposed Vivaldi antenna would be an attractive candidate element for microwave imaging of breast cancer tumor.**

I. INTRODUCTION

X-ray mammography has several limitations, especially when dealing with younger women who have dense breast tissues. It also requires painful and uncomfortable breast compression and exposes the patient to ionizing radiation. Currently, there are two main active methods that involve illuminating the breast with microwaves as an alternative especially to the X-ray mammography, such as microwave tomography and radar-based imaging. In microwave tomography, a nonlinear inverse scattering problem is solved to reconstruct an image of the spatial distribution of dielectric properties in the breast [1]. On the other hand, UWB radar-based microwave imaging approach deals with only to identify the presence and location of significant scattering obstacles such as malignant breast tumors [2]. The physical basis for microwave detection of breast tumor is the significant contrast in the electrical properties of the normal and the malignant breast tissues [2], which exists in the earliest stage of tumor development.

In the first part of the study, seven UWB Vivaldi antennas are located around a breast phantom on the full-wave electromagnetic simulator (CST Microwave Studio®), which is based on the Finite Integration Technique (FIT). All of the time-domain signals (S_{ii} and S_{ij}, $i \neq j$) coming from different antennas are obtained from the simulation model with and without 2 mm diameter tumor at 40 mm depth inside the breast phantom model, by feeding each antenna sequentially. Recorded data are processed on the DAS algorithm, and then images of the computed backscattered signal energies for each pixel are created as a function of position. Finally, a monostatic radar based measurement system with only one Vivaldi antenna is installed and a 10 mm diameter tumor at 31 mm depth inside the developed breast phantom is detected, experimentally.

II. ANTENNA DESIGN AND RESULTS

The planar Vivaldi antenna which is curved onto a hemi-sphere surface is aimed to be used as an UWB probe element of a half-spherical antenna array (Fig. 1). The results show that the -10 dB bandwidth of the antenna which is operating in the half-spherical antenna array surrounding the breast phantom extends from nearly 4.5 GHz to above 10.5 GHz (Fig. 2).

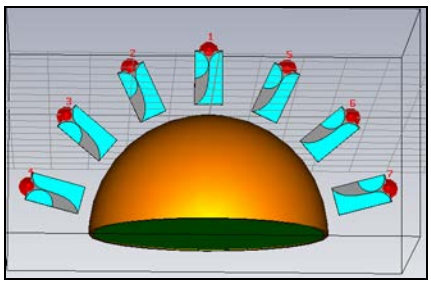

Figure 1. The geometry of proposed antenna array

On the Vivaldi antenna, the tapered microstrip line is applied as the antenna feeder and a 0.5 mm thick FR4 (ε_r=4.4, tanδ=0.025) material is used as a substrate. The upper and lower layers are copper layer which have a thickness of 0.035 mm. The length and width of the Vivaldi is 27.34 mm × 14 mm. The resulting 3D radiation pattern results are shown in Fig. 3.

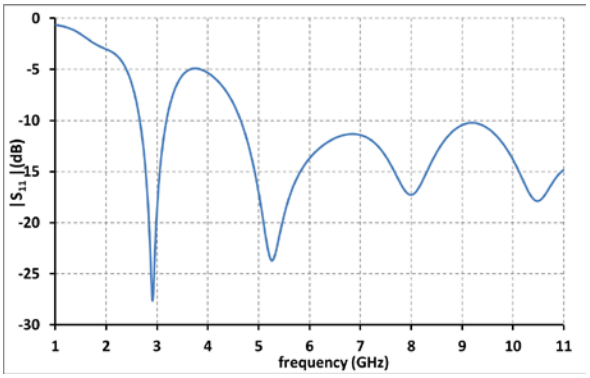

Figure 2. The return loss of the designed Vivaldi Antenna

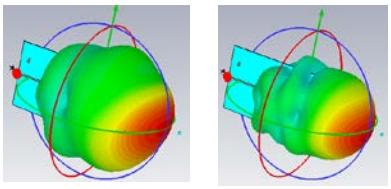

a. b.

Figure 3. Far-field radiation pattern of the Vivaldi antenna operating in coupling medium for a. 5 GHz and b. 9 GHz

When one of the seven UWB bow-tie antennas in the array is excited by Gaussian pulse, back-scattered time domain signals (S_{ii} and S_{ij}, i≠j) are recorded. This procedure is repeated by feeding each antenna sequentially, for cases with and without 2 mm diameter tumor. Therefore, 49 time-domain signals coming from different antennas are recorded for each case. Tumor response signals S_{ij}^{T} are obtained by calibrating the recorded signals, as in Eq. (1):

$$S_{ij}^{T} = S_{ij}\Big|_{with\,tumor} - S_{ij}\Big|_{without\,tumor}$$

The tumor response signals are additionally compensated for $1/r$ attenuation of electric fields inside the breast. Total tumor response for each pixel (Eq. (2)) is obtained, regarding computed time delays between each antenna and pixel points, one by one [3]. Then, images of the computed scattered signal energies for each pixel are created as a function of position.

$$T(\vec{r}) = \left[\sum_{i=1}^{5}\sum_{j=1}^{5} S_{ij}^{T}\left(\tau_{ij}^{d}(\vec{r})\right)\right]^{2}$$

Normalized imaging results of breast cancer tumor with 2 mm diameter are successfully presented in linear scale, as shown in Fig. 4.

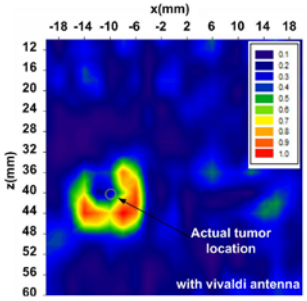

Figure 4. Microwave imaging result of the breast cancer tumor with 2 mm diameter.

The fabricated Vivaldi antenna with high loss material of FR4 and the developed breast phantom is also shown in Fig. 5. For the experimental studies, the breast phantom is sequentially rotated manually by 20° degrees and the backscattered signals (S_{11}) are recorded in the frequency range of 4.5–10.5 GHz, at each step. Totally measured 18 frequency-domain datas at each angle (separated by 20°) are recorded at 1001 frequency points, and its time-domain equivalent is obtained by using inverse FFT. Images of the computed signal energies are created as a function of position by using DAS algorithm. Inverse FFT is calculated as follows: First of all, the complex conjugate of S_{ii} data is taken, and then those values are located in the symmetrical negative- real axis (Eq. (3)).

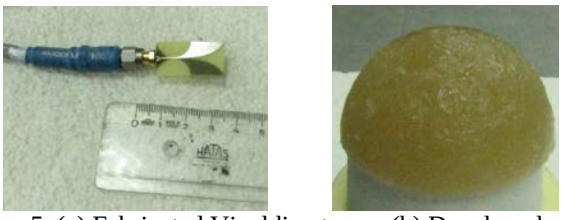

Figure 5. (a) Fabricated Vivaldi antenna, (b) Developed breast phantom

Then, an inverse FFT operation is done through MATLAB, with the aid of "ifftshift" and "ifft" functions, as well as zero padding. Microwave imaging results of breast cancer tumor with 10 mm diameter are successfully presented in linear scale, as shown in Fig. 6 (b) [3].

$$S_{ii}(-f) = S_{ii}^{*}(f)$$

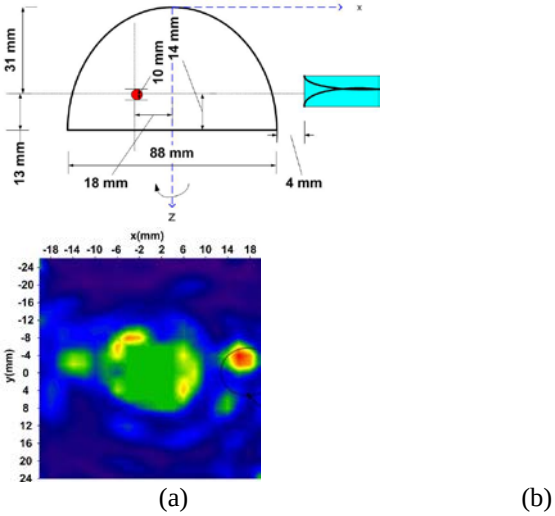

(a) (b)

Figure 6. a) Schematic drawing of the breast phantom, tumor and antenna locations, b) Microwave imaging result of the breast cancer tumor with 10 mm diameter.

III. CONCLUSION

A Vivaldi antenna array surrounding the breast has been designed and tested on a full-wave electromagnetic simulator, in order to investigate tumor detection capability of the microwave radar-based imaging system. The microwave images have been obtained successfully. Obtained simulation results are reasonably reliable and promising. On the other hand, a 10 mm diameter tumor phantom model inside the developed breast phantom has been detected experimentally, to observe the feasibility of the designed Vivaldi antenna.

REFERENCES

1. A. E. Bulyshev, S. Y. Semenov, A. E. Souvorov, R. H. Svenson, A. G. Nazarov, Y. E. Sizov, and G. P. Tatsis, "Computational Modelling of Three-Dimensional Microwave Tomography of Breast Cancer," IEEE Trans. Biomed. Eng., 48, Sep. 2001, pp. 1053–1056.
2. 2. X. Li, S. K. Davis, S. C. Hagness, D. W. van der Weide, and B. D. Van Veen, "Microwave Imaging via Space-Time Beamforming: Experimental Investigation of Tumor Detection in Multilayer Breast Phantoms," IEEE Trans. Microw. Theory Tech., 52, Aug. 2004, pp. 1856–1865.
3. İ. Ünal, PhD Thesis, "A New Ultrawide-Band (UWB) Microwave Imaging System with Minimized Mutual Coupling Effects for Breast Tumor Detection" Yeditepe Univ, 2013, İstanbul, Turkey.

Microstrip Lowpass Filter At 5.35 GHz

Veysel Ercağlar, Fatih Develi, Ibrahim Berber, Muhammet Edip Akay[1]
[1]Department of Electrical and Electronics Engineering
Antalya Bilim University
Antalya, Turkey

Oguzhan Salih Gungor[2],
[2]Department of Electrical and Electronics Engineering
Selcuk University
Konya, Turkey

S.Taha Imeci[3]
[3]Department of Electrical and Electronics Engineering
International University of Sarajevo
Sarajevo, Bosnia

***Abstract*—An effective technique to design compact lowpass filter made is proposed in this paper. The method that this paper consists of is highly effective in the applications of lowpass filters. The proposed filter unit structure can provide the bandwidth of 0 to 5.35 GHz and the frequencies between that interval will be allowed to pass. Having 5.35 GHz cut-off frequency has not been fabricated and tasted, however, it is expected that the experimental results will show excellent agreement with theoretical results and the validity of the modeling method for the proposed lowpass filter structure.**

Keywords—filter; lowpass filter; microstrip filter

I. INTRODUCTION

A filter in a set is any device which passes or does not pass each element in a set. A filter is a circuit that is designed to pass signals with desired frequencies and reject or attenuate others [1]. A low pass filter, which made up of a microstrip structure, specifically, is a filter which passes low-frequency signals and blocks, or impedes, high-frequency signals [2]. Furthermore, microstrip filters play a significant role in the field of microwaves. Planar filters that are implemented using printed-circuit board (PCB) technologies attract extensive attention owing to their easy fabrication, low cost and convenient integration with other microwave circuits. Conventional microstrip lowpass filters using shunt stubs and high-low-impedance transmission lines have already shown appreciable effects [3]. Lowpass filters with compact size and high performance are in great demand for communication systems to suppress harmonics and spurious signals [4]. The compact size and suppression of unwanted frequency components with excellent passband characteristics on the other hand, are the major concerns of the microwave low pass filter design. To achieve the compact size printed circuit technology is generally preferred to design the planar microwave filter. As Kumar [5] mentioned, this technique also provides easy fabrication, low costs as well as easy integration with other microwave circuits.

II. FILTER DESIGN

In this work, a microstrip lowpass filter with cutoff frequency of 5.35 GHz is designed and simulated. As a CAD tool, Sonnet Software has been used [6]. Figure 1 shows the top view of the filter with its dimensions.

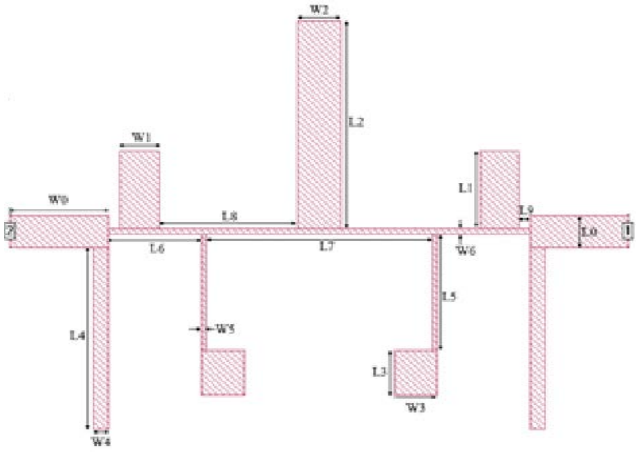

Fig. 1. The layout of the lowpass filter with L_0 = 3.5, L_1 = 3, L_2 = 8, L_3 = 1.7, L_4 = 7, L_5 = 4.5, L_6 = 3.3, L_7 = 8.15, L_8 = 4.95, W_0 = 1.2, W_1 = 1.4, W_2 = 1.55, W_3 = 1.55, W_4 = 0.55, W_5 = 0.15, W_6 = 0.2*mm*.

The filter is in a 22.5 x 25 mm box. Dielectric thickness is 0.508 mm and dielectric constant is 1. Figure 2 shows the 3-dimensional view of the filter.

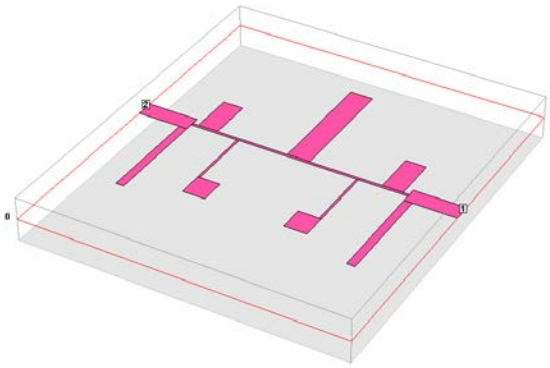

Fig. 2. The 3D view of the filter.

III. SIMULATION RESULTS AND PARAMECTİC STUDY

Change in S11 and S12 with the frequency is seen in Figure 3. The figure reflects the lowpass characteristic of the filter. -10dB of S11 was obtained around 5.3 GHz, and a stopband that is around 6 GHz wide was achieved.

Before achieving the conclusive result, several simulations were done with varied sizes that are shown in Figure 3. Although different dimensions were tested, the most evident size that resulted in clear changes of the cutoff frequency was the length L_5. With different length values of L_5, the cutoff frequencies that achieved as the results of their simulation are shown in Table 1. For greater values of L_5, the frequency that S11 reached -10dB level increased up to 5.35GHz.

TABLE I. CUTOFF FREQUENCY AT VARIED SIZES

Version	Parameters		
	L_1 (mm)	L_5 (mm)	Cutoff frequency[a] (GHz)
1	2.3	1.2	4.95
2	3	1.2	5.0
3	3	3	5.1
4	**3**	**4.5**	**5.35**

a. The frequency that S11 reaches -10dB.

Table 2 below shows the value of S11 at 5.35 GHz for all versions.

TABLE II. S11 AT 5.35 GHz AT VARIED SIZES

Version	Parameters		
	L_1 (mm)	L_5 (mm)	S11 at 5.35 GHz (dB)
1	2.3	1.2	-5.09
2	3	1.2	-5.61
3	3	3	-6.97
4	**3**	**4.5**	**-10.49**

As the versions from 1 to 4 are inspected, the cutoff frequency of the filter increased from 4.95 GHz to 5.35 GHz with the specified dimension changes. And consequently, the S11 of the versions 1, 2 and 3 are left above the -10dB limit. With the conclusive design, -10dB S11 was achieved at the frequency 5.35 GHz.

Figure 3 shows the result of the Version 4 of Table 1 and Table 2.

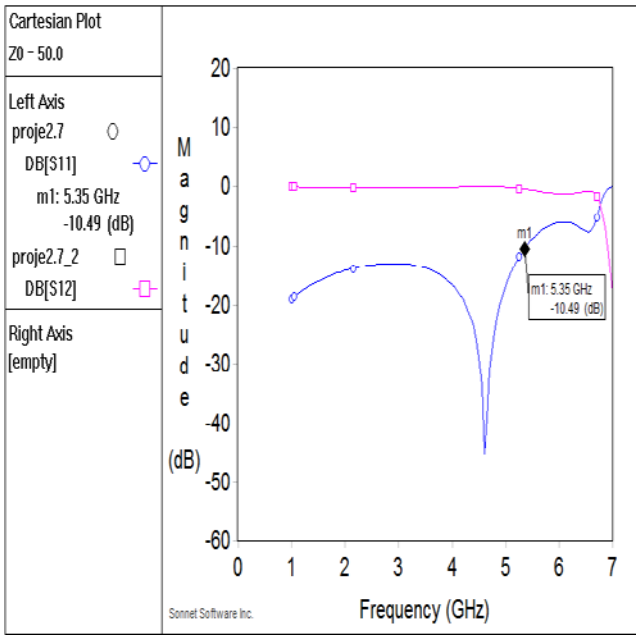

Fig. 3. Plot of S11 and S12 versus Frequency

IV. CONCLUSION

In this paper, a microstrip lowpass filter with cutoff frequency of 5.35 GHz is designated and simuated. In addition to this, similar versions with slightly different cutoff frequencies were observed by varying some parameters, however the 5.35 GHz version formed the conclusive design.

The main advantage of the proposed structure is to achieve the features of a lowpass filter with a very compact design. In addition to the simulation, we are optimistic that we would be able to fabricate the lowpass filter in practice. Since it has a simple geometry.

REFERENCES

[1] C.K. Alexander, M.N.O. Sadiku, Fundamentals of Electrical Circuits, McGraw-Hill, New York, USA, 2012, 5th ed.

[2] *Low Pass Filter- Explained*, http://www.learningaboutelectronics.com/

[3] D.M. Pozer, "Microwave engineering" (Willey, New York, USA, 2005, 3rd edn) pp. 412 –415.

[4] L. Ge, J.P. Wang and Y.-X. Guo, "Compact Mmicrostrip Mowpass Filter with Ultra-wide Stopband", Electronic Letters, vol. 46, issue 10, pp. 689-691, May 2010.

[5] D. Kumar, A. De, "Compact Low Pass Filter Design for L-Band Application", Journal of Electromagnetic Analysis and Applications, 3, pp. 115-117, April 2011.

[6] Sonnet Software, version 15.53, www.sonnetsoftware.com, 2014.

Metamaterial superstrate design for MPA

Hamid Torpi, Bilal Tütüncü
Electronics and Communication Engineering,
Yildiz Technical University, Esenler, Istanbul, Turkey

S.Taha İmeci
Electrical & Electronics Engineering,
International Univ. of Sarajevo, Bosnia and Herzegovina

***Abstract*—The directivity is a major problem at microstrip patch antennas and this study proposes to improve directivity by utilizing a Triangular Split Ring Resonator metamaterial lens layer at this antennas. This problem has been solved in an easy way in this study, without having to make a series of antennas on the same plane which is a classic method. Both the reference microstrip antenna and proposed metamaterial lens antenna are designed, and simulated. It was observed that the directivity of the reference antenna increased by 1.78 dB with the proposed metamaterial superstrate according to the simulation results at 12 GHz. Also 21˚ decrease in the HPBW is observed as an evidence of the directivity improvement.**

***Keywords*—Metamaterial, Microstrip Antenna, Directivity**

I. INTRODUCTION

In 1968, Vesalago presented that, refractive index may also be negative. He hypothesized that negative refraction can occur if both the electric permittivity ϵ and the magnetic permeability μ of a material are negative [1]. In the propagation of electromagnetic waves, the direction of energy flow is given by a right-hand rule, but when ϵ<0 and μ<0, the medium is Left-Handed and this materials are called Left-handed medium (LHM) or metamaterials (MM). If both the permeability (μ) and the permittivity (ϵ) parameters are set negative at the same frequency, an incident electromagnetic wave is inversely refracted and inverse refraction causes focusing [2]. If the electromagnetic wave can be focused instead of transmitting omnidirectional, the directivity and, so the gain will be increased. In the literature, MMs were mostly designed and used for C and X band to achieve this improvement in Microstrip Patch Antennas (MPA) [3]. In this study, a MM structure called Triangular Split Ring Resonator (TSRR) is designed at Ku frequency range with 12 GHz operating frequency and results are obtained. A 1.78 dB increase in the directivity is observed.

II. REFERENCE MPA DESIGN

The reference MPA is modelled through a copper-coated dielectric substrate Rogers RO4350B (ϵr =3.48, thickness h= 0.762 mm). The width (W) and length (L) of the substrate are taken as twice the size of patch width (Wp) and patch length (Lp) which are calculated by equations given in [4]. For 12 GHz; Wp =8.35 mm and Lp= 6.38 mm. For impedance matching, two adjacent parallel slits are extended until the desired resonance input impedance value (50 Ω) is achieved. The feed line extension of the patch “y” is calculated 1.91 mm and the width of the feed line "wf" is calculated as 1.7 mm and the gap of parallel slit is taken as half of wf (g = wf / 2 = 0.85 mm). Reference MPA top view shown in Fig. 1.

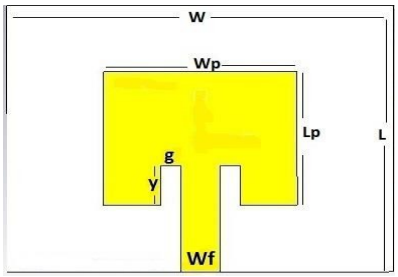

Fig. 1. The rectangular MPA shape

The S11 curve of the reference MPA according to the simulation results are shown in Fig. 2. As seen the bandwidth is 388 MHz. The upper frequency is 12.291 GHz, the lower frequency is 11.902 GHz and the center frequency is 12.08 and the return loss at the center frequency is -25.46 dB.

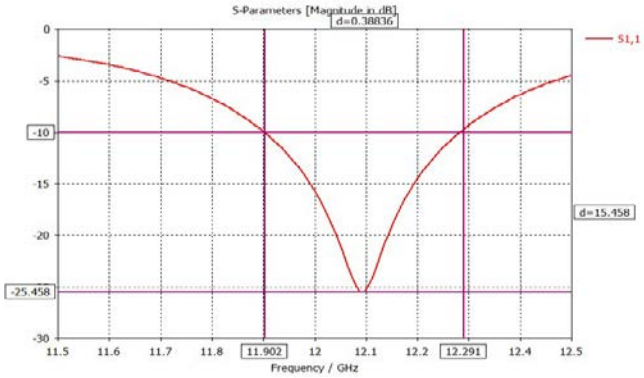

Fig. 2. S11 curve of the rectangular MPA

In order to view the increase in the directivity, the far field directivity pattern of MPA without superstrate is drawn for 12 GHz. The peak directivity is found 4.66 dBi as shown in Fig. 3. Also according to the simulation results Half Power Beam-width (HPBW) is 93.1°.

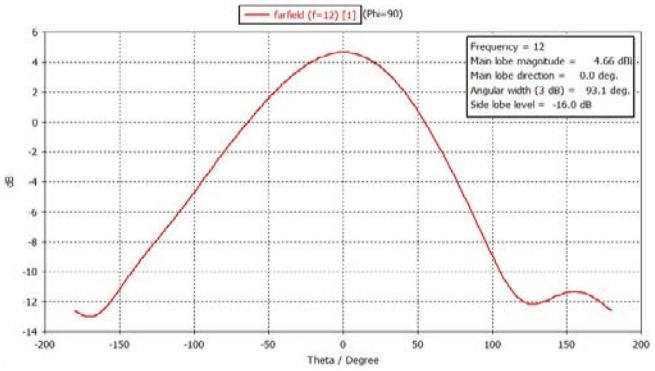

Fig. 3. Directivity pattern of the rectangular MPA at 12GHz

III. TSRR METAMATERIAL UNIT CELL DESIGN

In this structure, there are two nested triangles that are symmetrical to each other at the front side of the TSRR and a strip for negative permittivity on the back side. The gap of the outer triangle is at its base and the gap of inner triangle is at exactly 180° symmetrical to the gap of outer triangle. Both triangles are designed to be isosceles. The same substrate that is used for MPA with predefined characteristics and dimensions is used. With a few optimizations in CST, the dimensions of the unit cell are taken as follows; a=0.4mm, b=4.47 mm, c=3 mm, d=1.21 mm, k=1.36 mm, e=0.44 mm and the inner triangle width is 0.162 mm. The width of the back strip is 0.4 mm and the length of this strip is 4 mm. The shape of the designed TSRR is shown in Fig. 4.

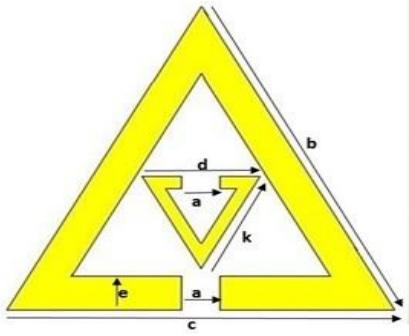

Fig. 4. TSRR unit cell

There are several different methods to obtain the media parameters (ε and μ) from the S parameters. In this study we chose robust method [5] and obtained the results graphically by MATLAB. Є and μ curves of TSRR are shown in Fig. 5. As seen the real values of ϵ and μ are negative at 12 GHz. (ϵ =-0.8 and μ= -3.9). We investigated whether the TSRR is LHM or not at 12 GHz, so we have concerned only the transmitted part of the electromagnetic waves. Thus the imaginary parts that represent the "loss energy" are ignored [6].

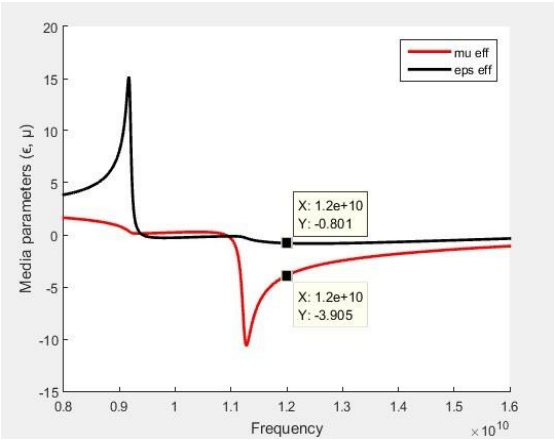

Fig. 5. Media parameters of TSRR unit cell

The TSRR unit cell, whose ϵ and μ parameters are confirmed to be negative at 12 GHz have to be converted into a periodic structure to use as a superstrate for a significant increase. Parametric studies is carried out in different quantities for a periodic structure to obtain optimal return loss and optimal radiation parameters and a 2 × 2 array at 12 mm × 12 mm dimensions are noted optimal. The directivity pattern of the reference MPA with TSRR that loaded at a half-wavelength distance (λ0 / 2 = 12.5 mm) is simulated. Fig.6 shows directivity pattern of the MPA with TSRR for 12 GHz.

Fig. 6. Directivity pattern of the rectangular MPA with TSRR at 12GHz

IV. RESULTS AND DISCUSSIONS

Enhancements on the directivity of the MPA with TSRR and HPBW are given in the Table 1. There is a 1.78 dB increase in the directivity of the reference MPA with a TSRR MM superstrate according to simulation results. Also the decrease in the HPBW is an evidence of the enhancement of the MPA directivity.

Table 1. Changes on the directivity and HPBW

Name	Directivity	HPBW
MPA	4.66 dBi	93.1˚
MPA+TSRR	6.44 dBi	72.1˚
CHANGE	+1.78 dB	-21˚

REFERENCES

[1] V.G.Veselago, 'The electrodynamics of substances with simultaneously negative values of ϵ and μ', Sov Phys Uspekhi., vol 10, pp. 509–514, 1968.

[2] J.B. Pendry, 'Negative refraction makes a perfect lens', Phys Rev Lett., vol 85(18), pp. 3966-3969, 2000.

[3] Y. Zheng, J. Gao, Y. Zhou, X. Cao, H.Yang, S. Li, T. Li, 'Wideband gain enhancement and rcs reduction of fabry-perot resonator antenna with chessboard arranged metamaterial superstrate' IEEE Trans Antennas Propag. , PP, (99), pp. 1-9, 2017.

[4] C.A. Balanis, Modern antenna handbook, John Wiley & Sons, Newyork, USA, 2011.

[5] X. Chen, T.M. Grzegorczyk, B.I. Wu, J. Pacheco, J.A. Kong, 'Robust method to retrieve the constitutive effective parameters of metamaterials', Phys Rev E, vol 70, pp. 1-7,2004.

[6] M. Çakır, N.U. Koçkal, Ş. Özen, A. Kocakuşak, S. Helhel, 'Investigation of electromagnetic shielding and absorbing capabilities of cementitious composites with waste metallic chips', J Microwave Power EE, vol 51, pp.31-42, 2017.

Lattice Filtering Based Fusion of CT and MR Images

Nur Huseyin Kaplan[1]
[1]*Department of Electrical and Electronics Engineering*
Erzurum Technical University
Erzurum, Turkey
huseyin.kaplan@erzurum.edu.tr

Isin Erer[2]
[2]*Department of Electronics and Communication Engineering*
Istanbul Technical University
Istanbul, Turkey
ierer@itu.edu.tr

***Abstract*—In this work, a fusion method for computed tomography (CT) and magnetic resonance (MR) images is proposed. The method first decomposes the input MR and CT images into their detail and approximation subbands by lattice filters. Then, the approximation and detail subbands of two images are combined with a predefined rule to obtain the fused subbands. Finally, the new subbands are reconstructed by inverse lattice filtering to obtain the fused image. The visual and quantitative comparisons with the conventional methods provide that the proposed method provides better results.**

***Index Terms*—Magnetic Resonance, Computer Tomography, Lattice Filtering, Image Fusion**

I. Introduction

Medical imaging has a crucial input for clinical diagnosis. In order to perform accurate diagnosis, images obtained from different devices, such as computed tomography (CT) and magnetic resonance (MR), are used. CT image has the ability to provide densed structures (e.g. bones), whereas MT image provides the soft structures like tissues. Therefore, medical image fusion has an increasing interest for researchers [1]. It is known that, the purpose of image fusion, is to obtain a single image from multiple images, in which better characteristics of input images are provided [1]–[3]. Therefore, fusion of MR and CT images is expected to contain both densed and soft structures.

Many image fusion methods are proposed in literature [4]–[6]. The simplest method for image fusion is to take the average of input images. However, this approach provides low contrast images. Multiscale transforms (MST) such as Laplacian pyramid, gradient pyramid, morphological pyramid, discrete wavelet transform (DWT), stationary wavelet transform (SWT) have been widely used in image fusion tasks [4]–[6].

In these methods, the source images are decomposed into their subbands (named as lowpass and highpass subbands) by MST, then the subbands are merged by a predefined rule, and finally the fused image is obtained by the inverse MST. The most popular MST methods are based on the discrete wavelet transform (DWT). In DWT based methods, the calculation cost is too high becuse of the convolution operation which requires the use of ffts. To make the calculations faster, some methods such as lifting wavelet transform (LWT) [7] have been presented. Because of the decimation process during decomposition, both DWT and LWT are not shift-invariant, which affects the quality of the fused image. To overcome this problem lifting stationary wavelet transform (LSWT) has been used for image fusion processes [8]. Recently, undecimated lattice filter based fusion method has been proposed [9].

Motivated by the results of [9], the algorithm is used for CT and MR image fusion in this paper. The method first decomposes the CT and MR images into their detail and approximation subbands by an undecimated lattice structure. Then, the obtained subbands are combined by a predefined rule. Finally, the fusion result is obtained by using undecimated lattice reconstruction step. The method is compared to conventional MST methods. Both qualitative and quantitative performance evaluations show that the proposed method is better than the former methods.

II. CT and MR Image Fusion based on Lattice Filtering

The undecimated Lattice filtering based decomposition and reconstruction for 1D signals are given in Fig.1. By applying the system shown in Fig.1.a to a 1 D signal, we obtain x_L and x_H, which are the lowpass and highpass filter outputs of the signal, as in classical wavelet deomposition. More details about image decomposition/reconstruction can be found in [9].

Since, the decomposition and reconstruction algorithms described above are for 1 D signals, in order to perform it for image decomposition, the algorithms are applied first to the rows of the image followed by columns of the image, or vice versa [**?**]

The steps of the proposed method can be given as:

1) The MR and CT images are decomposed into their detail and approximation subbands as seen in Fig.1.a
2) The subbands merged as the ways described in [9], namely simple and MSP-con-max.
3) The new subbands are reconstructed by the lattice reconstruction to obtain the fusion result as seen in Fig.1.b

III. Experimental results

The fusion results obtained by the proposed method are compared to the LSWT methods given in [8], namely LSWT-simple and LSWT-MSP-con-max. For LSWT and proposed

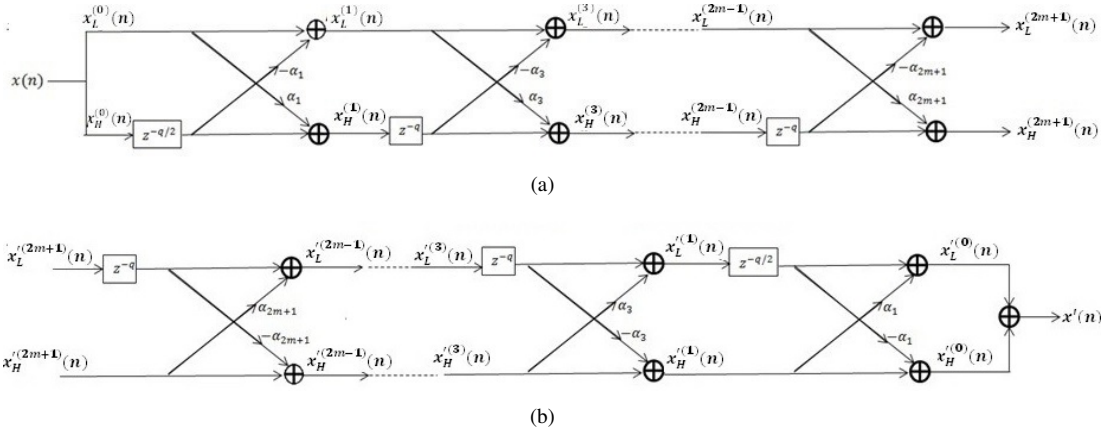

(a)

(b)

Fig. 1. Flowcharts for (a) Undecimated Lattice Decomposition, and (b) Undecimated Lattice Reconstruction

Lattice filtering methods the decomposition level is chosen as 2.

Fig.3.a,b shows the original CT and MR images respectively. Fig.3.c-f, show fusion results obtained for LSWT-simple [8], LSWT-MSP-con-max [8], and the proposed methods, respectively. For simple merging methdods, the edge are better transferred in Lattice based method as seen in Fig.3.d. MSP-con-max merging rule is better than the simple ones, as seen in Fig.3.e-f. A closer look demonstrates that the Lattice based method is better than the LSWT method.

In order to compare objectively, QAB and MI metrics are used. The quantitative comparion results are given in Table 1. According to Table 1, the proposed method outperforms LSWT method in all metrics, which means that the proposed method has preserved the important information of input images better.

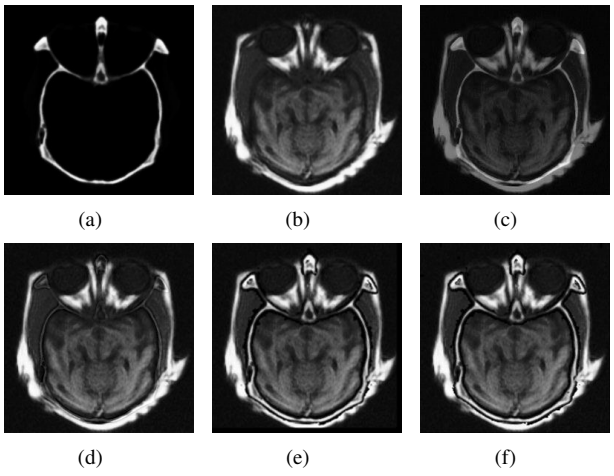

(a) (b) (c)

(d) (e) (f)

Fig. 2. (a) CT Image (b) MR image, Fusion Results for (c) LSWT-simple [8] (d) LSWT-MSP-con-max [8] (e) Lattice simple (f) Lattice-MSP-con-max

IV. Conclusions

The undecimated lattice filtering is used for MR and CT image fusion. The input images are decomposed into its detail and approximation subbands by lattice filtering. The obtained subbands are merged by a predefined rule to obtain the fused subbands. Finally undecimated lattice resconstruction is applied to provide the fused image. Both visual and quantitative comparisons demonstrate that the proposed method outperforms former methods by keeping the important information present in the input images.

TABLE I
Quantitative Comparison of Fig.3

Methods	QAB	MI
LSWT-simple [8]	0.4798	0.6386
Lattice-simple	0.6333	0.9035
LSWT-MSP-con-max [8]	0.8037	0.8746
LSWT-MSP-con-max	**0.8316**	**0.9897**

References

[1] P.Y. Barthez, I.A. Schaafsma, Y.W.E.A. Pollak, "Multimodality image fusion to facilitate anatomic localization of (99m)tc-pertechnetate uptake in the feline head." *Veterinary Radiology and Ultrasound*, vol. 47, no. 5, pp. 503-506, 2006.

[2] Y. M. Zhu, S.M. Cochoff, "An object-oriented framework for medical-image registration, fusion, and visualization." *Computer Methods and Programs in Biomedicine*, vol. 82, no.3, pp. 258-267, 2006.

[3] G. Pajares, J.M.D.L. Cruz, "A wavelet-based image fusion tutorial." *Pattern Recognition*, vol. 37, no. 9, pp. 1855-1872, 2004.

[4] Y. Chai, H.F. Li, J.F. Qu, "Multifocus image fusion using a novel dual-channel PCNN in lifting stationary wavelet transform", *Optics Communications*, vol. 283, pp. 35913602, 2010.

[5] Y.Chai, H.F. Li, M.Y. Guo, "Multifocus image fusion scheme based on features of multiscale products and PCNN in lifting stationary wavelet domain." *Optics Communications*, vol. 248, pp. 11461158, 2011.

[6] X.B. Qu, J.W. Yan, H.Z. Xiao, "Image fusion algorithm based on spatial frequency-motivated pulse coupled neural networks in nonsubsampled contourlet transform domain." *Acta Automatica Sinica*, vol. 34, pp. 15081514, 2008.

[7] W. Sweldens, "The lifting scheme: a construction of second generation wavelets." *SIAM Journal on Mathematical Analysis*, vol. 29, pp. 511546, 1998.

[8] H. Li, S. Wei, Y. Chai, "Multifocus image fusion scheme based on feature contrast in the lifting stationary wavelet domain." *EURASIP Journal on Advances in Signal Processing*, vol. 2012, no.1, pp.39, 2012.

[9] N.H. Kaplan, I. Erer, O. Ersoy, "Fusion of multifocus images by lattice structures." *Journal of Visual Communication and Image Representation*, vol. 38, pp. 848-857, 2016.

Ku Band Triangular Metamaterial Unit Cell Design

Hamid Torpi, Bilal Tütüncü
Electronics and Communication Engineering,
Yildiz Technical University, Esenler, Istanbul, Turkey

S.Taha İmeci
Electrical & Electronics Engineering,
International Univ. of Sarajevo, Bosnia and Herzegovina

***Abstract*—This study proposes a triangular shaped metamaterial unit cell at Ku Band. The permeability (μ) and permittivity (ε) of the metamaterial is extracted from the S parameters by using "robust method" to analyze whether the structure is double negative at Ku band or not. Media parameters are plotted by MATLAB. Microwave Studio by Computer Simulation Technology (MWS CST) is used for modeling and simulation. MM structure that is proposed in this paper can be used as a lens for directivity enhancement for a microstrip patch antenna in Ku band.**

Keywords—Metamaterial, Negative Refraction, TSRR

I. INTRODUCTION

Double negative materials (DNG), or, in other words, Metamaterials (MMs), are characterized by taking values of ε <0 and μ <0 at the same frequencies [1]. Recently, there has been growing interest in the study of MMs both theoretically and experimentally [2]. MMs are artificial materials synthesized by embedding specific inclusions, for example, periodic structures, in the host media [3]. Since the fundamental resonance behavior of the MM resonator structures is modeled as an LC resonance circuit, the resonance frequencies are very sensitive to variations in capacitive and inductive effects in the structure [4]. Inductive and capacitive effects vary according to the size and shape of the structure, so the designing and scaling of the MM structures requires precise measurements [5]. Modeling and simulation of complex MM structures can be done accurately and effectively using commercial full-wave electromagnetic 3D solver programs such as Ansoft HFSS (High Frequency Structure Simulator) and CST MWS (Computer Simulation Technology Microwave Studio) and we prefer to use CST in this study.

Several resonator structures have been introduced in the literature that exhibit MM characteristics over certain frequency ranges and the Triangular Shaped Ring Resonators (TSRR) are one of them [6] and in this paper a different version of it is initially modelled and scaled at Ku band. A Symmetric Triangular Structure is designed by using two isosceles triangles in a symmetrical position to each other.

II. DESIGN AND SCALE OF TRIANGLE MM

A. Symmetric Triangular Structure

In this structure, there are two isosceles triangles with the same size that is symmetric with respect to the +x axis on the front side of the dielectric substrate. At the base of the triangles there are gaps for capacitive effect. On the back side there is a conductive strip extending along the substrate for negative permittivity [7]. The schematic top view of the symmetrical triangular structure is given in Fig.1

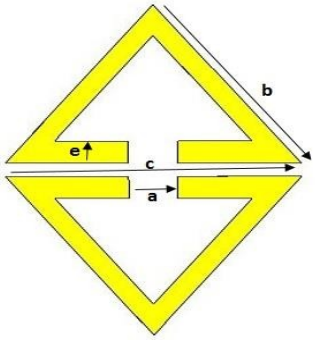

Fig. 1. Schematic top view of the symmetrical triangular structure

In order to take the transmission band to the Ku band, scaling experiments are performed by defining a "k" multiplier in the parameter list on the CST. The optimum values are obtained as follows; the long lengths of the isosceles b = 5 mm, the base length of the isosceles c = 6 mm, the gap a = 0.4 mm and the conductor width e = 0.67 mm. Rogers RO4350B is defined as a dielectric substrate. Dielectric constant is 3.48, loss tangent (tan δ) is 0.0037 and the thickness of this substrate is 0.762 mm. Substrate size is 9 mm x 9 mm. The thickness of the copper that is defined as the conductive part is 0.0035 mm. S11 chart is drawn to obtain the bandwidth and media parameters as shown in Fig. 2.

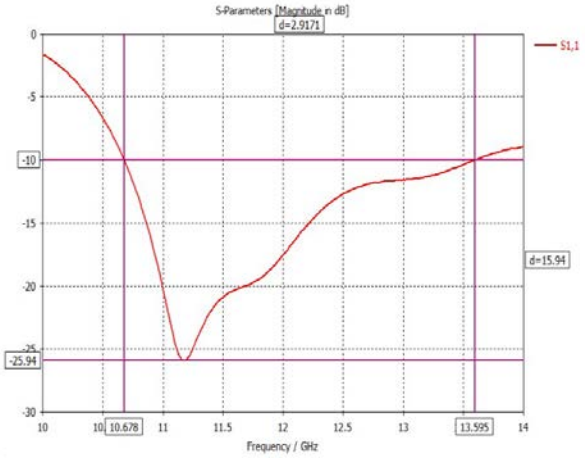

Fig. 2. S11 Curve of symmetrical triangular structure

B. *Extraction of Media Paremeters*

The symmetrical triangular structure has a bandwidth of 2.92 GHz between 10.68 GHz and 13.59 GHz (Fig. 2). To investigate the MM feature at this frequency range the “Robust Method” that is reported in [8] is used. In this method, the refractive index “n” and the impedance “z” that is obtained from the scattering parameters are used to extract the media parameters "ε" and "μ" of the material. The real and imaginary parts of S_{11} and S_{21} are separately taken and "ϵ" and "μ" curves are plotted by MATLAB.

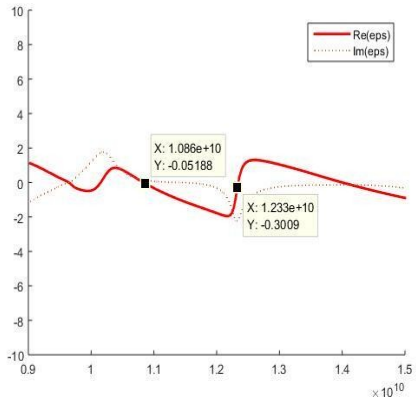

Fig. 3. ε curve of the symmetrical triangular structure

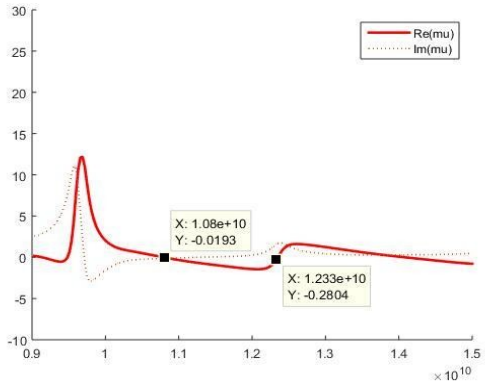

Fig. 4. μ curve of the symmetrical triangular structure

Fig. 3 shows the real and imaginary parts of the dielectric constant of the symmetrical triangular structure. The real part of "ε" between 10.86 GHz and 12.33 GHz is negative. Fig. 4 shows the real and imaginary parts of the magnetic permeability. The real part of “μ” is negative between 10.8 GHz and 12.33 GHz. As seen, the frequency range in which the real part of both media parameters takes negative values is between 10.8 GHz and 12.33 GHz, which includes the transmission band as shown in Fig. 2. The imaginary parts that indicates the "loss energy” are neglected [9].

III. RESULTS AND DISCUSSIONS

MMs are used in a wide spectrum from microwave regime to optical frequency range. In this study a TSRR is designed as a MM unit cell structure and MM characteristics of this structure at Ku band is verified by plotting media parameters. The values of "ε" and "μ" in the boundary frequencies for negative values are given in Table 1. Since the negative refraction helps to focusing and reduces the transmitted power loss, the proposed MM structure in this paper can be used as a lens for directivity enhancement for a microstrip patch antenna in Ku band [10].

TABLE 1 Media Parameters of TSRR

Media Parameters of TSRR	Frequency	
	10.8 GHz	12.33 GHz
Permittivity-ε	-0.05	-0.3
Permeability-μ	-0.019	-0.28

REFERENCES

[1] V.G Vesalago,"The electrodynamics of substances with simultaneously negative values of and μ," Soviet physics uspekhi, vol.10, pp. 509-514, 1968.

[2] M.A. Noginov and V.A. Podolskiy, Tutorials in metamaterials. CRC press, Newyork, 2011,

[3] B.-I Wu., W. Wang, J. Pacheco, X. Chen, T. Grzegorczyk and J. A. Kong "A study of using metamaterials as antenna substrate to enhance gain," Progress In Electromagnetics Research, vol. 51, pp. 295-328, 2005.

[4] R. Waterhouse, Microstrip patch antennas: a designer’s guide. Springer Science & Business Media, Berlin, 2013.

[5] C. Sabah, "Tunable metamaterial design composed of triangular split ring resonator and wire strip for S-and C-microwave bands," Progress In Electromagnetics Research, vol.22, pp. 341-357, 2010.

[6] M. Bakır, M. Karaaslan, F. Dinçer and C. Sabah, "Metamaterial characterization by applying different boundary conditions on triangular split ring resonator type metamaterials," International Journal of Numerical Modelling: Electronic Networks, Devices and Fields (ISSN: 1099-1204), vol. 30 (5), 2017.

[7] J.B. Pendry, A.J. Holden, D.J. Robbins, "Extremely low frequency plasmons in metallic mesostructures," Phys Rev Lett, vol.76 (25), pp. 4773-4776, 1996.

[8] X. Chen, T.M. Grzegorczyk, B.I. Wu, J. Pacheco, J.A. Kong, "Robust method to retrieve the constitutive effective parameters of metamaterials," Physical Review E, vol.70(1), pp. 016608/1-7, 2004.

[9] M. Çakır, N.U. Kockal, S. Ozen, A. Kocakusak, and S. Helhel, "Investigation of electromagnetic shielding and absorbing capabilities of cementitious composites with waste metallic chips." Journal of Microwave Power and Electromagnetic Energy, vol. 51(1), pp. 31-42, 2017.

[10] B. Tütüncü, H. Torpi and B. Urul, “A comparative study on different types of metamaterials for enhancement of microstrip patch antenna directivity at Ku-band (12 GHz),” Turk J Elec Eng & Comp Sci, in press

Inset fed multi slots T-shaped patch antenna

Abdul malek Naes, Ahmad Aljalmoud, Ahmad Alkhas, Khaled Tawakol
Electrical &Electronics Engineering Department
Istanbul Sehir University
Istanbul, Turkey
{abdulnaes, ahmadaljalmoud, ahmadkhas, khaledtawakol}
@std.sehir.edu.tr

Abstract— In this paper, a microstrip patch with multi rectangular slots and T-Shaped antenna is designed and simulated. This design is fed with a circuler shaped input of 1 mm diameter at the edge of the inset fed part of this antenna. In addition, the substrate material used there is RT6002 with dielectric of 0.76 mm. The results of this design could be used in backhauls broadcasting, NASA's Track Data Relay Satellite and radar guns speed detection since the gain is 7.49 dB at 15.4 GHz frequancy with -14.22 dB for S11 of designated antenna at Ku band spectrum.

Keywords — Microstrip patch antenna, slot antenna with rectangular shape.

I. INTRODUCTION

Modern communication systems frequently used micro strip patch antennas due to its low manufacturing cost and light-weight, such antennas used to transform RF signals [1, 2]. Inset fed micro strip patch antenna allows controlling the impedance and the feed configuration [3]. Therefore, it is used in the design. Never the less, using many slots in designing an antenna leads to decreasing in the resonant frequency [4].

II. DESIGN AND SIMULATION RESULTS

The design of this antenna is based on a substrate of Roger RT6002 material of 0.76 mm air thickness due to the measurements made to confirm such design. Many rectangular slots reduce the resonant frequency and stabilize it to a certain frequency. Manufacturer commonly uses T-shaped designs in micro strip patch antenna because it reflects toward the Ku band frequency as Fig 1 shows.

Moreover, inset fed has non-conducting areas on both sides of the inset fed which called notches. These notches effect on the resonant resonance frequency and the gain, which leads to decreasing the resonant input impedance until it is zero at the center [3]. The Inputs match of this design are (-14.22 dB) and radiation pattern 7.49 dB at 15.4 GHz as shown in Fig 2. The radiation pattern has a cross-polarization at 15.4 GHz as Fig. 3. shows, which it decreases as the notch gets narrower. The current distribution is shown in Fig. 4. The resonance frequency is concentrated at the edges of slots and notches where it reaches zero at the center.

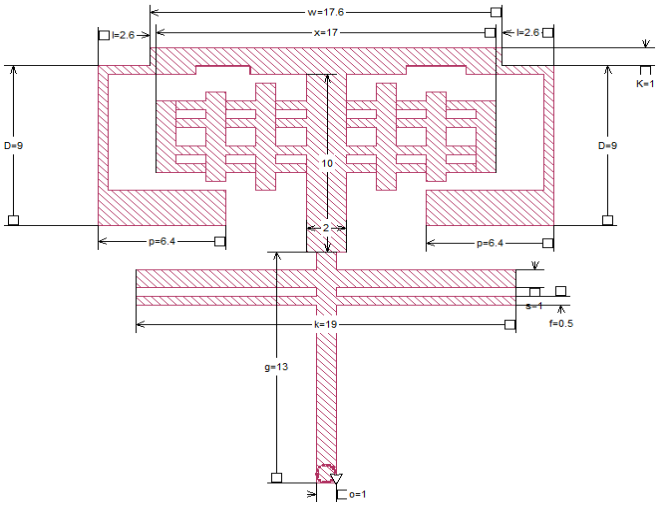

Fig. 1. Top View of the Final Design

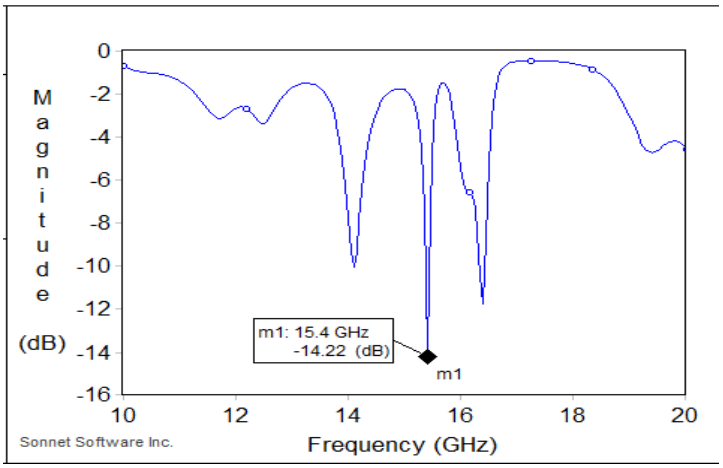

Fig. 2. Input Match S11

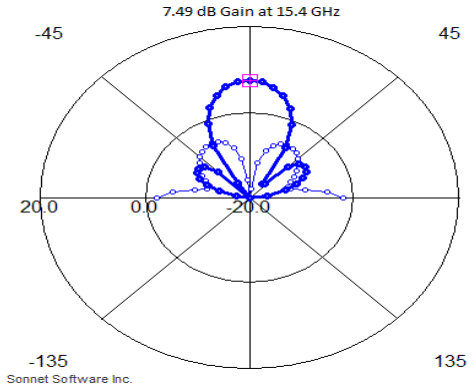

Fig. 3. Polar form and the Gain Value

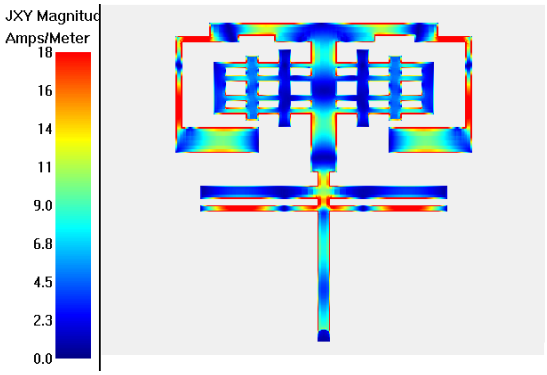

Fig. 4. Current distribution of patch antenna

Furthermore, the designed antenna was based on only one dielectric material with known thickness that were mentioned earlier. In order to confirm the design, the dielectric material changed to simulate the design and obtain different results. Table I presents the simulations' results. Those results indicate that this antenna may only work on the originally chosen material, as neither the reflection coefficient nor gain reached minimum requirements of -10 dB and 7 dB for both respectively.

TABLE I. DIFFERENT DIELECTRIC MATERIALS' SIMULATION RESULTS.

Dielectric Materials	Reflection Coefficient S11 (dB)	Resonance Frequency (GHz)	Gain (dB)
FR-4	-3.77	15.55	-6.41
ROGER RT6002	-14.22	15.4	7.49
Rogers RT6006	-5.86	14.95	-0.72
Rogers RT6010LM	-5.67	15.25	2.36

On the next step, the design was modified a couple of times and created duplicates with air thickness or dielectric thickness variation. Table II shows the simulations' results for each of those duplicates. In the beginning, the thickness of dielectric varied for each duplicate with at maximum 0.2 mm, while the air thickness varied starting with 3 mm and ending with 60 mm. The resonance frequency has shifted for each one with a maximum of 0.15 GHz above/below 15.4 GHz. While the reflection coefficient effected a lot, especially by the thickness of the material variations, so it concludes that thickness of the material is so important to be the same as the original design on the fabrication process. However, for the cases where the air thickness varied, it has affected but not as much as when material thickness varied. It is observed that 2 out of 4 cases the results for the coefficient value were valid, while none of the results was valid for the previous cases. On the other hand, gain values were all valid except for two cases, but without reflection coefficient being valid and below -10 dB the design would not be valid. It is also observed from the table that there was a better gain value attained when the air thickness was 5 mm instead of 4 mm, while the reflection coefficient was also valid. Therefore, it might be a better version of the original design.

TABLE II. DIELECTRIC \ AIR THICKNESS.

Air Thickness (mm)	Dielectric Thickness (mm)	Reflection Coefficient S11 (dB)	Resonance Frequency (GHz)	Gain (dB)
4	0.74	-1.84	15.5	1.01
4	0.75	-11.74	15.25	7.46
4	0.77	-7.41	15.35	7.19
4	0.78	-7.98	15.35	7.26
4	0.76	-14.22	15.4	7.49
3	0.76	-14.86	15.25	6.36
5	0.76	-12.06	15.3	8.09
10	0.76	-8.83	15.25	8.47
60	0.76	-2.06	15.4	8.13

III. CONCLUSION

Finally, this paper analyze a microstrip patch antenna with T-Shaped with rectangular slots. The antenna has a gain of 7.49 dB, S11 -14.22 dB at 15.4 GHz. Many simulations are completed with various dielectric, dielectric thickness, and air thickness. RT6002 dielectric substrate with 0.76 mm thickness and 4 mm air thickness gave the best result.

REFERENCES

[1] Singh, P., & Singh, S. (2016). Design and analysis of T shaped broad band micro strip patch antenna for Ku band application.

[2] W. Weedon, W. Payne, and G. Rebeiz, Mems-switched reconfigurable antennas, In Antennas and Propagation Society International Symposium, IEEE, (3), 2001, 654 –657.

[3] A. M. Naes, A. Aljalmoud, A. Alkhas, K. Tawakol, E. Kokach and T. Imeci, "Inset fed patch antenna with five slots," 2017 25th Signal Processing and Communications Applications Conference (SIU), Antalya, 2017, pp. 1-4.

[4] W. C. Araujo, A. G. d'Assunçào and L. M. Mendonça, "Analysis of multi-slot microstrip patch antennas using neural netwoks," Proceedings of the Fourth European Conference on Antennas and Propagation, Barcelona, 2010, pp. 1-3.

Fractional Derivative Method in the Problem of Diffraction of a Cylindrical Wave on An Impedence Strip

Kamil Karaçuha[1]
[1]*Informatics Institute of Istanbul Technical University*
Istanbul, Turkey
karacuha17@itu.edu.tr

Eldar Veliyev[1]
[1]*Informatics Institute of Istanbul Technical University*
Istanbul, Turkey
eldarveliev@itu.edu.tr

Ertuğrul Karaçuha[1]
[1]*Informatics Institute of Istanbul Technical University*
Istanbul, Turkey
karacuhae@itu.edu.tr

Osman Dur[1]
[1]*Istanbul Technical University*
Istanbul, Turkey
osmandur42@gmail.com

***Abstract*— In this paper, two dimensional problem of diffraction of a cylindrical wave on an impedance strip is studied. For fractional order equal to 0.5, the solution can be found analytically. In the paper, also numerical results for fractional order equal to 0.5, is presented.**

***Keywords*— cylindrical wave, diffraction, fractional boundary conditions, impedance strip**

I. INTRODUCTION

Earlier we considered [1, 2] application of the method of fractional derivatives to solve the two-dimensional problem of diffraction of a plane wave on an impedance strip. In [2], the concept of a fractional strip was introduced. Here, it is understood as a strip on the surface, which is subject to fractional boundary conditions. This problem has been studied quite well on the basis of various methods. As a rule, this problem is studied on the basis of numerical methods. The proposed approach, as shown below, allows one to obtain an analytical solution of the problem for fractional order $\boldsymbol{\nu} = 0.5$ and for fractional order of the interval (0, 1), the general solution is also investigated numerically.

II. FORMULATION OF THE PROBLEM

Let a two-dimensional strip of width *2a* be placed on the plane $\boldsymbol{y = 0}$. The tape along the z axis is infinite. The source of the cylindrical wave $\vec{J}_e = \vec{z}J_e\delta(x - x_o)\delta(y - y_o)$ is located at the point (x_o, y_o) shown in Figure 1.

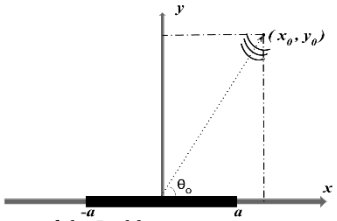

Fig. 1. Geometry of the Problem

Let us consider the case of an *E*-polarized wave, i.e. $\vec{E}_z^i(0,0,E_z), \vec{H}_z^i(H_x, H_y, 0)$. In this case, the source field has the form,

$$\vec{E}_z^i(x,y) = -\vec{J_e}\frac{\eta_0 k}{4}H_0^{(1)}\left(k\sqrt{(x-x_o)^2+(y-y_o)^2}\right) \quad (1)$$

Here $H_0^{(1)}(kx)$ is the Hankel function of the first kind and zero order, $\eta_0$is the impedance of free space, and $\boldsymbol{k}$ is the wave number. We set the time dependence as $\boldsymbol{e^{-i\omega t}}$ and then omit it. The total field can be represented as a superposition of $\vec{E}_z = \vec{E}_z^i + \vec{E}_z^s$, where $\vec{E}_z^i$ the source is field, and $\vec{E}_z^s$ describes the scattered field. To find the scattered field $\vec{E}_z^s$, it is necessary to subordinate the total field, as noted above, to a new boundary condition [1, 2], which we call the fractional boundary condition (FBC).

$$\mathfrak{D}_{ky}^{\nu}E_z(x,y)\big|_{y=\pm 0} = 0 \quad (2)$$

where $x, -a < x < a$, and $\boldsymbol{\nu}$ is fractional order (FO). Further, the fractional derivative $\mathfrak{D}_{ky}^{\nu}$ will be determined from the Riemann-Liouville equation [1, 2].

The fractional order $\boldsymbol{\nu}$ varies from 0 to 1. For the value $\boldsymbol{\nu = 0}$, the strip with FBC (2) corresponds to an ideally electrically conducting (PEC) strip, and for $\boldsymbol{\nu = 1}$, a strip with ideally magnetic conductivity (PMC) is obtained [3]. For intermediate values $\boldsymbol{0 < \nu < 1}$, FBC describes a fractional boundary with specific properties, which is investigated in this article. FBC leads to the use of the fractional Green's function (FGF) $G^{\nu}(x)$ [3] and the fractional Green theorem [1]-[3]. In this case, the scattered field can be represented as [1]

$$\vec{E}_z^s(x,y) = \int_{-\infty}^{\infty} f^{1-\nu}(x')\, G^{\nu}(x-x',y)dx' \quad (3)$$

Here, $f^{1-\nu}(x')$ is an unknown function, which we will call the fractional density of the potential, and the fractional Green's function $G^{\nu}(x)$ has the form [3]

$$G^{\nu}(x-x',y) = -\frac{i}{4}\mathfrak{D}_{ky}^{\nu}H_0^{(1)}\left(k\sqrt{(x-x')^2+y^2}\right)$$
$$= -i\frac{e^{\pm i\frac{\pi}{2}\nu}}{4\pi}\int_{-\infty}^{\infty} e^{ik\left[\alpha(x-x_o)\pm y\sqrt{1-\alpha^2}\right]}(1-\alpha^2)^{\frac{\nu-1}{2}}d\alpha \quad (4)$$

Representing (4) for the scattered field (3) by rewriting in Fourier transform, we obtain,

$$E_z^s(x,y) = -\frac{e^{\pm i\frac{\pi}{2}\nu}}{4\pi}\int_{-\infty}^{\infty} F^{1-\nu}(\alpha)e^{ik\left[\alpha x\pm y\sqrt{1-\alpha^2}\right]}(1-\alpha^2)^{\frac{\nu-1}{2}}d\alpha \quad (5)$$

$$F^{1-\nu}(\alpha) = \int_{-1}^{1}\tilde{f}^{1-\nu}(\xi)e^{-i\varepsilon\alpha\xi}d\xi\ ,\quad \tilde{f}^{1-\nu}(\xi) = af^{1-\nu}(\xi) \quad (6)$$

where,

$$\varepsilon = ka,\ \xi = \frac{x}{a} \quad \text{and} \quad \tilde{f}^{1-\nu}(\xi) = \frac{\varepsilon}{2\pi}\int_{-\infty}^{\infty} F^{1-\nu}(\alpha)e^{i\varepsilon\alpha\xi}d\alpha$$

Now, subjecting the total field $\vec{E}_z$ to the FBC (2) and taking into account (5) and (6) to determine the fractional Fourier transform $F^{1-\nu}(\alpha)$, we obtain the integral equation (IE) of the following form

$$\int_{-\infty}^{\infty} F^{1-\nu}(\alpha)\frac{\sin\varepsilon(\alpha-\beta)}{\alpha-\beta}(1-\alpha^2)^{\nu-\frac{1}{2}}d\alpha = -4A\pi e^{-i\frac{\pi}{2}\nu}\int_{-\infty}^{\infty} e^{i\left[-kx_0\alpha+ky_0\sqrt{1-\alpha^2}\right]}\frac{\sin\varepsilon(\alpha-\beta)}{\alpha-\beta}(1-\alpha^2)^{\frac{\nu-1}{2}}d\alpha \tag{7}$$

where, $A = -J_e\frac{\eta_0 k}{4\pi}$

As noted above, for values of fractional order ν = 0.5, IE (9) has an analytic solution that has the form

$$F^{0.5}(\alpha) = -4Ae^{-i\frac{\pi}{4}}\int_{-\infty}^{\infty}\frac{\sin\varepsilon(\beta-\alpha)}{(\beta-\alpha)}e^{i\left[(-kx_0\beta)+ky_0\sqrt{1-\beta^2}\right]}(1-\beta^2)^{-\frac{1}{4}}d\xi d\beta \tag{8}$$

Accordingly, the density of the fractional potential has the form

$$\tilde{f}^{0.5}(\xi) = -2\varepsilon Ae^{-i\frac{\pi}{4}}\int_{-\infty}^{\infty} e^{i\left[(\varepsilon\alpha\xi-kx_0\alpha)+ky_0\sqrt{1-\alpha^2}\right]}(1-\alpha^2)^{-\frac{1}{4}}d\alpha \tag{9}$$

Now we present the expressions for the radiation pattern (RP), monostatic and bi-static radar cross sections (RCS). These expressions will be used to analyze the electromagnetic characteristics of the scattered field.

Let's derive the expression for the field $\vec{E}_z^s$ in the far-zone kr → ∞. In the cylindrical coordinate system (r, φ) can be written by using following relations; x = r cos φ, y = r sin φ. The scattered field (5) becomes

$$E_z^s(r,\varphi) = \frac{i}{4\pi}\int_{-\infty}^{+\infty} F^{1-\nu}(cos\beta)e^{ikrcos(\varphi\pm\beta)}sin^{\nu}\beta d\beta \tag{10}$$

where the upper sign is chosen for the values φ ∈ [0, π], and the lower sign for φ ∈ [π, 2π]. If kr → ∞ we can use the method of stationary phase to derive the expression for $E_z^s(r,\varphi)$ as follows,

$$E_z^s(r,\varphi) = A(kr)\Phi^{\nu}(\varphi) \ \text{ while kr} \to \infty \tag{11}$$

where,

$$A(kr) = \sqrt{\frac{2}{\pi kr}}e^{ikr-i\pi/4};\ \Phi^{\nu}(\varphi) = -\frac{i}{4}(\pm i)^{\nu}F^{1-\nu}(cos\varphi)sin^{\nu}\varphi \tag{12}$$

The function $\Phi^{\nu}(\varphi)$ denotes the radiation pattern (RP) of the scattered field. In special cases when ν = 0.5 we have

$$\Phi^{0.5} = -\frac{i}{4}e^{\pm i\frac{\pi}{4}}F^{0.5}(cos\varphi)sin^{0.5}(\varphi) \tag{13}$$

where,

$$F^{0.5}(cos\varphi) = -4Ae^{-i\frac{\pi}{4}}\int_{-\infty}^{\infty}\frac{\sin\varepsilon(\beta-cos\varphi)}{(\beta-cos\varphi)}e^{i\left[(-kx_0\beta)+ky_0\sqrt{1-\beta^2}\right]}(1-\beta^2)^{-\frac{1}{4}}d\xi d\beta \tag{14}$$

The formula for the static RCS $\frac{\sigma_{2d}}{\lambda}$ is $\frac{\sigma_{2d}}{\lambda}(\varphi) = \frac{2}{\pi}|\Phi(\varphi)|^2$ and for monostatic RCS is $\sigma_{2d} = \frac{\sigma_{2d}}{\lambda}(\theta_o)$.

As shown in [2], the fractional order is related to the impedance

$$\nu = \frac{1}{i\pi}ln\frac{1-\eta}{1+\eta},\ \eta = -i\tan\left(\frac{\pi\nu}{2}\right) \tag{15}$$

The value ν = 0 corresponds to the impedance η = 0 (PEC) and ν = 1 corresponds to η = −i∞ (PMC). For the intermediate values 0 <ν< 1 the impedance has pure imaginary values between 0 and −i∞. Figures 2-4 show the RP, field distributions in the vicinity of the impedance strip for various values of the frequency parameter $\boldsymbol{\varepsilon}$ and the distribution of the source.

III. Numerical Results

Numerical calculations and simulations are done for $\boldsymbol{\nu} = 0.5$ In Figures 2-4, radiation pattern, electric field are shown by giving different parameters. In Figure 2, horizontal axis stands for y-axis and, vertical axis stands for x-axis.

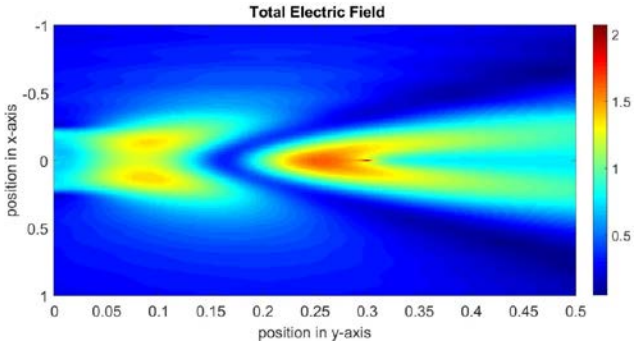

Fig. 2. Total Electric Field Distribution for for $\epsilon = 1.5\pi,\ k = 6\pi$

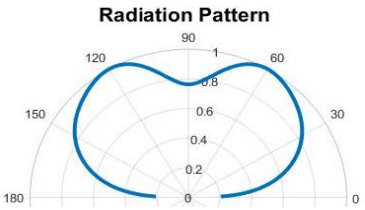

Fig. 3. Radiation Pattern for $\epsilon = 2\pi,\ k\rho_o = \pi/10$

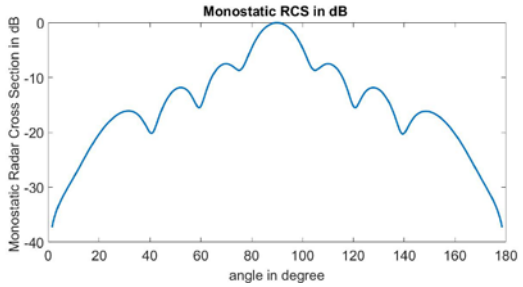

Fig. 4. Monostatic RCS for $\epsilon = 2\pi,\ k\rho_o = 2\pi^2$

References

[1] E. I. Veliev, M. V. Ivakhnychenko, and T. M. Ahmedov, "Fractional Boundary Conditions In Plane Waves Diffraction On A Strip," *Progress In Electromagnetics Research*, vol. 79, pp. 443–462, 2008.

[2] M. V. Ivakhnychenko, E. I. Veliev, and T. M. Ahmedov, "Scattering Properties Of The Strip With Fractional Boundary Conditions And Comparison With The Impedance Strip," *Progress In Electromagnetics Research C*, vol. 2, pp. 189–205, 2008. J. Clerk Maxwell, A Treatise on Electricity and Magnetism, 3rd ed., vol. 2. Oxford: Clarendon, 1892, pp.68–73.

[3] Veliev E. and N. Engheta. "Generalization of Green's Theorem with Fractional Differintegration". *2003 IEEE AP-S International Symposium & USNC/URSI National Radio Science Meeting, 2003.*

Evaluation of Systemic Risk between American and European Financial Systems

Assist. Prof. Vahit Ferhan BENLI
Department of Banking and Finance
Istanbul Commerce University
Istanbul, Turkey
vfbenli@ticaret.edu.tr

Safa MASTOURI
Department of Finance
Istanbul Commerce University
Istanbul, Turkey
mastourisafa@gmail.com

***Abstract* —** Present study focuses on the analysis of systemic risk in the American and European financial systems for a period from 20/08/2004 to 28/02/2014. The global crisis in 2007 has brought attention to the urgent need to understand the systemic risk issues and the stability of financial systems along with their actors. To assess systemic risk, Adrian and Brunnermeier (2011) advocated the use of conditional value at risk (CoVaR) methodology in integrating quantile regression. Instead of the Value at Risk (VaR), which is unable to detect systemic risk, we seek to use the CoVar methodology to calculate the systemic risk levels of the United States and European markets. In the light of related findings, we conclude that the insurance sector contributes most to the systemic risk in the USA, while in the Euro zone; it is the financial services sector that is much interconnected with systemic risks.

Keywords— Systemic Risk, Financial regulation, Value-at-Risk, CoVaR, Quantile regression.

I. INTRODUCTION

The financial system has always played a major and dominant role in the proper functioning of modern economies. Nevertheless, the recent financial crisis of 2007 clearly shows that its failure can be harmful for the interconnected network economies. This has prompted researchers and regulators to become aware of the insecurity of the financial systems and the seriousness of the vulnerabilities to “Systemic risks”. In this regard, our research paper aims for gaining insight into the systemic risk issues on the US and EU financial systems. It comprises of four main sections: Section (1) is devoted to the explanation of the concept of systemic risk and it addresses the regulatory reform component to minimize it. Section (2) describes the evolution of risks as well as the measures relating to each type. Section (3) is dedicated to the presentation of the data and the methodology considered. Section (4) reports the results obtained, accompanied by their interpretations and finally Section (5) concludes.

II. SYSTEMIC RISK AND FINANCIAL REGULATION

A. Systemic Risk

Following the studies of the FSB, IMF and BIS for the G20, the systemic risk can be identified as "a risk of disruption to financial services that is caused by an impairment of all or parts of the financial system and has the potential to have serious negative consequences for the real economy." According to Lepetit (2010), financial instability resulting from total or partial deterioration of the components of the financial system can have a negative impact on the real economy. In this respect, we can define a key element of systemic risk, namely the enhancement of fragility inside the financial system. This symmetric shock transmission capability is described in the sense that a contagious shock in a much “institutional way” is transmitted from one SIFI (systemicly important financial institution) to another causing financial imbalances for the entire financial system. This interaction and interconnectedness between the various institutions on the one hand and between the financial and economic spheres on the other is due to the contagion phenomenon studied in finance since the 1990s. However, this main risk transformation mechanism is often under-estimated or even neglected by professionals and regulators when quantifying the risk.

B. Systemic Approach to Financial Regulation

One of the biggest challenges for regulators and public authorities today is restoring financial and economic stability. The fragility of the financial system and its role in triggering systemic crises has led many regulatory institutions to monitor and regulate on a continuous basis the systemic risk. In 2010, the International Organization of Securities Commissions (IOSCO) has settled a research department whose principle is to monitor, mitigate and manage systemic risk by analyzing the perimeter of regulation on a continuous basis. By the same token, BIS has resolved the Systemic Risk issue in the context of Strengthening of the Global Capital within the Basel III Framework in 2010 (BCBS 2010).

III. EVOLUTION OF DIFFERENT RISK MEASURES

In 1952, the modern theory of portfolio was born with the publication of the founder Harry Markowitz. A decade later, in 1976, Ross developed an alternative to the CAPM called "Arbitrage Pricing Theory" (APT), based on a multi-factorial model (multi-beta). In 1992, Fama and French developed another multi-factorial model. According to Dowd (2005), these methods are not highly recommended for calculating market risk per se. The standard deviation and the betas do not

allow considering the market risk satisfactorily. Hence the publication of the Value-at-Risk (VaR) in the early 90s gave new pave to the measurement of market risk. VaR (t, q) defined as:

$P(X^i \leq VaR^i(t,q)) = q$ Where:

q: probability of adverse event where coverage rate, usually set at 1% or 5%

$\mathbf{X^i}$: represents the loss, it is a positive or negative random variable.

In 2011, Tobias Adrian, Senior Vice President and Head of Capital Markets at the FED New York, and Markus K. Brunnermeier, Prof. at Princeton, proposed a new systemic risk measure named CoVaR.

$CoVaR_q^{(i|j)}$ is written as follows:

$P(X^i \leq CoVaR_q^{(i|j)} | X^j = VaR_q^j) = q$

$CoVaR_q^{(i|j)}$ is defined as the VaR for an institution i (or loss) under the effect of an event C (X^J) of an institution j. This event is linked to the fact that the institution j reaches its level of VaR such that: $X^j = VaR_q^j$.

IV. ESTIMATION OF COVAR ON THE AMERICAN AND EUROPEAN MARKETS

A. Motivation

The authors opt for an approach combining studies already conducted on the financial sectors (cross-sectorial study) and financial institutions (inter-company study), distinguishing between life and non-life insurance. Subsequently, they plan to determine the CoVaR for two distinct regions: the United States and the "Euro" zone. Our goal is to guide the macro-prudential regulation actors towards sectors and institutions, whose role is predominant mitigation of systemic risk.

B. Presentation of the data

Data on the US and European market at daily frequency, cover the period from 20/08/2004 to 28/02/2014, i.e. 2314 observations. We will present the variables needed to estimate CoVaR, referring mainly to Adrain and Brunnermeier (2011) and Bernal et al. (2013). In order to define the control variable for each region we have extracted some inputs from Thomson Reuters and Bloomberg databases.

a) American Market

Adrian and Brunnermeier (2011) defined 7 control variables for estimating VaR and CoVaR in the US market, namely: VIX, which is a volatility index, listed in Chicago Board Options Exchange, Liquidity Spread short-term liquidity spread, the variation of the US sovereign bond rate of the same maturity, The Yield Spread, The Credit Spread, The US equity market return, and finally the performance of the US real estate sector.

b) European Market

By analogy with the US market, we will identify control variables related to the European market.

C. Model and methodology

We used the STATA11.2 software to establish the quantile regression on *CoVaR* equation (defined in section 3) also to apply the "two-sample kolmogorov-smirnov test" noted KS, and the OxMetric 7.2 software in order to produce the graphical representations.

V. CONTRIBUTION OF THE FINANCIAL SYSTEM TO THE SYTEMIC RISK : RESULTS

Commonly, it appears that the sector or institution with the highest VaR does not necessarily contribute the most to systemic risk. Comparing CoVaR to VaR, we found, first, that the sector or financial institution with the highest amount of loss does not necessarily contribute the most to the risk studied. In the light of findings related to the cross-sectorial study, the results show that the life insurance sector contributes the most to systemic risk in the US market, while in the European countries, the real economy is clearly more influential in case a problem arises in the banking and the financial services sector.Regarding the inter-companies study, our results reveal that, the major financial institutions do not automatically contribute the most to systemic risk, as has been proven by the study by Roengpitya and Rungcharoenkitkul (2011).

VI. CONCLUSION

Within the study, we aimed to define the sector and more precisely the institution that contributes the most to the “contagion phenomena” issued by this type of risk. It was a challenge when we analyzed the financial sectors; particularly that we conducted two level analysis cross-sectorial and inter-companies studies. However, we could conclude that for the European markets, the insurance sector leads the most to the appearance of the systemic risk while for US market it is both of banking and financial services. Moreover, we have been able to admit that the size criterion can be an effective source of error for financial regulators. Indeed, it has been shown that smaller institutions are likely to have negative impacts on the real economy than those classified as large companies. It is therefore essential to explore the most risky institutions systematically in consideration of other criteria, such as substitutability, complexity, interdependence or cross-border activities.

REFERENCES

[1] Adrian T. and Brunnermeier M.K., (2011), “CoVaR”, Federal Reserve Bank of New York Staff Reports, N° 348.

[2] Carlta Vitzthum , “IOSCO MEDIA RELEASE”, (July 2017), Madrid.

[3] Dowd K., (2005), “Measuring Market Risk”, John Wiley & Sons Ltd, Chichester.

[4] Lepetit Jean-François, (2010),“Rapport sur le risque systémique“, Ministère de l'économie, de l'industrie et de l'emploi, France.

[5] Racicot F. and Theoret R., (2006), “La Value-at-Risk : Modèles de la VaR, simulations en Visual Basic (Excel) et autres mesures récentes du risque de marché”, Quebec University.

[6] Roengpitya R.& Rungcharoenkitkul P.,(2011),“Measuring Systemic Risk and Financial Linkages in the Thai Banking System”, Bank of Thailand.

[7] Staff of the IMF and the BIS, and the SFSB, (2009), “Guidance to Assess the Systemic Importance of Financial Institutions, Markets and Instruments: Initial Considerations”, Report to the G-20 Finance Ministers and Central Bank Governors, 6-9.

E-Shaped Microstrip Patch Antenna Design For WLan Applications

Abdul malek Naes, Ahmad Aljalmoud,
Ahmad Al Khas, Khaled Tawakol
Department of Electrical and Electronics Engineering
Istanbul Sehir University
Istanbul, Turkey

Fatih Macit
Istanbul Commerce University
Department of Electrical and Electronics Engineering
Taha Imeci
International University of Sarajevo
Department of Electrical and Electronics Engineering

Abstract— This work presents an E-shaped patch antenna which works at three different frequencies. The AIR substrate with 25 mm thickness is used in this design. Simulation results show that the desired resonance frequency is 1.8 GHz with 9.3 dB, -20.05 dB for (S11) reflection coefficient. Since the antenna works within L band, then it can be used for satellite communication, such as; low earth orbit satellites and military satellites, terrestrial wireless connections like GSM mobile phones and WLAN.

Keywords— E-shaped patch antenna; L band; microstrip patch antenna; satellite communications.

I. INTRODUCTION

In the recent years, there has been rapid growth in wireless communication. Day by day users are increasing, but limited bandwidth is available, and operators are trying so hard to optimize their network for larger capacity and improved coverage quality. This surge has led the field of antenna engineering to accommodate the need for broadband, low cost miniaturized and easily integrated antennas [1]. Micro strip patch antennas are commonly used in wireless communications, like Bluetooth, Wi-Fi, WLAN, Wi Max applications due to their attractive features such as small size and hence conformal nature, easy to feed and design, low fabrication cost, robust nature, light in weight, and easily integrated with monolithic microwave integrated circuits [2]. For microstrip patch antenna there are three types of analysis methods which are transmission line model, cavity model, and full wave model. In this proposed design the transmission line model is used with copper substrate of 25 mm thickness on both sides [3]. It has an air thickness of Er=1 and a very compact size as follows (The edge length is 65mm, the lower length is 104mm and the middle slot length equals to 50 mm). E- shaped microstrip patch antenna is fed from the middle section [4]. The simulation results show that this antenna can be applied to serve WLAN applications since it works at L band frequency [5].

II. DESIGN AND SIMULATION RESULTS

The main purpose of this designated antenna is to have unique features and to ease the process of production in both shapes and coasts. The price of the dielectric material used is low compared to other materials' prices. The shape of the antenna is divided into two main dimensions; width and height of the 3 slots with respect to the whole antenna size. The antenna simulation is done under the constraint of thickness to be between 25 mm and 33 mm. The desired gain was achieved with the dimensions shown in Fig.1.

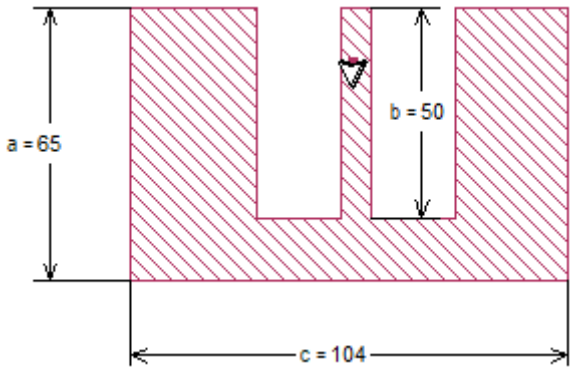

Fig. 1. Top View of The Design

Even though Changing the dimensions of the slots affects the gain critically, this design showed that having an error in the fabrication process within a=65mm to 69mm, b= 50mm to 53mm will not affect the performance of the antenna. The simulation values of the modified length of (a) and (b) is shown in Table I. It shows that if the length of the slots decreased, the gain drops critically while the frequency increases. On the other hand; increasing them gives a gain up to 8.86 to the frequency of 1.64 GHz.

TABLE I. FREQUENCY-GAIN-INPUT MATCH WHEN E SHAPED LEGS DICREASE

Design Steps	Frequencies	Gain (dB)	Input Match S11 (dB)
1- a=54 | b=43	*3.06 GHz*	*7.88*	*−14.76*
2- a=56 | b=45	*4.6GHz*	*5.2*	*−16.08*
3- a=60 | b=47	*2.98 GHz*	*5.6*	*−14.02*
4- a=65 | b=50	*1.8 GHz*	*9.3*	*−20.05*
5- a=69 | b=51	*1.72 GHz*	*8.9*	*−16.08*
6- a=71 | b=52	*1.68GHz*	*8.81*	*−17.09*
7- a=73 | b=53	*1.64 GHz*	*8.86*	*−18.36*

To observe the changes happens to the input match S11 and the gain by changing the thickness of the dielectric material, multiple simulations were examined with different thickness varying from 25mm to 33mm. TABLE 2 illustrates the results.

TABLE II. S11 AND GAIN RESULTS WITH DIFFERENT THICKNESS

Thickness	S11 (dB)	Gain (dB)
25 (mm)	*−20.05*	*9.3*
27(mm)	*−19.06*	*9.23*
29(mm)	*−16.6*	*9.1*
31(mm)	*−16.9*	*10.0*
33 (mm)	*−12.50*	*9.5*

The simulation results show that the maximum radiation value of the antenna S11 is -20.05 dB with 9.3 GHz gain at 1.8 GHz as shown in Figure 2.

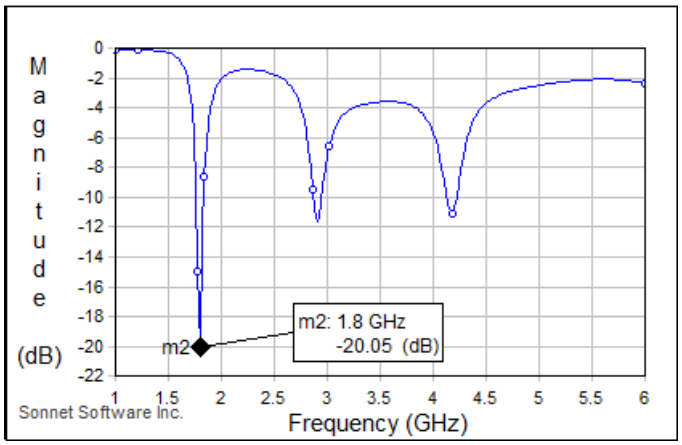

Fig. 2. Simulation input match result.

As seen in Figure 3. The current density is more concentrated on the edges of the E-shaped antenna while it is almost zero value at the center of the lower edge and the beginning of each slot [5].

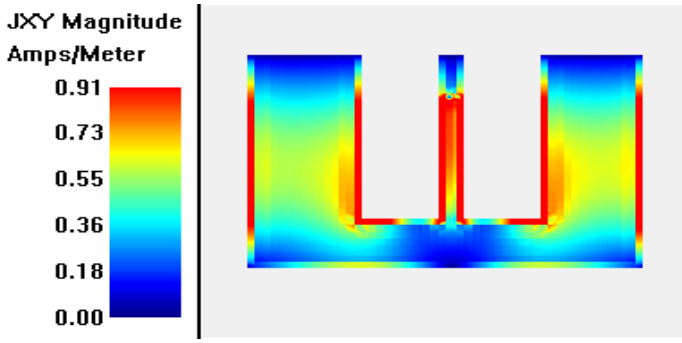

Fig. 3. Current distribution at 1.8 GHz

We can see the simulation results of the electric field. Theta (-12.52 dB) and E Phi polarized gains (9.3 dB) in the graph in figure 4.

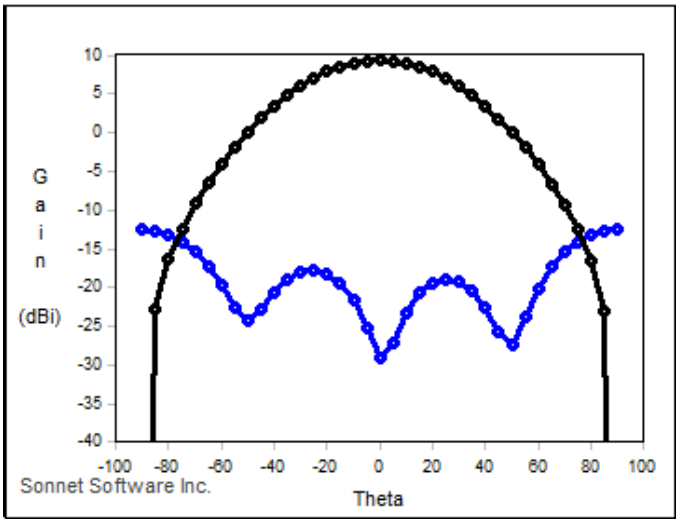

Fig. 4. Gain graph of the design.

III. CONCLUSION

In this project, an E-shaped, high gain, MPA has been designed, and simulated. The simulation results were obtained by using a planar 3D electromagnetic simulator, called Sonnet Suites. The future work is to fabricate the antenna. This antenna preferable for low profile, dimensions and high gain when compared to similar designs found in literature.

REFERENCES

[1] Churng-Jou Tsai, Chia-Hsn Lin, Wei-Chih Chen, Chen-Lin Lu and Jinn-KweiGuo, “A CPW-Feed Printed Antenna for Dual-band WLAN operations”, IEEE, 2011.

[2] K.-L. Wong, “Compact and Broadband Microstrip Antennas”, Wiley and Sons, Inc., New York, vol. 1, (2002), pp. 12-15.

[3] C. A. Balanis, “Antenna Theory, Analysis and Design,” ISBN 978-81-265-2422-8, John Wiley & Sons, Inc., U.K., 2013.

[4] A. A. Deshmukh and G. Kumar, “Compact broadband gap-coupled shorted L-shaped microstrip antennas,” in IEEE Antennas and Propagation International Symposium, vol 1, (Baltimore, Maryland), pp. 106–109, IEEE, July 2001

[5] Balanis, C. A., Antenna Theory Analysis and Design, John Wiley & Sons, Inc., 1997.

Empirical Analysis of The Performance of Radiometer for Digitally Modulated Signals

Özgür Alaca[§], Gamze Kirman[§], Ali Boyacı[‡], Serhan Yarkan[†]
İstanbul Commerce University,
[§] Department of Electrical–Electronics Engineering
[‡]Department of Computer Engineering
[†]Center for Applied Research on Informatics Technologies (CARIT)
Küçükyalı E5 Kavşağı, İnönü Cad., No:4, Küçükyalı, 34840, İstanbul, Türkiye
E–mails: {gamze.kirman, ozgur.alaca}@istanbulticaret.edu.tr
{aboyaci, syarkan}@ticaret.edu.tr

***Abstract*—Radiometer, which is also known as energy detector, is one of the most widely employed and studied spectrum sensing techniques due to its relatively computationally less complex design. In this study, performance of radiometer is investigated from the perspective of in–phase/quadrature (I/Q) branches via a flexible experimental setup. In addition, impact of digital modulation including both constant envelope and amplitude modulated techniques is studied as well. Results are provided along with relevant discussions.**

***Index Terms*—digital modulation, fading, line–of–sight (LOS), radiometer**

I. Introduction

It is obvious that a successful spectrum sensing operation depends upon the performance of the methods/techniques employed. Prominent factors in evaluating the performance of these methods are their accuracy, agility, and robustness. From the design perspective, accuracy and agility are contradicting requirements. Therefore, methods present in the literature attempt to find a design which yields a compromise between accuracy and agility [1, 2]. However, radiometer (energy detector) is a very special technique due to the following reasons: First, radiometer does not necessitate any sort of *a priori* knowledge of the signal to be detected. Therefore, radiometer yields a simplistic design. Second, it is the optimal detector under the absence of *a priori* knowledge of the signal to be detected [3].

As a non–coherent receiver, radiometer collects the energy of the received signal within a specific time interval at a particular frequency band. Putting aside its being the optimal detector in the absence of *a priori* knowledge of the signal to be detected, radiometer has several fundamental shortcomings. For instance, its performance is affected dramatically by the uncertainties in noise variance, low signal–to–noise ratio (SNR) regime, and spread–spectrum signals [4–6]. Beside theoretical studies, it is critical to understand and evaluate the performance of radiometer under practical conditions and applications. Impact of digital modulation, mobility, line–of–sight (LOS)/non–line–of–sight (NLOS), wide– and narrow–band reception are just to name few.

II. Measurement Results

The vector signal analyzer (VSA) is set to capture a time period of 100ms for all modulation types. Then, by playing with the variable N, different levels of degrees of freedom are obtained. Also, during the whole measurement period, the output power level of vector signal generator (VSG) is adjusted to be -25dBm in order to better observe the performance of radiometer under low–SNR regime.

First, it is desirable to check with the output of radiometer for each modulation type. Results for binary phase shift keying (BPSK) modulation is given in Figure 1. It is seen in Figure 1 that there is almost no difference between in–phase and quadrature branches. However, decision statistic changes drastically once in–phase/quadrature (I/Q) branches are taken into account simultaneously.

Results for quadrature phase shift keying (QPSK) modulation is given in Figure 2. In contrast to BPSK scenario, in–phase, quadrature, and I/Q branches together exhibit similar behavior for QPSK. This mainly stems from the fact that for QPSK signals, statistically speaking, both in–phase and quadrature branches are visited at the same rate, each of which corresponds to a complex number.

Up until this point, constant envelope modulations have been investigated. In order to check with the behavior of radiometer under inconstant envelope modulation, results for 16–quadrature amplitude modulation (QAM) given in Figure 3 could be investigated. It is observed in Figure 3 that 16–QAM yields a particular behavior which could be classified between behaviors of BPSK and of QPSK. BPSK yields a dramatically different behavior for its I/Q branch as compared to its in–phase and/or quadrature branch, whereas QPSK yields a similar pattern (with a different mean value) for all branches. Nevertheless, 16–QAM, as stated above, exhibits a progressive pattern across in–phase, quadrature, and I/Q branches.

Radiometer is always contaminated with the ambient noise. Therefore, behavior of radiometer under H_0 hypothesis should be investigated separately. Results for the output of radiometer H_0 hypothesis is in Figure 4. It is interesting to note that behavior of radiometer follows a similar pattern under H_0 hypothesis and for 16–QAM scenario. However, one should also state that the decision statistics for these cases are dramatically different from each other in terms of their amplitudes.

III. Concluding Remarks and Future Directions

Experimental results reveal that the performance of radiometer varies drastically with the type of digital modulation scheme employed at the unknown signal source. In addition, collected data show that constant envelope modulation behavior is different from amplitude modulation (AM) behavior for radiometer. Furthermore, it is observed that output of radiometer behaves differently for real and complex modulation types within the constant envelope modulation class as well.

Based on the experimental results collected, one could also infer that signal classification is possible by simply employing

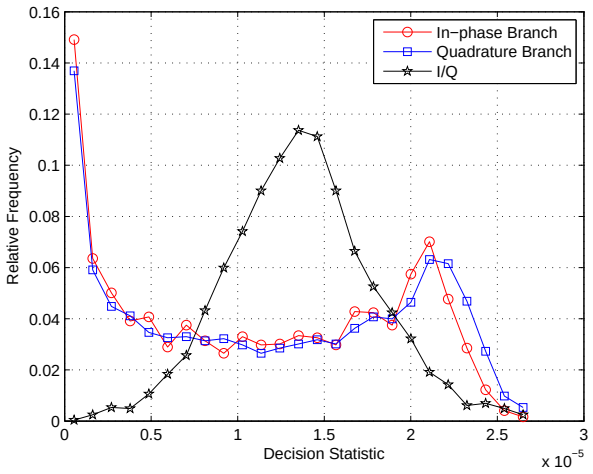

Figure 1. Output of radiometer for in–phase–only, quadrature–only, and I/Q input under BPSK modulation.

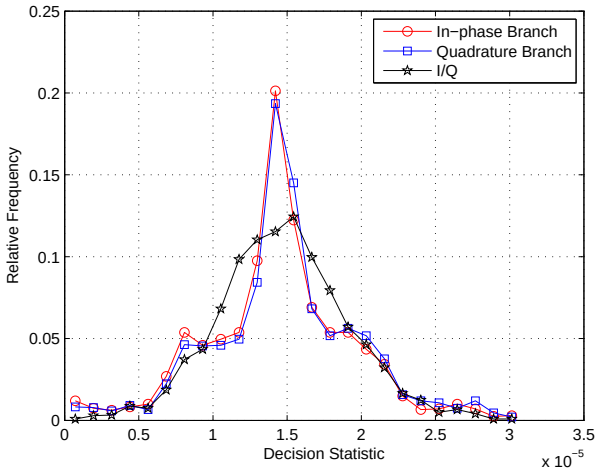

Figure 2. Output of radiometer for in–phase–only, quadrature–only, and I/Q input under QPSK modulation.

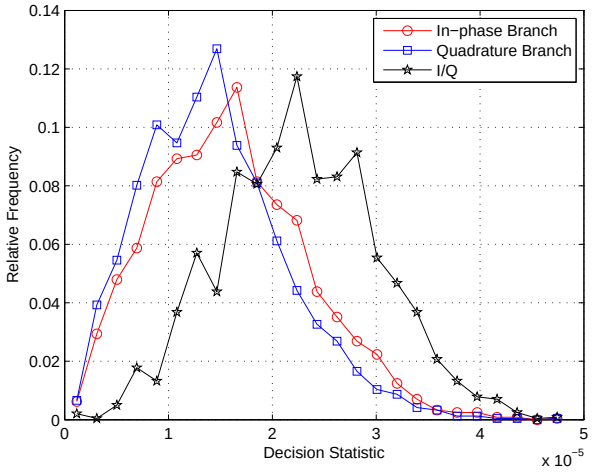

Figure 3. Output of radiometer for in–phase–only, quadrature–only, and I/Q input under QAM modulation.

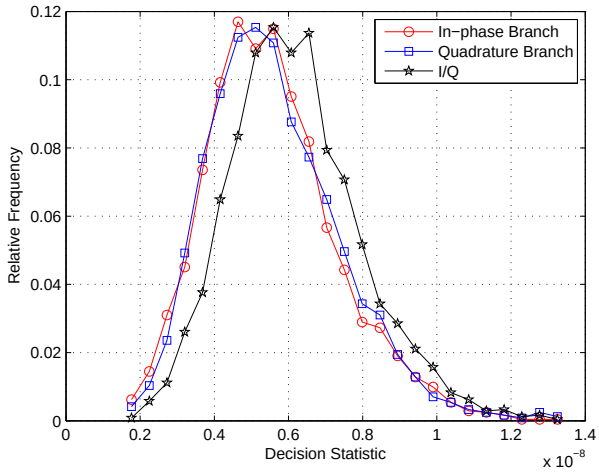

Figure 4. Output of radiometer for in–phase–only, quadrature–only, and I/Q input under H_0 hypothesis.

radiometer at the receiver side. As a future work, digital modulation classification with the use of radiometer could be investigated due to mild design requirements of radiometer. Also, impact of NLOS conditions along with mobility needs to be studied as well.

REFERENCES

[1] Y. Hur, J. Park, W. Woo, J. S. Lee, K. Lim, C.-H. Lee, H. S. Kim, and J. Laskar, "A Cognitive Radio (CR) System Employing A Dual-Stage Spectrum Sensing Technique : A Multi-Resolution Spectrum Sensing (MRSS) and A Temporal Signature Detection (TSD) Technique," in *Global Telecommunications Conference, 2006. GLOBECOM '06. IEEE*, San Francisco, California, USA, Nov. 27 – Dec. 1, 2006, pp. 1–5.

[2] W.-Y. Lee and I. F. Akyildiz, "Optimal spectrum sensing framework for cognitive radio networks," *IEEE Transactions on Wireless Communications*, vol. 7, no. 10, pp. 3845–3857, Oct. 2008.

[3] H. Urkowitz, "Energy detection of unknown deterministic signals," *Proceedings of the IEEE*, vol. 55, no. 4, pp. 523–531, Apr. 1967.

[4] A. Sonnenschein and P. M. Fishman, "Radiometric detection of spread-spectrum signals in noise of uncertain power," *IEEE Transactions on Aerospace and Electronic Systems*, vol. 28, no. 3, pp. 654–660, July 1992.

[5] H. Tang, "Some physical layer issues of wide–band cognitive radio systems," in *Proc. First IEEE International Symposium on New Frontiers in Dynamic Spectrum Access Networks (DySPAN)*, Baltimore, Maryland, U.S.A., Nov. 8–11, 2005, pp. 151–159.

[6] R. A. Dillard, "Detectability of spread-spectrum signals," *IEEE Transactions on Aerospace and Electronic Systems*, vol. AES-15, no. 4, pp. 526 –537, July 1979.

Effect of RF Fields Radiated by a Base Station on a Human Head

Fatih Kaburcuk
Electrical-Electronic Engineering Department
Erzurum Technical University
Erzurum 25700, Turkey
fatih.kaburcuk@erzurum.edu.tr

Atef Z. Elsherbeni
Electrical Engineering Department
Colorado School of Mines
Golden, CO 80401, USA
aelsherb@mines.edu

***Abstract*— Temperature rise and specific absorption rate (SAR) distribution in a human head due to radio frequency fields radiated by a base station are evaluated at multiple frequencies in a single simulation. An algorithm is developed to analyze the scattering from the human head included dispersive tissues by integrating the three-term Debye coefficients into the finite-difference time-domain method based on the auxiliary differential equation approach along with the use of bioheat equation for SAR and temperature computations. The tissue EM parameters are used from the available three-term Debye coefficients from 500 MHz to 20 GHz.**

Keywords—Dispersive; 5G; FDTD; SAR; temperature rise

I. INTRODUCTION

The temperature rise and specific absorption rate (SAR) distribution in the human head due to radio frequency (RF) fields [1-3] are investigated using the traditional nondispersive finite-difference time-domain (FDTD) algorithm. In the previous works [1-3], the SAR computations for the human head was conducted at only one frequency of interest in a single simulation because the human head tissues are dispersive. A dispersive algorithm is developed to obtain SAR and temperature distributions at multiple frequencies of interest from a single FDTD simulation. The dispersive algorithm is based on the integration of Debye model into FDTD method based on the auxiliary differential equation (ADE) as presented in [4] with the Pennes bioheat equation from [5]. The head tissue parameters for a wide range of frequencies (500 MHz to 20 GHz) used in this investigation are based on the three-term Debye coefficients calculated and tabulated in [6].

In recent years, a Fifth Generation (5G) mobile communication has gained enormous popularity and extensive research interest. Its possible effects on a human body are not studied significantly. In this paper, the interaction between a human head and the RF fields due to 5G base stations are investigated to show their effects on the head using the dispersive algorithm at multiple frequencies of interest below 6 GHz using a single simulation.

II. DISPERSIVE HEAD MODEL AND METHODS

The head model obtained from [7] consists of 8 tissues (skin, muscle, bone, blood, fat, lens, grey and white matter) and 172(width)×218(depth)×240(height) cubic cells. The cell size of the head model is 0.9 mm in all directions. The EM parameters of these tissues are dispersive. Thus, a solution at only one frequency can be obtained in a single simulation. A numerical procedure developed in [6] provides three-term Debye coefficients to accurately fit the experimental data from [8] for the frequency range 500 MHz to 20 GHz. RF fields radiated by the 5G base stations are considered as far-field sources generated somewhere outside of the FDTD problem domain. The FDTD problem domain involved the head model is illuminated by the incident plane wave produced from these sources. The total-field/scattered-field formulation [4] used here generates the incident plane wave in the FDTD problem domain. The power density of the incident plane wave is set to 50 W/m^2 which is maximum permissible exposure limit for controlled environment [9]. The human head is illuminated by a *z* polarized incident Gaussian plane wave traveling in the positive *y* direction.

A. SAR Computation

The SAR at each frequency of interest is considered the RF heat source and is defined at a given location as:

$$SAR(i,j,k)=\frac{\sigma(i,j,k)}{2\rho(i,j,k)}\left(\left|E_x(i,j,k)\right|^2+\left|E_y(i,j,k)\right|^2+\left|E_z(i,j,k)\right|^2\right) \quad , \tag{1}$$

where $\sigma(i,j,k)$ and $\rho(i,j,k)$ are the electric conductivity and mass density [kg/m^3] of the tissue, respectively, and *E* is the enduced electric field in the tissue.

B. Temperature Rise Computation

The temperature simulation is performed by solving the bioheat equation [5]. After the initial temperature distribution in the head is calculated by using the bioheat equation when no RF power (SAR=0), the final temperature distribution is calculated by inserting the SAR distribution into the bioheat equation. The temperature rise distribution is achieved by taking the difference between final and initial temperature distributions. The bioheat equation is defined as:

$$\rho\cdot C\cdot\frac{\partial T}{\partial t}=K\cdot\nabla^2 T+\rho\cdot SAR-B\cdot\left(T-T_b\right) \quad , \tag{2}$$

where T is the temperature of a tissue [^{o}C] at time t, C is the specific heat of a tissue [J/(kg$\cdot\,^o$C)], K is the thermal conductivity of a tissue [J/(m$\cdot\,^o$C)], B is the blood perfusion rate [W/(m^3.^{o}C)], and T_b is the blood temperature. The boundary condition between the skin surface and air for equation (2) is expressed as:

$$K\cdot\frac{\partial T}{\partial n}=-h\cdot\left(T-T_a\right) \quad , \tag{3}$$

where T_a is the air temperature, n is the normal vector to the skin surface, and h is the convection heat transfer coefficient [W/(m^2· ^{o}C)]. The derivative of T in (3) is with respect to the normal direction to the skin surface. The convection heat transfer coefficients (h) is set to 10.5 from the skin surface to air. In order to avoid the numerical instability, the temperature time-step must satisfy the criterion [2] of $\delta t \leq \frac{2\rho C d^2}{12K+Bd^2}$. The mass density ($\rho$) and thermal parameters of the head tissues are taken from [2]. The air temperature (T_a) and initial head temperature (T_b) were set to 20 ^{o}C and 37 ^{o}C, respectively.

III. Numerical Results

In this section, the temperature rise and SAR distributions due to RF fields are obtained using the developed dispersive algorithm at frequencies of interest in a single simulation and using the nondispersive FDTD algorithm by performing multiple simulations, each at a single frequency. In order the show the validity of the dispersive algorithm, the obtained results using the dispersive algorithm are compared with those reported in [2] using the nondispersive algorithm at 1.5 GHz. For the comparison, the results are tabulated in Table 1. The maximum 1 gram averaged SAR value in the head at 1.5 GHz is good agreement whereas the maximum temperature rise in the head is slightly different with that reported in [2]. The reasons for the difference in the compared results would come from using the different head model.

The temperature rise and SAR distributions of the head due to RF fields radiated by 5G base stations are calculated using the proposed dispersive algorithm at 3.4 and 3.8 GHz in a single simulation. The maximum 1 gram averaged SAR value and the maximum temperature rise in the head at the listed frequencies are shown in Table 2.

The 1 gram averaged SAR and the resulting temperature rise distributions in the *x-y* cross section of the head model at the listed frequencies are shown in Figs. 1 and 2, respectively. The maximum temperature variation in the head as a function of time is shown in Fig. 3 for each frequency of interest. It can be realized that the temperature increases rapidly over the first 6 minutes, then temperature increase slows down, and the maximum (steady-state) temperature is reached after 18 minutes. The SAR and temperature rise distributions obtained using the dispersive algorithm agree very well with the results obtained using the traditional nondispersive FDTD algorithm but with less computer resources.

Table 1: Comparison of maximum 1 gram averaged SAR and maximum temperature rise in the head at 1.5 GHz with the power density of 50 W/m^2.

	Max. SAR_{1gram} (W/kg)	Max. Temp. Rise (^{o}C)
Obtained Results	5.55	0.49
Results in [2]	5.62	0.35

Table 2: Maximum 1 gram averaged SAR and temperature rise in the head at the frequencies of interest.

Frequency (GHz)	Max. SAR_{1gram} (W/kg)	Max. Temp. Rise (^{o}C)
3.4	4.50	0.54
3.8	5.52	0.63

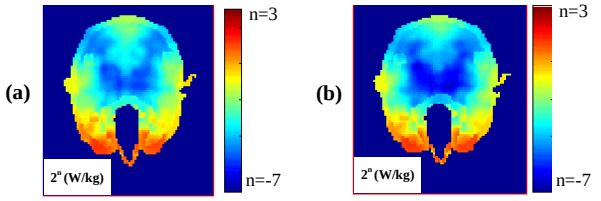

Fig. 1. 1 gram averaged SAR distribution at (a) 3.4 GHz and (b) 3.8 GHz.

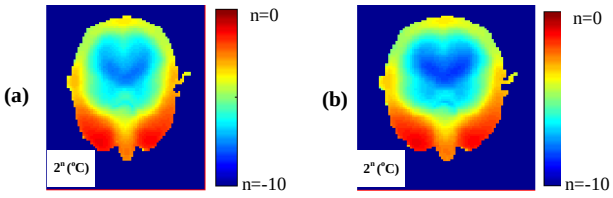

Fig. 2. Temperature rise distribution at (a) 3.4 GHz and (b) 3.8 GHz.

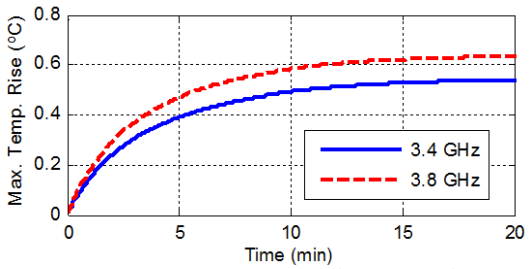

Fig. 3. Maximum temperature rise vs. time at frequencies of interest.

IV. Conclusion

The temperature rise and SAR distributions in a human head model due to the radiation from 5G base stations at 3.4 and 3.8 GHz are investigated using a proposed dispersive algorithm in a single simulation. Numerical results show that the values of SAR and temperature rise distributions in the human head are different for different frequencies of the RF fields.

References

[1] Y. Lu, et al. "Electromagnetic and thermal simulations of 3-D human head model under RF radiation by using the FDTD and FD approaches." *IEEE Transactions on Magnetics*, vol. 32, no. 3, pp. 1653-1656, 1996.

[2] O. Fujiwara, M. Yano, and J. Wang, "FDTD computation of temperature rise inside a realistic head model for 1.5-GHz microwave exposure," *Electron. Comm. Jpn. Pt. I*, vol. 82, no. 3, pp. 240-247, 1999.

[3] A. I. Sabbag and N. I. Dib, "SAR and temperature elevation in a multi-layered human head model due to an obliquely incident plane wave," *Progress In Electromagnetics Research M*, vol. 13, pp. 95-108, 2010.

[4] A. Z. Elsherbeni and V. Demir, *The Finite-Difference Time-Domain Method for Electromagnetics with MATLAB Simulations*, second edition, ACES Series on Computational Electromagnetics and Engineering, SciTech Publishing, an Imprint of IET, Edison, NJ, 2016.

[5] H. H. Pennes, "Analysis of tissue and arterial blood temperature in resting forearm," *J. Appl. Physiol*., vol. 1, pp. 93–122, 1948.

[6] M. A. Eleiwa and A. Z. Elsherbeni, "Debye constants for biological tissues from 30 Hz to 20 GHz," *ACES Journal*, vol. 16, no. 3, Nov. 2001.

[7] http://noodle.med.yale.edu/zubal/ [Online website 2017].

[8] S. Gabriel, R. W. Lau, and C. Gabriel, "The dielectric properties of biological tissues: III. Parametric models for the dielectric spectrum of tissues," *Phys. Med. Biol*., 41, pp. 2271–2293, 1996.

[9] 20 554"Evaluating compliance with FCC guidelines for human exposure to radio frequency electromagnetic fields," Fed. Commun. Commission, Washington, DC, Tech. Rep. OET Bull. 65, 1997.

Direction Finding Using 2×2 Horn Antenna Monopulse System

Hassan Sajjad[1], Sana Khan[1], Ahsan Altaf[1], Serhend Arvas[2], Tuncer Baykas[1],
Mehmet Kemal Ozdemir[1], and Ercument Arvas[1]
[1]Department of Electrical and Electronics Engineering, Istanbul Medipol University, Istanbul, Turkey.
[2]ENARGE, Istanbul, Turkey.
Email: hsajjad@st.medipol.edu.tr

***Abstract*—A monopulse system working in X-band using four E-plane sectoral horn antennas is presented. A Matlab algorithm has been developed to calculate the ratios of the difference to sum received signals. A lookup table of such values has been created for a range of azimuth and elevation angles. These ratios are used to find the direction of arrival of the incident signal by comparing the measured results from the monopulse system. The incident angles have been detected without any error when the system has no noise.**

Keywords— Direction finding, horn antenna, monopulse radar systems.

I. Introduction

Localization of sources of interference and non-authorized transmitters, detecting activities of potential enemies, radio astronomy, and earth remote sensing require direction finding. Among various electronic techniques for direction finding the Monopulse technique is the most accurate [1]. A monopulse extracts complete positional information about a target from a single radar pulse. In order to improve the target detection probability, the angular position of the target is obtained from multiple pulses. It uses two recevied signals from the system, namely, *sum* (Σ) and *difference* (Δ). The sum and difference signals result in a peak and null in the broadside pattern, respectively.

The satate of the art has used coplanar waveguides, microstrips, and metallic waveguides to design monopulse antenna in the microwave and millimeter frequency bands [2]-[4]. In this paper, we use four rectangular horn antennas to design a monopulse system. The system is optimized to work in the X-band (8-12 GHz).

II. Antenna Design And System Setup

The horn antennas for our monopulse system have been designed based on the 3 dB beamwidth requirements of 60^o and 30^0 in the azimuth and elevation planes, respectively. A single horn antenna is shown in Fig. 1a. Here, a=23 mm, b=11 mm, A=23 mm, B=25 mm, L_1=34.5 mm, and L_2=80 mm. Return loss of the designed antenna was below 20 dB over the X-band. The system used in this work is shown in Fig. 1b-c which consists of a two dimensional array of four similar E-plane sectoral horn antennas. A Matlab algorithm was developed using the equations for an E-plane sectoral horn antenna given in [5] which helped in simulating our designed system.

The structure is illuminated by a plane wave and the field at the center of each horn, shown by the dot on the horn aperture, is computed. In regular spherical coordinate system,

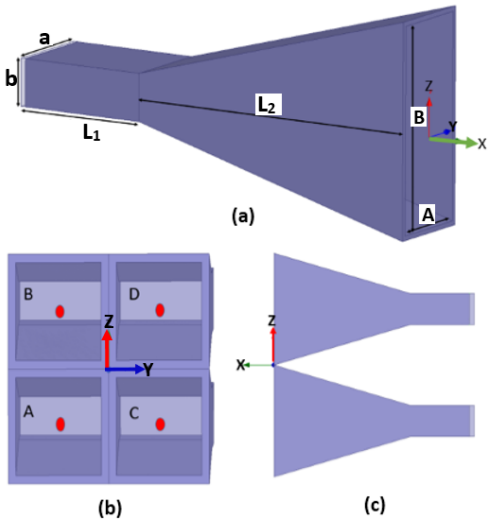

Fig. 1. (a) Single E-plane sectoral horn antenna, (b) Axial view of the horn array, (c) Side view of the horn array.

the phasor field of the incoming wave is given by,

$$E^{inc} = \mathrm{e}^{jk_o[x\sin\theta\cos\phi + y\sin\theta\sin\phi + z\cos\theta]} \tag{1}$$

where ϕ is the azimuth angle from the xz-plane towards y-axis and θ is the elevation angle from z-axis. For our structure, instead of regular θ we define an elevation angle E from the xy-plane (up) towards z-axis. Then $E = 90^o - \theta$. With this definition of E the incident field at the center of horn m becomes,

$$E_m^{inc} = \mathrm{e}^{jk_o[y_m\cos E\sin\phi + z_m\cos E]} \tag{2}$$

Similar equations can be written for each of the four horns. The signals received by the antennas are combined to form the sum and difference ($\Sigma - \Delta$) patterns. The $\Sigma - \Delta$ patterns for amplitude comparison in a monopulse radar are defined as

follows [1],

$$\textit{Sum:} \qquad S = \frac{1}{2}(A+B+C+D) \tag{3}$$

$$\textit{Difference Traverse:} \qquad D_{tr} = \frac{1}{2}[(C+D)-(A+B)] \tag{4}$$

$$\textit{Difference Elevation:} \qquad D_{el} = \frac{1}{2}[(A+C)-(B+D)] \tag{5}$$

where $A, B, C,$ and D are the signals from the horn antennas as shown in Fig. 1b.

III. Results

The Σ-Δ signals obtained from the above equations are used to generate two curves. The curves are obtained from the ratio of Δ and Σ signals, referred to as the difference over sum (d/s) curves. The d/s curves in the elevation (d_{el}/s) and traverse (d_{tr}/s) planes are shown in Fig. 2. In this study, it was

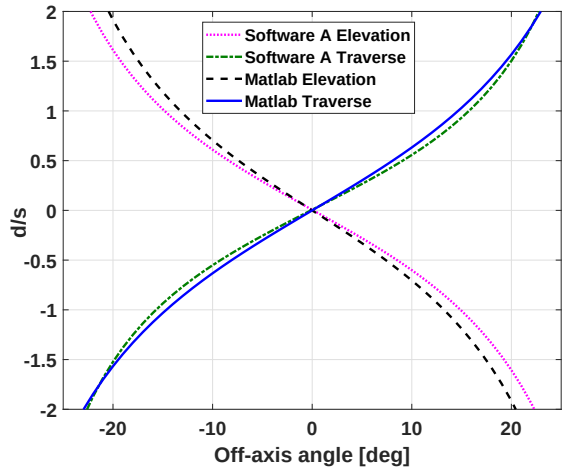

Fig. 2. Comparison of d/s curve for the elevation and traverse planes at 10 GHz.

observed that the d/s curve showed no variation with varying azimuth angle which can be seen from the equation after some simple algebraic steps. However, the d/s curve showed variation with changing elevation angle (E). A commercial software was used to verify the results generated from Matlab. Figures 3 and 4 show the detected azimuth and elevation angles, respectively. A lookup table of the d/s values is generated for a range of azimuth angles ($-20^o \leq \phi \leq 20^o$) and elevation angles ($-30^o \leq E \leq 30^o$). Any point in the scanned portion of the $\phi - E$ plane is represented by a 2×1 vector. First element of the vector is d_{el}/s and the second is d_{tr}/s. The difference between these values and the practical values, obtained from the monopulse system, is taken as the solution of the vector position angles that minimizes the norm of the vector. Here we consider a noiseless system which results in accurate estimation of the incident angles. Other results will be presented in the conference which were observed during this study.

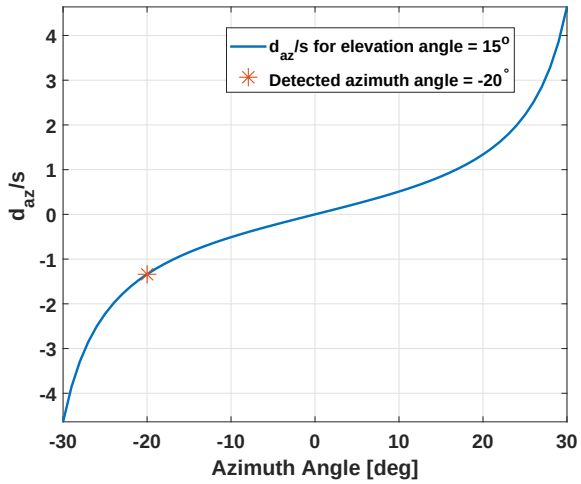

Fig. 3. Detected azimuth angle of the incoming signal on the d/s curve at 10 GHz.

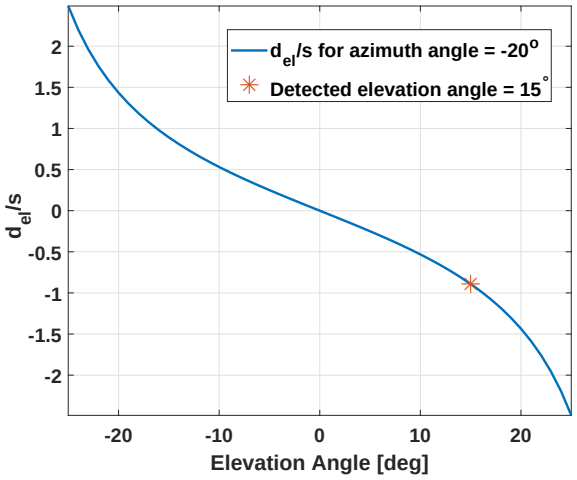

Fig. 4. Detected elevation angle of the incoming signal on the d/s curve at 10 GHz.

IV. Conclusion

A monopulse system consisting of four horn antennas used for direction finding has been designed. The system has been successfully simulated to detect elevation and azimuth angles of the incoming signals in a noiseless environment. Results generated from Matlab have been verified by a commercial software. The effect of noise on the presented approach is under investigation which will enable us to model the system in a more realistic manner.

References

[1] S. M. Sherman and D. K. Barton, *Monopulse Principles and Techniques*, 2nd ed. Boston, London: Artech House, 2011.

[2] M. Sierra-Castaner, M. Sierra-Perez, M. Vera-Isasa and J. L. Fernandez-Jambrina, "Low-cost monopulse radial line slot antenna," in *IEEE Transactions on Antennas and Propagation*, vol. 51, no. 2, pp. 256-263, Feb 2003. doi: 10.1109/TAP.2003.809098

[3] Biao Du, E. K. N. Yung, Ke-Zhong Yang and Wen-Jing Zhang, "Wideband linearly or circularly polarized monopulse tracking corrugated horn," in *IEEE Transactions on Antennas and Propagation*, vol. 50, no. 2, pp. 192-197, Feb 2002. doi: 10.1109/8.997994

[4] Hao Wang, Da-Gang Fang and X. G. Chen, "A compact single layer monopulse microstrip antenna array," in *IEEE Transactions on Antennas and Propagation*, vol. 54, no. 2, pp. 503-509, Feb. 2006. doi: 10.1109/TAP.2005.863103

[5] C. A. Balanis, *Antenna Theory Analysis And Design*, 4th ed. Hoboken, New Jersey: John Wiley and Sons, 2016.

Determination of Power Lines Radius by Electromagnetic Wave Scattering

Kamil Karaçuha[1]
[1]*Informatics Institute of Istanbul Technical University*
Istanbul, Turkey
karacuha17@itu.edu.tr

Sebahattin Eker[1]
[11]*Informatics Institute of Istanbul Technical University*
Istanbul, Turkey
sebahattin.eker@itu.edu.tr

***Abstract*—In this study, purpose is to detect the radius of power line by assuming the line as perfect electric conductor and having infinite length. This assumption for electromagnetic waves with high frequencies are acceptable to proceed in the problem. The radius is found by using scattering properties of the electromagnetic waves from objects. Also, numerical results are presented in the paper.**

Keywords—circular cylinder, electromagnetic scattering, remote sensing, power line

I. INTRODUCTION

The detection of any object located unreachable location or embedded under different layer or layers has always been study of engineering and still keeps the importance in many areas such as military, biomedical, electrical and construction application. In previous study, we have found the location of power line above flat earth assumption [1-6]. Here, perfect conducting, infinite length power line whose location known but, the radius not known is studied. By using previously obtained data for different frequencies and radii, we can predict the actual radius of the power line which is used in the region of interest. Our goal can be achieved when theoretically calculated data is compared to the data coming from the actual scattering field of power line with unknown radius value. Despite of assuming some exceptions such as infinite length cylinder and perfect electric conducting property, this study is a trial to start helping aviation sector to determine radius of power lines. After detecting the power line [1-6], the angle between power line and the observer is known. By having location and angle information, we can manipulate the scattering formula for getting radius information. Here both theoretical and numerical results are presented in the paper.

II. FORMULATION OF THE PROBLEM

We assume TM^z uniform plane wave is used for our purpose and time dependency is assumed as $e^{i\omega t}$ [7]. Our purpose is to solve Helmholtz Equation given as,

$$\nabla^2\varphi + k^2\varphi = 0 \tag{1}$$

It can be written as following in cylindrical coordinates.

$$\frac{\partial^2\varphi}{\partial\rho^2} + \frac{1}{\rho}\frac{\partial\varphi}{\partial\rho} + \frac{1}{\rho^2}\frac{\partial^2\varphi}{\partial\phi^2} + \frac{\partial^2\varphi}{\partial z^2} + k^2\varphi = 0 \tag{2}$$

The solution can be found as

$$\varphi(\rho,\phi,z) = [a_1 J_m(k\rho)][c_1\cos(m\phi) + c_2\sin(m\phi)]\,[Ae^{-inz} + Be^{inz}] \tag{3}$$

where, a_1, c_1, c_2, A, B are the constants found by boundary condition, k is wavenumber and $J_m(k\rho)$ stands for Bessel function of the first kind. In Figure 1, the geometry of the problem is shown. Here, assuming power line as a PEC infinite length cylinder, boundary condition can be predicted and unknowns constants mentioned above can be found.

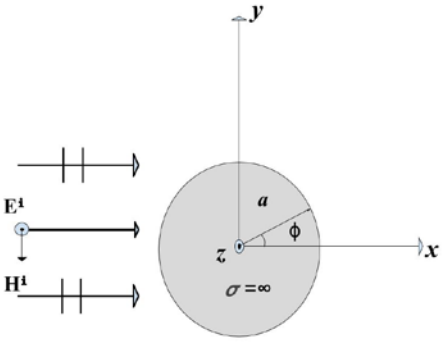

Fig. 1. Geometry of the Problem

Incidence wave can be writtens as

$$\vec{E}^i = \vec{a}_z E_o e^{-ikx} = \vec{a}_z E_o e^{-ik\rho cos\phi} = \vec{a}_z E_o \sum_{m=-\infty}^{\infty} i^{-m} J_m(k\rho) e^{im\phi} \tag{4}$$

We know that, due to having PEC, inside the cylinder, field is zero, this leads that scattered field can be only outward direction, therefore, the field is,

$$\vec{E}^s = \vec{a}_z E_z^s = \vec{a}_z E_o \sum_{m=-\infty}^{\infty} c_m H_m^{(2)}(k\rho) \tag{5}$$

Here $H_m^{(2)}(k\rho)$ is Hankel Function of the second kind. The function is defined as $H_m^{(2)}(k\rho) = J_m(k\rho) - iY_m(k\rho)$ where, $Y_m(k\rho)$ is knows as Bessel function of the second kind. Due to boundary condition, (6) needs to be satisfied as

$$E_z^t(\rho = a, 0 \le \phi \le 2\pi, z) = E_o \sum_{m=-\infty}^{\infty} [i^{-m} J_m(ka) e^{im\phi} + c_m H_m^{(2)}(ka)] = 0 \tag{6}$$

After applying Boundary Condition unknown coefficient for (5) and (6), found as (7)

$$c_m = -i^{-m} \frac{J_m(ka)}{H_m^{(2)}(ka)} e^{im\phi} \tag{7}$$

Putting (7) into (5), we get (8).

$$E_z^s = -E_0 \sum_{m=-\infty}^{\infty} i^{-m} \frac{J_m(ka)}{H_m^{(2)}(ka)} e^{im\phi} H_m^{(2)}(k\rho) \quad (8)$$

After finding (8), we can find what we look for, if other parameters are known. If radius of the cylinder and angle are known, we can find the scattered field in the known angle and direction or vice versa. Therefore, in order to find the radius of any power line, we can compare theoretical findings of power line with different radius values previously obtained via (8) and the data coming from the actual scattering of power line with unknown radius. In previous study [1], detection of the power line is achieved. Therefore, by detecting of the power line, actually, the angle between incidence wave and the power line is already known. At the end, comparing the data leads us to find the correct radius by minimizing the error function defined as $K(a')$ in (9).

$$K(a') = -E_0 \sum_{m=-\infty}^{\infty} i^{-m} \frac{J_m(ka)}{H_m^{(2)}(ka)} e^{im\phi'} H_m^{(2)}(k\rho') - \alpha(a') \quad (9)$$

where,

ρ' is the measurement distance from the cylinder center, ϕ' is the the angle the measurement location and the center on x-y plane and a' stands for the unknown radius. Lastly, (10) is the data obtained from the power line with unkown radius.

$$\alpha(a') = -E_0 \sum_{m=-\infty}^{\infty} i^{-m} \frac{J_m(ka\prime)}{H_m^{(2)}(ka\prime)} e^{im\phi\prime} H_m^{(2)}(k\rho') \quad (10)$$

III. NUMERICAL RESULTS

For different values of radius and angle, The graph of square of Electric Field versus changing values of unknown radius are presented in Figure 2-5.

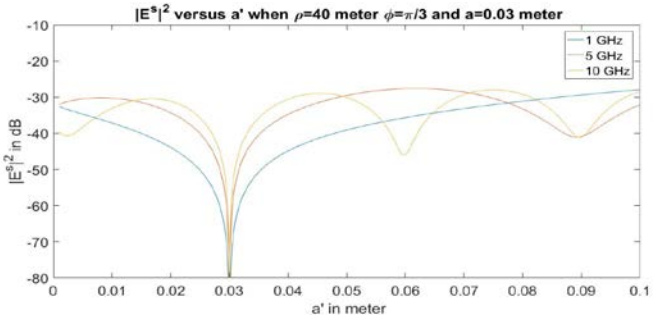

Fig. 2. Graph of $|E^s|^2$ versus a' with different frequencies

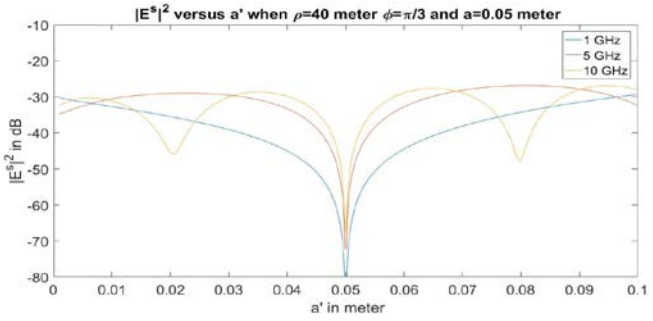

Fig. 3. Graph of $|E^s|^2$ versus a' with different frequencies

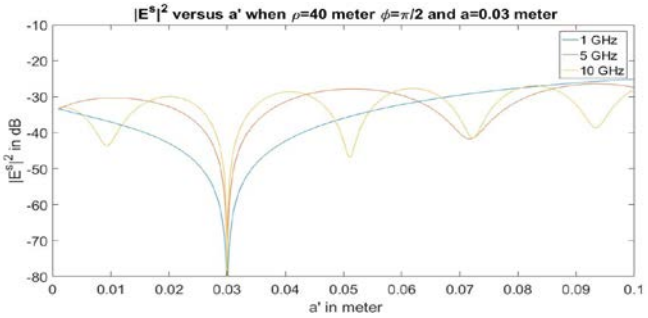

Fig. 4. Graph of $|E^s|^2$ versus a' with different frequencies

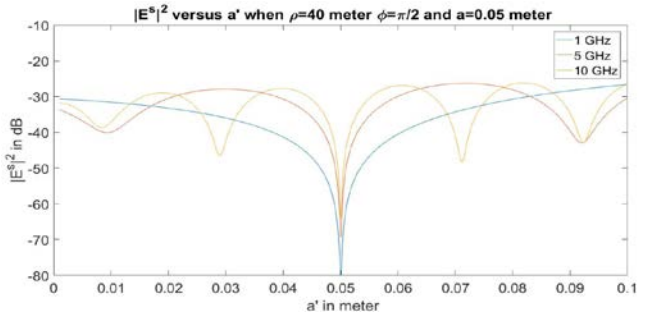

Fig. 5. Graph of $|E^s|^2$ versus a' with different frequencies

Here, It can be easily understood that, when the sweeping radius approaches to actual value such as 0.03 or 0.05 meter [8], the error function K in (9) approaches to zero when the radius is getting similar value with expected value. Therefore, the radius is estimated very successfully.

REFERENCES

[1] K. Karacuha, "Hava Araçlarının Enerji Nakil Hatlarına Çarpmasını Önlemeye Yönelik Bir Deneme ," *EEMKON2017*. [Online]. Available: http://eemkon.org.tr/wp-content/uploads/2017/12/eemkon2017_bildirilerkitab%C4%B1v3.pdf. (in Turkish)

[2] [1]D. L. Colton and R. Kress, *Inverse acoustic and electromagnetic scattering theory*. New York: Springer,2013

[3] [2] F. Frezza, G. Schettini, R. Borghi, F. Gori and M. Santarsiero, "Plane-wave scattering by N conducting circular cylinders arbitrarily placed near a partially reflecting flat surface," *IEEE Antennas and Propagation Society International Symposium. 1996 Digest*, Baltimore, MD, USA, 1996, pp. 772-775 vol.2.

[4] [3]I. C. C. Akkaya, *Radar temelleri*. İstanbul: Sistem Yayıncılık, 2004.

[5] [4] B. R. Mahafza, *Radar systems analysis and design using MATLAB*. Boca Raton, Fla.: Chapman & Hall/CRC, 2013.

[6] [5] J.-M. Jin, Theory and computation of electromagnetic fields. Hoboken: Wiley, 2015.

[7] C. A. Balanis, *Advanced engineering electromagnetics*. Hoboken: J. Wiley & Sons, 2012.

[8] *Elektrik-Elektronik Teknolojisi Havai Enerji Hatları*. Ankara: T.C. Milli Eğitim Bakanlığı, 2011. (in Turkish)

Designing and Optimization of Inset Fed Rectangular Microstrip Patch Antenna (RMPA) for Varying Inset Length and Inset Gap

Murat Doğan, Ertuğrul Çelik, Mehmet Metin
Antalya Science University Department of Electric and Electronic Engineering
Antalya, Turkey

Taha Imeci, Azra Yildiz
International University of Sarajevo Department of Electrical Engineering
Sarajevo, Bosnia and Herzegovina

***Abstract*---This paper investigates the detailed description about design and development of antenna for wireless application. Rectangular micro strip patch antenna (RMPA) systems demand low cost and low-profile antennas. RMPA was designed with 5GHz. This antenna is simulated using CST Design tool at resonance frequency of 5GHz. RMPA has better return loss, gain and radiation properties.**

Key-Words: Microstrip antenna, Inset-fed, Microstrip Line, Dielectric Constant, Return Loss.

I. INTRODUCTION

Patch antennas are low cost and easily fabricated and have a low profile. Microstrip or patch antennas are becoming increasingly useful because they can be printed directly onto a circuit board. The patch antenna, microstrip transmission line and ground plane are made of high conductivity metal which is generally made with copper. The patch is of length L, width W, and sitting on top of a substrate of thickness h with permittivity ε**.** [1]

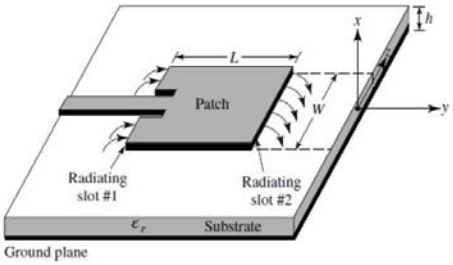

Fig. 1. Microstrip Patch Antenna Parameters

This paper presents the design, simulation and optimization of an inset fed patch antenna. The antenna is designed at resonant frequency of 5GHz.

The remainder of this paper is organized as follows: Section II briefly presents the proposed microstrip patch antenna design and antenna calculations. Section III summarizes the antenna simulations and results and finally Section IV concludes the proposed work.

II. ANTENNA DESIGN

A. Microstrip Patch Antenna

In this section, Microstrip Patch Antenna is developed. Microstrip antennas have a variety of configurations and are currently the most active field in antenna research and development. The microstrip antennas, due to their great advantages, have increasingly wide range of applications in wireless communication systems as hand held mobile devices, satellite communication systems, and biomedical applications. In most PCS, the handheld antenna is placed on a small plastic/shielding box that is near biological tissue of user body hence its radiation may cause health hazardous effects. Added to the operational requirements, the users and service providers usually demand wireless units with antennas that are small and compact, cost effective for manufacturability, low profile, and easy to integrate with other wireless communication system components.[2]

B. Design Principles

In designing rectangular microstrip patch antenna, the first is to calculate all the parameters with antenna specifications such as: [3]

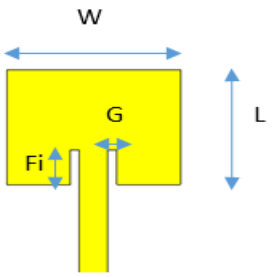

Fig. 2. General View of Designed Patch

ε_{reff} = Effective dielectric constant

ε_r = Dielectric constant of substrate

h = Height of dielectric substrate

W = Width of the patch

Fi= Feed inset length

G= Inset gap

$$\varepsilon_{reff} = \frac{\varepsilon_{r+1}}{2} + \frac{\varepsilon_{r-1}}{2}\left[1 + 12\frac{h}{W}\right]^{-\frac{1}{2}} \quad (1)$$

$$\Delta L = 0.412 \frac{(\varepsilon_{reff}+0.3)(\frac{W}{h}+0.264)}{(\varepsilon_{reff}-0.258)(\frac{W}{h}+0.8)} \quad (2)$$

The effective length of the patch L_{eff} now becomes:

$$L_{eff} = \frac{c}{2f_0\sqrt{\varepsilon_{reff}}} \quad (3)$$

Actual Length of Patch:

$$L = L_{eff} + 2\Delta L$$

Width of the Patch:

$$W = \frac{c}{2f_0\sqrt{\frac{(\varepsilon_r+1)}{2}}} \quad (4)$$

Width of the Ground:

$$L_g = 2L \quad (5)$$

Width of the Ground:

$$W_g = 2W \quad (6)$$

TABLE I. PHYSICAL DIMENSIONS OF MICROSTRIP PATCH ANTENNA

Operating frequency	5 GHz
Dielectric Constant	4.3
Length of the patch L	14mm
Width of the patch W	18 mm
Thickness(t) of the substrate	1.6mm
Substrate Length	28mm
Substrate Width	36 mm

III. SIMULATION AND RESULTS

A rectangular patch and microstrip antennas are designed and simulated with using CST Studio Suite. First inset gap is left constant then inset length is increased.

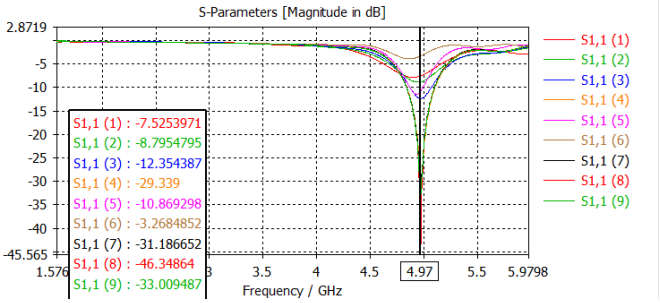

Fig. 3. S_{11} parameters for different Feed Inset Length and Gap

At Fig. 3 different feed length and gap effects patch's bandwidth, effective frequency and gain. When inset length is increased return loss is increases at a point, then decreases. Inset gap also effect return loss, when it decreases return loss increases. When Inset length is 4.211 mm and inset gap is 0.9 mm return loss reaches its minimum point which is -46.3 dB.

TABLE II. ITERATION RESULTS FOR RMPA USING DIFFERENT INSET LENGTH AND INSET GAP

Iteration	**Inset Gap (G) (mm)**	**Inset Length (Fi) (mm)**	**Resonance Frequency (Ghz)**	**Return loss S_{11}**
1	1	1	4.9	-7.84
2	1	2	4.945	-8.66
3	1	3	4.97	-12.35
4	1	4	4.975	-30.11
5	1	5	4.935	-11.49
6	1	6	4.865	-3.9
7	1	4.211	4.97	-31.18
8	0.8	4.211	4.97	-33
9	0.9	4.211	4.97	-46.34

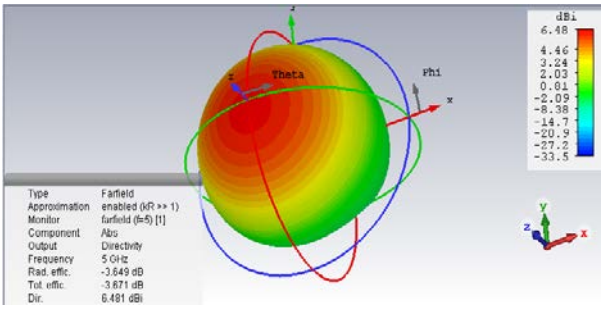

Fig. 4. Radiation Pattern for Patch

IV. CONCLUSION

In this work, a Microstrip rectangular patch antenna at resonant frequency of 5GHz has been reported. The radiation patterns and the return loss have been studied. We can easily analyze that with increasing inset gap and length increases return loss of the patch as well as gain, radiation, antenna efficiency and bandwidth. [4]

REFERENCES

[1] V. Samarthay, S. Pundir, B. Lal ,"Designing and Optimization of Inset Fed Rectangular Microstrip Patch Antenna (RMPA) for Varying Inset Gap and Inset Length" *International Journal of Electronic and Electrical Engineering*. ISSN 0974-2174 Volume 7, Number 9,pp. 1007-1013, 2014.

[2] N. Irfan, M. C. E. Yagoub, K. Hettak, "Design of a Microstrip-Line-Fed Inset Patch Antenna for RFID Applications" *IACSIT InternationalJournalofEngineeringandTechnology*,Vol.4,No.5,October 2012

[3] Rachmansyah, A. Irianto, A. Benny Mutiara, "Designing and ManufacturingMicrostripAntennaforWirelessCommunicationat2.4GHz" *InternationalJournalofComputerandElectricalEngineering*,Vol.3,No.5, October2011.

[4] H.R.Gajera,C.N. Anoop,M.M.Naik, S.P.Archana,N.R. Pushpitha,M.D. Kumar, "The Microstrip FedRectangular Microstrip Patch Antenna (RMPA) with Defected Ground Plane for HIPERLAN/1"*Dept.ofElectronics*,IJECTVol.2,Issue3,Sept.2011

Design, Optimization and Parametric Assessment of a Diamond-Hammer-Shaped Microstrip Patch Antenna

Said Ćosić, Yusuf Alper, Mahir Čengić
Department of Electrical and Electronics Engineering, International University of Sarajevo
Sarajevo, Bosnia and Herzegovina
said_cosic@hotmail.com, arcy_212@hotmail.com

***Abstract*— This paper introduces a new configuration of compact diamond and hammer-shaped design, microstrip-fed, low-profile antenna on FR-4 substrate. The research methods include antenna design architecture consideration, electromagnetic performance assessment, operational requirements analysis, and optimization through an analysis of different input parameters and simulation. As the result, the proposed antenna is composed of rectangular shaped patch containing ten stripes that form diamond shape at the edges of the rectangular patch, the feed line which is placed in the middle of rectangular patch, and the port which is located near the center of the feeding line. The antenna's effective bandwidth is from 2.73 – 2.9 GHz, where S11 < -10dB at the center frequency of 2.775 GHz and relatively stable gain of around 6.192 dB is reached with good radiation efficiency.**

Keywords—microstrip antenna; diamond-shaped; hammer-shaped; FR-4; parametric study; gain; bandwidth

I. INTRODUCTION

In nowadays world, rapid advancements in telecommunication technology have led to an increased requirement for efficient antennas capable of operating at wide frequency ranges. Since other demands of the modern communication systems include compactness, space-saving, adaptability and ease of operation, the concept of microstrip antennas was introduced and quickly became popular. These antennas are low profile, conformable to planar and nonplanar surfaces, simple and inexpensive to manufacture using modern printed-circuit technology, mechanically robust when mounted on rigid surfaces, compatible with MMIC designs, and very versatile in terms of resonant frequency, polarization, pattern, and impedance [1]. The rapidly developing markets, especially in personal communication systems, mobile satellite communications, direct broadcast, wireless local area networks and intelligent vehicle highway systems, suggest that the demand for microstrip antennas and arrays will increase even further [2]. In recent years, a vast number of methods and techniques of design, construction, and optimization of microstrip antennas was invented. These include an adaptive network-based fuzzy inference system [3], coplanar waveguide feed method [4], design using metamaterials [5], reactive loading and stacked dielectric multilayer [6]. They are being modeled and fabricated for a huge range of frequencies and shapes, such as split-ring antennas given in [7], rectangular patch antennas for dual band operation described in [8], diamond shaped antenna provided in [9], and square patch antennas depicted in [10].

This paper presents an elegant and compact design of a hybrid between a hammer-shaped and a diamond-shaped antenna with the center frequency of 2.775 GHz and excellent radiation efficiency. The research methods included evaluation of preliminary antenna dimensions, electromagnetic performance assessment, operational requirements analysis, parametric sensitivity analysis, simulation and optimization.

II. RESEARCH METHODOLOGY

A. Preliminary Antenna Dimensioning

The first step in the research was establishing a proper size and shape of the microstrip antenna. After a careful examination of many different shapes and available properties, it was concluded that a hybrid shape between hammer and diamond will be taken into consideration. The proposed design is shown in Fig. 1, whereas the system metrics are given in Table 1. Different widths of different slots (given by W1, W2, W3, and W4) and heights (H1, H2) have been optimized to obtain optimum outputs. The antenna was placed in a box whose size was 1000 x 300 mm, and the top cover was chosen to be free space. The antenna's main physical feature is its symmetrical structure about both axes. The height of the upper indentation is 1 mm, the feed line length is 138 mm and its width is 2 mm.

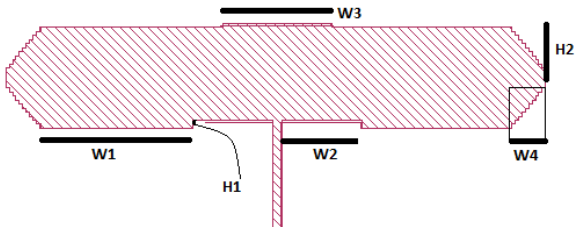

Fig. 1. The proposed antenna design.

TABLE I. THE PROPOSED SYSTEM METRICS

Parameter	*Size (mm)*	*Parameter*	*Size (mm)*
W1	38	W4	8.3
W2	20	H1	2
W3	28	H2	12.5

B. Electromagnetic Performance Assessment

The electromagnetic performance of the designed antenna depends highly on the dielectric layers composition and width, the metal type, and the port properties. The dielectric layers in the study are composed of a 1.6 mm-thick layer of FR-4 substrate with the relative permittivity of 4.4 and the dissipation factor of 0.02, and a layer of air whose thickness is 100 mm. Along with the dielectric constant and loss tangent, the metal type plays a crucial role in antenna performance. In this study, the simulated metal is lossless with infinite bulk conductivity. The fourth main factor that affects electromagnetic performance of the antenna is the feed line, which was attached to the middle point of the antenna and a port with the resistance of 50 Ω and auto-grounding capability was used.

C. Operational Requirements Analysis

For an efficient radiation of the proposed antenna design, the requirements were determined in accordance with the low profile and volumetric properties. Therefore, the operational considerations include linear and circular radiation capability, ability to be integrated with microwave circuits, high gain,

robustness and high efficiency. In the simulation process, the analysis was controlled by two techniques, namely the different frequency sweep combinations and the adaptive sweep (ABS) in the range of 2.5 – 3 GHz.

D. Fine Tuning and Parametric Sensitivity Analysis

In order to obtain an optimal solution for the antenna design, the effect of various sensitivity parameters on the reflection coefficient was considered. These parameters included dielectric thickness, feed point location, side angle, upper layer and lower layer lengths. By varying the parameters and comparing the center frequency, the corresponding gain, and the gains at zero-theta, the best design was reached. A shortened summary of the results is given in Table 2.

TABLE II. PARAMETRIC SENSITIVITY ANALYSIS

Dielectric Variation			
Thickness [mm]	***Central Frequency [GHz]***	***Gain [dB]***	***Gain at 0-theta [dB]***
1.56	2.735	-11.6	5.58
1.58	2.735	-11.3	5.61
1.62	2.725	-11.1	5.61
1.64	2.72	-11	5.64
Feed Point Location Variation			
Feed Point [mm]	***Central Frequency [GHz]***	***Gain [dB]***	***Gain at 0-theta [dB]***
-120	2.74	-33.6	5.9
-100	2.735	-5.4	5.82
-60	2.735	-26.6	6.22
-20	2.95	-17.7	2.32
Side Angle Adjustment			
Angle [°]	***Central Frequency [GHz]***	***Gain [dB]***	***Gain at 0-theta [dB]***
39.7	2.72	-25.2	5.58
42.3	2.725	-25	-3.539
47.7	2.71	-23.4	5.48
42.6	2.72	-21.4	5.45
Upper Layer Adjustment			
Shift [mm]	***Central Frequency [GHz]***	***Gain [dB]***	***Gain at 0-theta [dB]***
0.5	2.705	-13.2	5.53
1	2.69	-14.8	5.38
-0.5	2.73	-10.6	5.64
-1	2.74	-9.5	5.58
Lower Layer Adjustment			
Shift [mm]	***Central Frequency [GHz]***	***Gain [dB]***	***Gain at 0-theta [dB]***
0.5	2.705	-13.2	5.53
1	2.7	-12.6	5.523
-0.5	2.64	-15.2	5.022
-1	2.73	-11.1	5.631

E. Simulation and Optimization

The antenna simulation and optimization involved evaluation of all input parameters, system metrics and performance constraints in a software tool Sonnet, which is a full-wave 3D planar EM field solver software for high frequency EM simulation.

III. RESULTS

A Cartesian graph of the S11 response of our antenna scaled in the frequency range of 2.5 – 3 GHz is shown in Fig. 2. According to the simulated results, the bandwidth from 2.73 to 2.9 GHz is achieved, and the antenna's center frequency equals to 2.775 GHz.

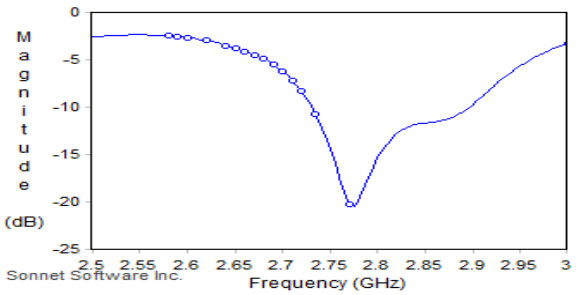

Fig. 2. The simulated S11 parameters

Moreover, the reflection coefficients and far-field radiation pattern were also examined. The far field antenna pattern was generated by using the current distribution information at the central frequency and viewed in a Cartesian plot (Fig. 4) for phi and theta directions.

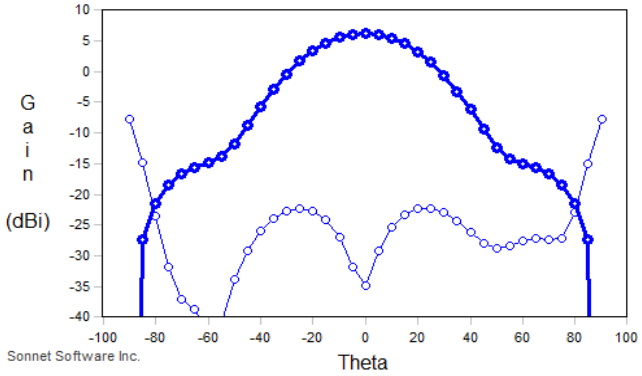

Fig. 3. Cartesian plot of the antenna's radiation pattern

IV. CONCLUSION

A novel microstrip patch antenna configuration containing a rectangular body, diamond-shaped edges attached to both sides of the body, and the feed line following the center of the rectangular body. Simulation is investigated by using different substrate materials for the same antenna design. The tests which were conducted for achieving better results involved altering the location of port on feeding line and dielectric material thickness, adjusting the indentations of the rectangular patch, and angle of the diamond edge, and concluded our test by combining the best results. Simulated results show that the proposed antenna can provide impedance bandwidth from 2.73 – 2.9 GHz at center frequency of 2.775 GHz. Gain of 6.192 dB was achieved with voltage standing wave ratio (VSWR) of 1.209.

REFERENCES

[1] C. A. Balanis, Antenna Theory Analysis and Design, 4th ed. New Jersey: Wiley, 2016, pp. 1-24.

[2] D. G. Fang, Antenna Theory and Microstrip Antennas, 1st ed. Boca Raton, FL: CRC Press, 2010, pp. 85-110.

[3] E. Demircioglu, M.H. Sazli, O. Sengul, S.T. Imeci, H.A. Ilgin, "Adaptive network-based inference system models on multiband patch antenna design," Turk J Elec Eng & Comp Sci, vol. 23, pp. 118-125, 2015.

[4] S. Choudhary, P. Jain, "CPW-fed microstrip patch antenna for WLAN Application at Resonant Frequency 2.3 GHz," The International Journal Of Science & Technoledge, vol. 2 (9), pp. 63-67, September 2014.

[5] I.M. Rafiqul, A. Alsaleh, M.W. Aminah, M.S. Yasmin, N.A.M. Farihah, "Design of dual band microstrip patch antenna using metamaterial," IOP Conf. Series: Materials Science and Engineering 260, 2017.

[6] J. Anguera, C. Puente, C. Borja, N. Delbene, J. Soler, "Dual-frequency broad-band stacked microstrip patch antenna," IEEE Antennas and Wireless Propagation Letters, vol. 2, pp. 36–39., 2003.

[7] S.C. Basaran, “Compact dual-band split-ring antenna for 2.4/5.2 GHz WLAN applications,” Turk J Elec Eng & Comp Sci, vol.20 (3), pp. 347-352, 2012.

[8] A.H. Rambe, K. Abdillah, “A low profile rectangular patch microstrip antenna for dual-band operation of wireless communication system,” IOP Conf. Ser.: Mater. Sci. Eng. 309, 2018.

[9] Y. Chourasia1, M.P. Parsai, “A Review on dfferent diamond shaped microstrip patch antenna,” International Journal of Engineering Science and Computing, vol. 7, no. 8, pp. 14437-14440, August 2017.

[10] J. S. Malik, U. Rafique, S.A. Ali, M.A. Khan, “Novel patch antenna for multiband cellular, WiMAX, and WLAN applications,” Turk J Elec Eng & Comp Sci, vol. 25, pp. 2005-2014, 2017.

Design of An Implantable Antenna for ISM and WMTS Band Biomedical Applications

Hasen Ahmed M. Al Werfali, Bahattin Türetken
Depart. of Electrical-Electronics Eng., Karabük University
Karabük, Turkey
hassanajrabe@gmail.com,
bahattinturetken@karabuk.edu.tr

İlhami Ünal
Materials Institute, MİLTAL
TÜBİTAK MAM
Gebze, Kocaeli, Turkey
ilhami.unal@tubitak.gov.tr

***Abstract*—In this paper, an implantable dual band miniaturized slot PIFA antenna is proposed for biomedical wireless telemetry applications. The designed antenna operates inside human muscle tissue at both the Industrial, Scientific, and Medical band (ISM) (2400-2480 MHz) and the Wireless Medical Telemetry Service (WMTS) band (1395-1400 MHz and 1427-1432 MHz). The size of the designed small dual band antenna is 12.6 mm x 8.5 mm x 2.4 mm. The antenna consisting of an L-shaped slot patch and a ground plane with 2.4 mm FR4 substrate layer is fed using an SMA coaxial connector. The antenna is designed using full-wave electromagnetic solvers (HFSS and CST) comparatively and its radiating patch dimensions are parametrically optimized in terms of return loss, radiation pattern and gain, as well as under size constraints. The antenna model is then fabricated and tested inside a muscle-mimicking liquid. The measured antenna performance parameters and simulation results are reasonably compared to each other. The promising simulation results show that -10 dB percentage bandwidth/max. gain at lower and higher bands are 3.02%/2.99 dBi and 3.73%/3.46 dBi, respectively. To the best of our knowledge, there isn't any other antenna operating both at ISM and WMTS bands ever proposed in literature. The proposed implantable dual band antenna would be an attractive candidate element for biomedical wireless telemetry applications, too.**

I. INTRODUCTION

Implantable antennas differ from wearable ones in terms of being more challengeable for in-body communication, because of the complicated and poor in-body operating environment [1]. Essentially, Implantable Medical Devices (IMDs) present significant improvements in the healthcare field by offering the assists in numerous lives saving [2] and various diseases management [3]. IMDs are capable to communicate wirelessly with various exterior devices. The RF link allows reaching longer distances with higher data rates, whereas the inductive link is utilized basically for short-range communications and requires using a coil antenna. Thus, the attention on the RF-linked IMDs increases over time [4].

II. THE ANTENNA DESIGN

The Figure 1 shows the geometry of proposed implantable PIFA antenna design embedded inside a muscle phantom, with a lumped port in High Frequency Structure Simulator (HFSS).

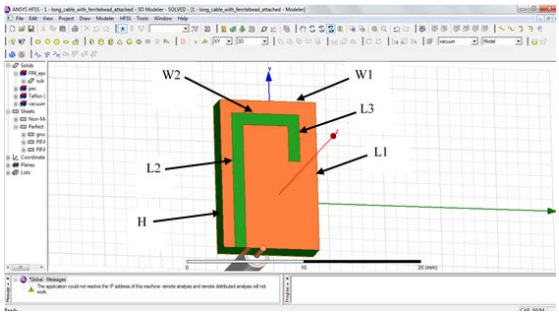

Figure 1. The geometry of proposed implantable antenna

Perfect Electric Conductor (PEC) is used for ground and patch in the simulations, and the substrate material of the antenna is FR4, of which the dielectric constant is 4.4, relative permeability is 1.0 and the loss tangent is 0.02.

The following illustrates the tissues dielectric properties with considering the critical two frequencies [5]. In this study, a homogeneous model using only muscle phantom will be used.

TABLE I. RELATED DIELECTRIC PROPERTIES FOR VARIOUS BODY TISSUES

Tissue	Permittivity		Conductivity (S/m)	
	1.433 GHz	*2.4 GHz*	*1.433 GHz*	*2.4 GHz*
Muscle	54	52.7	1.15	1.73
Fat	5.39	5.28	0.065	0.10
Skin	39.5	38	1.047	1.46

III. DESIGN AND SIMULATION OF PIFA ANTENNA USING HFSS

Return loss results obtained via HFSS and CST are compared to each other. Figure 2 shows the return loss of the design with cable, in both CST and HFSS. It can be seen that the results show good agreement.

The promising simulation results show that -10 dB percentage bandwidth/max. gain at lower (1.4 GHz central frequency) and higher (2.4 GHz central frequency) bands are 3.02%/2.99 dBi and 3.73%/3.46 dBi, respectively.

The antenna is produced using LPKF Protomat H100 and a long coaxial cable is attached to the antenna for insertion of the antenna to the muscle liquid phantom, easily (Figure 3).

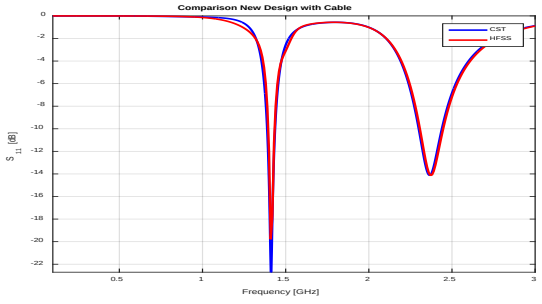

Figure 2. Comparison of the design with cable, in CST and HFSS

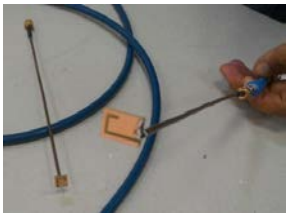

Figure 3. Fabricated Antenna

IV. Liquid Body Phantoms: Realization and Characterization

The recipes of liquid phantoms used in this paper and the obtained muscle-like dielectric properties tissue, are reported in dielectric properties are also measured using 85070E Dielectric Probe Kit and Agilent N5230A (10 MHz-40 GHz) Vector Network Analyzer, successfully.

TABLE II. Recipes and Dielectric Properties of the Equivalent Muscle Body Phantom

Frequency	Recipe	Target values	Measured values
ISM, 2.45 GHz	Water 73.20 % Salt 0.04 % DGBE 26.76 %	ε_r= 52.73 tan δ = 0.242	ε_r = 53.68 tan δ = 0.264

V. Measurement Results

Return loss and antenna pattern measurements are done using Agilent N5230A (10 MHz-40 GHz) Vector Network Analyzer at TUBİTAK MAM ME MİLTAL Laboratories. Figure 4 shows the measured return loss of the antenna in both air and muscle mimicking phantom, comparatively.

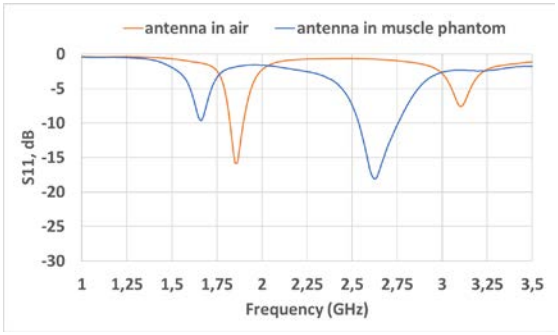

Figure 4. Measured return loss of the antenna in air and muscle mimicking liquid.

The main lobes are aligned along the same axis, approximately, in both simulated and measured results.

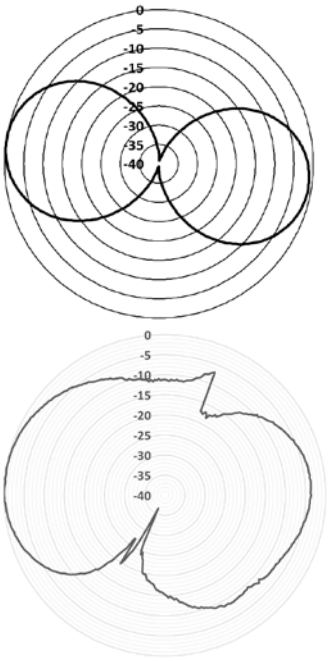

(a) (b)

Figure 5. (a) Simulated and (b) measured radiation pattern of the antenna in y-z plane, at around 1.8 GHz.

VI. Conclusion

The simulated performance of the proposed implantable antenna was carried out using both the CST and HFSS simulation softwares, comparatively, employing inside mimicking numerical phantoms. The antenna exhibits low reflection coefficient, wide band impedance matching and has small size. The proposed antenna would be used for biomedical wireless telemetry applications for both ISM and WMTS bands.

Acknowledgements

The authors would like to thank Coordinator of Scientific Research Projects at Karabük University for funding this study. The authors also would like to thank Sercan Erdoğan and Mustafa Kılıç for helps in production and measurements of the antenna, and Aysun Sayıntı for helps in measurement of the phantom at TÜBİTAK MAM ME MİLTAL Laboratories.

References

1. C. Liu, Y. X. Guo and S. Xiao, "A Review of Implantable Antennas for Wireless Biomedical Devices", Forum for Electromagnetic Research Methods and Application Technologies (FERMAT), 2015.
2. W. Kin-Lu, “Planar Antennas for Wireless Communications”, Wiley Publication, ISBN: 978-0-471-26611-2, January 2003.
3. D. T. Halperin, T. S. Heydt-Benjamin, B. Ransford, S. S. Clark, B. Defend, W. Morgan, K. Fu, T. Kohno, and W. H. Maisel, “Pacemakers and implantable cardiac defibrillators: Software radio attacks and zeropower defenses,” in IEEE Symposium on Security and Privacy, 2008.
4. P. David M., “Microwave engineering”, 4th ed., Wiley Publication, ISBN 978-0-470-63155-3, 2012.
5. R. W. P. King, S. Prasad, and B. H. Sandler, “Transponder antennas in and near a three-layered body,” IEEE Trans. Microw. Theory Tech., vol. 28, no. 6, pp. 586–596, 1980.

Design of a Tri-Resonance Coupled Microstrip Filter

Abdulwahab HAJAR, Mohamedou ABEWA, Youcef BELLALOU, Sana BELHADJ, Ihab YASİN [1]
[1] Department of Electrical Engineering
Antalya Science University
Antalya, Turkey

Taha İMECİ [2]
[2] Department of Electrical and Electronics Engineering
International University of Sarajevo
Sarajevo, Bosnia and Herzegovina

Mustafa İMECİ [3]
[3] Department of Electrical and Electronics Engineering
Ankara Yildirim Beyazit University
Ankara, Turkey

***Abstract*—This paper is concerned with the design of a tri-resonance coupled microstrip filter, with the following specifications:**

- **Substrate thickness of 1.6 mm, loss tangent of 0.0005, dielectric constant of 4.4**
- **Material used is copper**
- **Resonance frequencies of 2.1, 2.25, and 2.51 GHz.**

This design was made using electromagnetic simulating software namely Sonnet software, further analysis in the design of this filter was done by changing the main parameters of the design and observing the results of the corresponding changes.

I. INTRODUCTION

A lot of work and previous publications have been done about filters, as they have been essential components of some of the leading technology today in telecommunications, data transfer, etc. [1-3].

Furthermore, many designs have been modelled, worked on, and remodeled in order to satisfy a manufacturer's, company's or customer's need, it is as such that this paper is concerned with the design of a tri-resonance coupled microstrip filter, with the following specifications:

- Substrate thickness of 1.6 mm, loss tangent of 0.0005, dielectric constant of 4.4
- Material used is copper
- Resonance frequencies of 2.1, 2.25, and 2.51 GHz.

In addition to the previous specifications, the goal of this design was to reach a value of the parameter S11 which is close to -10 dB in order to minimize power loss, and a value of S12 which is close to -1 dB.

II. PARAMETRIC STUDY AND VARIATIONS

In this design, we started with an initial design based on the findings of other publications except for minor changes. The initial response of this design is shown in Fig. 1.

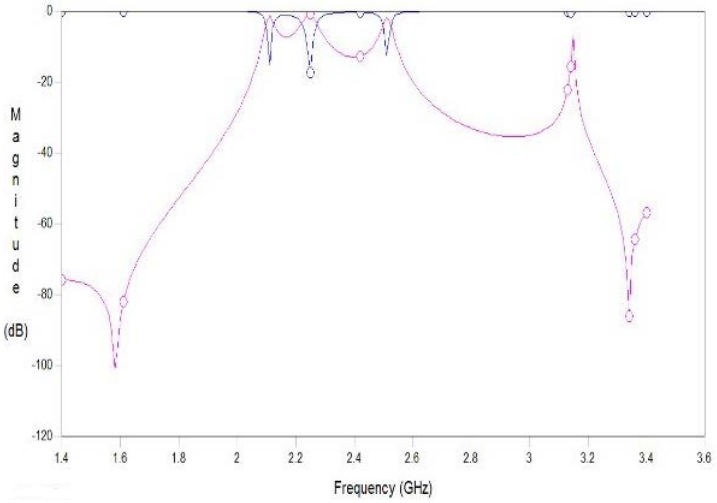

Fig.1. The variables S11 and S12 based on the initial design

The values of S11 and S12 of the initial design at its corner frequencies are displayed in Table 1 below.

Table 1. Values of S11 and S12 at corner frequencies of initial design

Original	Corner frequency (GHz, dB)	Corner frequency (GHz, dB)	Corner frequency (GHz, dB)
S11	(2.1, -15.17)	(2.25, -17)	(2.51, -12)
S12	(2.11, -1.30)	(2.25, -0.84)	(2.51, -1.73)

As it can be seen from Table 1, the values of S11 and S12 diverge from their corresponding ideal values (less than 10 dB and -1 dB respectively). The initial design of this filter is shown below and labelled in Fig. 2.

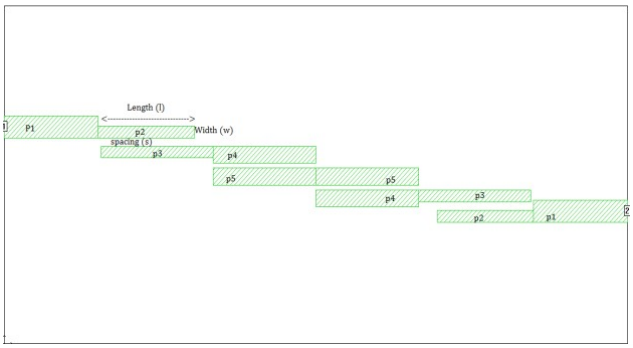

Fig. 2. The initial design of the filter, also labelled are the parameters of the design of the filter

In order to rework and improve the design of the filter above, each parameter of each of the parts labelled in Fig. 2 were changed separately, while keeping all other parameters unchanged, and the response (values of S11 and S12 at corner frequencies) were taken note of. Aiming to find an optimal change in the design of the filter, the following changes were made to the parts of the filter (refer to Fig. 2) and the corresponding changes found in the response are shown below.

** Changes to all parts were made, however only significant gains are displayed below.

** All changes are done in units of mils.

** Due to symmetry, any change in the left half of the filter, was also made in the corresponding right part of the filter.

A. CHANCES IN WIDTH

Table 2. Results found by doubling the width of p2

By altering p2 (doubling width)	Corner frequency (GHz, dB)	Corner frequency (GHz, dB)	Corner frequency (GHz, dB)
S11	(2.11, -11.34)	(2.26, -11.11)	(2.52, -6.65)
S12	(2.11, -2.37)	(2.26, -1.61)	(2.51, -3.87)

Table 3. Results found by halving the width of p2

By altering p2 (halving width)	Corner frequency (GHz, dB)	Corner frequency (GHz, dB)	Corner frequency (GHz, dB)
S11	(2.11, -12.67)	(2.24, -24.82)	(2.51, -19.310)
S12	(2.11, -1.08)	(2.23, -0.76)	(2.51, -1.06)

Table 4. Results found by doubling the width of p3

By altering p3 (doubling width)	Corner frequency (GHz, dB)	Corner frequency (GHz, dB)	Corner frequency (GHz, dB)
S11	(2.07, -11.84)	(2.22, -14.55)	(2.52, -10.77)
S12	(2.07, -2.40)	(2.22, -1.16)	(2.52, -2.29)

B. CHANGES IN LENGTH

Table 5. Results found by decreasing the length of p1 by 100 mils

By altering p1 (decreasing length by 100 mils)	Corner frequency (GHz, dB)	Corner frequency (GHz, dB)	Corner frequency (GHz, dB)
S11	(2.12, -12.54)	(2.25, -11.59)	(2.57, -11.83)
S12	(2.12, -1.71)	(2.5, -0.99)	(2.57, -2.51)

Table 6. Results found by decreasing the length of p4 by 100 mils

By altering p4 (decreasing length by 100 mils)	Corner frequency (GHz, dB)	Corner frequency (GHz, dB)	Corner frequency (GHz, dB)
S11	(2.21, -9.08)	(2.39, -10.18)	(2.62, -14.10)
S12	(2.21, -2.44)	(2.39, -1.04)	(2.61, -1.8)

III. CONCLUSION

After studying the findings, those shown included in this paper and excluded, the following results were found:

- The optimum value of S11 was found by altering p4 (decreasing its length by 100 mils), while keeping all other factors constant.
- The optimum value of S12 was found by altering p2 (halving its width), while keeping all the other factors constant.
- Changing the spacing didn't yield any beneficial result.
- Although It was expected that combining the changes which lead to the optimum S11 and optimum S12 would yield an optimum in both S11 and S12. The findings did not meet the expectations.
- Logically, it can be inferred that a superposition of more than one change can lead to an optimum response (of both S11 and S12). However, no direct relation was found between the change in each parameter separately and its corresponding effect.

REFERENCES

[1] Hsu C-L., Hsu F-C. and Kuo J-T., "*Microstrip Bandpass Filters for Ultra-Wideband (UWB) Wireless Communications*", Microwave Symposium Digest, 2005 IEEE MTT-S International, DOI: 10.1109/MWSYM.2005.1516698, 2005.

[2] Hong J-S., Lancaster, M. J., "*Couplings of microstrip square open-loop resonators for cross-coupled planar microwave filters*", IEEE Transactions on Microwave Theory and Techniques, vol. 44, issue 11, pp. 2099-2109, 11/1996.

[3] Hong J-S., Lancaster, M. J., Jedamzik D and Greed R. B., "*On the development of superconducting microstrip filters for mobile communications applications*", IEEE Transactions on Microwave Theory and Techniques, vol. 47, issue 9, pp. 1656-1663, 09/1999.

Design of a T Shaped Microstrip Bandpass Filter

Mustafa ÇAĞLAR, Ege İLHAN, Zikri G. DEMİREZEN,
Sıla KOÇER, Refik Can BİLGİÇ [1]
[1] Department of Electrical and Electronics Engineering
Antalya Science University
Antalya, Turkey

Taha İMECİ [2]
[2] Department of Electrical and Electronics Engineering
International University of Sarajevo
Sarajevo, Bosnia and Herzegovina

Mustafa İMECİ [3]
[3] Department of Electrical and Electronics Engineering
Ankara Yildirim Beyazit University
Ankara, Turkey

***Abstract*—This paper has design and simulation of a T-shaped microstrip bandpass filter. Substrate with a dielectric constant of 4.4 and thickness of 63 mils for the designed filter. Loss tangent of 0.0 and center frequency of 19.0 GHz. This bandpass was designed with the Sonnet software program then the length and width were changed. Furthermore, phase scattering response and current intensity distribution of the proposed filter have been discussed. Finally, the features of the proposed filter have been compared with other designed microstrip filters in literature.**

Keywords—Bandstop filters, bandpass filter, bandwidth, harmonic filter, harmonic suppression, microwave, passband, perturbation.

I. INTRODUCTION

Passive bandpass filter is the cut-off frequency or fc point in a simple RC passive filter can be accurately controlled using just a single resistor in series with a non-polarized capacitor, and depending upon which way around they are connected, we have seen that either a Low Pass or a High Pass filter is obtained [1]. Unlike a low pass filter that only pass signals of a low frequency range or a high pass filter which pass signals of a higher frequency range, a Band Pass Filters passes signals within a certain "band" or "spread" of frequencies without distorting the input signal or introducing extra noise. This band of frequencies can be any width and is commonly known as the filters bandwidth [2]. Bandwidth is commonly defined as the frequency range that exists between two specified frequency cut-off points (fc), that are 3 dB below the maximum center or resonant peak while attenuating or weakening the others outside of these two points. Then for widely spread frequencies, we can simply define the term "bandwidth", BW as being the difference between the lower cut-off frequency (fc_{LOWER}) and the higher cut-off frequency (fc_{HIGHER}) points. In other words, BW = $f_H - f_L$ [3]. Clearly for a pass band filter to function correctly, the cut-off frequency of the low pass filter must be higher than the cut-off frequency for the high pass filter. The "ideal" Band Pass [4-5]. Filter can also be used to isolate or filter out certain frequencies that lie within a band of frequencies, for example, noise cancellation [6]. Band pass filters are known generally as second-order filters, (two-pole) because they have "two" reactive component, the capacitors, within their circuit design [7]. One capacitor in the low pass circuit and another capacitor in the high pass circuit [8]. This paper presents the design of a narrow band-pass filter with wide stopband for WLAN and WiMAX applications [9]. In this paper, the T-shape stepped impedance resonators are adopted for the design of microstrip bandpass filters for wide harmonics suppression [10].

II. SIMULATION RESULTS

Fig. 1 shows the top view of the designed filter.

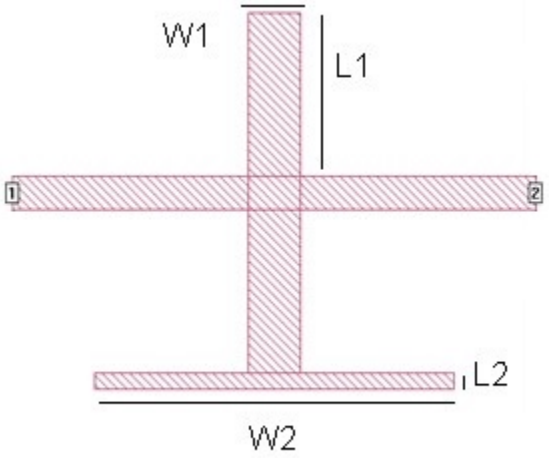

Fig. 1. Labelled design of the filter

All simulated values are in terms of mils. Tables show how bandwidth and S-parameters vary by changing each side lengths individually.

Table I. Bandwidth rate of changed L1

W1	L1	f	S11	S21	BW
10	50	19,8	-33	0,010	800
10	45	20,5	-33	0,013	800
10	40	21,1	-29	-0,04	900
10	35	21,8	-42,4	-0,02	1000

Table II. Bandwidth rate of changed W1

L1	W1	f	S11	S21	BW
50	10	19,8	-33	-0,010	800
50	12	19,7	-33	-0,011	700
50	14	19,7	-33	-0,04	600
50	16	19,7	-24	-0,015	500

Table III. Bandwidth rate of changed L2

W2	L2	f	S11	S21	BW
110	5	19,8	-33	-0,01	800
110	10	19,4	-37	-0,03	900
110	15	19,2	-35	-0,01	1000
110	20	19	-47	0,005	1000

Table IV. Bandwidth rate of changed W2

L2	W2	f	S11	S21	BW
5	110	19,8	-33	-0,01	800
5	112	19,7	-30	-0,06	700
5	114	19,7	-42	-0,02	700
5	116	19,7	-27	-0,06	600

Fig. 2 shows the main graphic of the filter.

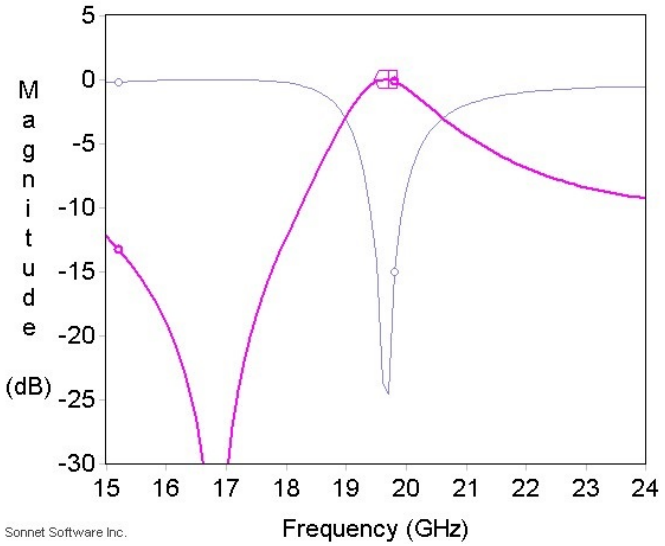

Fig. 2. Main graphic of bandpass filter

III. CONCLUSION

New dual degenerate mode microstrip bandpass filter based on SIR approach on all sides of the square loop resonator has been presented in this paper. The designed filter has been constructed from a dielectric material with a dielectric constant of 4.4 and a thickness of 63 mils to be applied at 19 GHz design frequency. Parametric study about the effect of perturbation element dimension on the filter response has been investigated. At the same design frequency, the proposed filter in this study has almost better electrical specifications than reported works in. Also, it has smaller surface area than all reported filters in, regardless of design frequency and electrical filter measurements.

ACKNOWLEDGEMENTS

We would like to thank Dr. James Rautio from Sonnet Software for his continuing support by providing the Sonnet Suites for Antalya Science University.

REFERENCES

[1] B. F. Zong, G. M. Wang, H. Y. Zeng and Y. W. Wang, "*Compact and High Performance Dual-band Bandpass Filter using Resonator Embedded Scheme for WLANs"*. Radio engineering Academic Journal, vol. 21, Issue 4, p. 1050-1053, Dec. 2012.

[2] J. Bonache, I. Gil, J. García-García and F. Martín, "*Novel microstrip bandpass filters based on complementary split-ring resonators*", IEEE Transactions on Microwave Theory and Techniques, vol. 54, no. 1, pp. 265–271, 2006.

[3] Bo Liu. *"Half Wavelength Open Circuit Stubs Filter Design"*, University of Gavle. Feb. 2013.

[4] M. Hookari and G. Karimi, "*Design of Microstrip Filter Using Modified T-shaped with Wide Stopband"*, International Journal of Engineering & Technology Sciences (IJETS) 2 (2), p. 138-145, March 2014.

[5] Mezaal YS, Eyyuboglu HT (2016) "*Investigation of New Microstrip Bandpass Filter Based on Patch Resonator with Geometrical Fractal Slot*", PLoS ONE 11(4): e0152615. https://doi.org/10.1371/journal.pone.0152615. April 7, 2016

[6] W. Menzel, L. Zhu, K. Wu and F. Bögelsack, *"On the design of novel compact broad-band planar filters,"* IEEE Transactions on Microwave Theory and Techniques, vol. 51, no. 2, pp. 364–370, 2003.

[7] X. Guan, W. Fu, H. Liu, D. Ahn and J. S. Lim, *"A Novel Dual-Mode Bandpass Filter Based on a Defected Waveguide Resonator"*, ETRI Journal, vol. 33, no. 6, Dec. 2011.

[8] J. Bonache, F. Martín, F. Falcone et al., *"Super compact split ring resonators CPW band pass filters,"* in Proceedings of the IEEE MITT-S International Microwave Symposium Digest, pp. 1483–1486, Fort Worth, Tex, USA, June 2004.

[9] S. Amiri, N. Khajavi and M. Khajavi, "*Design of Compact RF Filters with Narrow Band-Pass and Wide Stop-Band by Open-Stub & T-shaped Microstrip Resonators and Defected Ground Structure (DGS)"*. 2014 International Conference on Communications, Signal Processing and Computers, p.198-201, Switzerland, Feb. 22-24, 2014.

[10] R. Lerdwanittip, A. Namsang, and P. Akkaraekthalin, "*Bandpass Filters using T-shape Stepped Impedance Resonators for Wide Harmonics Suppression and their Application for a Diplexer*." Journal of Semiconductor Technology and Science, vol.11, no.1, March 2011.

Design and Simulation of Modified X Band Vivaldi Antenna for Radar Applications

Esma Mine Yildiz
Informatics Institute
Istanbul Technical University
Istanbul, Turkey
turkyilmazes@itu.edu.tr

Sebahattin Eker
Informatics Institute
Istanbul Technical University
Istanbul, Turkey
ekerseb@itu.edu.tr

***Abstract*— This paper describes comparision of reference Vivaldi antenna and modified Vivaldi antenna. Both antennas work at X Band. CST simulation program is used for Antenna simulations. Slot openings, circular cavities, and microstrip fed parameters and its effects will be described. S – Parameter, VSWR, farfield optimizations will be discussed for reference and designed Vivaldi antennas.**

Keywords*— Vivaldi antenna, X Band antenna, microstrip fed antenna, CST simulation of antenna

I. INTRODUCTION

Vivaldı antenna is a member of end-fire tapered slot antenna and it can take its special name from exponential tapered structure (ETSA). Its wideband structure, medium level gain and small sidelobes are primary specifications of tapered slot antennas [1]. Designed Vivaldi antenna is start point of Vivaldi array design project, optimum structure will be turned X band 1x8 vivaldi array.

Microstrip feed line, stripline to slotline converter, substrate layer, and radiating copper layer are main components of this work. Circular slot provides impedance matching, and rectangular slot provides microstrip transmission line coupling.

Described simulation will be produced with selected substrate material which is Rogers Inc. 4003C model lossy substrete and opper radiating sheath. Waveguide port feeding method is used for this simulation.

II. DESIGN AND SIMULATION

Reference Vivaldi [2] antenna designed with exponential slotline, circular cavity, stripline and stripline to slotline converter. Figure 1 (left) states model of this antenna. Proposed antenna includes chambers which locates both sides of antenna. Dimensions of this antenna is 40 mm width, 1.5 mm height and 80 mm length. Diameter of circular cavity is 3mm. Thickness of used substrate is 1.5 mm and copper layer is 0.035mm.

Minimum frequency of Vivaldi antenna is determined by flare length and circular cavity diameter. Maximum frequency value depends on slotline cavity, and angular stub [3]. Its reference impedance is 53 ohm.

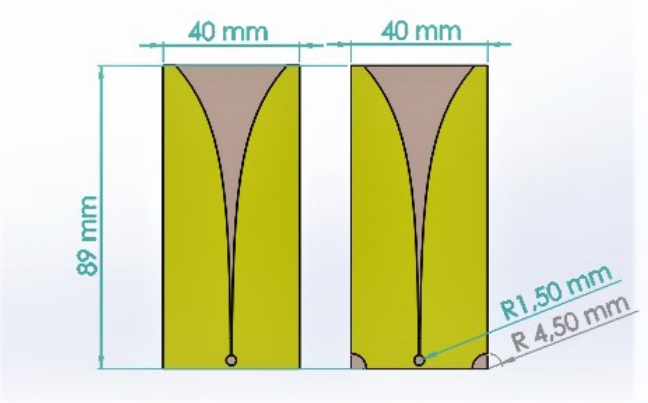

Figure 1 - Reference Antenna and Modified Antenna

Modified antenna has circular (Figure1 – right) cavity from both sides, radiusfactor parameter will change dimension of this cavity. According to simulations, taper factor changes impedance matching. Because of this optimum value of taper factor 3 was selected. As it can be seen, radius of circular cavities three times larger than center cavity.

Impedance matching of modified antenna is better than reference antenna especially at 9-9.5 GHz, 10-10.5 and 11.5 – 12 Ghz. Figure 3 states S11 parameter of reference antenna and Figure 2 states S11 parameter of modified antenna.

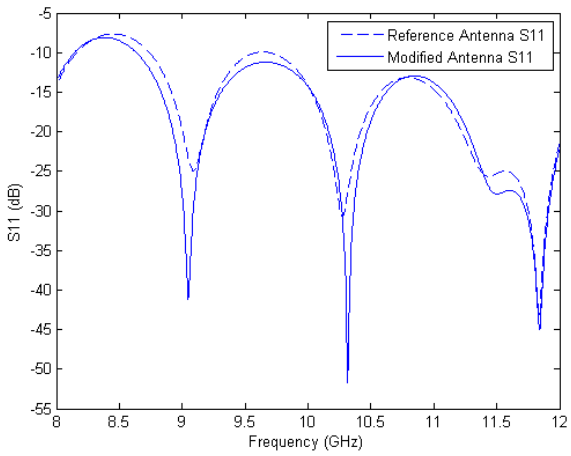

Figure 2- S11 Parameters of Reference Antenna and Modified Antenna

Voltage Standing Wave radios of modified antenna converges to one less than modified antenna and Figure 3 states both these values between 8GHz and 12 GHz.

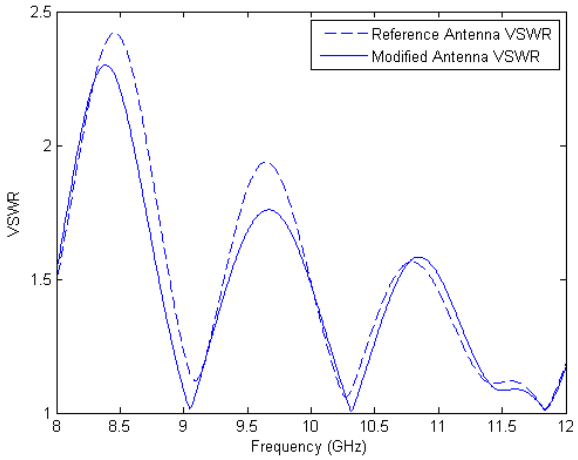

Figure 3-Voltage Standing Wave Ratios of Reference and Modifed Antenna

There is no primary change in farfield value. Figure 4 represents polar plots of realized gains of each antenna. Realized gain values changes at reference antenna from 7 dB to 9 dB and also, gain values of modified antenna have values which are in the same range.

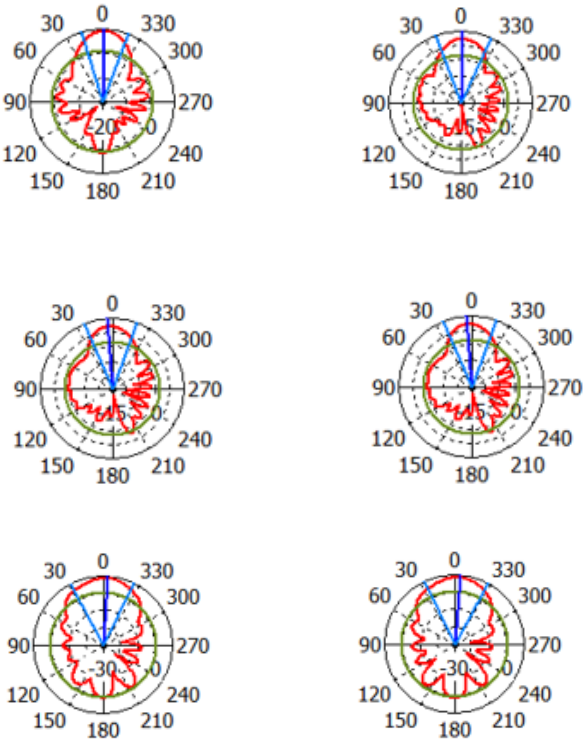

Figure 4 - Realized Gain Results of Reference (Left) and Modified (Right) Antenna at 8 GHz (Top), 10 Ghz (middle) and 12 GHz (Bottom).

In this simulation transient solver is used and both geometries divided more than 1 million meshcells.

III. Conclusion

Designed and modified antennas are compared in terms of three parameters; S11 values, VSWR values and farfields. There will be starting point of Vivaldi array design and production. Stripline to slotline conversion, and array generations are the next steps of this work After achieving all challenges, this application will be component of radar applications.

References

[1] K. S. Yngvesson, D. H. Schaubert, T. L. Korzeniowski, E. L. Kollberg, T. Thungren, and J. F. Johansson, "Endfire Tapered Slot Antennas on Dielectric Substrtates", IEEE Trans. Antennas and Propagation, vol. AP-33, no. 12, pp. 1392 – 1400, Dec. 1985.

[2] Chen, F. "An improved wideband Vivaldi antenna design", The University of Texas-Pan American, 2010.

[3] J. Chramiec, "Reactances of Slotline Short and Open Circuits on Alumina Substrate", IEEE Trans. MTT, vol. 37, no. 10, October 1989, pp. 1638 – 1641.

Design and Simulation of Band stop Filter using Sonnet Software

Elif Demirpolat, Fatih Tat, Gülsüm Gizem Aktaş,
Enver Eren Altınışık, Ömer Kürşad Çayır
Department of Electric and Electronics Engineering,
Antalya Science University
Antalya, Turkey

Taha Imeci, Azra Yildiz
Department of Electric and Electronics Engineering,
International University of Sarajevo, Sarajevo, Bosnia and Herzegovina

Ahmet Fazıl Yağlı
Aselsan Research Center
Ankara, Turkey

***Abstract*—This paper presents designing of band stop filter using Sonnet software. Use band stop filters when some unwanted interfering frequencies are particularly strong; or when high attenuation may be needed only at certain frequencies. They are easy to implement and fabricate features. The filter is designed to stop between 4 GHz and 5GHz with -49dB.**

Keywords – Band stop filter

I. INTRODUCTION

The Band stop Filter, (BSF) is another type of frequency selective circuit that functions in exactly the opposite way to the Band pass filter. The band stop filter, also known as a *band reject filter*, passes all frequencies except for those within a specified stop band which are greatly attenuated. If this stop band is very narrow and highly attenuated over a few hertz, then the band stop filter is more commonly referred to as a *notch filter*, as its frequency response shows that of a deep notch with high selectivity (a steep-side curve) rather than a flattened wider band. Also, just like the band pass filter, the band stop (band reject or notch) filter is a second-order (two-pole) filter having two cut-off frequencies, commonly known as the -3dB or half-power points producing a wide stop band bandwidth between these two -3dB points. Then the function of a band stop filter is too pass all those frequencies from zero (DC) up to its first (lower) cut-off frequency point f_L, and pass all those frequencies above its second (upper) cut-off frequency f_H, but block or reject all those frequencies in-between. Then the filters bandwidth, BW is defined as: ($f_H - f_L$). When the notch (band stop) filter was in designed process, Signal Interference technique was seen on paper[2]. Furthermore, the process can be implemented in all band stop and band pass filters. The notching out the 5-6GHz was influence the research community[3]. Opposite of that, the band stop filter was designed by people who wanted to study on Fıxed-Satellite, Radiolocation, Mobile, and Amateur Satellite Service.

II. DESIGN OVERVIEW

Filter Design

The main purpose of the design is that the 4GHz and 5GHz frequencies are going to be ignored by filter. The design has two s parameters, which means two cut-off frequencies. The filter implemented on FR4 with dielectric constant 4.4, loss tangent of 0.035, height of the dielectric (h) 200mils, for ground alumina is used dielectric constant 9.9. Z=50 ohm. At the end, trace plate was put after dielectric and it is alumina with 0.7mils thickness and 5.8e7 S/m conductivity. After the design issues were finished, the different length was tried on design to compare the results. The Table I is showing us how s parameter for port1 is changing with respect to port1 while the K and LL values are constant. Table II has same conditions but s parameter is analyzed with respected to port2. Table I and IV are for analyzing LL values while k and l1 lengths are constant. Table II for S11 and Table III is for s21. Table V and VI compare how the length of K is affecting s parameters while LL and L1 is constant.

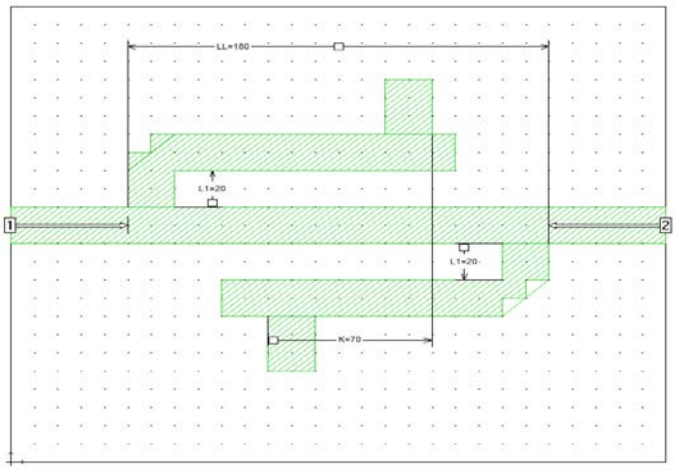

Fig. 1. The lengths of the filter

TABLE I. K AND LL LENGTH IS CONSTANT AND L1 IS CHANGING. THE VALUES ARE FOR S11.

L1	Values for S11		
	Frequency(GHz)	DB	Distance (mills)
1	4.26	-21.72	20
2	2.98	-12.13	30
3	3.28	-4.61	40
4	3.52	-3.14	50
5	5.48	-29.25	60
6	5.54	-27.54	70
7	5.32	-22.72	80

TABLE II. K AND LL LENGTH IS CONSTANT AND L1 IS CHANGING. THE VALUES ARE FOR S21.

L1	Values for S21		
	Frequency(GHz)	DB	Distance (mills)
1	5.72	-50.51	20
2	6.5	-53.62	30
3	5.5	-44.87	40
4	5.18	-45	50
5	1.56	-3.78	60
6	1.38	-4.62	70
7	1.38	-4.84	80

TABLE III. K AND L1 LENGTH IS CONSTANT AND L1 IS CHANGING. THE VALUES ARE FOR S11

LL	Values for S11		
	Frequency(GHz)	DB	Distance (mills)
1	5.44	-29.2	180
2	4.96	-18.8	120
3	4.84	-13.86	140
4	4.64	-11.86	160

TABLE IV. K AND L1 LENGTH IS CONSTANT AND L1 IS CHANGING. THE VALUES ARE FOR S21

LL	Values for S21		
	Frequency(GHz)	DB	Distance (mills)
1	5.58	-53.8	180
2	6.04	-49.03	160
3	6.02	-50.47	140
4	5.68	-45.06	120

TABLE V. L1 AND LL LENGTH IS CONSTANT AND K IS CHANGING. THE VALUES ARE S11

K	Values for S11		
	Frequency(GHz)	DB	Distance (mills)
1	4.2	-30.38	70
2	4.3	-12	60
3	4.4	-13.18	50
4	4.38	-13.95	40

TABLE VI. L1 AND LL LENGTH IS CONSTANT AND K IS CHANGING. THE VALUES ARE S21

K	Values for S21		
	Frequency(GHz)	dB	Distance mills)
1	5.7	-50.51	70
2	5.72	-54.31	60
3	3.98	-51.23	50
4	5.14	-50.68	40

III. RESULT

The graph of the s parameter presents the stop band of the filter.

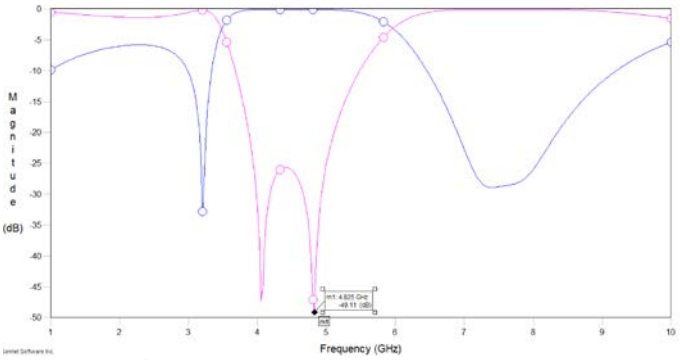

Fig. 2. Graph of the s parameters

Conclusion

This new design band stop filter is going to reject the 4Ghz and 5GHz frequency width. The data from different lengths were compared, the best length was chosen for designing band stop filter. However as a comment, K has 4.2 GHz frequency which is dropped the magnitude of the signal and K has the range 4 GHz to 5.78 GHz to get perfect gain. LL has 5.4 GHz frequency which drops the magnitude of the signal and LL has range for band stop filter which is 5.58-60.4 GHz. Last but not least, L1 has lots of frequency for dropping the magnitude of the signal, but the perfect chose is 5.48, range is 5.18-5.72. Overall, the design was suit for the applications which is not need 5-6Ghz frequency range. Also, the sonnet software has user-friendly environment and it is perfect for people who has no experience on the drawing. Simple drawings and prefect results. At the end, it can be used in advanced project easily.

REFERENCES

[1] Band Stop Filter. (2015). Retrieved June 02, 2017, from http://www.electronics-tutorials.ws/filter/band-stop-filter.html

[2] Madhan, M. G., Rani, G. F., Sridhar, K., & Kumar, J. S. (2012). Design and Fabrication of Transmission line based Wideband band pass filter. *Procedia Engineering*, *30*, 646-653.

[3] BalaSenthilMurugan, L., Raja, S. A. A., Chakravarthy, S. D., & Kanniyappan, N. (2012). Design and Implementation of a Microstrip Band-Stop Filter for Microwave Applications. *Procedia Engineering*, *38*, 1346-1351.

[4] Mohamed, A., Issam, A., Mohamed, B., & Abdellatif, B. (2015). Real-time Detection of Vehicles Using the Haar-like Features and Artificial Neuron Networks. *Procedia Computer Science*, *73*, 24-31.

[5] Hong, J. S. G., & Lancaster, M. J. (2004). *Microstrip filters for RF/microwave applications* (Vol. 167). John Wiley & Sons.

[6] Sonnet Sottware,version 16.54,www.sonnetsoftware.com,2017

Design and Simulation of a High-Frequency 10dB Directional Microstrip Coupler

Bučo Muamer, Kunovac Melisa,
Mešanović Adna
Department of Electrical and Electronics Engineering
International University of Sarajevo
Sarajevo, Bosnia

S.Taha Imeci
Department of Electrical and Electronics Engineering
International University of Sarajevo
Sarajevo, Bosnia

***Abstract* - In this paper, we will be discussing the design implications and simulation results of an asymmetric 10dB microstrip coupler with an 11GHz center frequency. The microstrip coupler is implemented with two parallel conductive strips on the Arlon AD1000 dielectric substrate. The results were achieved by observing the S-parameter response obtained with the Sonnet EM Simulation software. In the following text, we will explore the specifications of the design, simulation results and the behavior of S-parameters in response to slight variations of geometry, as well as the tolerance of the design to error in fabrication.**

Keywords: Coupler, Microstrip Coupler, 10dB Coupler

I. INTRODUCTION

The microstrip technology utilizes 3 layers, a solid dielectric below, a metallization layer and air above (fig. 1) – making it an inhomogeneous system. These mixed systems only support multi-modal propagation behavior at any given frequency [1]. Parallel line couplers are extensively used in a plethora of wireless and microwave applications due to the ease of implementation and simple incorporation with other circuitry [2]. The field patterns in microstrip applications usually show a predominantly TEM-like energy transmission mode, so propagation in microstrip is often called 'quasi-TEM. TEM stands for Transverse Electro-magnetic, meaning that both the magnetic and the electric fields are perpendicular to the direction of propagation [3]. Microstrip coupled lines are implemented with two parallel conducting strips(resonators) at a certain distance from one another, acting as coupled transmission lines. The behavior of coupled transmission lines can be described with S-parameters, as they reflect the coupling characteristics. As shown in Fig.2, the ports are labeled 1-4 and the S-parameters represent coupling of port 1 to each of the other ports, and to itself.

II. DESIGN SPECIFICATIONS

Simulation Parameters:

Bottom substrate: ArlonAD1000 [Erel = 10.2 Dielectric Loss Tan = 0.0023 Thickness = 0.6mm]

Top substrate: Air [Erel = 1 Dielectric Loss Tan = 0]

Metallization: Copper, Thickness = 0.1mm

Center frequency, f: 11GHz

Coupling, c: 10dB

Geometry parameters:

Table 1. Dimensions of The Transmission Lines

	Coupled Microstrip line	**Microstrip line**
Width	0.3mm	0.45mm
Length	3.1mm	3.2mm
Spacing	0.2mm	

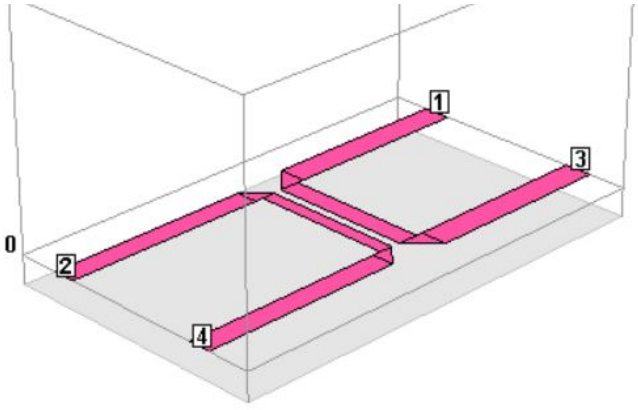

Fig. 1. 3D representation of the geometry

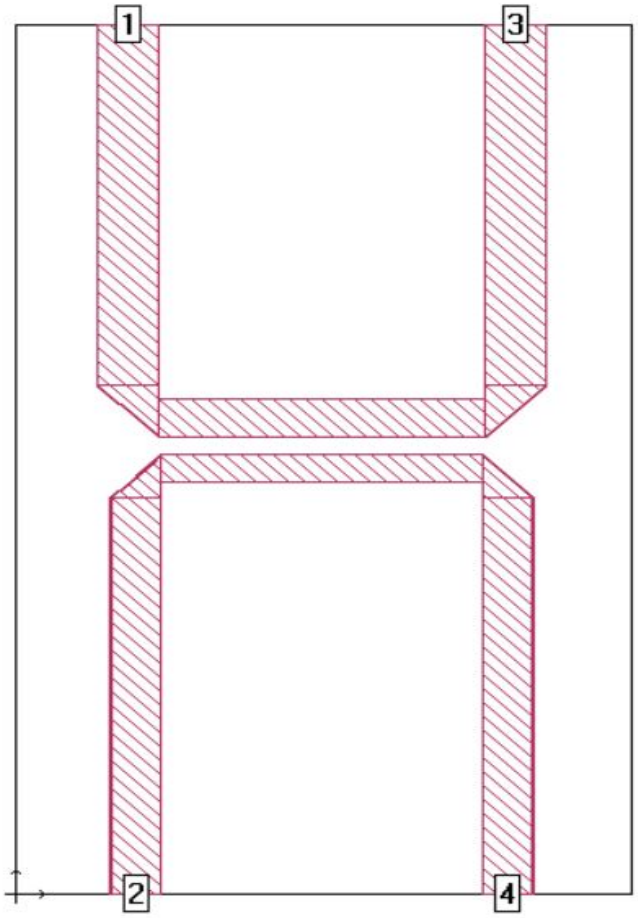

Fig. 2. 2D representation of the geometry

III. SIMULATION RESULTS

In the following figure, we see the behavior of S-parameters in the 6-18GHz range. As we can see in Figure 3, the purple S12 line represents the coupling throughout the frequency range, and the blue S11 line represents the reflection. Please note that the center frequency is 11GHz, but the overall operational range is fairly wide, with reasonable results obtained anywhere from 9GHz to 14GHz, with the deviation from nominal value limited to +-3%. The S12 coupling at center frequency f is 9.9dB.

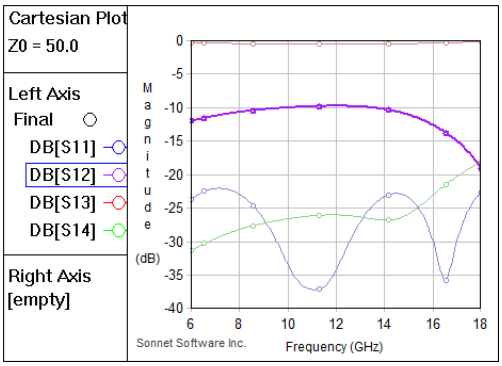

Fig. 3. Results of the simulation

IV. RESPONSE TO VARIATIONS

The behavior of the coupler is a direct consequence of the couplers' geometry and so variations in the construction and dimensions of the geometry will reflect on its performance [4]. Increasing the length of the microstrip lines shifts the operating frequency range and reduces coupling. Reducing the length will result in a similar response, but the S11 reflection will spike and the operational range will be slightly shifted to higher frequency. Increasing the width of the coupled lines can lead to reduced coupling, a significant increase in reflection and a slight delinearization of the response over the operational range. Most importantly, changes in the spacing between the microstrip lines can lead to some major changes in response. Increasing the spacing will lower coupling and shift the center frequency, and reducing the spacing will lead to higher coupling and a significant shift in the center frequency. Besides geometry, the utilized substrate also plays a key role. As the dielectric loss and relative permittivity are reduced, the acceptable operational frequency range is greatly diminished and behavior at higher frequency is also severely degraded.

As with any fabrication process, there is certain error associated with the production of the geometry. In light of these facts, the geometry is designed to minimize the sensitivity to slight variations, and so the acceptable deviation for the dimensions is about 10% from nominal(stated) values, depending on the required precision of the results. The only dimensional parameter within the geometry that is truly sensitive to change is the spacing between the coupled lines [5], where a 5% disparity can lead up to a 2% shift in coupling.

REFERENCES

[1] Azahar F. Zairi Ismael R. (2016). Design And Fabrication Of 12 Ghz Microstrip Directional Coupler For Rf/Microwave Application

[2] Edwards, T.C.; and Steer, M.B. (2002). Foundations of Interconnect and Microstrip Design (3rd ed.). England: John Wiley & Sons.

[3] Pozar, D.M. (1998). Microwave Engineering[] (2nd ed.). USA: John Wiley & Sons.

[4] Eroglu, A.; Goulding, R.; Ryan, P.; Caughman, J.; and Rasmussen, D. (2010). Novel broadband multilayer microstrip directional coupler. Proceedings of the Antennas and Propagation Society International Symposium. Toronto, Canada, 1-

[5] Pennock, S.R.; and Shepherd, P.R. (1998). Microwave Engineering with Wireless Applications (1st ed.). McGraw-Hill Professional.

Design and Analysis of Hairpin Bandpass Filter

Ahmed Babić and Adin Poljak
Department of Electrical Engineering
International University of Sarajevo
Sarajevo, Bosnia and Herzegovina
babicahmed@outlook.com
poljak.018@hotmail.com

Elmedin Skopljak
Department of Electrical Engineering
International University of Sarajevo
Sarajevo, Bosnia and Herzegovina
elmedinskopljak@hotmail.com

Abstract **- In this paper, design, simulation and analysis of hairpin bandpass filter is shown. Hairpin coupled line bandpass filters are compact structures they may conceptually be obtained by folding the resonator of parallel-coupled half wave length resonator. This type of U shape resonator is so called hairpin resonator. However, to fold the resonators it is necessary to take into account the reduction of the coupled-line lengths, which reduces the coupling between the resonators. The proposed frequency was 1.6-2.5GHz and 3.5-4.4GHz. Through the design and simulation, we have achieved frequency band from 1.72-2.62GHz and 3.66-3.90GHz.**

Keywords – filter, hairpin, bandpass filter, microwave, microstrip

I. INTRODUCTION

The hairpin filter is a classic design example of a minimized micro strip filter. It is used in modern wireless technology.[1] Important parameters include cutoff frequency, insertion loss, out of the band attenuation rate measured in dB per decade of the frequency. Hairpin filter is the most popular and widely used configuration in micro strip Bandpass filters due to their compact design and need no ground structure. The recent advance in materials and fabrications technologies, including High temperature super conductor (HTS), Low temperature co fired ceramic (LTCC), Monolithic microwave integrated circuit (MMIC), Micro electro mechanism system (MEMS) and micro machine technology have stimulated the rapid development of new micro strip and other filters for RF/ micro wave application. [2] The basic structure of Microstrip line consists of a conductive strip separated from ground plane by dielectric.[3] The line between two bends tends to shorten the physical lengths of the coupling sections, and the coupled section is slightly less than a quarter of wavelengths. [4] Brief specifications of the designed filter are:

* Dielectric constant Ɛr = 3.78 (Quartz-fused)
* Substrate thickness = 456 mils (air) 63mils (dielectric),
* Frequency range of 1.72-2.62GHz and 3.66-3.9GHz.
* The filter box space is 40 mm x 31.8 mm
* Cell size is 0.1x0.1mm

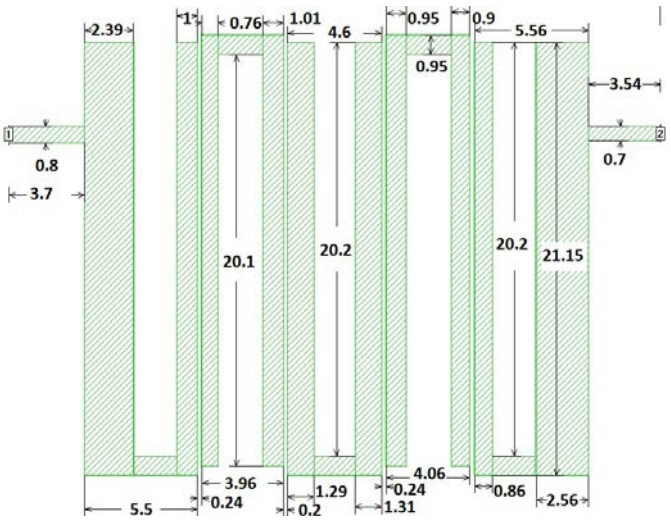

Fig. 1. Top view of hairpin bandpass filter

II. SIMULATION AND OUTPUT DATA

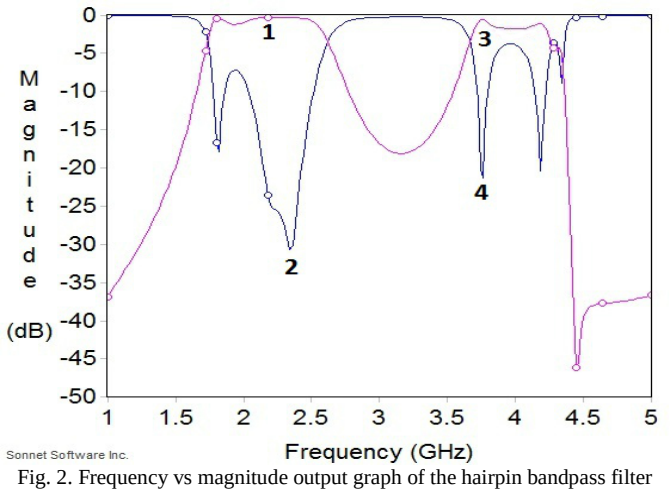

Fig. 2. Frequency vs magnitude output graph of the hairpin bandpass filter

Fig. 1 shows the simulation carried out in Sonnet Suites [5]. As it is shown on the graph, this filter passes frequencies between 1.72-2.62GHz and 3.66-3.9GHz. These values are satisfying our expectations which were 1.6-2.5GHz and 3.5-4GHz.

III. PARAMETRIC STUDIES AND VARIATIONS

On the hairpin line bandpass filter, physical properties and parameters were changed, and output is observed during the changes. Parameters that were changed in this case were metal type, thickness of metal, dielectric material, thickness of dielectric.

A. Changing metal type

TABLE I. S-PARAMETERS WHEN METAL IS CHANGED

Metal type	S11(dB) at 2	S12(dB) at 1	S11(dB) at 4	S12(dB) at 3
Copper	-24.8109	-0.3151	-15.9883	-0.9998
Gold	-30.6190	-0.3703	-20.6697	-0.8598
Aluminum	-30.5792	-0.3861	-20.7983	-0.7226
Brass	-29.9973	-0.5815	-21.5380	-0.7920

In this table frequencies observed are shown while metal type is changed. In all cases thickness of metal which is used is 1.4mm. Dielectric material is Quartz and its thickness is 1.6mm. By obtaining results of filter's metal type change, it is proposed that there is no significant change. All results are similar and acceptable, but Copper is the best one.

B. Changing thickness of metal

TABLE II. S-PARAMETERS WHEN THICKNESS OF METAL IS CHANGED

Thickness of metal	S11(dB) at 2	S12(dB) at 1	S11(dB) at 4	S12(dB) at 3
0.6	-24.8109	-0.3151	-15.9883	-0.9998
1.0	-24.8109	-0.3151	-15.9883	-0.9998
1.4	-24.8109	-0.3151	-15.9883	-0.9998
1.8	-24.8109	-0.3151	-15.9883	-0.9998
8.0	-24.8109	-0.3151	-15.9883	-0.9998

While observing the results, it was obvious that the best output was while copper was used. In this case metal type was not changed, but thickness of it was gradually changed by 0.4. There was no change in the output while thickness was changed by small amount, neither when thickness was changed for bigger amount.

C. Changing dielectric material

TABLE III. S-PARAMETERS WHEN DIELECTRIC MATERIAL IS CHANGED

Dielectric material	S11(dB) at 2	S12(dB) at 1	S11(dB) at 4	S12(dB) at 3
FR-4	-34.8836 1.8GHz to 2.4GHz	-2.0922 1.8GHz to 2.4GHz	-8.3585 3.6GHz to 3.8GHz	-4.3256 3.6GHz to 3.8GHz
Alumina 96%	-30.5293 1.2GHz to 1.6GHz	-0.4926 1.2GHz to 1.6GHz	-12.6382 2.4GHz to 2.8GHz	-0.7512 2.4GHz to 2.8GHz
Quartz (fused)	-24.8109 1.72GHz to 2.62GHz	-0.3151 1.72GHz to 2.62GHz	-15.9883 3.66GHz to 4.3GHz	-0.9998 3.66GHz to 4.3GHz

In this case, type of dielectric material is changed. Thickness of dielectric(1.6) and metal type(Copper) remained the same by default. Results which are obtained are interesting. All results are different and also range of frequencies are also different. It is obvious that the best result is the 3rd one in which Quartz as dielectric material is used.

D. Changing thickness of dielectric

TABLE IV. S-PARAMETERS WHEN THICKNESS OF DIELECTRIC IS CHANGED

Thickness of dielectric	S11(dB) at 2	S12(dB) at 1	S11(dB) at 4	S12(dB) at 3
1.6	-24.8109	-0.3151	-15.9883	-0.9998
1	-38.9247	-0.4452	-29.7267	-0.7902
0.4	-17.2663	-1.4290	-15.6353	-1.7397

Thickness of dielectric plays a huge role in designing filter. All obtained results are satisfied but still much different from each other. Optimum result is while 1.6 thickness is used.

E. Changing thickness of input

TABLE V. S-PARAMETERS WHEN THICKNESS OF INPUT IS CHANGED

Thickness of input	S11(dB) at 2	S12(dB) at 1	S11(dB) at 4	S12(dB) at 3
0.8	-24.81096	-0.31513	-15.9883	-0.9998
1.6	-11.47968	-1.66240	-15.6412	-1.5999
2.4	-8.83901	-2.03170	-16.2098	-1.5850

The final variation of parameters which is done is when thickness of input is changed. The best result gained was the first one, when thickness is 0.8mm.

IV. CONCLUSION

Full dimensions and layout of the filter is shown in the Figure 1. The best result of all simulations which are done during the design of the filter are represented in Figure 2. The proposed frequency was 1.6-2.5GHz and 3.5-4.4GHz. We have successfully achieved frequency band from 1.72-2.62GHz and 3.66-3.9GHz. Parameters which are changed during design of the filter are shown in the third part of the paper. Analyzing parameters and the results of simulations, deviations in length and bandwidth can be observed.

V. REFERENCES

[1] R. Ahmed, S.Emiri, Ş. Taha İmeci "Design and Analysis of a Bandpass Hairpin Filter"

[2] L. Singh, P.K. Singhal "Design and Analysis of Hairpin Line Bandpass Filter" IJARECE Volume 2, Issue 2, February 2013

[3] S.A.Vijaya Lakshmi, P.Muthukumaran "Design and Implementation of Hairpin Bandpass Filter Using Defected Microstrip Structures (DMS)." March 2016

[4] Jia-Sheng Hong, "Microstrip Filter For RF/Microwave Application", John Willey and Sons, Inc, Second edition, pp. 129– 133, 2001

[5] Sonnet Suites, ver. 16, Sonnet Software Inc., North Syracuse

Comparing the Estimates of SP500 Option Price by ANN and selective Black-Scholes

Sadi Fadda, Mahmet Can

Faculty of Business and Administration

Faculty of Engineering

International University of Sarajevo

Hrasnicka Cesta Ilidža, Sarajevo BiH 71210

sadifadda@gmail.com

mcan@ius.edu.ba

Abstract— **The Artificial Neural Networks (ANN) are used since the 1990s in the financial sector, in estimating both the volatility and the price of various financial instruments. Similar is the case for studying financial derivatives. The most popular parametric formula (B-S) used in pricing the European-style options is that of Black-Scholes (1973). The prediction power of (B-S) strongly rely on the accuracy of provided expected change measures of risk free interest rate and market volatility. This paper compares outcomes of better of the two B-S estimates, first uses the measure of impliwd volatility (IV) and second of GJR (1,1), with the ANNs outcome.**

***Keywords*— Options, pricing, volatility, ANN, Black-Scholes.**

I. INTRODUCTION

Developed through decades, starting from the dissertation by Bachelier [1], followed by [2], [3], [4], and [5], the Black-Scholes (1973) formula is considered the main progress which caused huge expansion in market options trade.

Ever since, the B-S [6] formula and its variations are used to parametrically price European-style options. The formula includes five parameters, spot price, *S*, strike price, *K*, time to maturity, *T*, risk free rate, *r*, and price volatility σ. For calls "c" or puts "p", their price formulas are

$$c = S\,N(d_1) - Ke^{-rT}\,N(d_2), \quad (1)$$

and

$$p = Ke^{-rT}\,N(-d_2) - SN(-d_1) \quad (2)$$

Where

$$d_1 = \frac{\ln(S/K)+(r+\sigma^2/2)T}{\sigma\sqrt{T}}, \quad (3)$$

and

$$d_2 = d_1 - \sigma\sqrt{T}. \quad (4)$$

In (1) and (2), N(x) is the standard normal distribution function. $N(d_2)$ measures the likelihood of exercising the option. N(d1) measures how much the present value of the asset exceeds its current market price [7].

Volatility estimation is a well-researched topic, and includes various parametric groups: historical, implied, stochastic, ARCH. Works of [8] and [9] argue that GJR outperforms other ARCH models when estimating volatility for stock indexes.

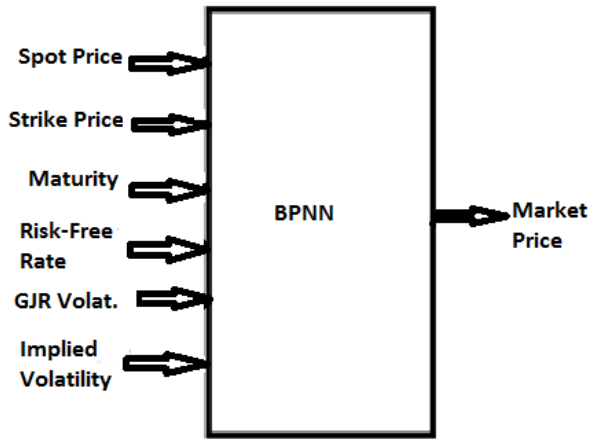

FIGURE I: INPUT/OUTPUT OF BPNN USED TO PRICE OPTIONS

In this article, ANN has two volatility inputs, the implied volatility provided by WRDS and the calculated GJR conditional volatility. While the implied volatility measure is available individually for every option, GJR is a daily estimate assigned to all the options of the day, irrespective of time to maturity. On the other hand, the B-S is calculated twice per group, once with the GJR volatility estimate followed by the I.V. provided. Selected is the B-S calculation with lower error measure of mean absolute percentage error (MAPE).

II. MATERIALS AND METHODS

The data analysed in this article is S&P 500 Index European Style call options also known as SPX calls. This study includes 59,662 call options throughout the year of 2010.

The choice of the artificial neural network was similarly made by [10], [11], [12], and [13], who applied it in option pricing using the backpropagation neural networks.

The set was divided into twenty groups, through five categories based on the measure moneyness (S/K) and four categories based on time to maturity. Trained are the neural networks for each of these groups. Tested are these groups and compared to B-S error outcomes. Tables 1,2 and 3, compare error measure of the two estimates, for randomly selected options from three of these groups. Shown as bold are the lower error estimates.

TABLE I: ESTIMATES BY B-S AND ANN FOR RANDOMLY SELECTED IN-THE-MONEY SHORT-TERM CALLS

	ANN			Black-Scholes		
Market Price	Price Est.	Error in $	MAPE	Price Est.	Error in $	MAPE
274.8	273.8	-0.96	0.0035	275.7	**0.90**	0.0033
207.9	209.5	**1.6**	0.0079	209.6	1.71	0.0082
275.8	254.2	-21.5	0.0782	278.5	**2.74**	0.0099
242.7	249.3	6.6	0.0272	244.7	**2.04**	0.0084
240.7	247.9	7.2	0.0301	243.3	**2.55**	0.0106
236	218.3	-17.7	0.0750	238.8	**2.77**	0.0118
322.8	326.5	3.7	0.0116	324.4	**1.59**	0.0049
241.5	243.9	2.4	0.0099	242.5	**1.02**	0.0042
240.2	242.7	2.5	0.0102	241.7	**1.52**	0.0063
311.5	293.5	-18.0	0.0577	312.7	**1.21**	0.0039

TABLE II: ESTIMATES BY B-S AND ANN FOR RANDOMLY SELECTED IN-THE-MONEY VERY-LONG-TERM CALLS

	ANN			Black-Scholes		
Market Price	Price Est.	Error in $	MAPE	Price Est.	Error in $	MAPE
356.2	350.8	**-5.4**	0.0152	401.4	45.2	0.1270
307.6	310.5	**2.9**	0.0093	313.1	5.5	0.0179
261.8	262.3	**0.5**	0.0020	262.6	0.8	0.0032
227	225.4	**-1.6**	0.0069	257.3	30.3	0.1336
269.2	252.3	-16.8	0.0626	277.2	**7.9**	0.0296
445.2	448.9	**3.7**	0.0083	473.8	28.6	0.0643
237.3	235.9	**-1.4**	0.0057	231.7	-5.6	0.0234
301.5	291.3	**-10.2**	0.0337	319.3	17.8	0.0589
284.5	287.2	**2.7**	0.0096	342.6	58.1	0.2041
428.9	436.7	7.8	0.0181	434.9	**6.0**	0.0140

TABLE III: ESTIMATES BY B-S AND ANN FOR RANDOMLY SELECTED OUT-OF-MONEY LONG-TERM CALLS

	ANN			Black-Scholes		
Market Price	Price Est.	Error in $	MAPE	Price Est.	Error in $	MAPE
37.7	39.6	**1.9**	0.0517	34.9	-2.8	0.0738
46.9	46.7	**-0.2**	0.0038	48.9	2.0	0.0424
23.9	22.7	**-1.2**	0.0511	30.4	6.5	0.2707
41.4	43.4	**2.0**	0.0482	37.4	-4.0	0.0978
56.1	54.1	**-2.0**	0.0349	64.0	7.9	0.1409
27.5	27.1	**-0.4**	0.0153	24.4	-3.1	0.1116
35	36.2	**1.2**	0.0344	43.7	8.7	0.2491
48.3	43.9	**-4.4**	0.0903	57.9	9.6	0.1987
21.6	22.7	**1.1**	0.0518	18.9	-2.7	0.1256
27.5	26.3	**-1.2**	0.0439	34.9	7.4	0.2704

3. CONCLUSIONS

While the ANN outperforms the parametric method of B-S as a whole, the weakness is identified in the short-term options. While the B-S calculation with the two volatility measures shows significant difference, both show much better performance versus ANN for the short-term option groups. In that sense, short-term options groups should either exclude time dependent input variables of volatility and risk-free rate, or they be multiplied by the time as a single input. In the meantime, ANNs will be avoided for short-term options.

REFERENCES

[1] Bachelier, L., 1900. *Théorie de la spéculation*. Gauthier-Villars.

[2] Kendall, M.G. and Hill, A.B., 1953. The analysis of economic time-series-part i: Prices. *Journal of the Royal Statistical Society. Series A (General)*, *116*(1), pp.11-34.

[3] Osborne, M.F., 1959. Brownian motion in the stock market. *Operations research*, *7*(2), pp.145-173.

[4] Boness, A.J., 1964. Elements of a theory of stock-option value. *Journal of Political Economy*, *72*(2), pp.163-175.

[5] Samuelson, P.A., 1965. Rational theory of warrant pricing. *IMR; Industrial Management Review (pre-1986)*, *6*(2), p.13.

[6] Black, F. and Scholes, M., 1973. The pricing of options and corporate liabilities. *Journal of political economy*, *81*(3), pp.637-654.

[7] Nielsen, L.T., 1992. *Understanding N (d1) and N (d2): Risk-adjusted probabilities in the Black-Scholes model*. INSEAD.

[8] Brailsford, T. J., & Faff, R. W. (1996). An evaluation of volatility forecasting techniques. *Journal of Banking & Finance*, *20*(3), 419-438.

[9] Taylor, J.W., 2004. Volatility forecasting with smooth transition exponential smoothing. *International Journal of Forecasting*, *20*(2), pp.273-286.

[10] Chang, T.Y., Wang, Y.H. and Yeh, H.Y., 2013. Forecasting of Option Prices Using a Neural Network Model. *Journal of Accounting, Finance & Management Strategy*, *8*(1), p.123.

[11] Lin, C.T. and Yeh, H.Y., 2009. Empirical of the Taiwan stock index option price forecasting model–applied artificial neural network. *Applied Economics*, *41*(15), pp.1965-1972.

[12] Wang, Y.H., 2009. Nonlinear neural network forecasting model for stock index option price: Hybrid GJR–GARCH approach. *Expert Systems with Applications*, *36*(1), pp.564-570.

[13] Wang, Y.H., 2009. Using neural network to forecast stock index option price: a new hybrid GARCH approach. *Quality & Quantity*, *43*(5), pp.833-843.

Class Level Code Smell Detection using Machine Learning Methods

Rialda Spahić
Faculty of Engineering and Natural Sciences,
International University of Sarajevo
Sarajevo, Bosnia and Herzegovina
rialda.spahic@gmail.com

Kanita Karađuzović-Hadžiabdić
Faculty of Engineering and Natural Sciences,
International University of Sarajevo
Sarajevo, Bosnia and Herzegovina
kanita@ius.edu.ba

***Abstract*— Code smells are indicators of bad design choices but not necessarily proven to be bad practices. Several commercial tools exist for detecting code smells, yet there are arguments on how the code smell detection is a matter of subjective interpretation. This paper examines different code practice features to be used in machine learning methods in order to select features that achieve the best results for detecting the most common code smells at the class level. The results show that by selecting relevant features, machine learning methods are able to detect code smells with high accuracy. The proposed selected features may be used in practice in order to help developers to produce better quality software.**

Keywords—code smells, machine learning, feature selection

I. INTRODUCTION

Design Patterns are validated solutions to recurring design problems in software development. Use of the patterns impacts defect proneness, maintainability and reliability of software systems. Detecting code smells and raising the awareness of bad practices are preventive mechanisms for destructive systems. Therefore, detection of bad coding practices may aid in development of software with higher quality. Code smells are signals of bad coding and design practices. They are closely related to object-oriented principles. This paper examines the most relevant features in generating common code smells. The paper focuses on two class level code smells, *Data Class* and *God Class*. *Data Class* is a class that only consists of *get* and *set* properties, the class does not process data, it rather contains access to the system's data. *God Class* is a class that centralizes the software system. This class is generally very complex, has too much of code that can be divided into other classes, uses big amounts of data that are imported from other classes and implements different functionalities.

This work aims to detect code smells by applying machine learning methods. It is a follow up of the work performed by Fontana et al. [1,2,3]. In [1,2,3] , Fontana et al. evaluate two class level code smells (God Class and Data Class with 66 features) and two method level code smells (Feature Envy and Long Method with 88 features) by using six machine learning methods, or the boosted version of the same methods. In this work we perform classification on class level, for Data and God class code smells. The main contribution of this work is to reduce the feature set used by Fontana et al. and select only the most relevant features used to detect class level code smells. Selected features may then help developers to focus on best coding practices to enhance the quality of developed software. In order to determine whether a particular software contains smelly code, lower feature number that needs to be extracted would considerably speed up the task and at the same time it could motivate the programmers to test the presence of smelly code using machine learning approach.

II. RELATED WORK

Only a few works have been performed on code smell detection using machine learning methods. Until recently, commercial tools for code smell detection and analysis such as Borland Together [4] and JDeodorant [5] were used instead of machine learning methods. In [1], Fontana et al. perform code smell detection using binary classification, (whether or not a code smell exists). Results that they obtained using binary classification are listed in Table 2. In their follow up work [2, 3], authors perform severity analysis where they classify code smell into four categories (no smell, non-severe smell, smell and severe smell) by using six machine learning methods.

III. DATASET

The dataset used for this work was obtained from [1]. The dataset contains 1,986 validated code smells obtained from 76 software systems of Qualitas Corpus that is composed of Java systems categorized into four subsets, a set for each of the four analyzed code smells, i.e. God Class and Data Class code smells for class level and Feature Envy and Long Method code smells for method level. In this work we perform the analysis of *class level* code smells and thus use the available dataset for God and Data class. Each set contains 420 instances, out of which 140 are positive and 280 negative instances. An important issue in classification is the selection of features. We extend the work for Fontana et al. [1,2,3] and reduce the number of features used to detect code smell by using the best attribute selection. Just like in [1], in this work we perform binary classification of code smells, rather than classification based on code smell severity. As already mentioned, the work of Fontana et al. contains 66 features for Data Class and God Class code smells. By experiment, we reduce this number to only 9 features for Data Class and 15 features for God Class code smells. Selected feature set is summarized in Table 1.

IV. METHODOLOGY

For comparison purposes, in this work, we use the same 6 machine learning methods as used in the work of Fontana et al. [1]: J48, JRip, Naïve Bayes (NB), Random Forest (RF), Sequential Minimal Optimization (SMO) and LibSVM. All the work was performed using Weka [6].

V. RESULTS

Table 2 presents the obtained results for each tested code smell using the proposed reduced feature set, including the results obtained by Fontana et al. [1]. Bolded results show the methods that produce the best accuracy results from the tested machine learning methods. For Data Class, *Random Forest* machine learning method achieves the best results, 98.57%. The best results for God Class are achieved by using the *JRip* method, 97.86%. The results show that the proposed feature set produces better results than those obtained by Fontana et al. [1] for the class level code smells.

VI. CONCLUSION

In this paper we extend the work of [1] to reduce the number of features used in code smell detection at the class level. Identified reduced feature set may be used to determine what coding practices are most likely to produce code smells in a software system. One of the future works is to expand the performed analysis and identify the reduced feature set for code smell detection at the method level as well.

REFERENCES

[1] F. A. Fontana, M. Zanoni and A. Marino, "Code Smell Detection: Towards a Machine Learning-based Approach," *2013 IEEE International Conference on Software Maintenance*, pp. 396-399, 2013.

[2] F. A. Fontana, M. V. Mäntylä, M. Zanoni and A. Marino, "Comparing and experimenting machine learning techniques for code smell detection," *Empirical Software Engineering*, vol. 21, no. 3, pp. 1149-1191, 2016.

[3] F. A. Fontana and M. Zanoni, "Code smell severity classification using machine learning techniques," *Elsevier*, vol. 128, pp. 43-58, 2017.

[4] Micro Focus, "Together," Micro Focus, 2016. [Online]. Available: https://www.microfocus.com/products/requirements-management/together/.

[5] Eclipse, "JDeodorant | Eclipse Plugins," Eclipse Foundation Inc., 17 March 2018. [Online]. Available: https://marketplace.eclipse.org/content/jdeodorant.

[6] Weka, "Weka 3: Data Mining Software in Java", Weka The University of Waikato, 2018. [Online]. Available: https://www.cs.waikato.ac.nz/ml/weka/.

TABLE 1. SELECTED FEATURES FOR CLASS LEVEL CODE SMELLS

Data Class	***God Class***
No. of Accessor Methods	No. of Classes
No. of Attributes	No. of Methods Overridden
No. of Inherited Methods	Access to Foreign Data
Response for a Class (RFC)	Lines of Code
No. of Children	Lines of Code Without Accessor or Mutator Methods
Weight of Class	Called Foreign Not Accessor or Mutator Methods
Weight Methods Count of Not Accessor or Mutator Methods	Tight Class Cohesion
No. of Packages	Response for a Class
No. of Private Methods	Weight Methods Count
	Weight Methods Count of Not Accessor or Mutator Methods
	No. of Interfaces
	No. of Protected Attributes
	No. of Attributes with Package Visibility
	No. of Final, Non-Static Attributes
	No. of Standardly Designed Methods

TABLE 2. PERFORMANCE RESULTS

Machine Learning Method		**Code Smell**	
		Data Class	**God Class**
J48	Fontana et al. [1]	97.6	96.4
	Proposed Features	98.33	97.38
JRip	Fontana et al. [1]	96.6	97.3
	Proposed Features	97.14	**97.86**
Naïve Bayes	Fontana et al. [1]	81.9	95.4
	Proposed Features	83.81	95.95
Random Forest	Fontana et al. [1]	97.8	97.3
	Proposed Features	**98.57**	97.38
SMO	Fontana et al. [1]	96.9	96.4
	Proposed Features	88.57	96.90
LibSVM	Fontana et al. [1]	94.7	76.6
	Proposed Features	82.14	66.67

Coupled-line Bandpass Microstrip Filter

Nermin Sejdić, Zemir Drinjak, Haris Pašić
Department of Electrical Engineering
International University of Sarajevo
Sarajevo, Bosnia and Herzegovina
nermin.sejdic@hotmail.com
zemir.drinjak@gmail.com
harispasic@ymail.com

***Abstract* – In this project we proposed Coupled-line Bandpass Microstrip Filter with its projection, design, simulations and final analysis. This filter is implemented using a multiple-mode resonator (MMR) and transmitting signals in whole CBMF filter from 5.8 – 7.3 GHz. Parallel coupled lines are stretched in order to raise frequency-dispersive coupling degree. After many simulations, ideal CBMF filter is achieved.**

***Keywords* - Multiple-mode resonator (MMR), Coupled-line Bandpass Microstrip Filter (CBMF), Bandpass filter (BPFs);**

I. INTRODUCTION

Ultra-wideband (UWB) technology has attracted considerable interests for short-range large capacity wireless communication systems and sensor networks due to many advantages, such as high data-rate, huge bandwidth, low power consumption, low spectral density, and immunity to multipath fading [1]. In particular, for the design of wide bandpass filters, different solutions have been proposed to solve the ultra-wideband bandpass filter and new wireless communications requirements [2], [3]. Main challenge of using this type of technology is that we need to control undesired interferences. In order to have filter that successfully operates, large bandwidth is required. For CBMF, the fractional bandwidth of BPFs usually exceeds 100%. Based on the traditional parallel-coupled line structure, very strong coupling structure will be a must for such a wide bandwidth. Tolerance of a micro strip fabrication process, however, imposes an upper limit upon coupling levels for coupling structures. For increasing the coupling special arrangement such as three-line structure [4] can be incorporated into the filter structure for wideband design. Bandwidths of the filters presented in [4], are still no more than 70%. In [5], a wideband passband of 49.3% was achieved in terms of two stopbands of a filter block with the two tuning stubs on a ring resonator. However, this filter configuration was found theoretically difficult to be directly employed for the design. It was initially exhibited, that the first two resonant modes of the constituted MMR could be utilized together with the input/output parallel-coupled lines to achieve a 70% wide passband. The coupling degree of the input and output parallel coupled line sections is largely raised. Later on, all the predicted parameters, losses are experimentally verified in a wide frequency.

II. CBMF (COUPLED-LINE BANDPASS MICROSTRIP FILTER)

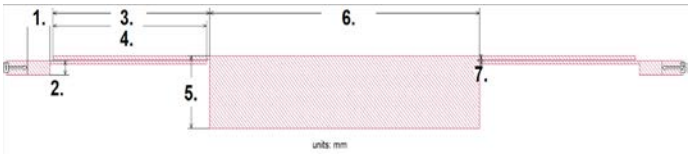

Figure 1. – Top view of CBMF

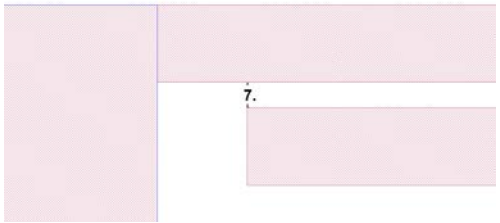

Figure 2. – Zoom in - Spacing measurement (no. 7)

TABLE I. FILTER MEASUREMENTS

Each number in Figure 1. ("Top view of CBMF") is showing its values in tale below.

Name	No.	Length	No.	Width
Box 1.	1.	0.5 mm	2.	0.25 mm
Coupled lines	3.	3.4 mm	4.	0.04 mm
Box 2.	5.	5.98 mm	6.	1.235 mm
Spacing			7.	0.02 mm

TABLE II. FILTER PARAMETERS

Parameters	Values
Dielectric thickness (Ɛr)	1.00
Cell size	0.01 mm
Box size	15x10 mm
Frequency	4.1 – 9.5 GHz

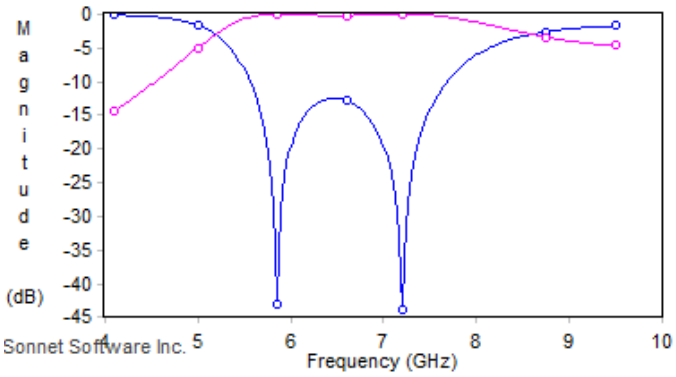

Figure 3. – Frequency vs magnitude output graph

III. PARAMETRIC STUDIES

In this table below, we checked how the frequencies are changing while we change and try different dielectric and air thicknesses. We observe S11 and S12 to make it ideal as possible.

TABLE III. CHANGING OF DIELECTRIC THICKNESSES AND AIR SPACE

Dielectric Thickness / Air (mm)	S11 (dB)	S12(dB)
0.4 / 2.0	7.38 GHz / -14.068057	7.4 GHz / -0.1596500
1.0 / 5.0	6.46 GHz / -12.519357	7.2 GHz / $-1.8676e^{-4}$
1.2 / 5.0	6.36 GHz / -10.155949	5.66 GHz / $-1.8646e^{-4}$
1.4 / 6.0	6.26 GHz / -8.5316479	7.2 GHz / $-3.7947e^{-5}$
1.6 / 6.0	6.18 GHz / -7.5196339	7.18 GHz / $-1.1422e^{-4}$

Table IV is representing how data is drastically different while changing specifications of filter. These calculations are made upon ideal dimensions shown in Figure 1. To be precise we had changed spacing (SP) and width (W) of filter measured in units of mm. Fig. 2 plot is showing simulation of S11 and S12 frequencies in wide range from (5.8 GHz – 7.3 GHz).

TABLE IV. CHANGING SPACING (SP) AND CENTER BOX WIDTH (W)

Spacing (SP) / Width (W)	S11(dB)	S12(dB)
0.02 / 0.415	6.48 GHz / -5.0162249	7.96 GHz / $-6.5440e^{-5}$
0.04 / 1.345	6.92 GHz / -11.847557	7.64 GHz / $-1.3612e^{-3}$
0.06 / 0.715	7.2 GHz / -5.7317447	6.3 GHz / $-1.8414e^{-3}$
0.06 / 1.595	7.22 GHz / -12.715234	7.88 GHz / $-1.6604e^{-3}$

Data set below is showing how the variables are depending on each other. Changeable variables are: spacing (SP), width (W), dielectric thicknesses and air space. We found these parameters most important factors in project. With slightly changes, measurements and outputs of filter are varying. Last column is representing ideal and our final Ultra–Wideband Bandpass filter. S11 has to be bellow -10dB while S12 should be close to -1dB. Closer it is, we get cleaner passing limit without disturbances. After many simulations and tries, we had found most suitable and ideal CBMF (filter).

TABLE V. CHANGING: SPACING (SP), WIDTH (W), DIELECTRIC THICKNESS, AIR SPACE

Spacing (SP) / Width (W)	Dielectric Thickness / Air	S11(dB)	S12(dB)
0.04 / 1.042	1.4 / 6.0	6.68 GHz / -6.52281	7.72 GHz / -0.01201
0.05 / 1.165	1.2 / 6.0	6.96 GHz / -7.74077	7.96 GHz / $-6.447e^{-4}$
0.03 / 1.315	0.8 / 5.0	6.9 GHz / -16.8775	7.44 GHz / $-1.718e^{-4}$
0.02 / 1.235	**1.0 / 5.0**	**5.8 GHz / -12.5092**	**7.3 GHz / $-1.879e^{-4}$**

IV. CONCLUSION

In this project a novel Coupled-line Bandpass Microstrip Filter is proposed with its scheme and outputs. The main characteristic of this design is to find as good as possible filter in order to obtain ideal response and to meet nowadays requirements with wireless communication technologies [4], [5]. After numerous analysis and tries, we had approached to the frequency outputs that meets our recquirements. There are many factors that may influence your design and outputs. Some of those are spacing between streached-coupled lines and width of central box. The range of dielectric thickness that we sticked to it is from (0.4 – 1.6 mm), because of manufacturing limit. We had followed rules of S11 frequency, not to exceed frequency passing limit of -10(db). This project had acknowledged us in many ways of engineering life.

V. REFERENCES

[1] 1. D. Porcine, P. Research, and W. Hirt, "Ultra-wideband radio technology: Potential and challenges ahead," IEEE Commun. Mag. 41, 66-74(2003).

[2] J.-T. Kuo and E. Shih, "Wideband bandpass filter design with three-line micro strip structures," in Proc. 2001 IEEE MTT-S Int. Microwave Symp.Dig.,pp.1593-1596.

[3] Saito, H. Harada, and A. Nishikata, "Development of band pass filter for ultra-wideband (UWB) communication," in *Proc. IEEE Conf. Ultra-Wideband Systems Technology*, 2003, pp. 76–80.

[4] H. Wang, L. Zhu and W. Menzel, "Ultra-Wideband Bandpass Filter with Hybrid Micro strip/CPW Structure," IEEE Microwave and Wireless Components Letters, vol. 15, pp. 844-846, December 2005

[5] L. Zhu, H. Bu, and K. Wu, "Aperture compensation technique for innovative design of ultra-broadband micro strip bandpass filter," in *IEEE MTT-S Int. Dig.*, vol. 1, 2000, pp. 315–318

Application of Machine Learning Techniques for the Prediction of Financial Market Direction on BIST 100 Index

Afan HASAN*, Oya Kalıpsız*, Selim Akyokuş†
*Computer Engineering Department, Yildiz Technical University, Istanbul, Turkey
{ahasan, okalipsiz}@yildiz.edu.tr
†Computer Engineering Department, Doğuş University, Istanbul, Turkey
{sakyokus}@dogus.edu.tr

***Abstract*—Because of the highly nonlinear nature of the financial time series, prediction of financial market direction accurately is very challenging task. Even small improvements in forecasting performance can provide tremendous profits. In this study, a set of sixty-four technical indicators has been examined based on their application in technical analysis as input feature to predict the oncoming (one-period-ahead) direction of BIST 100 national index. For predicting the direction of movement in Borsa Istanbul (BIST) National 100 Index (BIST100), Support vector machine (SVM), Random Forest (RF) and Linear Regression (LR) classification techniques are used for classification and performance of these models is evaluated on the basis of various performance metrics such as testing accuracy, precision, recall and F1score. To improve prediction accuracy we propose a new set of input variables for machine learning models. The result of this study shows that the prediction of the next period's direction with machine learning classification techniques provides a promising method for financial market forecasting.**

Index Terms*—*Financial market direction prediction*; *BIST100*; *Machine Learning*; *Finance*; *Time Series Classification.

I. Introduction

The financial market prediction has always been a topic of great interest, and it seems that it will continue to be an attractive research subject as long as there is profitability on predicting future movement. The attractiveness of the stock market prediction is that it offers great potential for investor to make huge profits in a short time. While offering the potential to generate huge profits, it can also cause huge losses at the same time. Like a double-sided sword, it is very profitable when used correctly and can be very harmful when used incorrectly. But people generally focus on the lucrative side and ignore the harmful side.

There are two analytical methods commonly used in the literature for estimating future stock price or direction [1]. The first method is a technical analysis based on the past prices of stocks. By examining the hourly, daily, monthly and yearly historical prices of the stock, the future stock price or stock direction is estimated. This approach uses Time Series Analysis techniques and the timing of the process is very important [2]. The second method is the fundamental analysis, which examines important numeric values about the structure of the economy and companies. When fundamental analysis is used, an attempt is made to make an estimation using characteristics such as interest rates, inflation, percentage of unemployment and economic growth [3].

TABLE I
BIST 100 HOURLY DATA STRUCTURE

Date	Open	High	Low	Close	Volume
2008010209	55160.2	55171.04	54889.51	54951.62	180514
2008010210	54891.5	55281.66	54821.49	54854.45	132182
2008010211	54853.8	54951.23	54481.52	54638.57	76451
2008010212	54527.59	54527.59	54527.59	54527.59	25427
2008010214	54741.95	54939.83	54584.49	54618.13	136968

In this study, we focused on technical analysis method and predictions are made based on past prices of BIST 100 index. The index direction was estimated by using technical indicators as input vectors. The machine learning techniques SVM, Random Forest and Logistic Regression are used to construct prediction models. These models are used to classify index data and predict the direction of BIST 100 index.

II. Dataset Description and Prepraretion of Features

In this study, nine years BIST 100 index data from Jan 2008 to Dec 2016 is obtained from Borsa Istanbul. We used open, high, low, close price and volume of index data within daily, hourly and 30 min periods. Daily, hourly and 30 min datasets are composed of 2093, 18314 and 33673 rows respectively. An example of Hourly dataset is shown in Table 1. Eighty percent of dataset, which forms in-sample period, is used for training and twenty percent of dataset, which is considered as out-of-sample period, is used for evaluating forecasting performance.

When publications about stock predictions are reviewed, it can be seen that technical indicators used in technical analysis

TABLE II
SELECTED TECHNICAL INDICATORS

Name	Description
OP	Open price
HI	High price
LO	Low price
CL	Closing price
ROC(x)	Price rate of change
ROCP(x)	Rate of change percentage
%K	Stochastic %K
%D	%D is the moving average of %K
BIAS	x-days bias
MA(x)	x-days moving average
EMA(x)	x-days exponential moving average
MOM(x)	MOM(x) Momentum
MACD(x, y)	x days moving average convergence and divergence
TEMA(x)	Triple exponential moving average
PPO(x, y)	Percentage price oscillator
CCI(x)	Commodity channel index
WILLR(x)	Larry William's %R
RSI(x)	Relative strength index
ULTOSC(x, y, z)	Ultimate oscillator
RSI(x)	Relative strength index
RDP(x)	Relative difference in percentage
ATR(x)	Average true range
MEDPRICE(x)	Median price
MIDPRICE(x)	Medium price
SignalLine(x, y)	A signal line is also known as a trigger line
HH(x)	x days Highest price
LL(x)	x days Lowest price

are generally utilized to generate feature sets of prediction models [4].

Technical indicators are mathematical calculation methods used to analyze the prices of financial instruments. After some specific calculations on time series data, the most of indicators help investors to forecast price movement trends in future. Some indicators, on the other hand, try to show whether a trend will continue or not. Indicators are calculated for a specific moment and period to direct the investors.

There are literally hundreds of technical indicators that can be used for forecasting. Some of these indicators extract similar information and produces similar signals. The selection of the right and diverse set of indicators is important so that a diverse set of measures/indicators can be used as features in the formation of prediction models. The names and descriptions of the selected technical indicators used in the study are given in Table 2. Similar abbreviations have been used for the definition of indicators in Kumar [5] and Gündüz [6] studies. The same naming conventions are used in this study.

After the selection of the technical indicators, we have to determine time periods and the type of price data to be used to calculate these indicators. For example, the SMA, EMA, ROCP, and MOM indicators were calculated using the closing price of the BIST 100 index and on 3, 5, 10, 15, and 30 previous values of time series on daily / hourly / 30 minute

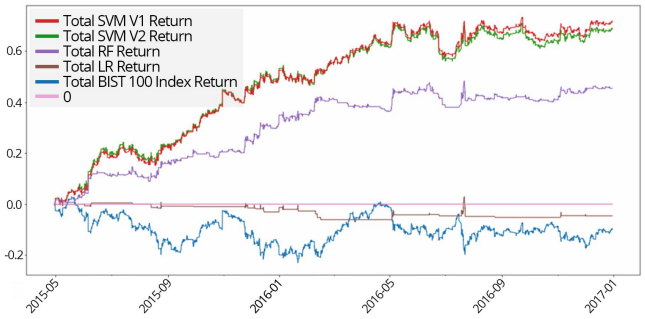

Fig. 1. Total return curves for hourly BIST 100 index with SVM model

interval periods. The WILLR, CCI, UO and ATR indicators were found using the daily maximum, minimum and closing prices of the BIST 100 index. These values are calculated using 4 time periods for WILLR, and a time period for CCI, UO and ATR. With the calculation of different indicators on different time periods, we obtained 97 features for each period of the BIST 100 index. All calculated attributes have been applied with min-max normalization.

III. EXPERIMENTS AND THE BEST RESULT ON HOURLY DATASET

In this study, the direction of the closing price of the BIST 100 index was estimated by using machine-learning methods Logistic Regression, Random Forest and Support Vector Machines. Inspired by the successful practice of machine learning methods in many different areas, the performances of the BIST 100 predictions were explored and the successes of the methods were evaluated.

We observed that the most successful machine learning method in the hourly dataset is Support Vector Machines (SVMs). It achieved a return of over 60% with 55% accuracy. Total return curves for hourly BIST 100 index with SVM model is shown in Fig.1.

REFERENCES

[1] T. Hellström and K. Holmström, "Predicting the Stock Market, Technical Report Series," *IMATOM*, vol. 1997, no. 07, 1998.

[2] M. Abdullah and D. V. Ganapathy, "Neural Network Ensemble for Financial Trend Prediction," *TENCON*, vol. 3, no. 3, pp. 157–161, 2000.

[3] G. Gidófalvi, "Using news articles to predict stock price movements," *TENCON*, vol. 3, no. 3, pp. 157–161, 2001.

[4] I. P. Markoviç, M. B. Stojanoviç, J. Z. Stankoviç, and M. M. Božiç, "Stock market trend prediction using support vector machines," *Automatic Control and Robotics*, vol. 13, no. 3, p. 147–158, 2014.

[5] D. Kumar, S. Meghwani, and M. Thakur, "Proximal support vector machine based hybrid prediction models fortrend forecasting in financial markets," *Journal of Computational Science*, vol. 17, no. 1, p. 1–13, 2016.

[6] H. Gündüz, Z. Cataltepe, and Y. Yaslan, "Stock daily return prediction using expanded features and feature selection," *TÜBİTAK Turkish Journal of Electrical Engineering and Computer Sciences*, 2017.

An Energy Starving Radio for Integrated Bio-Sensors and Actuators

Huseyin S. Savci
Istanbul Medipol University
Kavacık Mah. Ekinciler Cad. No.19
34810, Istanbul, Turkey
hssavci@syr.edu

Fatih Kocan
Istanbul Sabahattin Zaim University,
Halkalı cad. No: 2
34303, Istanbul, Turkey
fatih@iszu.edu.tr

***Abstract*—The implantable medical bio-sensors and actuators have been used as diagnostic and therapeutic purposes over the last decade. Some of them are designed to fulfil the pre-defined tasks either autonomous or upon a command received wirelessly. They are supposed to sustain proper operation up to a decade without a need for battery replacement. The data processing and communication blocks have to be designed for minimum power as they are the most power hungry ones. In typical system radio wakes up periodically and sniffs the channel for commands. Until then the remaining portions of the entire system should be in sleep. In this paper ultra-low power operation and detailed circuit topologies for blocks of CMOS sniffer radio will be explained.**

Keywords—WBAN, IMD, implantable electronics, channel sniff radio, uncertain-IF

I. INTRODUCTION

The wearable and implantable bioelectronics systems have become the integrated part of the medical practice in today's world. Current advancements for implantable medical devices (IMD) and wearable medical sensors and actuators are now exploiting wireless communication technologies. Wireless Body Area Network is presented as a wireless communication protocol for medical devices such as cardiac defibrillators, neuro-stimulators, automated-drug delivery systems, cochlear implants [1].

The most important components of these wireless body area networks are the implantable sensors and actuators. A typical WBAN has many wireless sensors which invasively or non-invasively monitor the particular functions in the patient's body [2] and many actuators fulfil certain tasks. Each device is configured to continuous, automated and unobtrusively monitor the signs or to fulfil pre-defined operations upon a command. WBAN not only allows physicians to monitor patients within their natural physiological state but also reduces the cost of health system by diagnosing procedures, allowing supervised recovery from a surgical procedure and handling emergency events in a timely manner [3]. It can also be used as real-time health monitoring system for people in dangerous work environment [4].

This paper is organized as follows. The application specifications of medical bio-sensor and actuator implants as well as wearable bioelectronics will be given in Section II. Section III explains the architecture level information of the proposed sniffer radio and circuit level design details of its sub-blocks. Finally system level summary is given in Section IV.

II. WIRELESS MEDICAL SENSOR AND ACTUATOR IMPLANTS

After the concept of wireless body area network has been deployed, a globally common portion of frequency spectrum, 402-405MHz, is allocated for the Medical Implant Communications Service as the secondary user. It is aimed to enable individuals and medical practitioners to utilize potential life-saving medical technology without causing interference to other users in the spectrum [5]. This band is chosen due to being optimal in terms of the antenna size, signal propagation characteristics through the human flesh loss, reasons [6].

Batteries are the primary technology limit for implants. There has been some prominent researches on next generation implantable power sources in the form of flexible and biodegradable batteries and supercapacitors with nanoscale materials [7]. Regardless of the type and status of the energy sources, all implants should efficiently do wireless communication. Low battery power consumption, biocompatibility of package materials, small size and high reliability are the primary design concerns. The implants are designed to work for almost a decade without a need to have a surgery for battery replacement. Low power consumption also leads smaller battery size thus shrinking overall implant devices. Burning less current also helps to maintain low heat dissipation of entire design. Low power designs are generally very sensitive to temperature variations. It is medically accepted that normal body temperature range should be between 35 °C, hypothermia limit, and 41.5 °C, hyperpyrexia limit which is pretty narrow and relaxes the design specs of the temperature control circuits.

III. CHANNEL SNIFFER RADIO

A typical bio-sensor and actuator medical implant is shown in Figure 1. The entire system can be integrated in a bio-compatible package and requires no additional components. The scope of this research which is the channel sniffer radio, is shown with the red dashed lines in the figure.

The channel sniffer radio is the most active portion of the entire system. It has 2 main blocks; receiver and frequency synthesizer. Based on the system power budget the overall power consumption of entire radio should be in the range of micro-Watts. The widely used receiver architectures such as

homodyne and heterodyne could not be used for this design as they have power hungry sub-blocks. Thus a new architecture called uncertain-IF topology is adopted for ultra-low power dissipation.

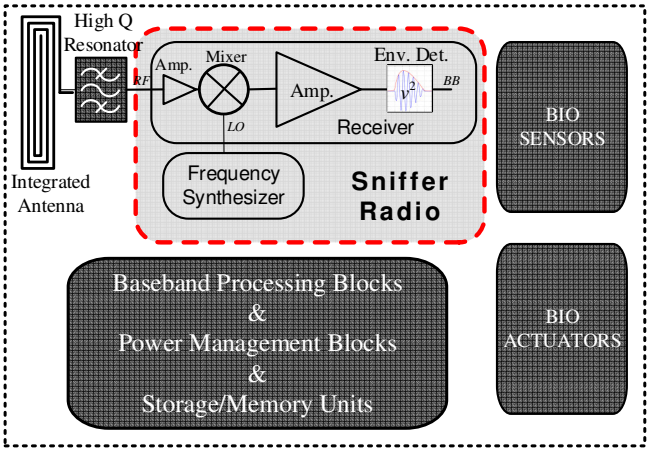

Fig. 1. The proposed CMOS sniffer radio in a medical sensor/actuator implant system

The operation of radio is as follows. The received RF signal through integrated antenna is filtered by a high-Q resonator such as BAW. This blocks signals other than 403MHz. The signal is then mixed with a DLO output which can be any at any frequency within MICS band (402-405MHz). The resultant IF signal is called uncertain-IF and could be at any frequency between 1MHz – 3MHz. After the high amplification, the baseband signal is generated by the envelope detector.

The frequency synthesizer is an un-locked digital local oscillator. Its topology is shown in Figure 2. It is designed by cascading the odd number of proper sized inverters into a loop. The n-Bit tuner controls a resistor bank for coarse adjustment of the LO frequency in 3MHz span by changing the inverter supply voltages. Vfine_cont changes the varactor capacitance to fine tuning.

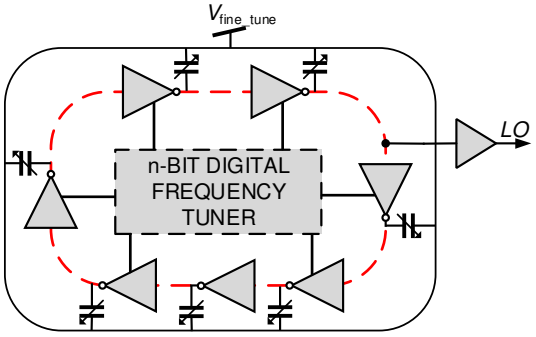

Fig.2. Unlocked Frequency Synthsizer

Figure 3 shows the schematic of receiver. The common-source transistor of mixer is used as RF gain stage and cascode device works as the switch for mixing. The RC load is optimized for matching and filtering. The overall conversion gain is 14dB.

The mixer is followed by a two-stage single-in-differential-out amplifier and couple two-stage differential pairs. Total gain is 70dB. This is enough for the desired receiver sensitivity. The amplifiers are followed by an envelope detector.

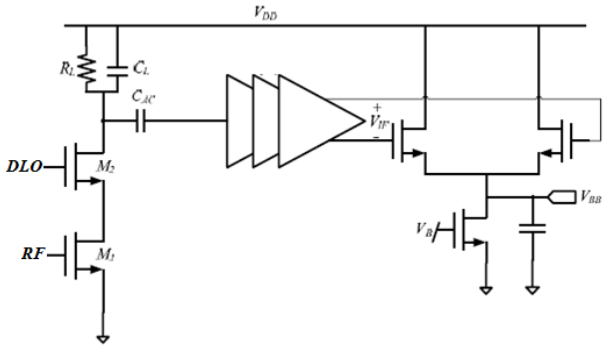

Fig.3. Mixer, IF Amplifiers and Envelope Detector

CONCLUSION

The design and simulation of power starving CMOS radio of the wireless medical bio-sensor and actuator implants is presented. A power efficient uncertain-IF architecture and an unlocked free-running digital local oscillator is used for the radio. The circuits are optimized for low power consumption by utilizing sub-threshold operation and body biasing techniques. A triple-well RF CMOS process with FETs operable under 1V supply is chosen. The design is iteration are done by simulating over process corners, supply voltage tolerance and Monte-Carlo analysis to ensure proper operation.

From the simulations of the entire system, the overall receiver sensitivity is obtained as better than -62dBm and total power consumption is only 60uW with 25uW for synthesizer, 24uW for mixer, 10uW for amplifiers and 1uW for the detector.

ACKNOWLEDGMENT

The authors of this paper would like to thank TUBITAK BIDEB for partial funding of this research.

REFERENCES

[1] T. G. Zimmerman, *"Personal area networks: near-field intrabody communication,"* IBM Syst. J., 1996. pp. 609-617.

[2] N. Gu, Y. Jiang, J. Zhang and H.-T. Zheng, "*An Implementation of WBAN Module Based on NS-2*," 2013 Int. Conf. on Computer Sciences and Applications (CSA), pp.114-118, Dec. 2013

[3] S. Ullah, H. Higgins, B. Braem, B. Latre, C. Blondia, I. Moerman, S. Saleem , Z. Rahman and K. Sup Kwak, "*A Comprehensive Survey of Wireless Body Area Networks On PHY, MAC, and Network Layers Solutions*," Journal of Medical Systems, vol. 36, pp 1065-1094, June 2012.

[4] Y. Geng, J. Chen, K. Pahlavan, "Motion detection using RF signals for the first responder in emergency operations: A PHASER project," IEEE Int. Symposium on Personal Indoor and Mobile Radio Communications (PIMRC), pp. 358-364, Sep. 2013.

[5] C. Falcon, Inside Implantable Devices. Medical Design Technology, pp. 24-27, 2004.

[6] H. S. Savci, A. Sula, Z. Wang, N. S. Dogan, and E. Arvas, "MICS transceivers: regulatory standards and applications," IEEE SoutheastCon 2005, pp. 179–182, April 2005.

[7] A. Kim, M. Ochoa, R. Rahimi, B. Ziaie, "New and Emerging Energy Sources for Implantable Wireless Microdevices," in *Access, IEEE* , vol.3, no., pp.89-98, 2015.

An Empirical Formulation for Estimation of the Seljuk Star Patch Antenna Dimensions for a Given Frequency

S. T. Imeci
Department of Electrical and Electronics Engineering, International University of Sarajevo Ilıdza, 71210, Bosnia and Herzegovina
simeci@ius.edu.ba

E. Yaldiz
Department of Electrical and Electronics Engineering Selcuk University, Konya, 42031, Turkey
eyaldiz@selcuk.edu.tr

M.F. Unlersen
Department of Electrical and Electronics Engineering Necmettin Erbakan University, Konya, 42090, Turkey
mfunlersen@konya.edu.tr

***Abstract*-The microstrip patch antenna is a popular printed resonant antenna for narrow-band microwave wireless links that require semi-hemispherical coverage. Although it has various advantages like being easy to produce, standing with own electronic circuit on the same PCB, having high adaptivity, etc., having a narrow bandwidth is the most important disadvantage. Even if there are some methods like "creating notches or adding grounding pins" which make patch antenna bandwidth wider, the antenna should be designed with the operating frequency very close to the antenna resonance frequency. This situation poses that the dimensions of patch antenna need to be determined with more precision. In this study, a basic formulation has been obtained in order to determine the Seljuk Star patch antenna dimensions for an aimed working frequency. In the calculations of patch antenna working frequency, the openEMS library has been used. The openEMS is a free and open electromagnetic field solver using the FDTD method. Octave is used as scripting interface. As the result, the proposed formulation calculates the dimensions of Seljuk Star patch antenna with the accuracy of 2.08% for a specified working frequency.**

I. Introduction

In literature, there are many books that mention microstrip antenna design. For many years, various formulas are used [1-3]. Although an initial parameter is provided by these formulas, all of them need some adjustments to ensure required frequency or parameters of the patch antenna.

Mathur et al. present a method for quickly estimation the physical dimensions of a rectangular microstrip antenna. The simulation and measurement results of designs are in good agreement with the proposed estimation method [4]. Thakare V. V. and Singhal P. observed the relationship between antenna parameters and working frequency. For this purpose, various Artificial Neural Networks (ANN) are investigated. The ANNs results are more in agreement with the simulation findings [5]. Das et al. investigated the effect of slot position on a slotted antenna. Change of return loss, resonant frequency, and bandwidth parameters with the position of the slot are examined and compared [6].

There is various formulation about the determination of rectangular patch antenna dimensions but there is not a well-known formulation of other shapes. Although it is difficult to analyze patch antennas in complex shapes, formulas can be produced that can estimate the size for the desired frequency in the patch antennas has symmetrically shaped structures. In this study, Octagram (Eight-Pointed Star, also called Seljuk Star) shaped patch antenna is investigated.

II. Material and Methods

In this study, a new formulation to use in the determination the dimension of Seljuk Star (SS) shaped patch antenna is proposed. For this purpose, a standardization is done on the patch shape. A radius called r is chosen in order to form the Seljuk Star. This radius determines the distance between the center of shape and furthest point of the star's one of the corners as seen in Figure 1.

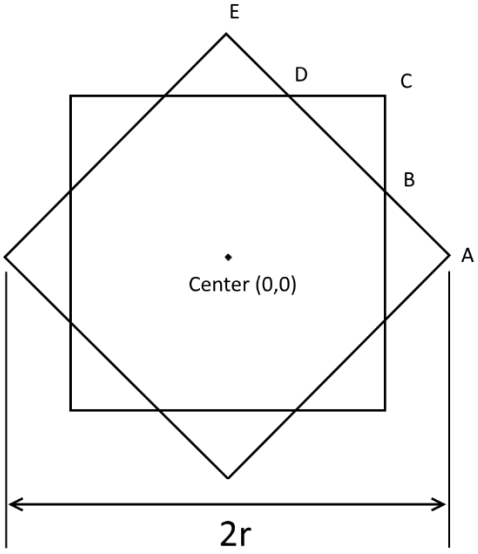

Fig. 1. Determination the coordinates of Seljuk star corners

If the coordinates of corners illustrated by a letter are determined, the coordinates of the other corners could be obtained by the symmetry of known corners. It is easy to see that the coordinates of point A is (r,0) and similarly the point E is (0,r). By analyzing the shape, it can be recognized that the point C is the corner of a square whose diagonal distance is 2r. So the coordinates of point C is $(\frac{r\sqrt{2}}{2}, \frac{r\sqrt{2}}{2})$. With some trigonometric operations, the coordinates of point B and point D can be obtained as $(\frac{r\sqrt{2}}{2}, r - \frac{r\sqrt{2}}{2})$ and $(r - \frac{r\sqrt{2}}{2}, \frac{r\sqrt{2}}{2})$ respectively.

For analysis of patch antennas, a dataset is created. The parameters changed in the dataset are the relative dielectric constant ε_r of used

material, the distance between the ground plane and the patch d, and the dimension of patch r. The probe feed is chosen and the coordinate of the feeding point is $(\frac{2r}{3}, 0)$.

The relative dielectric constant ε_r changed between 1.5 to 4.5 with 1 steps. For the distance between the ground plane and the patch, three value is chosen as 1, 1.5 and 2 (in millimeters). And the dimension of the patch is changed between 10mm to 30mm with 2mm steps. So 4 different value of Er, 3 different value of d and 11 different value of r creates 4x3x11 = 132 records in the dataset.

The openEMS library was used when creating the dataset. The openEMS is a free and open electromagnetic field solver using the FDTD method. Octave are used as an easy and flexible scripting interface presented in Figure 2.

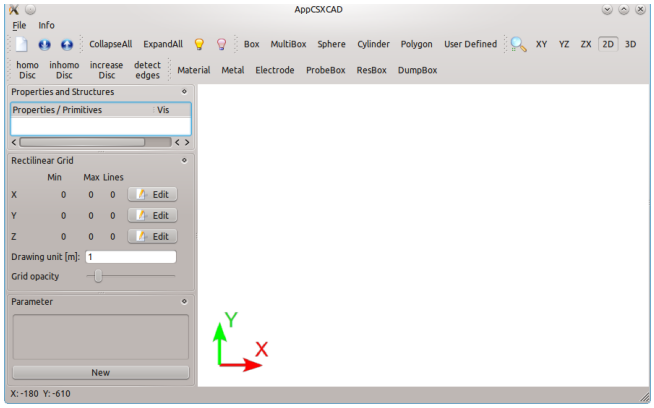

Fig. 2. The openEMS dialog box

The openEMS accepts both parametric patch creation and drawing through dialog box. In this study, parametric creation is used due to the ability to change parameters by using three for loops. The openEMS creates 3-D far-field radiation pattern, 2-D H, and E plane radiation patterns, S11, and VSWR parameters between determined frequencies.

In this study, the S11 parameter is used to determine the first resonant (FR) frequency. For each parameter change, the FR frequency is recorded.

It is clear that the dimension of the patch has a close relation with wavelength. So the data is investigated about a relation between the wavelength and parameters. While keeping two parameters constant, the effect of the change in the third parameter is observed on the dimension of patch r. The curves between the other three parameters versus dimension of patch r are obtained. And some forecasts are tried about the curve equation. And parameters of forecasted curve equation are calculated. Then the effect of the change in another parameter on the curve parameters is investigated. These operations are performed recursively. As the result, the expression for patch dimension r is obtained as in Equation 1.

$$r = (0.2287e^{-0.3933\varepsilon_r} + 0.1086)\lambda + (0.06689\varepsilon_r - 0.5772)d - 0.2129\varepsilon_r + 0.229 \quad (1)$$

For error calculation, 50 new simulations (different from the first dataset) are done. Some of the records in this simulations are presented in Table 1.

TABLE I
THE NOVEL FORMULATION PERFORMANCE

#	Patch Parameters				openEMS Sim. Results (GHz)
	ε_r	h (mm)	f (GHz)	Calculated r (mm)	
1	2.80	1.5	2.15	24.81	2.10
2	2.80	1.5	2.45	21.66	2.49
3	3.30	1.5	2.15	22.86	2.12
4	3.30	1.5	2.30	21.30	2.31
5	3.30	1.5	2.45	19.94	2.39
6	3.80	1.5	2.15	21.25	2.18
7	3.80	1.5	2.30	19.79	2.30
8	3.80	1.5	2.45	18.52	2.40
9	4.30	1.5	2.15	19.91	2.08
10	4.30	1.5	2.45	17.34	2.46

III. CONCLUSION AND RESULTS

In this study, an investigation of a relation between Seljuk Star shaped patch antenna dimension and operating frequency has been performed. The Relative Root Mean Square Error (RMSE) has been used as the performance indicator. The relative RMSE has been calculated about 2.08%. Although the proposed expression lacks the theoretical infrastructure, it is thought to be useful for the initial study of patch antenna design.

REFERENCES

[1] R. Garg, *Microstrip Antenna Design Handbook*. Boston, USA: Artech House, 2011.

[2] J. L. Volakis, *Antenna Engineering Handboook*. New York: McGraw-Hill, 2007.

[3] G. Kumar, *Broad Band Microstrip Antennas*. Norwood: Artech House, 2003.

[4] D. Mathur, S. K. Bhatnagar, and V. Sahula, "Quick Estimation of Rectangular Patch Antenna Dimensions Based on Equivalent Design Concept," *IEEE Antennas And Wireless Propagation Letters*, vol. 13, p. 4, 01.07.2014 2014.

[5] V. V. Thakare and P. Singhal, "Artificial Intelligence in the Estimation of Patch Dimensions of Rectangular Microstrip Antennas," *Circuits and Systems*, vol. 2, p. 8, 15.08.2011 2011.

[6] A. Das, C. Banerjee, B. Datta, and M. Mukherjee, "Estimation of Slot Position for a Slotted Antenna," in *Computational Advancement in Communication Circuits and Systems*, K. Maharatna, G.K. Dalapati, P.K. Banerjee, A.K. Mallick, and M. Mukherjee, Eds., 2nd Edition ed India: Springer, 2014, p. 521.

A Simple Architecture, High-Performance Current-Mode LTA-MIN Circuit

Turgay Temel, PhD

Bursa Technical University, Department of Mechatronics Engineering, Bursa, Turkey
turgay.temel@btu.edu.tr, ttemel70@gmail.com

I- ABSTRACT

A new high-performance current-mode looser-take-all minimum circuit is proposed. It alleviates most of the shortcomings in major previous designs such as not involving constant biasing and additional switching circuitries. The new circuit is shown to outperform major predecessors in terms of design and electrical characteristics.

II- INTRODUCTION

Minimum (MIN) is a major operation to identify the smallest input to a multi-input information processing systems including fuzzy logic systems [1-4], higher-radix arithmetic units such as adders [5-6], and multi-valued logic representation [7]. Due to such advantages as design simplicity, higher-dynamic range and faster switching, most MIN circuits termed also as looser-take-all (LTA-MIN) are implemented with current-mode design approaches. Despite straightforward realization of maximum operation as winner-take-all maximum (WTA-MAX) [8], major current-mode MIN designs mostly adopt indirect methods, which can be referred to three main groups: The first group, e.g. [1] and [3], involves comparing stacked input currents and codes the resultant (almost digital) output node voltages such as to yield LTA-MIN functionality. This approach has a disadvantage that the number of inputs to be maintained by supply voltage is restricted leading to high level of complexity as the number of inputs increases. The second group, e.g. [7], [9-10], resort on the duality between MIN and MAX in De Morgan's law with use of auxiliary operations such as bounded-difference to express minimum in an algebraic form. Despite straightforward algebra involved, the designs that fall in this group have the disadvantage of high-level, i.e. polynomial, complexity in number of inputs. The third group tackles, [11-13] the LTA-MIN design problem by utilizing the WTA within a feedback loop to attain the desired DC transfer characteristics. Despite the advantage of simultaneous processing of multiple inputs as well as modularity, their performance is determined by the feedback circuitry. A straightforward and simple LTA-MIN design has been given in [14] where only three transistors are required per input. However, the circuit involves a biasing current source and a switching circuitry on output current path, which restricts overall performance.

In this paper, we present a novel, current-mode multi-input LTA-MIN with very simple and modular architecture derived as a dual of well-known WTA-MAX, e.g. in [8]. New circuit involves only three transistors per input similar to [14]. However, it eliminates the need for biasing and switching circuitries. New design and major predecessors were implemented and simulated by using TSMC 0.25µm HSPICE level-49 design parameters for power supply of 2.1V for comparison. It is shown that the new circuit exhibits better transient response, lower power consumption and smaller layout area than those previous designs in statistical terms.

III- DESCRIPTION OF NEW LTA-MIN CIRCUIT

An *n*-input LTA-MIN circuit can be devised by exploiting conventional source-follower WTA paradigm as shown in Fig. 1 with use of a diode-connected PMOS transistor (M_A) on the input current path. It should be noted that the circuit does not involve any biasing and switching circuitries as opposed to most minimum circuits discussed previously. All cells are identical and having transistors M_A, M_B and M_C with device conductances $\beta_A = (KP_A)(W/L)_A$, $\beta_B = (KP_B)(W/L)_B$ and $\beta_C = (KP_C)(W/L)_C$ where *KP* and W(µm)/L(µm) are process transconductance and aspect ratio of the transistor of interest.

Transistor	M_A	M_C	M_O, M_B
W(µm) / L(µm)	1.25 / 0.5	1.0 / 0.5	0.75 / 0.5

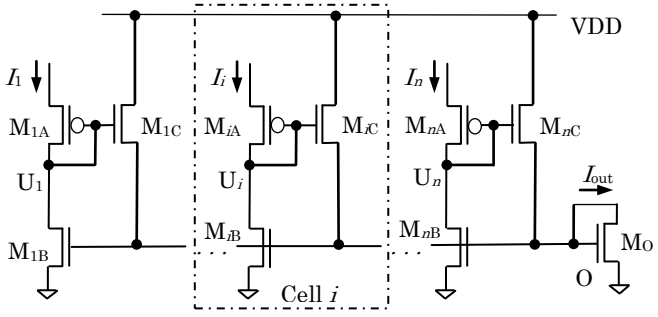

Fig. 1. Proposed *n*-input LTA-MIN and transistor aspect ratios for the design parameters and supply voltage used.

The voltage at node O is driven by the largest gate voltage variation of M_C transistors owing to source following. Assuming that all input currents are equal then the output current I_{out} is contributed equally by each M_C transistor subject to conduction with respective gate-to-source voltage larger than their threshold voltage. In case one of the input currents, e.g. I_i, is decreased by increasing the gate (consequently the drain node U_i) voltage of M_{iA} with respect to its source, then,

almost the same voltage increase will appear at the source of M_{iC}. Hence, the gate of the output transistor M_O will be driven by source of M_{iC}, which will then drive respective M_{iC} transistor into saturation while driving other M_C transistors into triode region. In this case, M_C of *i*-th cell will take over the output current I_{out} as a replica of the respective input current I_i upper-bounded. Hence, the proposed design will perform the minimum operation as a multi-input LTA-MIN circuit.

IV- SIMULATIONS AND RESULTS

The new design and previous designs given in [3], [7], [12-14] were implemented for comparison of their electrical and design characteristics as three-input circuits with most appropriate transistor sizes for most optimum DC behavior possible. They were simulated including body-bias effect with full post-layout extraction by using TSMC 0.25µm level-49 HSPICE parameters for VDD = 2.1V. All designs employed a diode-connected NMOS transistor M_O with W(µm)/L(µm)=0.75/0.50. The bias currents I_b, for [12] and [14] was fixed at 1µA by using a diode-connected PMOS transistor with W(µm)/L(µm)=0.50/1.50 placed between VDD and respective node indicated within the circuit of interest, e.g. node U in [14]. If necessary, currents were replicated and then redirected with current mirrors. Fig. 2 shows the simulation results for the proposed.

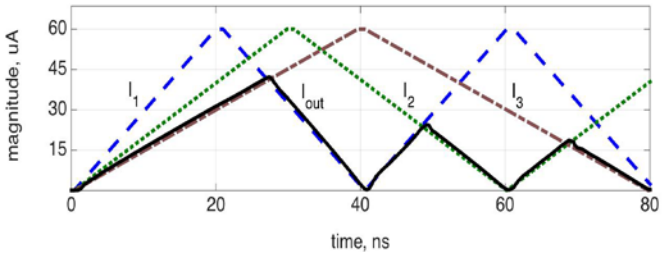

Fig. 2 Three-input and corresponding output simulation waveforms for the proposed LTA-MIN circuit where I_{out} is shown in solid lines.

The designs above were also studied in terms of their characteristics and behavior against random variations due to design deviations and mismatches. Deviation of I_{out} with respect to a chosen particular input, e.g. I_1, which was incremented from 15µA to 45µA by 15µA while I_2 and I_3 were kept at 30µA was considered in simulations. At each I_1 value, 100 Monte Carlo DC experiments were performed where VTO and (W/L) values of transistors were varied around their nominal values with random perturbations drawn from zero-mean normal Gaussian densities with standard deviations $\sigma_{\Delta W/W,\Delta L/L} = 10\%$ and $\sigma_{\Delta VTO} = 25$, respectively. In evaluating the robustness, the quantity $\delta = \max(|I_{out} - I_{min}| / I_{min})$ as output randomness where $I_{min} = \min(I_1, I_2, I_3)$ is considered. In Table 1, some important design and electrical performance characteristics are presented in terms of average (avg.) and standard variation (σ) for designs: avg(P_{VDD}) refers to average power drawn from VDD while avg(τ_{delay}) is the average delay in average for the inputs in Fig. 2.

TABLE I
IMPORTANT ASPECTS OF LTA-MIN CIRCUITS STUDIED

Design	# of Trans.	avg(τ_{delay}) (ns)	avg(P_{VDD}) (mW)	Layout Area $(\mu m)^2$	σ_δ (%) (I_1=15/30/45, µA)
New	10	1.4	0.20	3.6	2.5/2.3/2.3
[3]	18	3.0	0.29	5.6	3.5/3.1/2.7
[7]	16	2.7	0.32	5.9	4.0/3.4/3.1
[12]	18	2.6	0.26	5.4	3.7/3.3/2.9
[13]	14	2.4	0.25	4.8	3.4/2.9/2.8
[14]	13	1.8	0.26	4.1	2.9/2.5/2.1

V- CONCLUSIONS

A new, simple architecture, high-performance multi-input current-mode looser-take-all minimum circuit is described. Contrary to major predecessors, new design does not employ biasing circuitry, which leads to more robust and more constrained-free implementation. New circuit and some major predecessors were also implemented for comparison. Simulations reveal that the proposed circuit outperforms those major previous designs regarding to transient response, power drawn from the supply and robustness in statistical terms.

VI- REFERENCES

[1] C. Dualibe, M. Verleysen, and P. Jespers, "Design of Analog Fuzzy Logic Controllers in CMOS Technologies: Implementation, Test and Application," Netherlands: Springer, 2003.

[2] T. Temel, "System and Circuit Design for Biologically-Inspired Intelligent Learning," IGI Global, PA, USA, 2010, doi: 10.4018/978-1-60960-018-1.

[3] K. P. Abdulla and A. F. Azeem, "A CMOS Current-mode Implementation of Multiple Input Fuzzy MIN and MAX Circuits for Analog Fuzzy Processors," *Int. Jour. of Scientific & Engineering Research*, vol. 4, no. 4, pp. 928-932, 2013.

[4] T. S. T. Mak, K. P. Lam, H. S. Ng, G. Rachmuth and C. –S. Poon, "A Current-Mode Analog Circuit for Reinforcement Learning Problems," *Proc. IEEE Int. Symp. on Circuits and Systems (ISCAS 2007)*, pp. 1301-1304, 2007.

[5] T. Temel, A. Morgul, and N. Aydin, "A novel signed higher-radix full-adder algorithm and implementation with current-mode multi-valued logic circuits," *Proc. IEEE Euromicro Symp. on Digital System Design (DSD 2004)*, pp. 80-87, 2004.

[6] T. Temel, A. Morgul, and N. Aydin, "Signed higher-radix full-adder algorithm and implementation with current-mode multi-valued logic circuits," *IEE Proc-Circuits, Devices and Systems*, vol. 153, no. 5, pp. 489-496, 2006.

[7] T. Temel, "Current-mode CMOS Design of Multi-valued Logic Circuits," PhD Thesis, Bogazici University, Department of Electrical and Electronics Engineering, 2002.

[8] J. Lazzaro, R. Ryckebusch, A. Mahowald, and C. Mead, "Winner-take-all networks of O(n) complexity," in D. Touretzky, Eds, Advances in Neural Information Processing systems I', Morgan Kaufmann, CA, USA, pp. 703-711, 1989.

[9] B. Mesgarzadeh, "A CMOS Implementation of Current-Mode Min-Max Circuits and A Sample Fuzzy Application," *Proc. IEEE Int. Conf. on Fuzzy Systems*, vol. 2, pp. 941-946, 2004.

[10] M. A. Yakout, E. I. El-Masry, A. I. Abd-El Fattah, "Hardware realization of analog CMOS current-mode minimum circuit'. *Proc. Nat. Conf. on Radio Science*, pp. D8/1-D8/7, 1998.

[11] N. Donckers, C. Dualibe, and M. Verleysen, "A current-mode CMOS loser-take-all with minimum function for neural computations," *Proc. IEEE Int. Symp. on Circuits and Systems (ISCAS 2000)*, vol. 1, pp. 415-418, 2000.

[12] M. Asloni, A. Khoei, and K. Hadidi, "Design of analog current-mode looser-take-all circuit," *IEICE Trans. Electron.*, vol. E89-C, no. 6, pp. 819–822, 2006.

[13] C. Y. Huang, C. J. Wang and B. D. Li, "Modular current-mode multiple input minimum circuit for fuzzy logic controllers," *Electron. Lett.*, vol. 32, no. 12, pp.1067-1069, 1996.

[14] T. Temel, "High-performance current-mode multi-input loser-take-all minimum circuit," *Electron. Lett.*, vol. 44, no. 12, pp. 718-719, 2008.

A Reflectarray Unit Cell Design based on Split Ring Loaded with Triple Dipoles

Orcun Kiris, Kagan Topalli,
Fahri Ozturk, Mesut Gokten, Lokman Kuzu
Microwave and Antenna Systems Group
TUBITAK Space Technologies
Research Institute
Ankara, Turkey
orcun.kiris@tubitak.gov.tr

Mehmet Unlu
Electrical and Electronics Eng. Dept.
TOBB Economy and
Technology University
Ankara, Turkey
munlu@ybu.edu.tr

***Abstract*—This paper presents a novel reflectarray unit cell comprising of a split ring loaded with triple dipole at a frequency of 8.23 GHz. The proposed structure is compared to the conventional phi-shaped unit cell designed at the same frequency on the same substrate keeping the sizes of the unit cell same, which is half wavelength at the design frequency. The simulations are carried out using the infinite array approach implemented with Floquet modal expansion. The results indicate an improvement in both the reflection loss and phase variation range, which is about 175°, making the proposed unit cell suitable for wide bandwidth reflectarray antenna applications.**

Keywords—antenna, satellite communication, reflectarray, split ring, unit cell element

I. INTRODUCTION

The high gain antennas are essential elements of most space and satellite communication systems for long distance communication. Parabolic reflectors and arrays are conventional solutions to meet high gain requirements in long distance applications. In recent years a new type of antenna, namely "reflectarray" has been introduced for high gain applications in order to alleviate the issues related with either the parabolic reflector or the conventional array antennas providing a low-profile, low-weight, planar, and readily-deployable alternative solution in particular for space applications. A reflectarray antenna is a planar array of printed radiating elements illuminated by a feed source. Printed radiating elements, i.e., unit cell elements, on a reflectarray surface can be predesigned with a particular phase shift provided by each unit cell. The unit cells will reflect the field received from the feed antenna forming an equiphase front in the desired direction [1]. Recently, reflectarray studies in literature are focused on efficient solutions for some common issues and on some innovative techniques, architectures and realizations such as patches integrated with variable-length stubs [2], double cross loops [3], single-layer multiresonant double square rings [4], variable-sized stacked patches [5], [6], aperture coupled patches [7], and parasitic dipoles [8].

This paper presents a novel unit cell consisting of variable-length triple dipoles with a split ring. Triple dipoles are simultaneously varied parametrically in order to obtain phase delay. The proposed design provides a phase variation higher than 360° which is crucial for a wider bandwidth of operation at the array level implementation. It should also be noted that the phase variation is linearly dependent to the dipole length allowing the precise tuning of the phase shift. This feature makes the proposed unit cell easy-to-apply for the array level designs considering manufacturing tolerances. The following sections of the paper introduce the physical parameters of the design and the computational method used by the simulation environment.

II. UNIT CELL DESIGN AND SIMULATION RESULTS

In a reflectarray design, phase adjustment of a unit cell is the vital feature of the antenna design. All unit cells that are placed on the array surface should have a different amount of spatial phase delay due to its planar structure. The phase values of all unit cells should compensate spatial phase delay due to physical difference in the distances from the unit cell to the feed antenna. The unit cells reflect the electromagnetic waves to equalize the phases of the radiated waves so that the main beam points at the desired direction. The structure given in [9] called phi-shaped unit cell element has a uniform size split ring and a variable dipole designed at an operating frequency of 20 GHz implemented on a 0.79 mm-thick RT/Duroid 5880 (ε_r = 2.2, tanδ = 0.004) substrate. In the frame of the study, we re-designed the phi-shaped element at a frequency of 8.23 GHz on a 1.575 mm-thick RT/Duroid 5880 in order to achieve similar phase range and characteristics. The most practical method of obtaining the phase variation of a unit cell is the infinite array approach. In this approach, the array is formed by replicating the identical unit cells periodically. Infinite array approach is implemented using Ansys HFSS®, which is a commercially available finite-element method based electromagnetic solver [10]. In order to satisfy this periodicity, periodic boundary conditions are implemented by utilizing master and slave boundaries on the unit cell walls. The arrangement of the array allows the approximation of the infinite array fields with Floquet modal expansion. Floquet ports are defined on the apertures of the unit cell as an interface to unbounded medium and the fields on the ports are represented by a set of Floquet modes. Fig 1 (a)-(c) shows the physical geometry of the re-designed phi-shaped unit cell, phase variation with respect to dipole length, and reflection loss, respectively. Table I gives the physical dimensions of the unit cells presented in Fig 1 (a) and (d). The gap of the split ring, the width of the ring and the dipole widths are kept in both the phi-shaped design and the

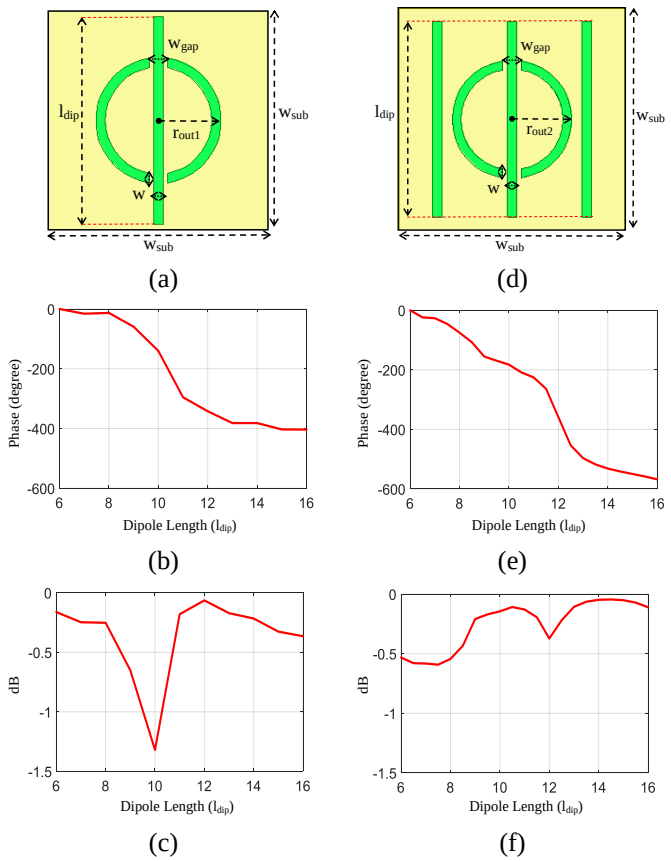

Fig. 1. Re-designed phi-shaped unit cell: (a) The physical geometry, (b) Phase response, and (c) Reflection loss. Split ring loaded with triple dipole: (d) The physical geometry, (e) Phase response, and (f) Reflection loss.

proposed structure. It should be noted that for both of the designs, the widths of the dipoles and the ring are kept to be the same at 0.73 mm.

It is observed that a maximum phase variation of about 400° and 1.32 dB reflection loss is obtained for the re-designed phi-shaped element. In order to improve the phase variation range and reflection loss of the unit cell, a new design is proposed where two dipoles are added at the left and right sides of the split ring. These additional dipoles are identical to the center dipole resulting in a structure comprising of triple dipoles as shown in Fig. 1 (d). These three dipoles are simultaneously varied in the simulation environment parametrically. The phase variation and reflection loss of the unit cell comprising of a split ring loaded with the triple dipole are presented in Fig. 1 (e) and (f), respectively.

TABLE I. DESIGN PARAMETERS OF THE UNIT CELLS (mm)

w_{sub}	w_{gap}	r_{out}	r_{out1}	w	l_{dip}
18.226	1.46	4.86	5	0.73	6 - 16

The results show that the phase variation is 575° indicating an improvement of about 175° compared to the re-designed phi-shaped element. The maximum reflection loss is also improved, which is found to 0.6 dB for the split ring loaded with triple dipoles.

III. CONCLUSION

We present a reflectarray unit cell based on a split ring loaded with triple dipoles where the dipole length variation provides a phase shift of 575°. The unit cell has improved phase shift compared to the conventional phi-shaped unit cell configuration. The improvement in the phase shift is crucial for bandwidth enhancement in particular for high gain antennas due to required large aperture sizes. Moreover, the presented design yields a reduction in the reflection loss which, in turn, increases the aperture efficiency of a reflectarray antenna. The unit cell can be a promising solution for wide bandwidth and high gain antennas required for satellite and space communication systems.

ACKNOWLEDGMENT

This work is partially supported by TUBITAK Space Technologies Research Institute (TUBITAK UZAY) within the scope of the 7I150800 (YADAS) project.

REFERENCES

[1] J. Huang and J. A. Encinar, Reflectarray Antennas. John Wiley & Sons, 2007.

[2] H. Hasani, M. Kamyab and A. Mirkamali, "Broadband reflectarray antenna incorporating disk elements with attached phase-delay lines," IEEE Antennas and Wireless Propagat. Letters, Vol. 9, pp. 156-158, 2010.

[3] M. R. Chaharmir, J. Shaker, M. Cuhaci, and A. Ittipiboon, "Broadband reflectarray antenna with double cross loops," Electronic Letters, Volume 42, Issue 2, pp. 65-66, Jan. 2006.

[4] M. R. Chaharmir, J. Shaker, M. Cuhaci, and A. Ittipiboon, "A broadband reflectarray antenna with double square rings," Microw. Opt. Technol. Lett., vol. 48, no. 7, pp. 1317–1320, Jul. 2006.

[5] J. A. Encinar,"Design of two-layer printed reflectarray using patches of variable size," IEEE Trans. Antennas Propagat., Vol. 49, pp. 1403-1410, Oct. 2001.

[6] J. A. Encinar and J. A. Zornoza,"Broadband design of three-layer printed reflectarrays," IEEE Trans. Antennas Propagat., Vol. 51, No. 7, pp. 1662-1664, Jul. 2003.

[7] E. Carrasco, M. Barba and J. A. Encinar, "Reflectarray element based on aperture-coupled patches with slots and lines of variable length," IEEE Trans. Antennas Propagat., Vol. 53, No. 3, pp. 820-825, Mar. 2007.

[8] L. Li, et al., "Novel broadband planar reflectarray with parasitic dipoles for wireless communicarion applications," *IEEE Antennas and Wireless Propagat. Letters*, Vol. 8, pp. 881-885, 2009.

[9] Seong Won Oh, "Wideband Reflectarray Using Compact Coupled Element And Rectifying Antenna Combined With Reflectarray", PhD Thesis, Texas A&M University, August 2011.

[10] ANSYS® HFSS, Version 13, Online Help, Master and Slave Boundaries.

A New LVQ Classification Algorithm and its Application to Recognition of Handwritten Characters

Turgay Temel, PhD

Bursa Technical University, Department of Mechatronics Engineering, Bursa, Turkey
turgay.temel@btu.edu.tr, ttemel70@gmail.com

I- ABSTRACT

In this study, a new LVQ classifier algorithm is proposed. The algorithm remedies a major LVQ issue for assigning labels to training samples. Experiments with publicly available handwritten digital character dataset for recognition reveal that new algorithm improves classification performance compared to major predecessors.

II- INTRODUCTION

Traditional Learning Vector Quantisation (LVQ) and its variants have been considered a group of the most successful classifiers well-suited to classification problems, [1-4]. They are based on Hebbian-learning winner-take-all and nearest-neighbourhood in terms of class-associated prototype/weight vectors in feature space. The main problems with standard LVQ classifiers are choice of similarity measure in training and initialisation of weight vectors. Major remedial LVQ studies have mainly focused on developing an adaptive metric for expressing dissimilarities during training: Generalised Learning Vector Quantisation (GLVQ) simultaneously performs both learning and optimizing a hypothesis-testing based cost function with gradient descent [5-6], which lads to a generalization almost independent of data representation for small dimensions. However, weight vectors exhibit saliency with increased data dimension in case of a correlated data, which may be attributed to a functional relevance, [7]. Generalised Relevance Learning Vector Quantisation (GRLVQ) in [8] suggests a possible solution to this by scaling proximities of individual samples. The study in [9] suggests an algorithm called Optimally Generalized Learning Vector Quantization (OGLVQ) against possible unstable weight dynamics due to arbitrary weight initialization. OGLVQ is based on sliding-mode approach [10-12], for minimizing a cost function in terms of weight update power. It was shown to lead weight convergence in a predictive manner while ensuring high classification accuracy. However, the weight update rule tracking has the possibility of misleading in learning process in case a sample falls in the middle prototype vectors.

In this study, we present a new algorithm to overcome above shortcoming. New algorithm and major LVQ algorithms are applied to hand-written character trajectory recognition problem in a public dataset. The experimental results reveal that the proposed scheme brings in consistent improvement in classification accuracy despite a slightly higher training time complexity.

III- DESCRIPTION OF LVQ ALGORITHMS AND THE NEW ALGORITHM

LVQ classifier operation, which is shown in Fig. 1, allocates categories or class labels which are known *a priori* for inputs to be classified. A given L-dimensional input column vector $\mathbf{x} = [x_1 \dots x_L]^T$ is assigned to the output class label corresponding to the closest weight vector out of K classes, $C_{i=1,\dots,K}$, where the weight vector corresponding to the j-th class label C_j is $\mathbf{w}^j = [w^{j1} \dots w^{jL}]^T$.

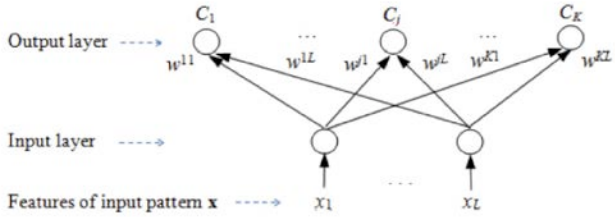

Fig. 1. General operation of LVQ classifiers.

In training phase of original LVQ with N_{train} samples per epoch, for the k-th input sample vector $\mathbf{x}_k = \mathbf{x}(k)$, $k = 1,\dots, N_{train}$, only the weight vector of the winning class label, $\mathbf{w}_k^* = \mathbf{w}^*(k)$, is adjusted by

$$\mathbf{w}_{k+1}^* = \mathbf{w}_k^* \pm \xi(\mathbf{x}_k - \mathbf{w}_k^*) \quad (1)$$

until a predefined convergence is satisfied, e.g. $\mathbf{w}^j(k) = \mathbf{w}^j(k\text{-}1)$ for $j = 1 \dots K$. The sign '$\pm$' is taken '+' if $\mathbf{x}_k$ has been correctly classified otherwise '$-$'. The winning output vector is determined according to $\mathbf{w}_k^* = \arg\min_{\mathbf{w}^j} d(\mathbf{x}_k, \mathbf{w}^j)$ where $d(\mathbf{x}_k, \mathbf{w}^j)$ is the squared Euclidean distance between $\mathbf{x}_k$ and $\mathbf{w}^j$. Other variants of original LVQ, e.g. LVQ2.1 and LVQ3, adjust weight vectors of some other classes, e.g. closest loser prototype of having the same class label as the sample, [8]. On the other hand, training with a (G/GR)LVQ classifier also aims at optimizing the number of correctly classified samples in terms of a cost function such as

$$E = \frac{1}{2}\sum_{\forall k} f(\mu_k) \quad (2)$$

where the classifier function is $f(u) = \frac{1}{1+e^{-u}}$ and proximity

measure $\mu_k = \mu(\mathbf{x}_k) = \frac{d_k^+ - d_k^-}{d_k^+ + d_k^-}$. Dissimilarity measure $d_k^\pm = d(\mathbf{x}_k, \mathbf{w}_k^* = \mathbf{w}^\pm) = \left\|\mathbf{x}_k - \mathbf{w}^\pm\right\|^2$ is the squared distance of $\mathbf{x}_k$ to the closest prototype $\mathbf{w}^+$ being the same class label as $\mathbf{x}_k$ or the best matching prototype $\mathbf{w}^-$ with a class label different from that of $\mathbf{x}_k$, respectively. The weight update is

$$\mathbf{w}_{k+1}^* \leftarrow \mathbf{w}_k^* \pm \underbrace{\xi \frac{\partial f}{\partial \mu_k} \frac{d_k^\pm}{(d_k^+ + d_k^-)^2} (\mathbf{x}_k - \mathbf{w}_k^*)}_{\Delta \mathbf{w}_k^*} \tag{3}$$

where '$\pm$' refers to the appropriate sign as the superscript of respective $\mathbf{w}_k^*$, i.e. $\mathbf{w}_k^* = \mathbf{w}^+$ or $\mathbf{w}_k^* = \mathbf{w}^-$ as described previously. When training samples have not been pruned and/or classes are highly overlapped and/or weights are initialized improperly, weights and updates may exhibit instability. As a solution to this problem, OGLVQ in [9] considers minimizing the cost function

$$J = \left(\frac{1}{2}\right) \sum_k \|\Delta \mathbf{w}_k^*\|^2 \tag{4}$$

based on sliding-mode convergence rule [11-12],

$$(\Delta \mathbf{w}_k^*)^T \mathbf{w}_k^* \leq -\eta \|\mathbf{w}_k^*\|^2 \tag{5}$$

where $\eta > 0$. Taking $\mathbf{w}_{k-1}^* = \mathbf{w}_k^* - \Delta \mathbf{w}_{k-1}^*$, and arranging terms for (k-1)-th term will give

$$(\Delta \mathbf{w}_k^*)^T = (\Delta \mathbf{w}_{k-1}^*)^T (1 \mp \mu_k \mathbf{A}_k) \tag{6}$$

where $\mathbf{A}_k = \frac{\Delta \mathbf{w}_{k-1}^*}{(d_k^+ + d_k^-)^2} \left[d_k^+ \frac{\partial d_k^+}{\partial \mathbf{w}_k^+} - d_k^- \frac{\partial d_k^-}{\partial \mathbf{w}_k^-} \right]$ is an L-by-L matrix since $\frac{\partial d_k^\pm}{\partial \mathbf{w}_k^\pm} = 2(\mathbf{x}_k - \mathbf{w}^\pm)^T$ with sign previously given for (G/GR)LVQ. The sign '-' (+) in (6) refers to $\mathbf{w}_k^*$ and $\mathbf{w}_{k-1}^*$ be same (different) class label(s).

It should be noted that (6) does not ensure convergence in case a train sample is the same distance to the patterns in the same class label and differing label. Thus it is desirable to avoid such a situation. For this purpose we suggest a modification such that

$$\mu_k = \mu(\mathbf{x}_k) = \frac{\sum_{i=1}^{\Gamma} \left| d_{k,i}^+ - d_{k,i}^- \right|}{\sum_{i=1}^{\Gamma} \left| d_{k,i}^+ + d_{k,i}^- \right|} \tag{7}$$

where Γ is a performance-related integer such that the number of correctly classified samples exceeds a certain threshold, e.g. 90% past N_{train} samples. A care should be taken when selecting the value since random initialization of weight vectors may lead this condition never to be met. To avoid this problem, threshold value can be chosen much lower e.g. 50% and it is increased as the number of epoches increases.

IV- EXPERIMENTS

In order to illustrate the performance improvement with new algorithm for a real-world dataset, a set of 100 experiments were conducted with cross-validation as the average of K = 10 subgroup outputs as K-fold model building and evaluating the performance of new and some of the previous LVQ algorithms. For this purpose, Character Trajectories Dataset, Character Trajectories Dataset (http://archive.ics.uci.edu/ml/machine-learning-databases/character-trajectories/) was used. The dataset consists of 3-dimensional 2858 labeled samples of pen tip segment trajectories for the 20 single pen-down characters, e.g. 'a', 'e', 'w'. The feature vectors are composed of respective coordinates x, y, and pen tip force. From the dataset, randomly chosen 2850 samples from the dataset were utilized Cross-validation was implemented by setting one out of ten subgroups of the dataset for testing while the remaining nine was used for model building or training. Table I presents some major characteristics of the classifiers studied in statistical terms, i.e. average and statistical deviation of classification accuracy in testing and training time.

TABLE I
PERFORMANCE OF LVQ ALGORITHMS STUDIED FOR CLASSIFICATION OF HANDWRITTEN CHARACTER TRAJECTORIES DATASET.

Algorithm	Classification success in testing, %, Average / std. deviation		# of training epochs, Average / std. deviation	
	$\xi = 0.05$	$\xi = 0.1$	$\xi = 0.05$	$\xi = 0.1$
New	87.0 / 3.1	86.5 / 3.4	33.9 / 3.5	32.6 / 3.2
OGLVQ	82.8 / 3.3	84.6 / 3.0	28.6 / 2.5	31.8 / 3.0
LVQ2.1	70.9 / 4.8	66.6 / 4.7	40.8 / 4.6	39.6 / 4.4
GLVQ	79.2 / 3.7	81.0 / 3.8	44.3 / 4.2	42.5 / 4.0

From Table I, it is observed that for the dataset studied, the new LVQ algorithm brings in an improvement in classification performance while it leads to a training time complexity slightly higher. However, classification performance becomes more statistically consistent against variation in learning parameter ξ and random initialization in weight vectors than the other LVQ classifiers.

V- REFERENCES

[1] D. Nova and P. Estévez, "A review of learning vector quantization classifiers," *Neural Computing and Applications*, vol. 25, no. 3-4, pp. 511-524, 2013.

[2] G. R. Lloyd, R. G. Brereton, R. Faria J. C. Duncan, "Learning Vector Quantization for Multiclass Classification: Application to Characterization of Plastics," *J. Chem. Inf. Model.*, vol. 47, no. 4, pp 1553–1563, 2007.

[3] T. Temel and B. Karlik, "An improved odor recognition system using learning vector quantization with a new discriminant analysis," *Neural Network World*, vol. 17, no. 4, pp. 287-294, 2007.

[4] T. Temel, "System and Circuit Design for Biologically-Inspired Intelligent Learning," IGI Global, PA, USA, 2010, doi: 10.4018/978-1-60960-018-1.

[5] P. Schneider, B. Hammer and M. Biehl, "Adaptive relevance matrices in learning vector quantization," *Neural Computation*, vol. 21, no. 12, pp. 3532-3561, 2009,

[6] A. Cataron and R. Andonie, "Energy Generalized LVQ with Relevance Factors," *Proc. IEEE Int. Joint Conf. Neural Networks, IJCNN*, pp. 1421-1426, 2004.

[7] B. Hammer, D. Hoffmann, F. –M. Schleif and X. Zhu, "Learning vector quantization for (dis-)similarities," *Neurocomputing*, vol. 131, pp. 43-51, 2014.

[8] M. Kaden, M. Lange, D. Nebel, M. Riedel, T. Geweniger and T. Villmann, "Aspects in Classification Learning - Review of Recent, Developments in Learning Vector Quantization," *Foundations of Computing and Decision Sciences*, vol. 39, no. 1, pp. 79-105, 2014.

[9] T. Temel, "A New Classification Algorithm: Optimally Generalized Learning Vector Quantization (OGLVQ)," *Neural Network World*, vol. 27, no. 6, pp. 569-576, 2017.

[10] T. Temel and H. Ashrafiuon, "Sliding-mode control approach for faster tracking," *Electron. Lett.*, vol. 48, no. 15, pp. 916-917, 2012.

[11] T. Temel and H. Ashrafiuon, "Sliding-mode speed controller for tracking of underactuated surface vessels with extended Kalman filter," *Electron. Lett.*, vol. 51, no. 6, pp. 467-469, 2015.

[12] S. Janardhanan and B. Bandyopadhyay, "On Discretization of Continuous-Time Terminal Sliding Mode," *IEEE Trans. Automatic Control*, vol. 51, no. 9, pp. 1532-1536, 2006.

A New High-Performance Current-Mode WTA-MAX Circuit

Turgay Temel[1] (PhD), Taha İmeci[2] (PhD)

[1]Bursa Technical University, Department of Mechatronics Engineering, Bursa, Turkey
turgay.temel@btu.edu.tr, ttemel70@gmail.com
[2]International University of Sarajevo, Faculty of Natural Sciences, Department of Electrical Engineering,
Hrasnicka cesta 15, 71210 Sarajevo, BiH, simeci@ius.edu.ba

I- ABSTRACT

A novel multi-input current-mode maximum circuit is presented. The new design employs feedback for sensing changes in input currents to ensure faster decision-making in multiple inputs with smaller switching voltage compared to conventional design approaches. Full post-layout simulations demonstrate that the presented circuit outperforms major predecessors in transient response with lower power consumption due to reduced switching voltage.

II- INTRODUCTION

Maximum (MAX) is a major operation in linear and nonlinear systems such as fuzzy controllers [1-2], multiple-valued logic [3], and higher-radix arithmetic adders [4-5] to determine the largest input. Owing to advantages such as design simplicity, higher-dynamic range and faster switching, major MAX designs are by using current-mode design approaches. However, despite these advantages, current-mode design approaches have some disadvantages: A common design scheme called winner-take-all maximum (WTA-MAX) for implementing the MAX operation relies upon the source-following architecture e.g. [6]. In this design paradigm, inputs compete to take privilege as the winner at low driving point impedance. Although they have high level modularity and design simplicity, their transient and frequency responses are usually poor. Design schemes employing rounded-difference operation as a piecewise linear function approximation, e.g. [3], [7], have a possibility that use of rounded-difference can be lead in realization of varying algebraic representations of maximum operation. However, design with larger number of inputs will involve cascading these blocks, which causes increased mismatch in mirroring the intermediate current levels. The resulting circuit will exhibit distorted linearity and reduced dynamic range for even moderate-complexity switching function realizations. A different group of WTA-based MAX designs, e.g. [8-9], allow simultaneous operation with larger number of inputs. However, due to considerably large voltage swings required to charge/discharge increased intrinsic and parasitic capacitive nodes involved, they commonly have poor frequency and transient responses. Moreover, mismatch issues become serious as the number of inputs increases, hence yielding realization with degraded reliability in output linearity with respect to winner input.

Here, a current-mode multi-input winner-take-all maximum architecture is presented alleviating major shortcomings stated above. The new design utilizes a feedback circuit to sense input current variations, which yields faster switching. The proposed circuit and some of the well-known predecessors have been implemented with TSMC 0.25µm CMOS technology level-49 HSPICE design parameters for 2.1V power supply. Simulation results reveal that the new circuit operates at higher speed with lower power consumption in statistical terms.

III- DESCRIPTION OF NEW WTA-MAX CIRCUIT

Proposed WTA-MAX circuit with *n* inputs is depicted in Fig. 1. All cells are identical and each consisting of transistors M_A, M_B and M_C with respective device conductances $\beta_A = (KP_A)(W/L)_A$, $\beta_B = (KP_B)(W/L)_B$ and $\beta_C = (KP_N)(W/L)_C$. Here, *KP* and W(µm) / L(µm) are the process transconductance and aspect ratio of the respective transistor.

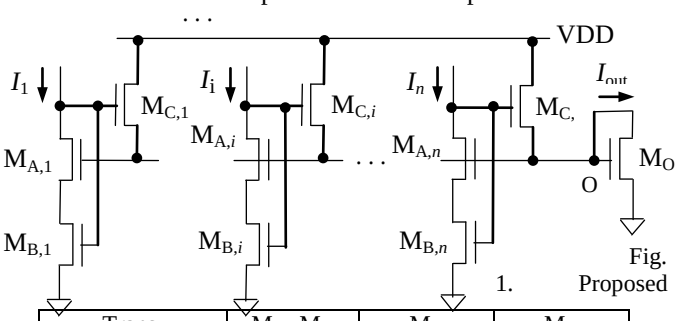

Fig. 1. Proposed *n*-input WTA-MAX circuit and transistor aspect ratios for the design parameters and supply voltage used.

Trans.	M_A, M_B	M_C	M_O
W(µm) / L(µm)	1.0 / 0.5	1.0 / 0.5	0.75 / 0.5

For each cell, transistor M_B acts as a sensing/feedback circuit. A gate voltage increase due to an increase in input current will be translated to an amplified voltage decrease at respective drain node, which forces it into triode (saturation) region while driving respective M_A into saturation (triode) region. Since respective M_C acts as a source follower, each cell will compare and takes switching action between currents those generated by gate-to-source voltages of M_B and M_A. Owing to this behavior, it should be noted that a WTA-MAX design employing M_B in feedback as depicted in Fig. 1 is expected to operate with reduced input current and voltage variation for switching due to amplification involved compared to those WTA-MAX designs, e.g. [6], that do not exploit such an approach.

Having described the behavior of an individual cell above,

n-input maximum operation can be attributed to by WTA-MAX paradigm. For a particular voltage V_O at common (output) node O, an input current flow is associated to an input voltage at the gate of M_B, which satisfies $V_{GS,B} \approx V_O > VTO_B$ driving both M_A and M_B into conduction in triode region where VTO is the zero body-bias threshold voltage of respective transistor. However, this condition does not necessarily ensure flow of an output current (I_{out}) as a replicate of an input. Increasing the gate voltage of M_B further such that $V_{GS,C} > V_{th,C}$ where $V_{th,C}$ is the threshold voltage of respective M_C including body-bias effect will drive M_C toward conduction, hence initiating an output current. As a result, respective M_A is driven into saturation due to further reduced drain voltage of M_B being maintained in triode region and its drain node almost connected to ground. Since all cells are identical, the equal current will flow on M_C of each cell for equal input currents. If a particular cell e.g. *i*-th cell is driven with larger input current than the others the respective input voltage variation will be followed at output node O, which then drives $M_{C,i}$ into saturation. On the other hand, M_Cs of other cells are forced into triode region due to their reduced drain-to-source voltage with very small current flow contribution to I_{out}. In this case, M_C of *i*-th cell will provide the output current I_{out} as a replica of the respective input current I_i upper-bounded by $I_i > (\beta_{C,i}/2)\left[(V_{DD} - VTO) - \sqrt{2I_{out}/\beta_O}\right]^2$. Hence, the proposed design will perform maximum operation as a multi-input WTA-MAX circuit.

IV- SIMULATIONS AND RESULTS

New circuit and previous designs in [3], [6], [8-9], were implemented for comparison of their electrical and design characteristics as three-input circuits with most appropriate transistor sizes for most optimum DC behavior possible. They were simulated including body-bias effect with full post-layout extraction by using TSMC 0.25µm level-49 HSPICE parameters for VDD = 2.1V. All designs employed a diode-connected NMOS transistor M_O with W(µm)/L(µm)=0.75/0.50. If necessary, currents were replicated and/or redirected with current mirrors. Fig. 2 illustrates the simulation results for the proposed design.

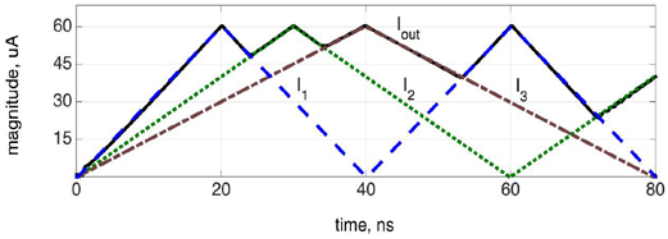

Fig. 2 Three-input and corresponding output simulation waveforms for the proposed WTA-MAX circuit with I_{out} shown in solid lines.

The designs above were also examined in terms of their characteristics against random variations due to design deviations and mismatches as described by [10]. Deviation of I_{out} with respect to a chosen particular input, e.g. I_1, which was incremented from 15µA to 15µA by 15µA while I_2 and I_3 were kept at 30µA was considered in simulations. At each I_1 value, 100 Monte Carlo DC experiments were conducted. In experiments, VTO and (W/L) values of transistors were varied around their nominal values with random perturbations drawn from zero-mean normal Gaussian densities with standard deviations $\sigma_{\Delta W/W,\Delta L/L} = 12.5\%$ and $\sigma_{\Delta VTO} = 32.5mV$, respectively. In evaluating the robustness of designs against these random variations, the quantity ρ = max ($|I_{out} - I_{max}|/I_{max}$) as output randomness where I_{max} = max (I_1, I_2, I_3) is considered. In Table 1, some important design and electrical performance characteristics are presented in terms of average (avg.) and standard variation (σ) for studied circuits: The measure avg(P_{VDD}) refers to the average power consumed from VDD while avg(τ_{delay}) is latency in transient response or delay in average for the inputs in Fig. 2.

TABLE I
IMPORTANT ASPECTS OF WTA-MAX CIRCUITS STUDIED

Design	avg(τ_{delay}) (ns)	avg(P_{VDD}) (mW)	σ_ρ (%) (I_1=15/30/45µA)	# of transistors	Layout Area (µm)^2
New	0.9	0.17	2.8/2.6/2.1	10	59.6
[3]	1.9	0.21	3.4/3.0/2.9	18	84.8
[6]	2.1	0.24	3.2/2.8/2.5	14	117.3
[8]	1.9	0.21	3.1/2.7/2.2	12	96.3
[9]	2.1	0.17	2.8/2.4/2.1	9	90.2

V- CONCLUSIONS

A new high-performance multi-input current-mode maximum circuit is proposed. New design employs feedback for sensing to ensure fast switching against input current changes. It is shown that the proposed circuit operates better in terms of transient response and it consumes less power from the supply in statistical terms compared to major previous designs.

VI- REFERENCES

[1] C. Dualibe, M. Verleysen, and P. Jespers, "Design of Analog Fuzzy Logic Controllers in CMOS Technologies: Implementation, Test and Application," Netherlands: Springer, 2003.

[2] T. Temel, "System and Circuit Design for Biologically-Inspired Intelligent Learning," IGI Global, PA, USA, 2010, doi: 10.4018/978-1-60960-018-1.

[3] T. Temel, "Current-mode CMOS Design of Multi-valued Logic Circuits," PhD Thesis, Bogazici University, Department of Electrical and Electronics Engineering, 2002.

[4] T. Temel, A. Morgul, and N. Aydin, "A novel signed higher-radix full-adder algorithm and implementation with current-mode multi-valued logic circuits," *Proc. IEEE Euromicro Symp. on Digital System Design (DSD 2004)*, pp. 80-87, 2004.

[5] T. Temel, A. Morgul, and N. Aydin, "Signed higher-radix full-adder algorithm and implementation with current-mode multi-valued logic circuits," *IEE Proc-Circuits, Devices and Systems*, vol. 153, no. 5, pp. 489-496, 2006.

[6] J. Lazzaro, R. Ryckebusch, A. Mahowald, and C. Mead, "Winner-take-all networks of O(n) complexity," in D. Touretzky, Eds, Advances in Neural Information Processing systems I', Morgan Kaufmann, CA, USA, pp. 703-711, 1989.

[7] M. Sasaki, T. Inoue, Y. Shirai, and F. Ueno, "Fuzzy multiple-input maximum and minimum circuits in current-mode and their analyses using rounded difference equations," *IEEE Trans. Computing*, vol. 39, no. 6, pp. 768-774, 1990.

[8] I. Baturone, J. L. Huertas, A. Barriga, and S. S. Solano, "Current-mode multiple-input MAX circuit," *Electron. Lett*., vol. 30, no. 9, pp. 678-680, 1994.

[9] C. Y. Huang, B. D. Liu, "Current-mode multiple input maximum circuit for fuzzy logic controllers," *Electron. Lett*., vol. 30, no. 23, pp. 1924-1925, 1994.

[10] T. Temel, "High-performance current-mode multi-input loser-take-all minimum circuit," *Electron. Lett*., vol. 44, no. 12, pp. 718-719, 2008.

A Multi-pole Model for Oxygen Absorption of 60 GHz Frequency Band Communication Signals

Müberra Arvas[1] and Mohammad Alsunaidi[2]
[1]Department of Electrical Engineering, Istanbul Medipol University, Istanbul, Turkey
[2]Electrical and Electronics Engineering, Marmara University, Istanbul, Turkey

***Abstract*—Estimation of attenuation levels of future 5G communication systems relies on accurate channel modeling. We present a simple and efficient time-domain simulation algorithm for the analysis of atmospheric Oxygen absorption of electromagnetic signals in the 60 GHz frequency band using available experimental data. The presented methodology and algorithm can be used to simulate the propagation of 60 GHz-band signals at sea level or at any other elevation.**

***Keywords*— Dispersion; 5G communications; FDTD method; Lorentz model; Oxygen absorption.**

I. INTRODUCTION

One of the most important obstacles that face 5G communications using the 60 GHz frequency band is atmospheric attenuation. This attenuation peaks at 60 GHz, with a value of over 15 dB/km. Oxygen absorption constitutes over 95% of atmospheric attenuation. The successful adoption of this frequency band for wireless and radio communications hinges on the introduction of novel antenna designs and communication strategies to overcome the channel loss. Although there has been a lot of emphasis on measurement techniques of atmospheric attenuation [1-3], little has been reported in accurate modelling of this effect in electromagnetic simulators. Customarily, empirical fits to measured data are used to approximate attenuation levels as a function of frequency and elevation. These empirical models are not suitable to be imported into standard time-domain electromagnetic simulators, because they involve expressions and functions that make field retardation calculations unfeasible. On the other hand, analytical solutions can utilize these empirical functions but only for the treatment of simple situations. The objective of this paper is to develop a material model of atmospheric attenuation that can be incorporated in a FDTD algorithm.

II. TIME-DOMAIN MODEL

Considering a linear material response, one can write the frequency-dependent electric flux density, $D(\omega)$, as,

$$D(\omega) = \varepsilon_o \varepsilon_\infty E(\omega) + P_{LN}(\omega) \tag{1}$$

where ε_o is the free space permittivity, ε_∞ is the high frequency dielectric constant and ω is the frequency. The first order linear polarization $P_{LN}(\omega)$ is related to the electric field intensity, $E(\omega)$, in the frequency domain by the linear electric susceptibility $\chi^{(1)}$ as,

$$P_{LN}(\omega) = \varepsilon_o \chi^{(1)}(\omega) E(\omega) \tag{2}$$

The dispersion relation for the electric susceptibility can be represented by a general Lorentz model function of the form

$$\chi^{(1)}(\omega) = \frac{a}{b + jc\omega - d\omega^2} \tag{3}$$

where *a*, *b*, *c* and *d* are model parameters usually obtained from material characteristics or by fitting to experimental data. Equation 2 can be expressed in the time domain using the general FDTD algorithm (GA-FDTD) reported in [4]. In this case, the time domain update equation for the linear polarization becomes

$$P_{LN}^{n+1} = C_1 P_{LN}^{n} + C_2 P_{LN}^{n-1} + C_3 E^n \tag{4}$$

where, $C_1 = \frac{4d - 2b\Delta t^2}{2d + c\Delta t}$, $C_2 = \frac{-2d + c\Delta t}{2d + c\Delta t}$ and $C_3 = \frac{2a\Delta t^2}{2d + c\Delta t} E^n$. In (4), n is the time index and Δt is the time step. The algorithm starts with the calculation of electric flux densities from available magnetic field samples using Maxwell's curl equation. Next, the linear polarization vector is updated using (4). Finally, the electric field intensity component is updated using

$$E^{n+1} = \frac{D^{n+1} - \sum^{N} P_{LN}^{n+1}}{\varepsilon_o \varepsilon_\infty} \tag{5}$$

where N represents the number of poles of the material dispersion relation.

III. MULTI-POLE ATMOSPHERIC MODEL

The atmospheric attenuation measurements used in this work are adopted from a recent report by the International Telecommunication Union [3]. In this report, an estimate of gaseous attenuation computed by summation of individual absorption lines for the frequency range 1 GHz to 1 THz is given. Also given is a simplified approximate method to estimate gaseous attenuation for the frequency range 1-350 GHz.

The strategy for using the experimental data is as follows. For any given frequency range and elevation, frequency-dependent data for the complex permittivity are obtained from attenuation readings. These readings are fitted to standard

material models with as many poles as required. Out of the fitting process, the required parameters for the time-domain simulator are obtained. Here, we use a Lorentzian dielectric function of the form,

$$\varepsilon_r(\omega) = \varepsilon_\infty + (\varepsilon_s - \varepsilon_\infty) \sum_{i=1}^{p} \frac{A_i {\omega_i}^2}{{\omega_i}^2 + j2\delta_i\omega - \omega^2} \quad (6)$$

with $a_i = (\varepsilon_s - \varepsilon_\infty){\omega_i}^2$, $b_i = {\omega_i}^2$, $c_i = 2\delta_i$ and $d_i = 1$ being the parameters used in (4). In (6), ε_s is the effective static dielectric constant, A_i is the pole strength, ω_i is the resonance frequency, δ_i is the damping parameter and p is the number of poles. Table I shows the parameters for the two Lorentz poles used for atmospheric attenuation modeling. The resulting dielectric constant curves (real and imaginary parts) are shown in figure 1, together with the reference empirical data.

TABLE I. LORENTZ POLE PARAMETERS FOR ATMOSPHERIC ATTENUATION AT SEA LEVEL.

Pole	a	*b*	*c*	*d*
1	1.7367×10^{16}	1.4063×10^{23}	3.6×10^{10}	1.0
2	3.1545×10^{15}	1.5093×10^{23}	2.0×10^{10}	1.0

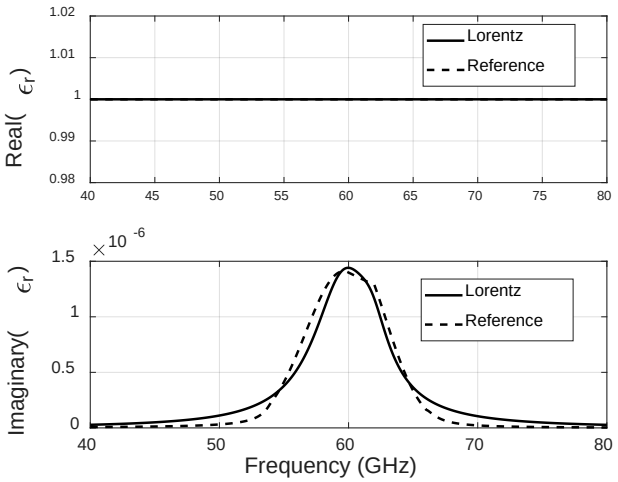

Fig. 1. Real and imaginary dielectric constant curves of the atmosphere as obtained by the empirical attenuation function (Ref 2, dashed line) and the corresponding 2-pole Lorentz fit (solid line) for sea level conditions.

IV. SIMULATION RESULTS

An antenna is assumed to produce a time-limited signal of a Gaussian form given by

$$A(t) = A_0\, e^{-[\frac{t-t_0}{t_p}]^2} \cos\left[\omega_c\,(t - t_0)\right] \quad (7)$$

where A_0 is the initial pulse amplitude, t is time variable, t_0 is the offset time, t_p is the pulse waist and ω_c is the central frequency. The parameter t_p is used to adjust the frequency contents of the pulse such that it covers the full 60 GHz band. The central frequency ω_c is set at 60 GHz to center the input frequency spectrum at that frequency. In this study, a plane wave propagation is considered. The simulation parameters are set such that numerical dispersion is minimized with a spatial step Δ=0.01 mm. This value is a very small fraction of the wavelength of a 60 GHz signal (5 mm). It is used to insure that numerical dispersion is significantly minimized and channel dispersion is correctly represented. The algorithm is stable with a time step of 0.03 ps. With this level of space resolution, the memory requirement for the simulation of hundreds of meters of propagation distance becomes unaffordable. To solve this problem, the rotating boundary conditions are used. In this case, the propagating pulse exits the computational domain and re-enters from the other boundary to start propagating the domain again. The initial size of the computational domain is set to half a meter. The choice of this initial domain size insures that it is wide enough to comfortably accommodate the pulse during the whole simulation time, even with the resulting dispersion due to the channel. The pulse trans passes the computational domain for multiple of times to achieve a certain propagation distance. A reference simulation in a lossless atmosphere was also carried out such that comparisons are possible. Figure 2 shows the variation of the transmitted signal power with distance. A signal at 60 GHz lose more than half its initial power within the first half a kilometer.

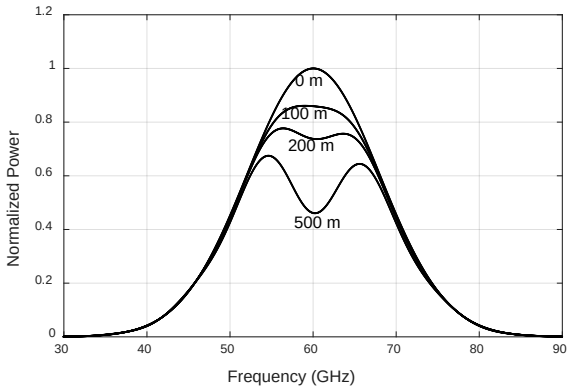

Fig. 2. Normalized signal power at different propagation distances vs. frequency.

V. CONCLUSIONS

A time-domain simulation model for atmospheric absorption of 60 GHz band signals has been presented. The numerical simulator incorporates a multi-pole material dispersion model of the atmosphere and uses the rotating boundary conditions to allow for long propagation distance. The results are useful in the prediction of propagation power loss such that methods for compensation can be devised.

REFERENCES

[1] G. Frank, J. Wentz and T. Meissner, "Atmospheric absorption model for dry air and water vapor at microwave frequencies below 100GHz derived from spaceborne radiometer observations," Radio Sci., 51, 2016.

[2] D. S. Makarov, M.Yu. Tretyakov, P.W. Rosenkranz, "60-GHz oxygen band: Precise experimental profiles and extended absorption modeling in a wide temperature range," *Journal of Quantitative Spectroscopy & Radiative Transfer*, 112 (2011) 1420–1428.

[3] International Telecommunication Union, Attenuation by atmospheric gases, Recommendation ITU-R P.676-9, 02/2012.

[4] M. A. Alsunaidi and A. Al-Jabr, "A General ADE-FDTD Algorithm for the Simulation of Dispersive Structures," *IEEE Photonics Tech. Lett.*, vol. 21, pp. 817-819, June 2009.

A Combined Triple U-shaped Microstrip Patch Antenna for K_u-Band operation

Furkan Gecekuşu, Ahmet Uğur Kökcü, Fatih Akgeyik, Muhammed Zafer Şahintürk
Department of Electrical and Electronics Engineering,
Antalya Science University
Antalya, Turkey

Taha Imeci, Azra Yildiz
Department of Electrical and Electronics Engineering, International University of Sarajevo,
Sarajevo, Bosnia and Herzegovina

Ahmet Fazil Yagli
Aselsan Research Center
Ankara, Turkey

***Abstract*- In this paper, a combined and compact triple U-shaped K_u-band microstrip patch antenna is designed for bandwith enhancement. The proposed rectangular antenna is fed by a 50Ω microstrip line. FR-4(Lossy) is used as a substrate to design the recommended antenna which has a condensed structure of 18x20 mm^2. The operating zone of this antenna is within 12.4GHz to 13.1GHz that covers some part of K_u band. The gain of antenna is 5.62dBi which symbolized its ability to work for satellite communication. Regarding the antenna, the results are obtained in terms of gain, s pattern, farfield.**

Keywords- Microstrip antenna, High gain, K_u band operation.

I. INTRODUCTION

Antenna is a key in communication. Microstrip patch antenna was the one of the types and options. Since they are easy to construct [1], it was chosen by the group members. By examining [2,4], different type of antennas were evaluated. One of the articles was chosen and same antenna designed on Computer Simulation Technology (CST) microwave studio software. Then mostly same results were obtained. After this step all design was changed and new design was simulated. Results were evaluated with Associate Professor Taha İmeci. As a final stage by changing the parameters, results wanted to be improved.

II. ANTENNA DESIGN

The shape and dimensions of the antenna, characteristic of a dielectric substrate are influential in designing and fabricating an antenna. For example, small changes on dimensions effect the radiation pattern, directivity, resonant frequencies, return loss and other parameters substantially.

In [3], which was inspiration for design of our antenna, the gain was improved by making some changes.

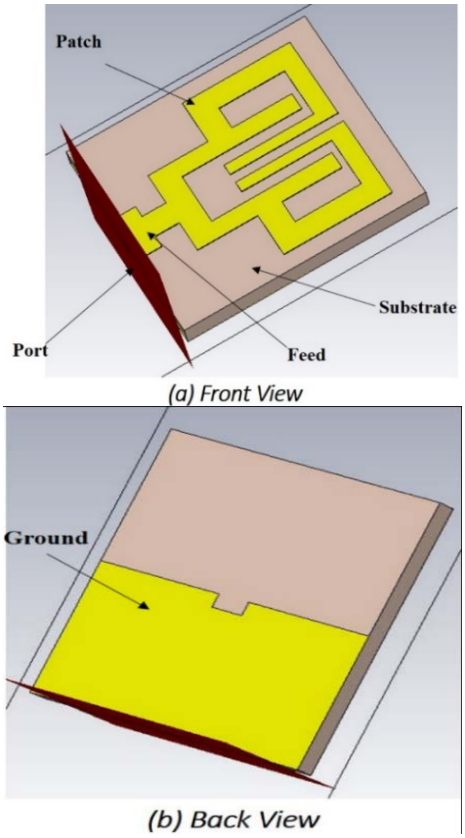

Fig. 1: (a) Front and (b) back view of new design

The rectangular antenna consists of three layers. These are ground, substrate and patch. The ground layer and the patch are comprised with copper annealed and the substrate is having a height of 1.6 mm and relative dielectric constant (ε_r) 4.4. The dimensions of the antenna are 18x20x1.67mm^3 with patch thickness.

III. RESULTS AND DISCUSSION

The overall analysis is made on S-paramaters, gain and farfield. Simulation was done with in a rangeof 1 to 20GHz. S11 describes the relationship between input and output ports in an electrical system. This is the parameter of an antenna that explains the quality regarding impedance match between the source and the receiving end. This S11 has to be below -10dB to persuade a good mode of radiation. And in this case, the propagating wave stays below -10dB line from 12.4 to 13.1 and 16.4 and 17.1GHz. The return loss found from the Fig. 2 is -11.5dB at 12.74GHz.

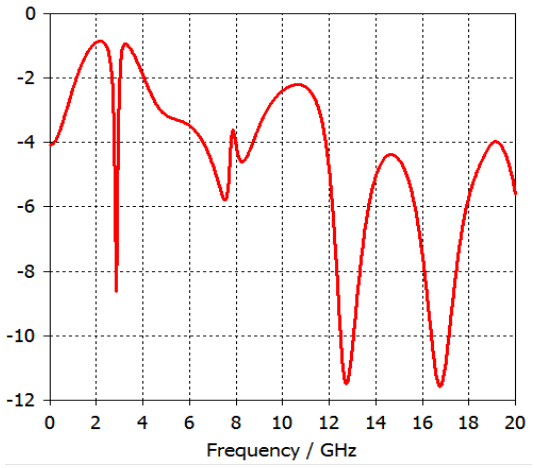

Fig. 2: S-Parameters(Magnitude in dB)

Fig. 3 and Fig. 4 illustrate the farfield of the mentioned antenna. This farfield results or directivity is the parameter that indicates directionality of the radiated power of the antenna.

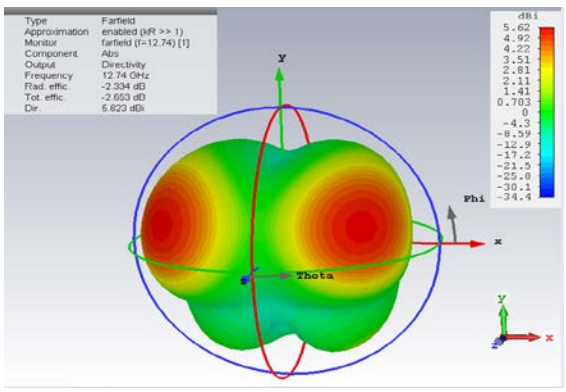

Fig. 3: Farfield at 12.74GHz

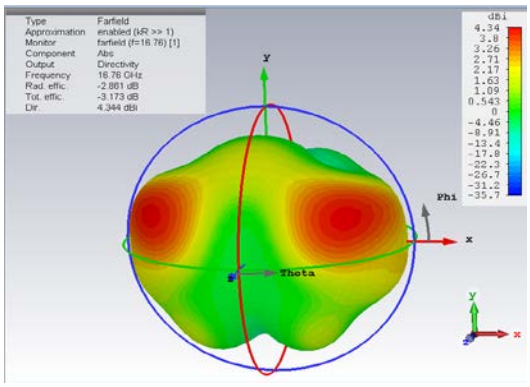

Figure 4: Farfield at 16.76GHz

IV. CONCLUSION

In this paper, a compact and combined triple U-shaped microstrip patch antenna is introduced for satalite communication. This antenna operates well within a range of 12.4 to 13.1GHz that covers the some part of K_u band. Moreover, the result of S Parameters, farfield and gain are enough to apply the antenna in practical field. In spite of using the FR-4 as substrate, the antenna is only 1.67mm thick. This combined triple U-shaped MPA is a good competitor for the K_u band operation.

REFERENCES

[1] Md. J. Alam, M. R. I. Faruque,Md. I. Hossain, M. T. Islam and S. Abdullah "A Combined Double H-shaped Microstrip Patch Antenna for X-Band operation" *International Conference on Electrical, Computer and Communication Engineering (ECCE), February 16-18, 2017, Cox's Bazar, Bangladesh*

[2] M. Bugaj, J.Bugaj, and M. Wnuk "U Shape Microstrip Wideband Antenna" *2016 Progress In Electromagnetic Research Symposium (PIERS), Shanghai, China, 8–11 August*

[3] S.C. Basaran, "Compact dual-band split-ring antenna for 2.4/5.2 GHz WLAN applications" *Turk J Elec Eng & Comp Sci, vol. 20, pp. 347352, 2012.*

[4] D. Delikanlı, S. Keskiner "E shaped antenna surrounded with u shape"

[5] B. Kul, G. Kirman, P. Ergül, Z. B. Kartal "L, U, T and F-Shaped Slots in Patch Antenna"

3dB Branchline Coupler Design

Omer Ates
Electrical &Electronic Engineering Department
Istanbul Commerce University
Istanbul, Turkey
oatesch@gmail.com

Ethem Yigit Gurer
Electrical &Electronic Engineering Department
Istanbul Commerce University
Istanbul, Turkey
yigitgurer@gmail.com

Abstract:This paper presents design and simulate of a 3 dB 90º hybrid microstrip branch-line coupler between 3 GHz and 4.8 GHz. The simulated results are presented as, S-parameters, phase difference between the coupled ports and current distribution. An amplitude balance of 0.57 dB is achieved at the center frequency of 3.63 GHz. The band width where the device has better than 14 dB return loss (1.5:1 VSWR) is 900 MHz, or 24.8%. Port impedances and the coupled section impedance are the same. The coupler can be used in many applications within the frequency range of 3-4.8GHz.

Keywords—Coupler;3dB; Branchline..

I. INTRODUCTION

Branch-line couplers with compact size and high-performance are demanded in many microwave communication systems. A range of new novel devices have then been fabricated utilizing new LH structure, such as a leaky backward-wave antenna (Liu et al., 2000), a dual-frequency branch-line coupler (Lin et al., 2004) and a highly directive coupled-line couplers (Islam and Eleftheriades, 2003). [1] In the RF chain, branch-line couplers, that always provide equal amplitude and quadrature phase outputs within the designed operating frequency band, have attracted more and more interests, especially for those ones which can operate at dual band frequency and occupy smaller circuit size simultaneously.[2] Recently, the considerable attention is directed to couplers, which may have arbitrary output power division at the two operation bands. [3] Branch-line coupler is one of the most important microwave device widely utilized in other components such as power combiners/ dividers, balanced mixers, balanced amplifiers and Butler matrix systems.[4] Branch-line coupler is one of the fundamental components in RF/microwave front-end systems. It is a 4-port device that divides and/or combines power simultaneously with port-to-port isolation and 90∘ phase shift. [5] The four-port couplers are used with active or passive components, additional matching circuits are necessary to obtain the desired output performance. If they can be terminated in arbitrary impedances, no matching circuit is required and the total size of microwave integrated circuit can be reduced. [6] One of the problem that are related to the BLC is that when loose coupling is required for example 10-dB coupling, the width of the microstrip line will be very small which complicates the fabrication process and reduces the power handling capability [7]. The branch-line coupler has several applications in the design of microwave devices such as balance amplifiers, balance mixers and phase shifters. The branch-line coupler employs quarter wavelength transformers to realize a simple square-shaped configuration that is used for power dividing or power combining functions and is suitable for low-cost fabrication [8]. A performance comparison with other dual-band planar topologies is presented. Finally, a 3 dB quadrature hybrid for dual band (2.4 and 5 GHz) wireless local area network systems was fabricated, aimed to cover the bands corresponding to the standards IEEE802.11a/b. The measurements show a 16% and 18% bandwidth for the lower and upper frequency, respectively, satisfying and exceeding the bandwidth requirements for the above standards [9]. The designed 3 dB micro strip coupler has a single layer and uniplanar platform with quite easy fabrication process. This optimized 180◦ coupler also shows a perfect isolation and insertion loss over the UWB frequency range of 3.1–10.6 GHz. [10]. Stepped-impedance stubs are used in the branch-line coupler to achieve dual-band applications. Parameters of the structure are chosen and provided for design guidelines. Broader operating frequency ratios and compactness are achievable. For the purpose of validation, a microstrip coupler operating at 2.4/5.2 GHz is fabricated and measured [11].

II.DESIGN AND SIMULATION RESULTS

As with the Wilkinson power splitter, the bandwidth of a branchline coupler can be improved by adding sections However, the tradeoff for the extra bandwidth in real life will be added loss of the second box section, not to mention the added size. In fact, there are other circuits for a broad-band hybrid, such as a Lange coupler, tandem coupler.Although they show wide-band performances with small sizes, most of them need multilayered or air-bridged structures for tight coupling and signal routing (crossover) over a wide frequency range. The requirement for air-bridges results in more masks and fabrication processes, leading to more costs. Moreover, these air-bridges would represent a bottle neck for power handling and, hence, limit the applications of Lange and tandem couplers. To this end, it would be desirable to develop an alternative hybrid that can achieve a better trade off between bandwidth, size, and power handling [12]. The phase difference between the coupled ports is almost 90º along the frequency band as seen in Figure 4.The zoomed in plot of amplitude balance (0,5 dB) at the center frequency of 4.2 GHZ in new design is shown in Figure 3. The phase difference between the coupled ports is almost 90º along the frequency band as seen in Figure 3.

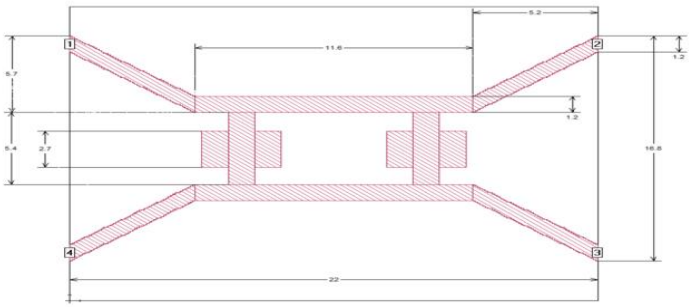

Fig.1 Top view of the re-designed coupler.

Figure 1 shows the Scattering parameters. This graph shows that the bandwidth where the device has better than 14 dB return loss (1.5:1 VSWR) is 900 MHz, or 24.8%

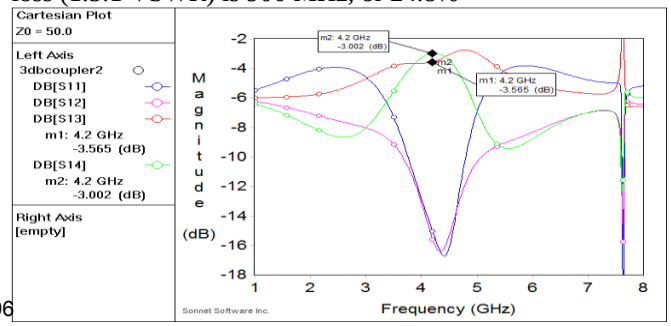

Fig. 2.S-parameters of the re-designed Coupler.

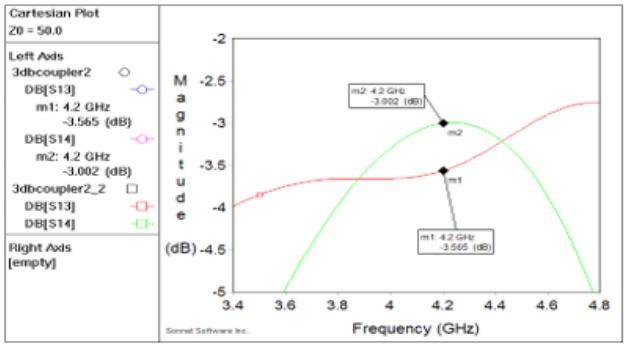

Fig.3 Zoomed in on coupled ports of new design

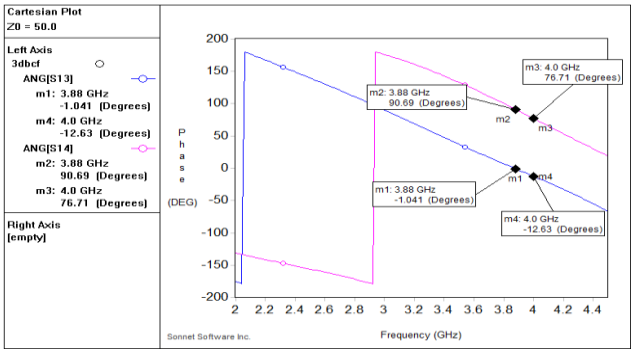

Fig.4 Phase difference between the coupled port

A parametric study of the bandwidth and amplitude balance of the coupler is analyzed. Note that stub widths and lengths which are shown in Figure 1 play important role on the bandwidth and the amplitude balance of the coupler. When stub length is reduced to 2.7 mm, bandwidth is reduced. When the stub length was 3.3 mm, amplitude balance gets worse also. Likewise when the stub widths were 1.1 mm and 1 mm. amplitude balance gets worse. Table 1 has those data. Table 2 has the dielectric thickness analysis.

TABLE I. TOLERANCE ANALYSIS CHANGING THE BRANCH LENGHT AND WIDTHS

Stub Lengths(mm)	Stub Widths(mm)	S11 (3.88 GHz)	S12 (3.88 GHz)	S13 (3.88 GHz)	S14 (3.88 GHz)
3.1-6.4	1.05-1.1	11.83	15.8	4.15	2.98
3.2-6.4	**1.2-1.1**	**15.41**	**16.66**	**3.96**	**2.75**
3.3-6.4	1.2-1.1	20.74	18.98	3.86	2.97

The dimensions of the branch-line coupled lines are determined by the design equations..The dielectric material used is Rogers TMM13 with dielectric constant of 10.2 and thickness of 1.27 mm. The air thickness on top of this material was 5 mm.The Table II shown that changes.

TABLE II. TOLERANCE ANALYSIS CHANGING DIELECTRIC THICKNESS

Dielectric(air) Thickness(mm)	S11 (3.88GHz)	S12 (3.88 GHz)	S13 (3.88 GHz)	S14 (3.88 GHz)
4	12.92	17.44	3.808	3.132
5	**15.41**	**16.66**	**3.96**	**2.75**
6	13.16	17.88	3.748	3.14

Current distribution in Figure 5 clearly shows that the current is equal in 3 dB ports (3and 4) since they have same (half) power and almost no current flows to the isolation port (2).In this figure port 1 has 4 subsections vertically with cell size of 0.05. In order to have a finer mesh, cell size was reduced to 0.001 and 7 subsections were seen but 3 different computer give simulation erors due to memory.

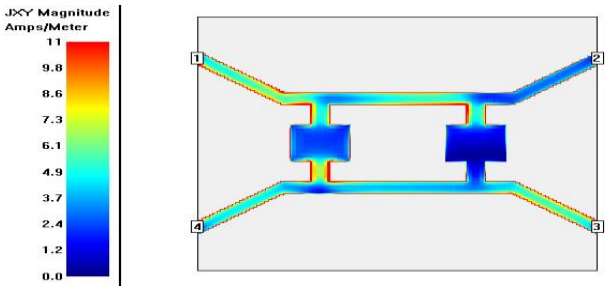

Fig. 5 Current distribution

III. CONCLUSION

In this paper, a 3 dB branch-linemicrostrip 90º hybrid coupler is designed and simulated for the 4-5 GHz band. According to the simulation results of Sonnet Suites [13], all results are satisfactory. Simulation results of the amplitude balance of the coupled ports is (0,25 dB)at the center frequency. A Parametric study is conducted by changing various parameters of the coupler. In order to increase the bandwidth of the branch-line coupler, the stub length and widths are optimized and 14 dB return loss bandwidth of 900 MHz, which is 24.8%, is achieved. Next step of the design is fabrication of the coupler.

References

[1] Zhang Yu, Hu Li, He-Sai Ling "A Tunable Dual-broad-band Branch-line Coupler Utilizing Composite Right/left-handed Transmission Lines" Journal of Zhejiang University SCIENCE,2005

[2] D.C. Ji, B.Wu, X.Y. Ma and J.Z. Chen "A Compact Dual-Band Planar Branch-Line Coupler" Progress in Electromagnetics Research C, Vol. 32, 43-52, 2012.

[3] Prudyus I., Oborzhytskyy V "Design of Dual-Band Two-Branch-Line Couplers with Arbitrary Coupling Coefficients in Bands" Radioengineering, Vol. 23, No.4, Deceember 2014.

[4] Dawar P. , "Analysis of Microstrip Branchline Coupling using Sonnetlite" IJECT Vol.3, Issue 1, Jan-March 2012

[5] Chiu L., "Wideband Microstrip 90 Hybrid Coupler Using High Pass Network" , Hindawi Publishing Corporation,Internattional Journal of Microwave Science and Technology, Volume 2014,Article ID 854346, 6 pages

[6] Saadi A., Salhi M. , Bri S. "Design of an Asymmetric Branch-Line Coupler Using Implicit Space Mapping" International Journal of Advances in Computer Science and Technology (IJACST), Vol.2 , No.11, Pages : 14 – 17

[7] Singh S., Kumar A., Kumar K., Singh Tomar R.,Kumar P. "Extended Port Dual Band Planar Branch Line Coupler" , International Journal of Emerging Technology and Advanced EngineeringVolume 4, Special Issue 1, February 2014

[8] Nosrati M. and Virdee B. "Realization of a Compact Branch-Line Coupler Using Quasi-fractal Loaded Coupled Transmission-Lines" In Electromagnetics Research C, Vol. 13, 33-40, 2010.

[9] Guo-Cheng Wu, Guang-Ming Wang, Li-Zhong Hu, Ya-Wei Wang, and Cang Liu "A Miniaturized Tripled-Band Branch-Line Coupler Based On Simplified Dual-Composite Right/Left Handed Transmission Line" Progress In Electromagnetics Research C, Vol. 39, 1-10, 2013.

[10] Mohammad Jahanbakht and Mohammad TondroAghmyoni "Optimized Ultrawideband and UniplanarMinkowski Fractal Branch Line Coupler" Hindawi Publishing Corporation International Journal of Antennas and Propagation Volume 2012, Article ID 695190, 4 pages doi:10.1155/2012/695190.

[11] N. Zheng, L. Zhou, and W.-Y. Yin "A Novel Dual-Band II-Shaped Branch-Line Coupler With Stepped-Impedance Stubs" Progress In Electromagnetics Research Letters, Vol. 25,11-20,2011

[12] Young-HoonChun, andJia-Sheng Hong "Compact Wide-BandBranch-LineHybrids" IEEE Transactions onMicrowaveTheoryandTechniques, vol. 54, no. 2, february 2006.

[13] Sonnet Suites, version 13.56, 2013. www.sonnetsoftware.com.

Angled Coupledline Bandpass Filter

Sulejman Lužić, Merjema Mehmedović
Department of Electrical and Electronics Engineering
International University of Sarajevo
Sarajevo, Bosnia and Herzegovina

Emina Fajić
Department of Electrical and Electronics Engineering
International University of Sarajevo
Sarajevo, Bosnia and Herzegovina

Abstract-This paper represents a microstrip coupled bandpass filter with few perturbations, which operates in the range between 2,6-3,1 GHz. This filter has a slightly more different geometry than the bandpass filters that we had a chance to see until now, and its geometry is what gives us a chance to achieve much better results if using that specific result. It is pretty easy to produce, and also pretty cheap, due to the fact that we used FR4, which is one of the cheapest dielectric materials, but although it's cheap, it does not mean that it is not good. Au contraire, this filter does its job very good, with he benefit of its low price.

Keywords - bandpass; filter; perturbations; FR4;

I. INTRODUCTION

"Microstrip bandpass filter (BPF) is an indispensable part in the RF front end of various communication systems. It plays a vital role in filtrating the desired signals in the specified frequency band and suppressing the out of band clutter and interference signals. Consequently, the design of microstrip BPFs is always a hot research topic in wireless communication systems."[1] "FIlter design is one of the most interesting fields in microwave engineering. A wide number of different topologies allows to obtain specific responses for a wide range of applications. Inductive filters constitute a strategy of special interest due to their simplicity and easy manufacturing processes associated with these configurations."[2] Over the past decades, the standard traditional parallel-line coupled bandpass filters were widely studied and used in RF front-ends design, but the limited field reliability of those filters challenged people to introduce new kinds of coupled bandpass filters. A bandpass filter is a device which passes frequencies within a certain range, and and rejects frequencies that are outside of that range. Microstrip lines can make good resonators and filters, and they may offer a better compromise regarding the size and performance, than the compromise which is offered by lumped element filters. "The process of manufacturing the microstrip filter is pretty simple, in comparison with the process of manufacturing printed circuit boards. Microstrip coupled bandpass filters have the advantage of largely being planar."[3] These filters are produced by using a thin-film process, and higher Q factors may be easily obtained by using low loss tangent dielectric materials for substrate, such as sapphire or quartz, and lower resistance metals, such as gold, or its cheaper equivalent. Filters, as passive devices, which generally take the greatest percentage of the size of the system, are extremely important when it comes to minimizing the size of the circuit, while keeping the good performance. This paper presents the angled coupledline filter which includes few perturbations, that give the regular coupled bandpass filter a whole new dimension and that expand their operation range.

II. DESIGN AND SIMULATION RESULTS

A new thing related to coupled bandpass filters that was inroduced by Yi-Ming Chen, Yung-Huey Jeng, Sheng-Fuh Chang, and Yu-Jen Huan, in their paper "Dual-Mode Bandpass Filter Using Coupled Ring Resonator", is exactly the usage of that ring resonator. and J. S. Hong and M. J. Lancaster, who incorporated a loop resonator in their paper "Microstrip Bandpass Filter Using Degenerate Modes of a Novel Meander Loop Resonator", while we chose to stick to the old symmetric shape, with incorporating some perturbations.[4] Firstly, we have to mention that we tested and simulated the filter many times with many different possible options (changing d, changing spacings...), and just as J.S. Hong and M. J. Lancaster, who changed the value of their d from 1,5 up to 2,5mm in their paper, we have changed the values of our d from 120 to 150 mils, and the results that we obtained are shown in the table below.[5] We have set some default values for our filter: Dielectric FR-40mils and Air-120 mils, also with the default dimensions and geometry of the filter,that is also shown in the picture below, and when we obtained the result due to our default values, we decided to change those values in order to get as better possible result as we could. The highest freqeuncy that has been resonated in Hong's and Lancaster's paper was about 1,57GHz, while the highest frequency obtained with our filter is 3,2GHz, along with the highest bandwith of 800MHz.

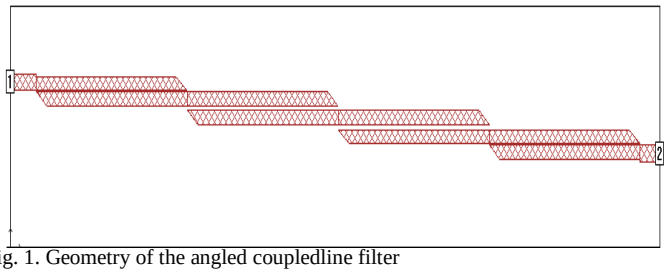

Fig. 1. Geometry of the angled coupledline filter

As we can see in the picture above, we have 8 parts of the filter with dimension of 595x30mils, one part with the dimensions of 101x36mils, and one part with the dimensions of 77x36mils. So, those are the default dimensions that we

didn't change during the project. Also, we have 8 perturbed parts, and the length of that perturbation is 40 mils, which is also a default value that we did not change during the project. On the other hand, we did change spacings between microstrip lines, and we actually divided our spacings in two parts: spacing between the first and the fourth couple of microstrip lines, which we changed from 3-8 mils, and the spacing between microstrip lines of the second and third couple of microstrip lines, that we changed in the range from 10 mils up to 22 mils. The best result that we achieved by changing the spacings between the parts of our filter, with the default d of 120mils is the one with the 4mils-18mils spacing (S11=-14,82dB and S12=-2,06dB).

TABLE I CHANGING SPACINGS BETWEEN THE CENTERED LINES

SPACINGS (mils)		BANDWITH (MHz)	S11	S12
6	18	450	-11,54	-2,13
6	19	550	-12,1	-2,18
6	20	500	-12,61	-2,2
6	21	450	-13,15	-2,26
6	22	450	-13,66	-2,3

TABLE II CHANGING SPACINGS BETWEEN THE EDGED LINES

SPACINGS (mils)		BANDWITH (MHz)	S11	S12
4	18	500	-14,82	-2,06
5	18	500	-13,1	-2,07
6	18	450	-11,54	-2,13
7	18	450	-10,23	-2,2
8	18	550	-9,07	-2,26

Then, we decided to improve our results, so we changed the value of the d from the default one, which was 120 mils. After that, the best result that we have obtained is the one with the 3mils-10mils spacings, with d=150mils, and Air=450mils. Our S11=-12,25 and S12, which is reflection, has the lowest value with these changes that we have introduced, which was our aim, and it equals -1,69 mils.

TABLE 3 CHANGING SPACINGS AND DIELECTRIC CONSTANTS

SPACINGS (mils)		BANDWITH (MHz)	Dielectric constant (mils)	S11	S12
3	10	800	150	-12,25	-1,69
3	12	750	150	-13,43	-1,76
3	14	700	150	-14,6	-1,84
3	15	450	150	-15	-1,88
4	16	500	140	-13,76	-1,95
7	20	500	120	-11,22	-2,27
7	20	550	130	-11,26	-2,25
7	20	500	140	-11,31	-2,23

We have designed, simulated and tested all these various combinations in order to obtain the best result, which is the highest S11, and the lowest possible S12, by using the Sonnet Software, which is a very good designing and simulating program, because it is pretty simple, but still offers various options and combinations, and this software is widely used by many other students and scientist, as it is mentioned in the paper "Dual-Band Bandpass Filter by Using Square-Loop Dual-Mode Resonator". [6]

This picture shows how our graph looks like, and it shows those values of S11 and S12, bandwith and the operating frequency.

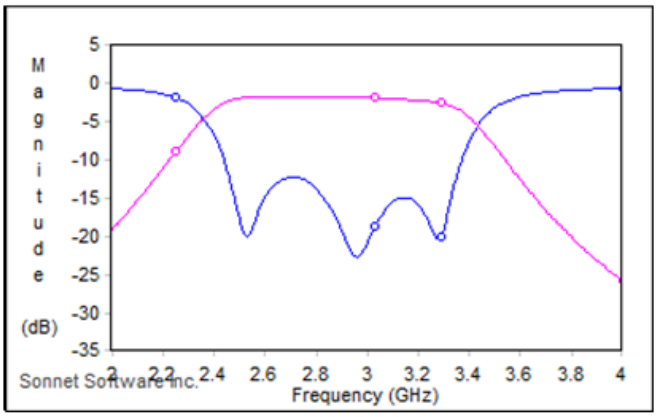

Fig. 2. The graph of the best obtained result

III. CONCLUSIONS

In this paper, we have tried to propose a new topology and a new way of implementing bandpass filters. The structue is formed out of angled coupled lines, and this paper has shown that this kind of filter structure, with the right dimensions, spacings, dielectric constants and some other variables, gives extremely good results in terms of the funcionality of the filter, which was our aim.

REFERENCES

[1] Hongshu LU, Weiwei WU, Jingjian HUANG, Xiaofa ZHANG, Naichang YUAN, "Compact Dual-mode Microstrip Bandpass Filter Based on Greek-cross Fractal Resonator", College of Electronic Science and Engineering, National University of Defense Technology, Changsha, Hunan, 410073, China

[2] Francisco Javier Pérez Soler, Mónica Martínez Mendoza Fernando Daniel Quesada Pereira, David Cañete Rebenaque Alejandro Alvarez Melcon, and Richard J. Cameron., "Design of Bandpass Elliptic Filters Employing Inductive Windows and Dielectric Objects", IEEE Trans. Microw. Theory Tech., vol. 54, no. 11, Nov. 2006, pg.1-2

[3] Belle A. Shenoi (2006)." Introduction to digital signal processing and filter design", John Wiley and Sons. p. 120

[4] Yi-Ming Chen, Yung-Huey Jeng, Sheng-Fuh Chang, and Yu-Jen Huang,"Dual-Mode Bandpass Filter Using Coupled Ring Resonators", Department of Electrical Engineering and Electronics, Center for Telecommunications, National Chung Cheng University, Taiwan, ROC, pages 1-3

[5] J. S. Hong, M. J. Lancaster, "Microstrip Bandpass Filter using Degenerate Modes of a Novel Meander Loop Resonator", IEEE Microwave and Guided wave letters, Vol.5, No. 11, November 1995, pages 371-372

[6] Atallah Balalem, Jan Machac, Abbas Omar, "Dual-Band Bandpass Filter by Using Square-Loop Dual-Mode Resonator", Chair of Microwave and Communication Engineering, University od Magdeburg, 39016 Magdeburg, Germany, pages 1-5

INTERNATIONAL
UNIVERSITY OF SARAJEVO